Cavity quantum electrodynamics with a single spin : coherent spin-photon coupling and ultra-sensitive detector for condensed matter

Matthieu Dartiailh

THÈSE DE DOCTORAT

de l'Université de recherche Paris Sciences et Lettres
PSL Research University

Préparée à Ecole Normale Supérieure

Cavity quantum electrodynamics with a single spin : coherent spin-photon coupling and ultra-sensitive detector for condensed matter

École doctorale n°564

PHYSIQUE EN ÎLE DE FRANCE

Spécialité CONDENSED MATTER PHYSICS

COMPOSITION DU JURY :

Mr Jean-Michel Raimond
Université Paris 6, Jury member

Mr Ferdinand Kuemmeth
Niels-Bohr Institute, Referee

Mr Thomas Ihn
ETH Zurich, Referee

Mrs Julia Meyer
Université Grenoble-Alpes, Jury member

Mr Tristan Meunier
Institut Néel, Jury member

Mr Takis Kontos
Ecole Normale Supérieure, Supervisor

Mr François Mallet
Université Paris 6, Invited member

Mrs Audrey Cottet
Ecole Normale Supérieure, Invited member

Soutenue par **Matthieu Dartiailh**
le 28 11 2017

Dirigée par **Takis Kontos**

ENS ÉCOLE NORMALE SUPÉRIEURE | PSL RESEARCH UNIVERSITY PARIS

Abstract

This thesis work is centered around two key aspects of quantum technologies: quantum information processing and quantum sensing. It builds up onto the microwave light toolbox, developed in circuit quantum electrodynamics, to investigate the properties of mesosocopic circuits. Those circuits, here made out of carbon nanotubes, can be designed to act as quantum bits of information or as condensed matter model systems and this thesis explores both aspects. The realization of a coherent spin-photon interface illustrates the first one. The experiment relies on ferromagnetic contacts to engineer an artificial spin-orbit coupling in a double quantum dot. This coupling hybridizes the spin and the charge degree of freedom of the electron in this circuit. By embedding this circuit into a microwave cavity, whose electrical field can be coupled to the charge, we realize an artificial spin-photon interface. A second project, started during this thesis, focuses on using quantum dot circuits as model systems for studying condensed matter problems. This project consists in coupling, via a microwave cavity, a superconducting qubit, that will serve as a delicate probe, and a single quantum dot circuit. Such a circuit can display several behaviors including the Kondo effect which is intrinsically a many-body effect. In this work, we present both a theoretical study of some possible outcomes of this experiment, and experimental developments. Finally, a theoretical proposition to detect the self-adjoint character of Majorana fermions using a microwave cavity, is presented.

Key words: cQED, quantum dots, spin, carbon nanotube

Résumé

Ce travail de thèse est centré autour de deux aspects des technologies quantiques: le calcul quantique et la mesure quantique. Il s'appuie sur la boîte à outils de la lumière micro-onde, développé en électrodynamique quantique, pour sonder des circuits mésoscopiques. Ces circuits, fabriqués ici à base de nanotubes de carbone, peuvent être conçus comme des bits quantiques ou comme des systèmes modèles de la matière condensée, et cette thèse explore les deux aspects. La réalisation d'une interface spin-photon cohérente illustre le premier. L'expérience repose sur l'utilisation de contacts ferro-magnétiques pour induire un couplage spin-orbit artificiel dans une double boîte quantique. Ce couplage hybride les degrés de liberté de charge et de spin de l'électron. En incluant ce circuit dans une cavité micro-onde, dont le champ électrique peut être couplé à la charge, nous réalisons une interface spin-photon. Un second project est centré sur l'utilisation de boites quantiques comme systèmes modèles pour l'étude de problèmes de matière condensée. Ce projet consiste à coupler, via une cavité micro-onde, un qubit supraconducteur, qui servira de sonde peu invasive, et une boîte quantique unique. Un tel circuit peut exhiber différents comportements dont l'effet Kondo, qui est un effet à N-corps. Dans ce travail, nous présentons à la fois une étude théorique, et des travaux expérimentaux. Finalement une proposition théorique pour détecter le caractère auto-adjoint des fermions de Majorana en utilisant une cavité micro-onde, est présenté.

Mots clés : cQED, boîte quantique, spin, nanotube de carbone

Acknowledgements

This has been a long work and as one can expect I have a number of people to thank.

First, I would like to thank the members of the committee. The very interesting scientific discussion we had during the defense was a real pleasure and a very nice conclusion to this work. I also thank Pr Thomas Ihn and Pr Ferdinand Kuemmeth for reading in details this lengthy manuscript, and for their useful comments on how to improve it.

Je tiens ensuite à remercier Takis mon directeur de thèse, pour m'avoir accueilli dans son équipe et m'avoir donné l'opportunité de travailler dans un environnement exceptionnel. Son optimisme infini, même s'il m'a parfois tapé sur les nerfs, participe pour beaucoup de l'ambiance de l'équipe et nous permet à tous d'avancer. J'ai beaucoup appris à son contact lors de nos nombreuses discussions et je le remercie de sa disponibilité. Une autre de ses qualités est de laisser chacun s'exprimer comme il le souhaite. Son enthousiasme pour l'effort que j'ai fourni pour moderniser le système de contrôle informatique des expériences a beaucoup compter pour moi. Jérémie Viennot, qui m'a formé tant en salle blanche que sur les mesures, mérite lui aussi toute ma gratitude, je n'en serais jamais arrivé là sans lui. Un grand merci à lui. Viennent ensuite Audrey Cottet et François Mallet. Audrey est toujours disponible pour nous discuter les points théoriques de nos expériences et sa rigueur est une source d'inspiration pour moi. François qui a rejoint l'équipe au début de ma dernière année de thèse et qui a grandement participé à remonter mon moral défaillant après une fin de deuxième année compliqué. Les expériences n'ont pas toutes marchées mais je suis heureux d'avoir eu l'occasion de travailler avec lui. Je tiens aussi à remercier tous les autres thésards et post-doc de l'équipe: Laure, Matthieu Desjardins, Matthieu Baillergeau, Tino, Laurianne et Fédérico avec qui j'ai eu l'occasion de travailler. Ce fut toujours un plaisir et j'espère vous recroiser tous à l'avenir. Je dois aussi remercier les deux stagiaires que j'ai eu l'occasion d'encadrer: Filippo et Camille. Ni l'un ni l'autre n'ont vu le meilleure côté des expériences et j'en ai toujours été désolé. J'essaye de penser que ce n'est pas à cause ça que tous deux font désormais de la théorie. Après en avoir beaucoup entendu parler en début de thèse, j'ai eu l'occasion de travailler brièvement avec Matthieu Delbecq lorsqu'il a rejoint l'équipe et je lui souhaite beaucoup de réussite.

Mais le laboratoire et le département sont bien plus grand que l'équipe HQC. Je remercie tous les membres de l'équipe d'électronique quantique Benjamin, Landry, Emmanuelle, Philippe, Danijela, Nathanael, Quentin et aussi Zaki et Raphaël qui ont désormais rejoint la HQC. Ce fut toujours un plaisir de discuter avec vous et j'y ai aussi beaucoup appris. Je n'oublie pas les autres membres du groupe de physique mésoscopique Bernard,

Gwendal, Arthur, Quentin, Holger, Rémi, David et Erwann avec qui j'ai eu l'occasion d'interagir, toujours de façon constructive et agréable.

Mais la thèse ce n'est pas que la recherche et je tiens à remercier tous les enseignants avec qui j'ai eu l'occasion de travailler: Arnaud et Frédéric pour l'IPT, Jihad, Gabriel, Tigrane et Sophie pour les TD de relativité.

Mais il y a encore bien d'autres personnes sans qui ce travail n'aurai pu avoir lieu. En haut de cette liste, se trouvent les deux ingénieurs de salle blanche Michaël et José. J'ai passé bien du temps en salle blanche et même si j'aurais aimé que certaines choses marchent mieux, c'est sans aucun doutes grâce à eux que la salle blanche fonctionne. Je remercie aussi les fantastiques membres du service de cryogénie qui ont toujours fait en sorte que les expériences restent à froid (même l'été ou à Noël), un grand merci à Olivier, Aurélien et Florent. Le service électronique a permis des améliorations clefs de nos montages et je tiens à remercier David, Anne et Philippe. Je remercie aussi les membres du bureau d'étude et de l'atelier: Nabil, Arnaud, Pascal, Jules et Mathieu. Enfin je remercie Anne et Olga, les deux secrétaires du laboratoire, qui fournissent un travail héroïque pour passer toutes nos commandes et géré nos déplacements, ainsi que Jean-Marc et Jérôme les directeurs du laboratoire durant ma thèse.

Mais la vie ne se limite pas au laboratoire. Je tiens à remercier ma merveilleuse épouse Lise, qui m'a soutenu pendant toutes ces années et n'a pas douté de moi même quand je ne pouvais en dire autant. Puisse notre vie continuer à être aussi douce et épanoui. Je tiens aussi à remercier ma mère qui jamais ne se plaint lorsque je lui raconte tous mes ennuis de labo même si elle n'en comprends qu'une fraction. Je remercie aussi mon père qui n'est sans doute pas étranger à ma passion pour les science et qui m'a transmis une partie de sa rigueur et de ses intuitions. Et tous les membres de ma famille et de celle de Lise pour leur soutien. Je remercie aussi tous mes amis: Thomas et David nos témoins de mariage, Anil, Anna, Alexandre, Constance, Louis, Lilly, Marie, Cyrille, Yoann, François, Paul.

Finalement parce j'ai tout de même beaucoup codé pendant cette thèse je tient à remercier certains développeur avec qui j'ai eu l'occasion de collaboré en particulier:

- @sccolbert for developping the fantastic library enaml and for allowing me to join the adventure too
- @hgrecco for PyVISA and a number of stimulating discussion
- @sklam, @pitrou, @seibert for their great work on the Numba project and their patience with me when I contributed

Résumé long

Parmi les phénomènes dont l'explication a mené à l'émergence de la mécanique quantique, on peut citer l'effet photo-électrique. Cet effet, qui ne peut être expliqué dans une description purement ondulatoire de la lumière, força les scientifiques à reconsidérer la lumière dans une approche corpusculaire. Dans cette approche, les quantas de lumière, les photons, ne se comporte pas uniquement comme des sphères dures mais aussi comme des ondes. Cette dualité s'applique aux photons mais aussi à n'importe quel autre object en principe. Et tandis que pour les photons, la représentation classique est la représentation ondulatoire et la quantique la représentation corpusculaire, pour la plupart des objets c'est l'inverse. Un exemple est la molécule de fullerène dont il a été démontré qu'elle interférait de façon similaire à la lumière dans une expérience de fentes d'Young[1]. Il convient cependant de noter que ces propriétés ne se manifestent pas seulement dans le cas d'objets isolés mais aussi dans la matière condensée.

Dans un système de matière condensée, les électrons peuvent, sous certaines conditions, présentés des comportements liés à leur nature ondulatoire. Bien entendu, la cohérence des fonctions d'onde électroniques peut être détruite de bien des manières: lors de collisions avec d'autres électrons ou avec les atomes du réseau cristallin lorsqu'ils vibrent par exemple. C'est pourquoi dans les conditions ambiantes, la description corpusculaire des électrons suffit à décrire les circuits électriques. Cependant lorsque la taille des circuits devient faible, que l'on améliore la qualité des matériaux et si la température est abaissée, la fonction d'onde électronique peut se propager sur de longues distances sans être perturbée. Les phénomènes d'interférences peuvent dès lors fortement modifier les propriétés du circuit. De tels phénomènes ne peuvent être décrit classiquement et forment les fondations du transport quantique. Parmi les phénomènes observables on peut citer: la formation d'interféromètres de type Fabry-Pérot, la localisation faible ou forte d'électrons dans certaines portions du circuit, l'anti-localisation, ou l'effet Aharonov-Bohm.

Les circuits dans lesquels se manifestent ces effets n'appartiennent ni au monde macroscopique ni réellement au monde microscopique puisqu'ils contiennent, malgré leur taille,

encore des milliards d'atomes. On les qualifie généralement de circuits mésoscopiques. Expérimentalement, il est généralement nécessaire de les refroidir à des températures proches du zéro absolu (sous 4K ou de façon équivalente $-269°C$), pour que des phénomènes non-classiques soient observables.

Depuis les années 1980, ce champ de recherche s'est constamment élargi avec le développement de nouveau matériaux et la conception de nouveaux circuits. Partant de circuits composés uniquement de métaux, agencés soit en couches, fils ou poussant les systèmes à leurs limites d'un atome unique joignant deux ilots métalliques, ce champ de recherche s'est étendu aux semi-conducteurs, aux oxydes et aux molécules. Dans chaque cas, les propriétés du circuit sont le résultat non seulement des propriétés intrinsèques des matériaux mais aussi de la manière dont ils sont combinés. L'utilisation d'électrodes ferromagnétiques ou supraconductrices permet, au travers de l'effet de proximité, d'induire ce type de propriétés dans des matériaux qui ne les possèdent pas. Ce type de combinaison a donné naissance aux champs de la spintronique et de la supraconductivité mésoscopique.

Dans ce travail de thèse, nous nous intéressons à une sous classe particulière de circuits: les boites quantiques [2]. Dans ce type de structure, toutes les dimensions spatiales (hauteur, largeur, longueur) sont réduites de façon à ce que le vecteur d'onde de la fonction d'onde électronique soit quantifié dans toutes les directions. Une telle quantification conduit à l'existence d'un ensemble discret d'état autorisé similaire à ceux d'un atome. Ces boîtes à électrons peuvent être réalisées à partir d'objets de plus haute dimension, telle qu'un fil unidimensionnel ou un gas électronique piégé dans un plan, dès lors que les électrons peuvent être confinés en utilisant, par exemple, des contacts métalliques ou des champs électriques. Dans le cadre de cette thèse, nous utilisons des nanotubes de carbone (CNT) qui sont des conducteurs unidimensionnels. En les contactant à des électrodes métalliques, les électrons sont confinés dans la dernière dimension ce qui conduit à la formation de boîtes quantiques [3]. Comparé aux atomes "naturels", dont les propriétés sont fixées, les propriétés ces structures peuvent être ajusté sur de large gammes grâce à des leviers macroscopiques. L'application de potentiels électrostatiques est un de ces leviers. Un grand nombre de phénomènes de transport quantique peuvent être observés dans les boîtes quantiques dont l'effet Kondo qui résulte de la formation d'un état intriqué à N-corps. Cet effet résulte de l'interaction du spin d'un électron piégé dans la boîte quantique avec les électrons de conduction des électrodes, et modélise ce qui peut se passer dans un métal au voisinage d'une impureté magnétique.

De tels atomes artificiels pourraient trouver des applications dans le cadre du traitement quantique de l'information. En particulier, le spin de l'électron est une système à deux niveaux naturel qui peut être utilisé comme qubit [4]. De plus, son faible couplage

naturel à son environnement permet d'espérer de long temps de cohérence qui sont clefs dans le cadre de l'information quantique, comme discuté dans le chapitre 1.

Historiquement, l'information quantique expérimental a émergé à la fin des années 1990 dans les communautés de la résonance magnétique nucléaire [5] et de l'optique atomique et moléculaire. En particulier, le champ de l'électrodynamique quantique en cavité (QED), qui s'intéresse à l'interaction lumière-matière à l'échelle la plus élémentaire en couplant un atome unique à un unique photon, a développé un grand nombre d'outils permettant de contrôler et de mesurer de petits systèmes quantiques[6]. Le développement d'atomes artificiels dans la matière condensée, à base de circuits supraconducteurs, a permis de transférer ces idées aux circuits [7]. Ce nouveau champ est dénommé électrodynamique quantique sur circuit (cQED).

Le champ, auquel ce travail de thèse appartient, est le champ voisin de l'électrodynamique quantique mésoscopique dans laquelle le circuit supraconducteur, utilisé comme atome artificiel, est remplacé par un circuit mésoscopique tel qu'un contact atomique [8] ou une boîte quantique [9, 10, 11, 12, 13]. L'émergence de ce champ a, dans un premier temps, été motivé par la possibilité de coupler des qubits distants via une cavité comme démontré en cQED [14, 15]. Jusqu'à très récemment [16], les qubits réalisés dans des circuits de boîtes quantiques ne pouvaient être couplé de manière fiable entre eux [17], et donc la perspective de coupler deux systèmes distant via une cavité semblait très intéressante. Cependant, cette possibilité n'était qu'une des multiples possibilités qui ont émergé avec ce nouveau champ. Par exemple, la possibilité de réaliser un MASER, dans lequel le circuit de boîtes quantiques joue le rôle de milieu amplificateur, avait déjà été envisagée en 2004 [18]. Même si la réalisation du couplage de deux systèmes distants reste un but à long terme, un MASER a été réalisé récemment [19].

De part la double nature des circuits de boîtes quantiques, atomes artificiels d'une part et systèmes modèles pour la matière condensée, ce champ est plus large que le traitement quantique de l'information. En particulier, il est possible de transposer les techniques développé dans le cadre de la cQED et de les adapter pour réaliser des mesures de haute précision sur des systèmes modèles de la matière condensée. Ce travail de thèse s'efforce d'illustrer cette double nature du champ.

Le manuscrit est divisé en six chapitres. Le premier est une brève introduction des technologies quantiques et de la manière dont elles ont inspirés les travaux présentés dans cette thèse. Ce chapitre est divisé en deux parties. La première traite de l'encodage de l'information quantique dans un bit d'information. Elle traite notamment des phénomènes de relaxation et de de décohérence, et introduit deux plateformes qui ont servi à la réalisation de qubit: les circuits supraconducteurs et les spin-qubits. L'objectif de ce chapitre étant principalement introductif, seul les principes de fonctionnement de

base de ces systèmes sont abordés. Toujours dans la même partie, l'interaction de qubits avec un mode bosonique, pouvant servir de canal de communication entre deux qubits, est introduite, à nouveau sur des considérations assez générale. La seconde partie de ce premier chapitre traite de l'utilisation de systèmes quantiques comme sonde de précision. Elle discute dans un premier temps l'utilisation des photons piégés dans une cavité de grande finesse, avant de discuter le cas des systèmes à deux niveaux qui est illustré sur l'exemple du centre NV^- du diamant. Ces différentes approches peuvent être transposé à la situation expérimentale du chapitre 5.

Le second chapitre se concentre plus directement sur les systèmes utilisés dans le cadre de cette thèse et est divisé en deux parties. La première traite des circuits mésoscopiques utilisés. Cette partie commence par présenter les propriétés des nanotubes de carbone à partir desquels sont réalisées les boîtes quantiques utilisées dans le cadre de ce travail de thèse. La physique des boîtes quantiques est ensuite discutée. On s'intéresse tout d'abord aux boîtes quantiques uniques qui seront utilisés dans le chapitre 5 et notamment à leur susceptibilité de charge. Deux principaux régimes sont discutés: d'une part le régime de blocage de Coulomb, dans lequel la susceptibilité peut-être calculée analytiquement, et le régime Kondo pour lequel des techniques numériques sont utilisées. La physique des doubles boîtes quantiques est discutée dans la section suivante et sert de base au chapitre 4. Finalement, cette partie se conclue sur la présentation du transmon, un qubit supraconducteur, qui est utilisé dans le cadre du chapitre 5. La seconde partie discute les propriétés des résonateurs/cavités supraconductrices utilisées comme boîtes à photons, la manière dont on peut y coupler les circuits mésoscopiques présentés précédemment ainsi que les différents régimes de couplage qui peuvent en résulter.

Le troisième chapitre est dédié aux techniques expérimentales mises en œuvre dans le cadre de ce travail. La conception des échantillons est tout d'abord discutée et notamment l'apport des outils de simulations numériques. On montre notamment comment la structuration du champ électrique micro-onde à des échelles bien inférieures à la longueur d'onde peut permettre d'augmenter le couplage entre les photons de la cavité et les circuits mésoscopique (Figure 1).

La fabrication des échantillons, les techniques de mesure nécessaire à leur caractérisation, et les outils d'interfaçage informatique mis en œuvre pour automatiser les mesures sont ensuite discuter.

Les trois derniers chapitres se concentrent chacun sur un aspect particulier de ce travail de thèse.

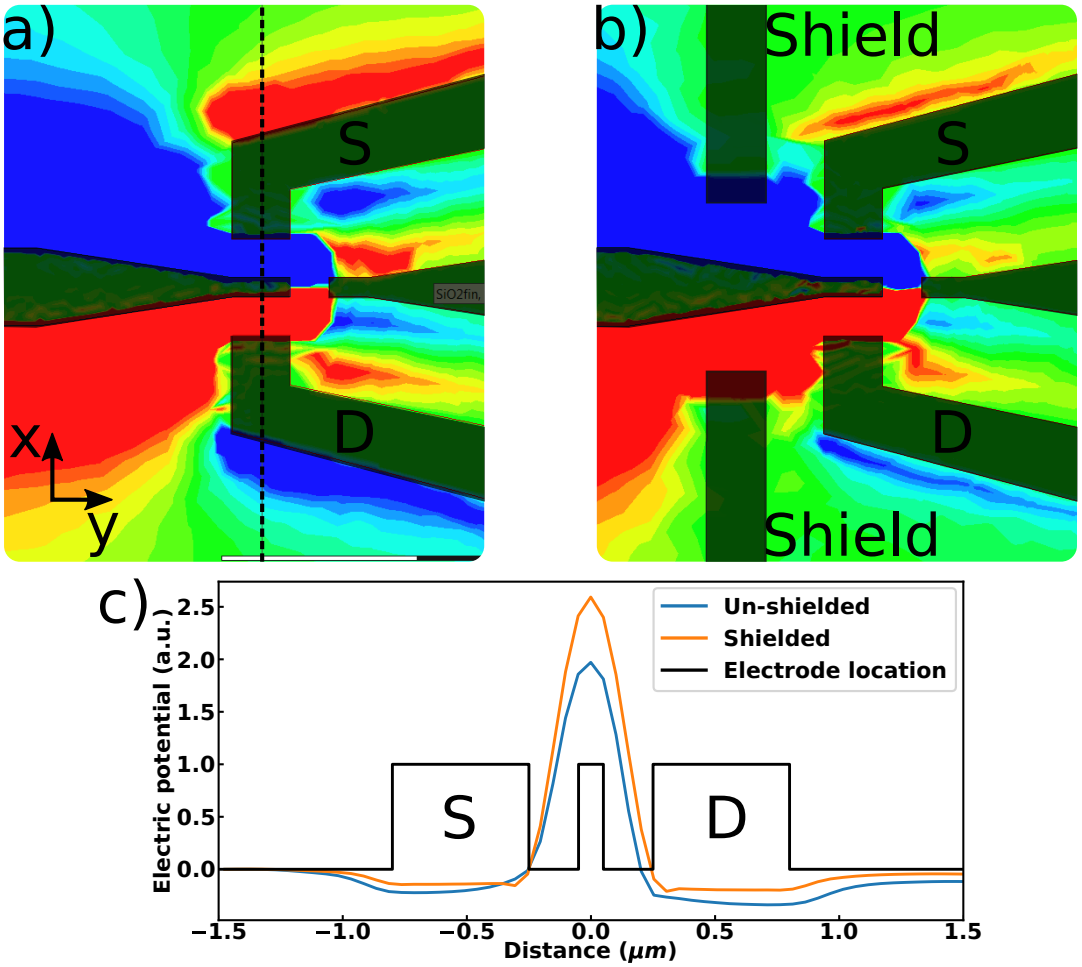

FIGURE 1: Ecrantage d'une boîte quantique unique:

a), b) Champ électrique simulé (composante selon x) d'un mode à 7.5 GHz (longueur d'onde $\sim$ 1 cm) dans deux géométries a) non-écranté b) écranté. Les régions grisé correspondent à l'emplacement d'électrodes métalliques (100 nm de large pour la plus fine). L'échelle de couleur est la même pour les deux tracés mais est tronquée pour aider le lecteur à identifier les différences dans la géométrie du champ.

c) Tracé du potentiel électrique (intégrale du champ) le long de la ligne pointillé de la figure a). L'origine du potentiel est prise à gauche du tracé, ce qui n'est pas exact comme le montre le fait que le potentiel est non-nul pour les grandes valeurs de x. On peut noter une augmentation du maximum du potentiel de l'ordre de 30% dans la situation écrantée.

Couplage spin-photon cohérent dans une architecture de cQED

Le quatrième chapitre présente une expérience dont le but était d'atteindre le régime de couplage fort entre le spin d'un électron unique piégé dans un circuit mésoscopique et les photons piégés dans une cavité. L'architecture de circuit que nous avons utilisé pour réaliser cette expérience a été proposé en 2010 dans [20]. Cette architecture,

présenté dans la figure 2, repose sur une double boîte quantique contactée à des électrodes ferromagnétiques.

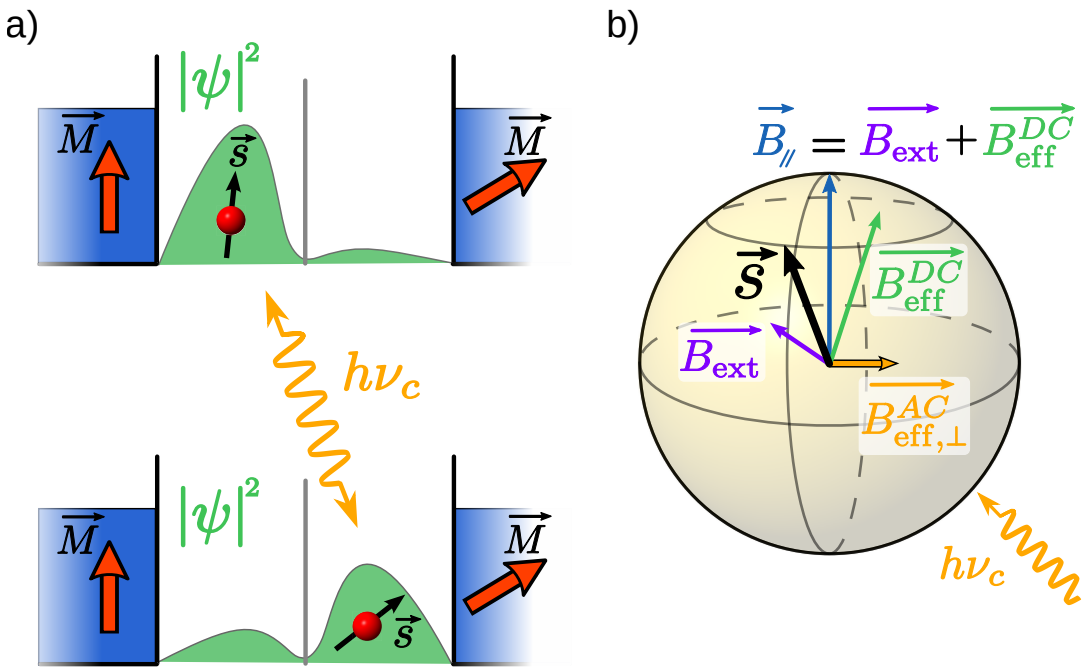

FIGURE 2: Couplage spin-orbite artificiel dans une double boîte qunatique à base de CNT :
On considère un électron de spin $\vec{s}$ piégé dans une double boîte quantique. On représente sa densité de probabilité de présence $|\psi|^2$ en vert. Chaque boîte est connectée à une électrode ferromagnétique, dont l'aimantation est notée $\vec{M}$. L'aimantation induit une polarisation de spin de la fonction d'onde. Cependant, comme les aimantations des électrodes ne sont colinéaires, les axes de quantification dans chaque boîte ne le sont pas non plus, comme illustré en a). Ainsi en induisant des oscillations de l'électron entre les deux boîtes grâce à un champ électrique alternatif, l'électron voit un champ magnétique AC effectif qui est orthogonal à son axe de quantification. Ce champ effectif peut-être utilisé pour contrôler le spin. L'axe de quantification est défini par les champs induits par les électrodes et par le champ magnétique extérieur appliqué.

Les aimantations des électrodes ne sont pas colinéaires si bien que les axes de quantification du spin de l'électron dans chaque boîte ne sont pas colinéaires. Lorsque l'électron passe d'une boîte à l'autre, le spin tourne ce qui peux être vu comme le résultat d'un couplage spin-orbit. Ce couplage permet de coupler le degré de liberté orbital de l'électron et son spin. Le degré de liberté orbital peut être couplé au photons piégés dans la cavité, ce qui permet de au final d'obtenir un couplage spin-photon. Grâce à l'expérience acquise dans le laboratoire lors d'expériences précédentes [13], nous avons inclut ce circuit dans une cavité micro-onde, cf figure 3.

Dans ce système nous avons démontré l'existence de transitions hybrides mêlant le degré de liberté orbital et l'état de spin (figure 4) ainsi qu'un couplage cohérent entre

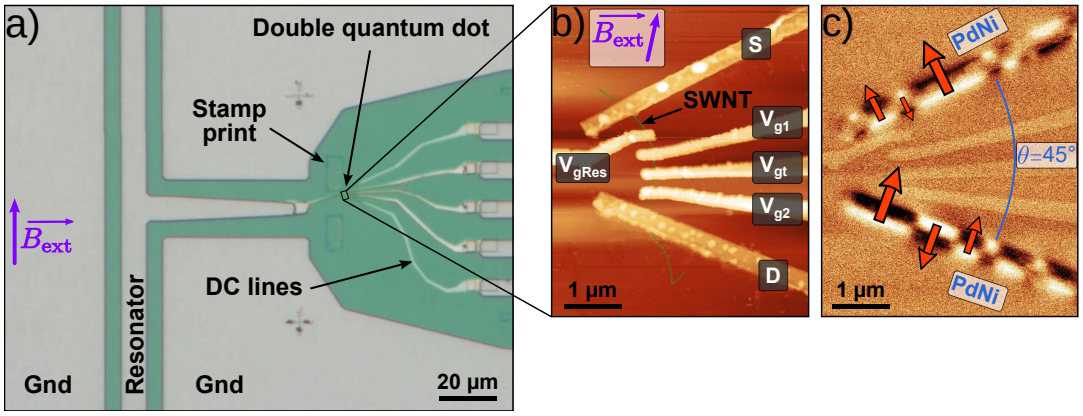

FIGURE 3: Échantillon:

a Image (microscope optique) de l'échantillon étudié centré sur la double boîte quantique.

b Image de microscopie à force atomique de l'échantillon sur laquelle le CNT apparaît en fausses couleurs.

c Image de microscopie à force magnétique. L'aimantation des électrodes ferromagnétiques apparaît dans le damier blanc et noir où les zones blanches et noires correspondent aux pôles Nord et Sud de l'aimantation.

les photons micro-ondes et une transition associée à un changement de l'état du spin électronique [21]. Le couplage ainsi obtenu est de l'ordre du MHz, ce qui est un ordre de grandeur inférieur au couplage aux états orbitaux mais 5 ordre de grandeur supérieur au couplage magnétique direct que nous pourrions obtenir dans ce système.

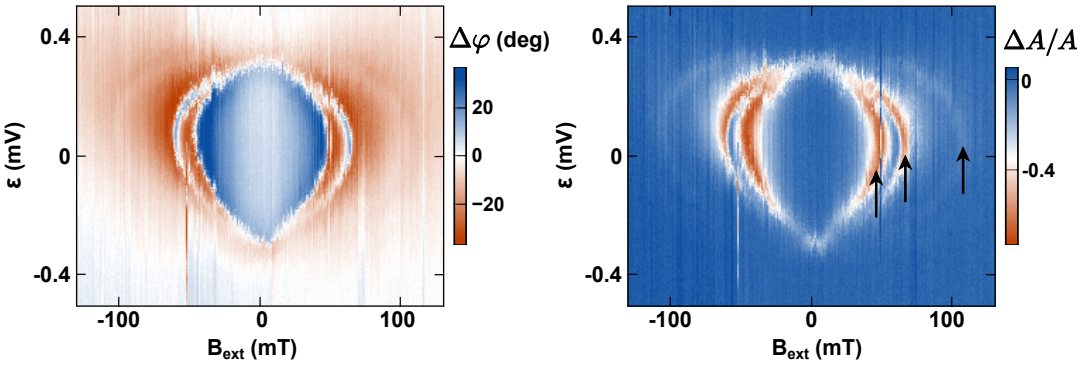

FIGURE 4: Dispersion des états du système fonction de la grille ϵ et du champ magnétique externe B:
La carte de la transmission de la cavité (figure de droite) présente trois creux correspondants à la mise en résonance de trois transitions avec la cavité. Ces trois transitions dépendent à la fois de la grille et du champ magnétique, ce qui montre leur nature hybride.

Finalement ce chapitre discute l'influence de la parité du nombre d'électron dans la double boîte sur le spectre du système.

Sonder les dynamiques d'une boîte quantique à l'aide d'un transmon:

Le cinquième chapitre explore la possibilité d'utiliser un qubit supraconducteur (un transmon) comme une sonde de grande sensibilité des propriétés d'une boîte quantique. Il se concentre sur les boîtes quantiques uniques qui peuvent être utilisé comme systèmes modèles pour la matière condensée. Dans de précédents expériences menés dans le laboratoire [22, 23], l'utilisation d'une cavité micro-onde a été cruciale pour révéler certaines propriétés de ces circuits. L'addition d'un transmon à de tels expériences ouvre plusieurs nouvelles perspectives. Tout d'abord le transmon pourrait être utilisé pour analyser le champ photonique de la cavité et mesurer, pour la première fois de façon quantitative, le couplage entre le champ photonique et la boîte quantique. Dans les expériences précédemment citées, seul le produit du couplage par le nombre de photon dans la cavité a été mesuré et le nombre de photons ne pouvait être mesuré avec précision. Une autre perspective, exploré de manière théorique dans une première partie, consiste à utiliser transmon comme spectromètre, ce qui peut fournir de nouvelles informations sur la dynamique interne de ces circuits dans le régime de blocage de Coulomb et dans le régime Kondo.

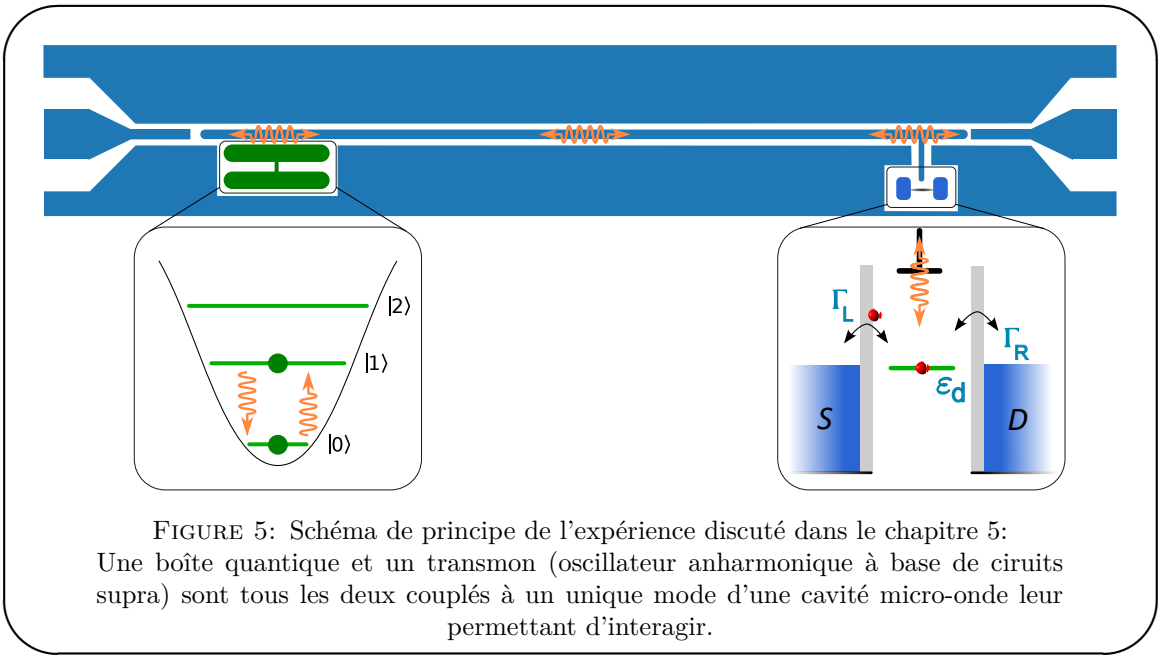

FIGURE 5: Schéma de principe de l'expérience discuté dans le chapitre 5: Une boîte quantique et un transmon (oscillateur anharmonique à base de ciruits supra) sont tous les deux couplés à un unique mode d'une cavité micro-onde leur permettant d'interagir.

La partie expérimentale ne comporte que des résultats préliminaires, notamment la caractérisation d'un des premiers transmon réalisé. L'absence de résultats plus significatifs tient aux difficultés rencontrées lors de la fabrications des échantillons.

Probing Majorana fermions using a cavity:

Le sixième et dernier chapitre est dédié à un travail théorique centré sur l'étude des circuits topologiques hybrides grâce aux photons d'une cavité micro-onde [24]. Les circuits hybrides combinant des nano-conducteurs dotés d'un fort couplage spin-orbit contactés à des électrodes supra-conductrices ont été proposés comme base pour obtenir des fermions de Majorana [25, 26]. Jusqu'à présent, ces structures ont été principalement étudié via des mesures de transport DC qui révèle la densité d'état de ces circuits [27, 28, 29, 30, 31, 32]. Dans ce travail nous proposons un protocole permettant de mettre en évidence le caractère auto-adjoint des fermions de Majorana reposant sur la mesure couplé des propriétés de transport du système et de celles d'une cavité micro-onde à laquelle le système est couplé. Une particularité de ce travail est qu'il traite l'intégralité des effets du contact supraconducteur, et notamment la densité d'état résiduelle sous le gap supra souvent observé dans les réalisations expérimentales. La signature du caractère auto-adjoint de la paire d'état de Majorana dont chacun des membres est localisé à une des extrémités du fil provient de leur absence de couplage au champ photonique. Le protocole proposé permet de déterminer indépendamment de toute théorie les énergies auxquelles une signature d'un couplage entre la photons et les états de Majorana serait attendu. Il permet de plus de vérifier que l'absence de signature n'est pas le fruit de l'absence de couplage entre le circuit et les photons en utilisant la signature d'une transition entre les états de Majorana et la densité sous le gap du supraconducteur.

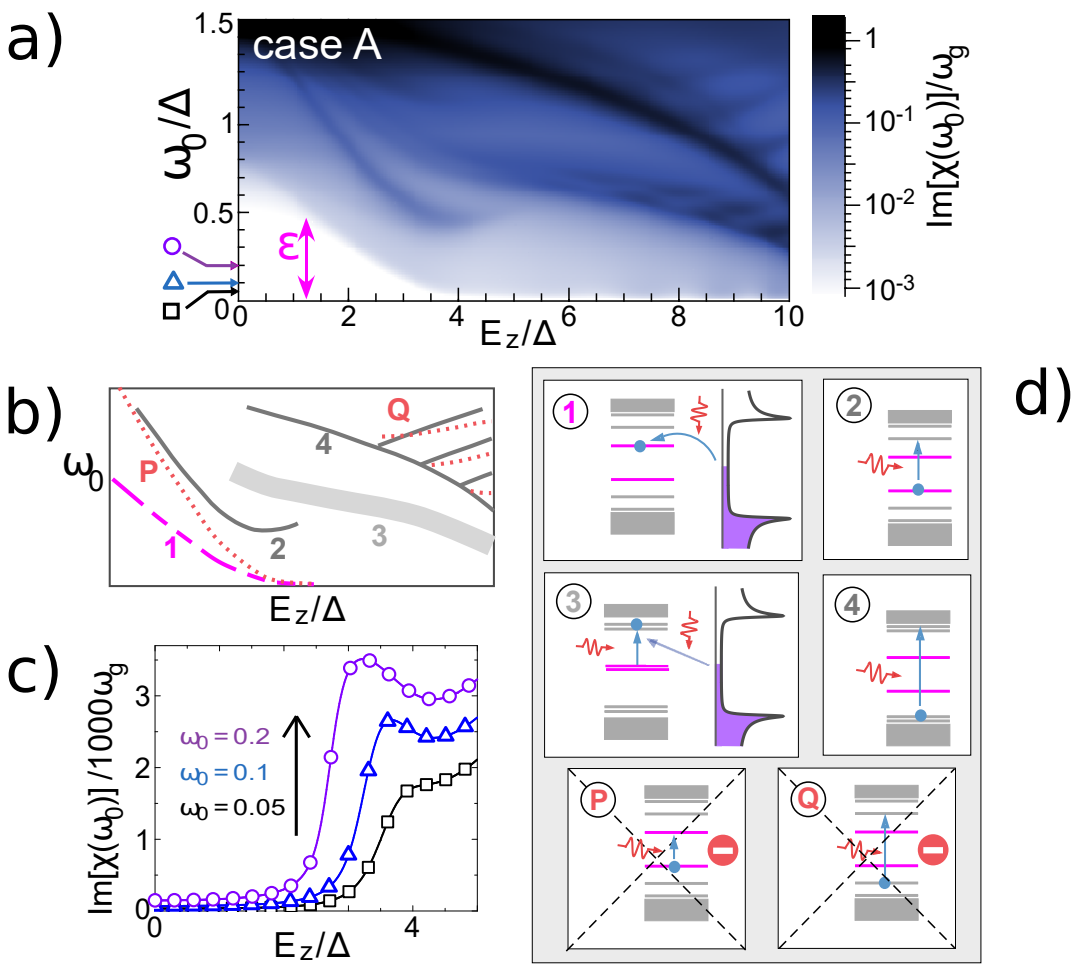

FIGURE 6: Dissipation induite par le circuit hybride fonction du champ magnétique externe appliqué E_Z et de l'énergie considérée ω_0:
La figure a) présente les résultats d'une simulation menée sur une chaine unidimensionnelle discrète avec couplage spin orbite et couplage à un contact supraconducteur. On peut y discerner un grand nombre de strcutures qui sont schématisées dan la figure b). La figure c) présentent trois coupes prises à trois énergies différentes de la structure 1. Les marqueurs utilisées correspondent à ceux présents sur le coté gauche del afigure a). La figure d) décrit la nature des transitions associées à chacune des structures de la figure b).

1 Cette structure correspond à une transition entre la densité sous le gap et les états de Majorana. Elle apparaît quand la fréquence de la cavité est égale à différence en énergie entre les deux états de Majorana $\omega_0 = \epsilon$

2 Cette structure correspond à une transition entre l'état de Majorana à basse énergie et un état d'Andreev.

3 Cette structure correspond à un processus implicant à la fois les états de Majorana et la densité sous le gap.

4 Cette structure correspond à des transitions entre états d'Andreev.

P and Q Ces structures, qui sont absentes des résultats de simulations, correspondrait à des transitions entre les deux états de Majorana ou deux états non-dégénérés d'Andreev. Leur absence prouve le caractère auto-adjoint des états de Majorana.

Cette figure est tirée de [24]

Contents

Abbreviations

QED	Quantum electrodynamics
cQED	Circuit quantum electrodynamics
JJ	Josephson junction
SIS	Superconductor-Insulator-Superconductor
CNT	Carbon nanotube
SWCNT	Single wall carbon nanotube
SD	Single quantum dot
DQD	Double quantum dot
mQED	Mesoscopic quantum electrodynamics
NV	Nitrogen vacancy
SOC	Spin-orbit coupling
2DEG	2-dimensional electron gas
SQUID	Superconducting quantum interference device
B/AB	Bonding/Anti-bonding
CPW	Coplanar wave guide
PCB	Printed circuit board
SEM	Scanning electron microscope
MIBK	Methyl isobutyl ketone
IPA	Iso-propanol
CVD	Chemical vapor deposition
AWG	Arbitrary waveform generator
DOS	Density of state
MBS	Majorana bound states
ABS	Andreev bound states

Introduction

Among the phenomena whose explanation ultimately led to the emergence of quantum mechanics, one can cite the photo-electric effect. This effect, which cannot be explained in a purely ondulatory description of the light, forced people to reconsider that light may be made out of quanta. These quanta, the photons, behave not only as hard particles but also as waves. This duality applies to photons in quantum mechanics but in principle also to any object. And while for photons, the classical representation is the wavy one, and the quantum representation the particle one, for many other objects it goes the other way around. One can think of large objects such as molecules like fullerene that were demonstrated to interfere similarly to light in Young slits experiments [1]. But actually those properties do not manifest only for isolated objects but also in condensed matter systems.

In condensed matter systems, electrons can under certain conditions exhibit behaviors that are linked to their wavy nature. Of course, the coherence of the electronic wave can be destroyed in many ways: through collisions with others electrons or with atoms vibrating in the crystal lattice. This is why under ambient conditions, we can perfectly describe electric circuits using a corpuscular representation of the electrons. However when the size of the circuits becomes very small, the quality of the material improves and if the temperature is reduced, the electronic wave can propagate without being disturbed over large distances, resulting in interference between different waves. Such phenomena cannot be described classically and are at the foundations of the field of quantum transport in which one can observe for example: electronic Fabry-Perot interferometers, weak or strong localization of the electrons in particular areas, or the Aharonov-Bohm effect.

Because the circuits in which those effects manifest themselves belong neither to the macroscopic world nor to the truly microscopic world as they still contain billions of

atoms, they are often referred to as mesoscopic circuits. Experimentally, they usually need to be cooled down to cryogenic temperatures (below 4K or equivalently below $-269°C$) to display a truly non-classical behavior.

Since the 1980s, this field has constantly broadened as new materials were developed and new circuits have been designed. Starting from purely metallic circuits, either in layers, wires, or pushing the systems to their limits and limiting the contact between two islands to a single atom, the field grew to include semi-conductors, oxides and molecules. In each case, the properties of the circuit are tailored, not only by the intrinsic properties of materials, but also by how they are combined. Using ferromagnetic contacts or superconducting contacts can induce those properties in materials lacking them through proximity effects, which gave birth to the fields of spintronics and mesoscopic superconductivity.

In this thesis, we are interested in a particular subclass of circuits called quantum dot circuits [2]. In such structures, all the spatial dimensions (height, width, length) are reduced such that the allowed wave vector for the electronic wavefunction is quantized along all directions. This means that those structures exhibit a discrete spectrum similar to the one of an atom. These electron boxes can be realized starting from higher-dimensional objects, provided that the electrons can be ultimately confined using either metallic electrodes or electrostatic fields. For example, in this work, we use carbon nanotubes which are naturally unidimensional conductors. By contacting them to metallic electrodes, we confine the electrons in the last available dimension hence fabricating our quantum dots circuits [3]. Compared to natural atoms, whose properties are fixed, the properties of those structures can be tuned over large ranges using macroscopic knobs, such as DC voltages. Quantum dot circuits display most of the quantum transport phenomena mentioned above. An important effect, which can be studied in quantum dots, is the Kondo effect which reveals many-body interactions. The spin of an electron confined in the quantum dot is interacting with the many electron spins of the contacting electrodes, which models the presence of a magnetic impurity in a metal.

Such artificial atoms appear as a potential resource for quantum information processing. In particular, the spin of a trapped electron is a natural two-level system that can be used as a qubit [4]. Furthermore, its natural weak coupling to its environment promises

long coherence times which is a key property in the perspective of quantum information, as discussed in chapter 1.

Historically, experimental quantum information emerged in the late 90's in the Nuclear Magnetic Resonance (NMR) [5] and Atomic Molecular and Optical (AMO) physics communities. In particular, the field of cavity quantum electrodynamic (QED), which studies the light matter interaction at the most elementary level by coupling a single atom to a single mode of the electromagnetic field, developed a large toolox to control and measure small quantum systems [6]. The development of artificial two-level systems in condensed matter, based on superconducting circuits, has allowed to transfer these ideas to circuits [7]. This new field was named circuit QED (cQED).

The field, into which this thesis work falls, is the related field of mesoscopic QED, in which the superconducting circuit used as an artificial atom is replaced by a mesoscopic circuit such as an atomic contact [8] or a quantum dot circuit [9, 10, 11, 12, 13]. The emergence of this field was at first driven by the possibility to couple distant qubits through the cavity as demonstrated in cQED [14, 15]. Up to very recently [16], solid state qubits based on quantum dot circuits could not achieve in a reliable fashion a coupling between two qubits [17], the perspective of long distance coupling through a microwave cavity hence appeared promising. However, this was only one among several directions that emerged with this new field. For instance, the realization of MASERs had already been envisionned in 2004[18]. Even though the coupling of two distant qubits remains a long term goal, a MASER has been demonstrated recently [19].

Thanks to the dual nature of quantum dot circuits, artificial atoms on one side and condensed matter model systems on the other, this field encompasses more subjects than quantum information processing. In particular, one can transpose techniques developed in the context of cQED and adapt them to high sensitivity measurements of condensed matter model systems. This thesis work will try at best to illustrate this dual nature of the field.

This manuscript is divided into six chapters. The first one serves as a brief introduction to quantum technologies and how they have inspired this thesis. It does not go into the details of the discussed systems but rather provides broad overviews. The second one focuses more directly on the devices used in this thesis, namely quantum dots, transmon qubits, superconducting cavities, and their multiple regimes of interactions. The third

chapter is dedicated to the experimental techniques, ranging from the design of the samples to their fabrication and the measurement techniques required to characterize them. The three remaining chapters focus each on one particular topic of this thesis work and are summarized below.

Coherent spin-photon coupling in a cQED architecture

The fourth chapter discusses an experiment whose goal was to achieve strong coupling between a single electronic spin trapped in a mesoscopic circuit and the photonic field of a microwave cavity. The spin qubit we used, has been proposed in [20] and is based on a double quantum dot contacted by ferro-magnetic electrodes. Building upon a previous experiment carried out in our lab [13], we embedded it into a microwave cavity and demonstrated a coherent coupling between spin-full transitions and the microwave photons trapped inside the cavity [21]. We have further studied the role of parity of the number of electrons inside the double quantum dot and showed that it can strongly affect the system spectrum.

Probing single-dot dynamics using a transmon qubit:

The fifth chapter explores the possible use of a transmon superconducting qubit as a tool to probe quantum dot circuits properties with a high sensitivity. It focuses on single quantum dots that can be used as condensed matter model systems. In previous experiments [22, 23], the use of a microwave cavity proved to be instrumental in revealing such circuits properties. The addition of a transmon to such experimental setup provides several interesting opportunities. First, the transmon could be used to analyze the cavity field and allow the first quantitative determination of the coupling between single quantum dots and cavity photons. In previous experiments, only the product of the photon number by the coupling have been measured and the photon number could not be determined with accuracy. Furthermore, the transmon could be used as a sensitive spectrometer and provide further insight into the properties of quantum dot circuits. The chapter discusses this problem both from the theoretical point of view for a quantum dot at equilibrium in either the Coulomb blockade regime or the Kondo regime and from the experimental point of view.

Probing Majorana fermions using a cavity:

The sixth and last chapter is dedicated to a theoretical work on the investigation of topological hybrid circuits with cavity photons [24]. Hybrid nano-circuits combining nano-conductors with spin-orbit interaction and superconducting contacts have been proposed to obtain Majorana fermions [25, 26]. So far the structures have been studied mainly through the DC current measurements which essentially reveal the DOS of the devices [27, 28, 29, 30, 31, 32]. We propose a protocol to evidence the self-adjoint character of Majorana fermions relying on the use of microwave cavity coupled to standard transport measurements. One specificity of this work is that it treats fully the effects of the superconducting contact including the residual subgap density of states often observed in experiments.

Chapter 1

Quantum technologies

In the last decades, experimental studies of the basic laws of quantum mechanics, describing the light matter interaction, have opened the possible use of quantum resources for computation, communication, simulation and sensing using quantum systems. Those works were first carried out using trapped ions [33] or Rydberg atoms [34]. Thanks to the advances in material science and nano-fabrication techniques, they have been nowadays extended to the domain of condensed matter with great success.

The development of those so called quantum technologies offer a lot of interesting perspectives both from the fundamental and applied point of views, as they require unprecedented understanding and control of the physical systems they are built upon, while providing new tools to study physical problems, such as extremely sensitive probes. In the following, I will discuss how information can be encoded and manipulated in such quantum systems. I will also focus on how the use of bosonic modes, such as photons trapped in a cavity, has been demonstrated as a very efficient way to exchange and extract information between/from quantum systems. Finally, I will discuss how those ideas can be transposed to probe, in a very delicate fashion, condensed matter systems.

1.1 Quantum information encoding :

Classical information can be encoded as a sequence of binary values, so called bits of information. A quantum bit of information, usually denoted as qubit, can, just as a classical bit, takes two distinct values. But it can also be in any superposition of those two states. The key idea of quantum computation is to take advantage of quantum superposition to execute in "parallel" a large number of operation in a single step. A very naive way to look at it is illustrated in Fig 1.1. A slightly more involved example is discussed below.

Let's say we are interested in knowing whether a function returns the same output (0 or 1) for all inputs or if it returns 1 for half of them and 0 for the other. Considering that the function can have 2^n different inputs, classically it takes at least $2^{n-1}+1$ evaluations to actually test that property. Using a quantum computer it can be shown that actually a single evaluation is enough. The rough principle is the following :

- starting from n+1 qubits, a large superposition of all possible input values is created

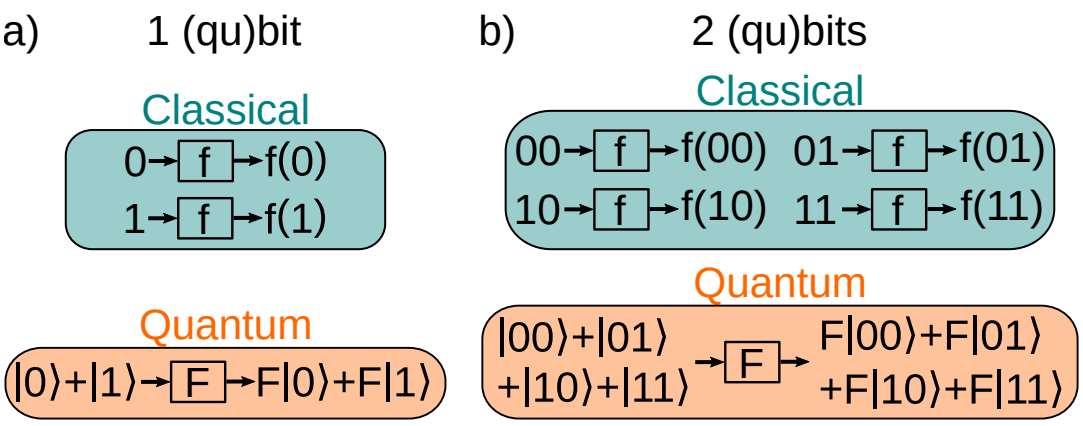

FIGURE 1.1: Quantum information processing :
Given a certain function taking n bits as its input a classical computer will need to perform 2^n evaluations of the function to determine its behavior. On the other hand, a quantum computer can use a superposition state as input and get a superposition of the outputs. For one (qu)bit, we go from 2 evaluations to 1 as illustrated in a. For two (qu)bits as shown in b, we go from 4 evaluations to 1. In a classical computer the computational powers increases linearly with the number of bits, whereas in a quantum one it increases in an exponential fashion.

- that superposition is used as input for the function to test
- after the evaluation a final transformation is applied to all qubits
- the qubit states are measured (actually it is sufficient in theory to measure only one)

If the function is balanced (returns 1 only half of the time), the outputs corresponding to different inputs will interfere destructively and all qubits will end up in 0. On the other hand for a constant function we would get 1. This algorithm is known as the Deutsch–Jozsa algorithm [35].

For such a simple problem, the actual speed-up is not very large, in the sense that it scales only as N. Some other possible quantum algorithms have been demonstrated to provide an exponential speed-up (e^N). The most widely known of such algorithm is probably the Shor algorithm [36] that applies to number factorization. The development of such an algorithm has been a strong drive to develop quantum based computers.

In order to build a quantum computer, the first building block one needs is a quantum bit or qubit. In the following sections, we will present a brief overview of the main figures of merit of a single qubit along with some of the existing qubits in condensed

matter, and look into the many interesting features coming from coupling such systems to bosonic modes.

1.1.1 Quantum bits :

Just like in a classical computer, the qubit is the basic unit that is used to store the information and perform operations. It corresponds to a quantum two-level system. Compared to a classical bit, a qubit is, in a sense, much richer due to the existence of superposed states. However, the information it carries is also much more fragile as we will see.

As a qubit does not only take two discrete values but can actually be in any superposition of those two, its state $|\psi\rangle$, or more precisely its density matrix, defined as $\rho = |\psi\rangle\langle\psi|$, is conveniently described on the Bloch sphere as presented in Fig 1.2. In the lab frame, the X and Y axis rotate at the qubit frequency, and it is hence convenient and we will do so in the following, to work in a frame rotating at the qubit frequency. In order to move from the north (0 state) to the south (1 state) pole, one needs to be able to induce rotations of the qubit state around an axis lying in the xy plane. However in order to take full advantage of the possibility offered by quantum computation, such a control is not sufficient as it does not allow to prepare the qubit in an arbitrary state. To achieve this, one needs, at least, to be able to perform operations on a second axis non colinear to the first one. One figure of merit of a qubit is the speed at which such operations can be performed. This speed will fundamentally fix the maximal speed of a quantum processor. Another figure of merit is the accuracy at which those operations can be performed. Contrary to a classical computer, in which the only manipulation error is discrete in nature as it corresponds to a failed flip (or unwanted flip), in a quantum computer, manipulation errors are essentially continuous and can be accumulated in a more complex fashions leading to different kind of errors.

Those errors can fall in two categories:

- bit flip errors: those are errors similar to the ones happening in classical bits and lead to a 0 becoming a 1.
- phase flip errors: those errors are specific to qubits and correspond to unwanted rotation around the z-axis of the state vector.

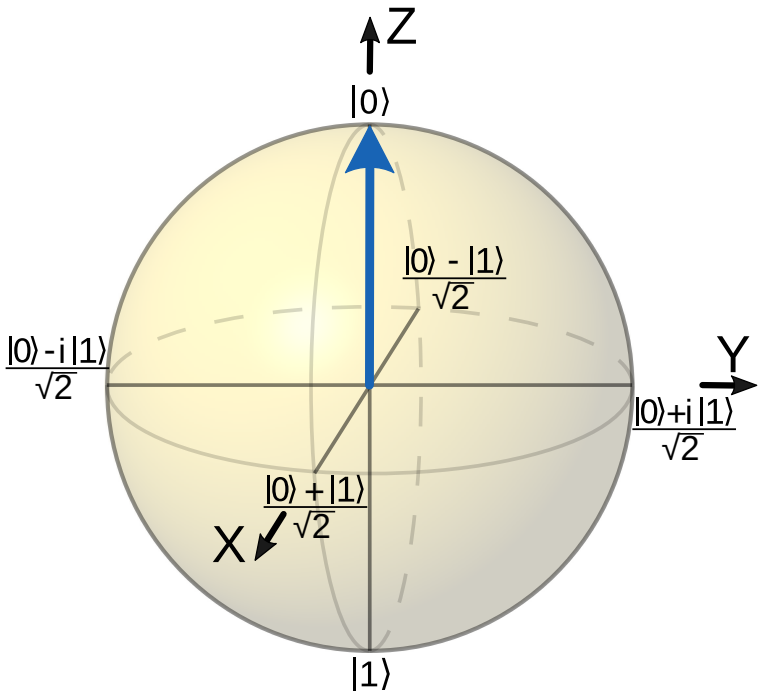

FIGURE 1.2: Bloch sphere representation of a qubit state:
Any two levels system density matrix $\rho = |\psi\rangle\langle\psi|$ can be described using the Pauli matrices usually noted $\sigma_x, \sigma_y, \sigma_z$ and the identity matrix. In that matrix representation, the identity does not carry any information and can be discarded, leaving only three components that can be represented as a vector in a 3 dimensional space. Because a quantum state is normalized, this vector is unitary and hence lives on the surface of a sphere. In that representation one can identify specific points:

- the north and south poles corresponding respectively to $|0\rangle$ and $|1\rangle$.
- the equatorial plane associated with equal superposition of $|0\rangle$ and $|1\rangle$.

Quantum computation is actually equally sensitive to both kinds of errors and hence both should be minimized.

However, active manipulation is not the only possible source of errors in a quantum computer. Just like in a classical computer, the qubits cannot be perfectly isolated from their environment. In the case of classical computer, thermal fluctuations can induce bit flip. Those are exponentially suppressed as the energy difference between the two state of the bit increases (or conversely when the temperature decreases) and are usually quite rare (for example there is no need to correct for them in laptops). For a quantum bit, the situation is more complex. The interaction between the qubit and its environment will entangle the qubit with the environment, but because the environment state is not usually accessible, the information is lost. Depending on the kind of interaction between the qubit and the environment, this can lead to different kind of errors as illustrated

in Fig 1.3. Because we forget about the environment, the state cannot be represented anymore by a wave function. However we can represent such a state as a vector with a norm smaller than one. The vector is not anymore confined to the surface of the Bloch sphere but can be anywhere inside it.

If the environment can exchange energy with the qubit, it will be able to induce flip between the 0 and 1 state. Such a process, similar to the effect of thermal fluctuation in the classical case, will cause the state to collapse towards a thermal state. This collapse, which is equivalent to a contraction of the Bloch sphere, happens usually in an exponential manner and is characterized by a time T_1. This time is usually referred to as the **relaxation time**. On the other hand, if the environment cannot exchange energy but can induce fluctuations in the energy difference between the 0 and 1 state, the state of the qubit will precess in a random fashion around the z-axis. This will lead to a different kind of collapse: the probabilities that the qubit occupies the state 0 or 1 are not affected however the knowledge of angle between the x-axis and the state is completely lost. Once again this collapse can be, usually, described by an exponential decay whose characteristic time is noted T_2^*. This time is usually referred to as the **dephasing time**. From the previous arguments and from Fig 1.3, it should appear obvious that actually the relaxation necessarily limits the coherence.

When trying to characterize a qubit, it is important not to consider those numbers in an isolated way. For example, a qubit with a very long relaxation time but on which one can only operate at a limited speed may not be better than a qubit with fast operation and limited lifetime. The ratio of the operation rate to the dephasing/relaxation rate is usually more meaningful.

One key step of any computation has not been mentioned so far: the read out of the result. Once the set of operations, we are interested in, has been carried out, we are usually interested in knowing the actual result. For a classical bit, the possible answers are straightforward: we get either 0 or 1. As a quantum bit does not carry actually more information than a classical bit we cannot hope to extract more than a binary answer. However, for a quantum bit, one more degree of freedom exists, i.e. one can choose the Bloch sphere axis on which to measure. It is for example perfectly possible that at the end of the computation, the information is carried by the fact that the qubit is in 1 along the x-axis rather than the z axis. Usually only one axis is straightforward

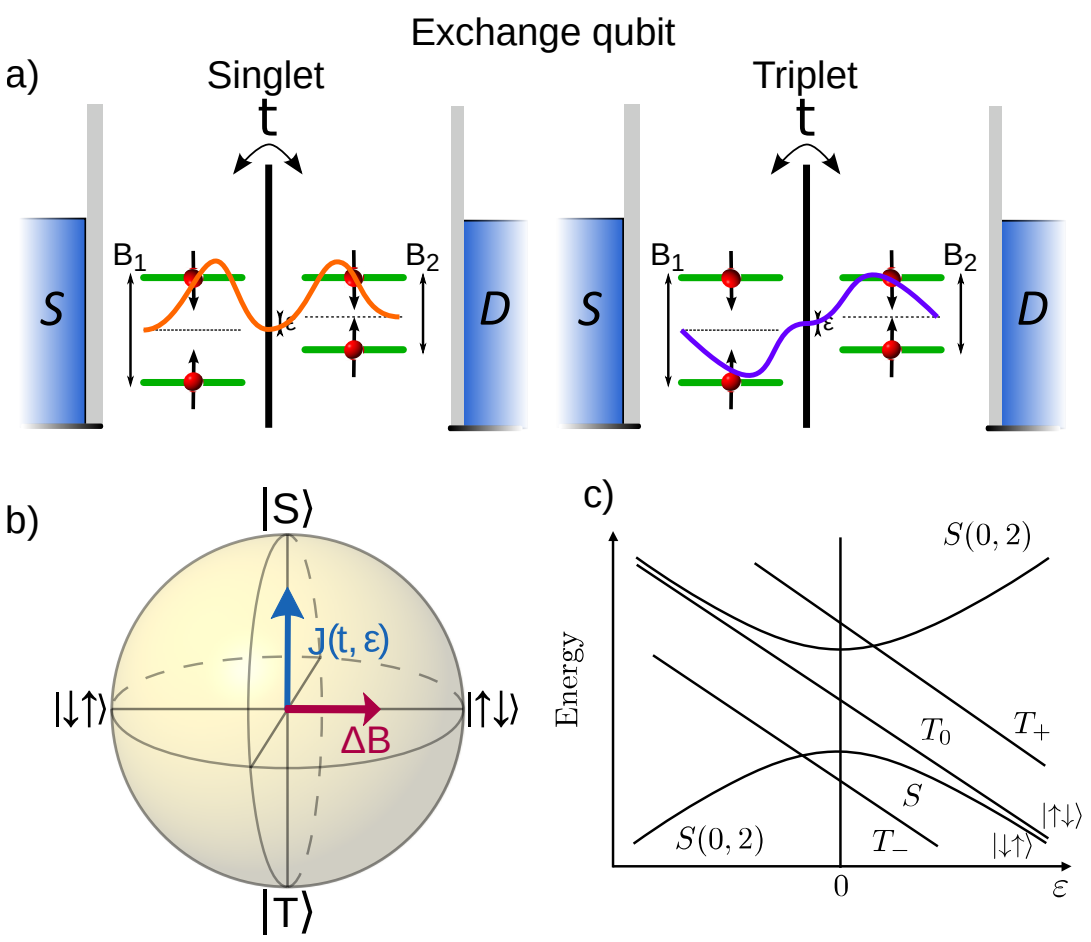

FIGURE 1.3: Qubit relaxation and dephasing:
When two quantum systems interact they tend to entangle. However, when measuring only one system, we discard any information stored in the second one. This is exactly what happens in the case of a noisy environment. This loss of information can be represented in the Bloch sphere picture, by drawing a vector whose norm is less than 1. In the figure, the yellowish surface represents the "sphere" to which the vector is bounded. Relaxation and dephasing affects the system in different ways:

- dephasing is an energy conserving process, hence the z axis component is unaffected as it represents the probability to find the qubit in $|0\rangle$ or $|1\rangle$.
- relaxation on the other hand leads to a complete loss of information (with different rates on the different axes).

to measure but, using qubit manipulation, it is actually possible to measure on any axis by properly mapping the axis of interest to the measurable axis.

From a naive point of view, it would hence looks like that, by measuring on multiple axes, we could extract more than one bit of information. But that would be forgetting that the measurement is not without consequences for a quantum system. Actually if a measurement is projective, i.e. its outcome allows to perfectly discriminate the two

states, the state of the qubit after the measurement is actually the measured state. Such a measurement is also called "strong measurement". For example, let's assume that we start from a qubit in $(|0\rangle + |1\rangle)/\sqrt{2}$ and we measure along the z-axis. The result we are going to get will mean that the qubit is projected in $|0\rangle$ or in $|1\rangle$ with equal probability. The main point is that the final state of the qubit is not the initial one and hence measuring along a different axis is actually meaningless as illustrated in Fig 1.4.

Read-out schemes can of course be differentiated by how well they can discriminate two states, but there can actually be one more key difference between two schemes: whether or not the state resulting from the measurement survives the measurement. Let's take an example. Let's say we need to know when an atom has emitted a photon. In the optical domain, this would usually be done by collecting the photon on an avalanche photo-diode and converting it into a classical electrical signal. After such a measurement the photon does not exist anymore. This is what is called a non-QND measurement by opposition to a Quantum Non Demolition (QND) measurement in which, even after the detection of the photon, the photon would still exist. Such measurements have been carried out in many systems, such as Rydberg atoms coupled to microwave photons [37], superconducting qubits [38], and are particularly well suited to the study of the electromagnetic field.

Now that we have introduced some basic ideas about the working principles of a qubit we will do a quick overview of two kinds of qubits that are of interest in this thesis. First, we will discuss the superconducting qubits, which is one of the most advanced platform for quantum computation in condensed matter. Second we will discuss be another broad family of qubits: the spin qubits.

1.1.1.1 Superconducting qubits:

Superconductors are appealing for quantum information processing because of their lack of dissipation promising long lifetime of the information stored in them. The simplest electrical circuit one can think of to store information is the LC resonator. It is an harmonic oscillator and one could think about encoding information in the presence or absence of a single excitation in it. However, because its energy levels are equally spaced, one cannot address individually the energy levels using a classical exitation. For example if one injects energy in an attempt to go from the state 0 (ground state) to the state 1

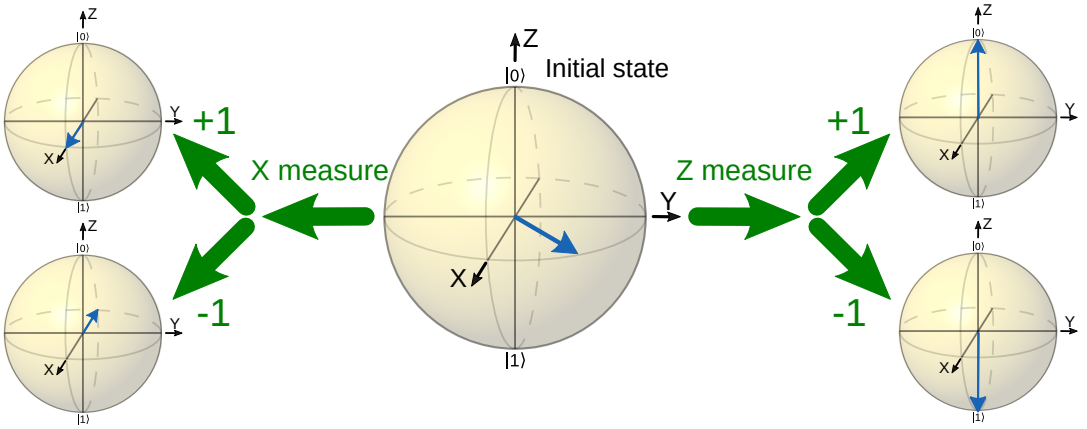

FIGURE 1.4: Qubit read out:
Like any measurement in quantum mechanics, the read-out of a qubit has a back action. The state of the system after the measure is not, in general, the state preceding the measure, and is actually identical to the measured state. Hence, if we start from an arbitrary state on or inside the Bloch sphere and measure along the z-axis, we have a certain probability to measure 0 or 1 depending on the z-component of the Bloch vector. If we measure 0, after the measure no matter the initial state, the system will be in $|0\rangle$. In particular, any information about the x and y axes has been lost. This last fact, is related to the non-commutativity of the operators associated to the measure on orthogonal axes.

(first exited state), actually all energy levels will be populated not just the first one [1]. To circumvent this issue one needs to introduce a non-linear element to get unequally spaced levels. The anharmonicity of the system then allows to address selectively the transition between the two lowest levels and to effectively reduce the system to an effective two level system. This non-linear element is the Josephson junction (JJ), a SIS junction (superconductor-insulator-superconductor). It behaves like a non-linear and non-dissipative inductance, and is, with usual capacitance and inductance, the key element in superconducting qubits. It is characterized by a critical current I_c delimiting the linear and non-linear domain of operation of the JJ. This current increases with the area of the junction. The JJ physical properties will be discussed in more details in Chapter 2 and its fabrication in Chapter 3.

Many different kinds of superconducting circuits have been investigated over the years. Fig 1.5 presents some of them along with the level spectrum and their characteristics. The key difference between the designs is the amount of energy stored in each of the component:

[1] Schemes exists to encode information in harmonic oscillator and build qubit out of them [39] but they are outside the scope of this manuscript

- charging energy E_C: this is the energy stored in the capacitance
- inductive energy E_L: this is the energy stored in the purely linear part of the system inductance.
- Josephson energy E_J: this is the energy stored in the Josephson junctions. When trying to engineer a large inductance it is usual to use Josephson junctions in their linear regime. In such qubits E_J refers to the smaller junctions (small I_C) contribution while the large junction contribution enters E_L

Thanks to their macroscopic nature, superconducting qubits can be efficiently coupled to the outside world for manipulation and read-out. For example, the large capacitance of the transmon qubit provides a large electric dipole that can be coupled to time-varying electric fields. This large coupling allows one to perform fast operation of those qubits, with π rotation in the Bloch sphere performed in typically 10 ns using pulses at the frequency of the qubit transition between its lowest levels. It should be noted that the operation is not only limited by the coupling strength between the qubit and the drive tone but potentially also by the limited anharmonicity of the qubit. If the operation is performed in a very short time, the spectral content of the pulse will be broad. If this broadness is larger than the system anharmonicity, there is a risk to populate more exited states of the qubit above the states 0 and 1.

Having a large coupling to the outside world is not always an advantage as it makes the qubit more sensitive to noisy signals that can increase both its relaxation and dephasing. In that respect, superconducting qubit, because of the versatility of their circuit design, have achieved impressive improvement over the last decades. For example, going from the Cooper pair box (CPB) to the transmon design has allowed to increase the dephasing time by a factor of more than 40. The main source of decoherence in a CPB arises from the charge noise, which is also an issue in many other setups. Charge noise is responsible for fluctuations of the charge on the capacitance plate of the qubit. This induces fluctuations of the transition frequency between the two levels of the qubit resulting in the qubit dephasing. The charge noise effect is stronger when the qubit has a large charging energy. The transmon design mitigated this effect by decreasing the charging energy through the use of a very large capacitance as illustrated in Fig 1.5.

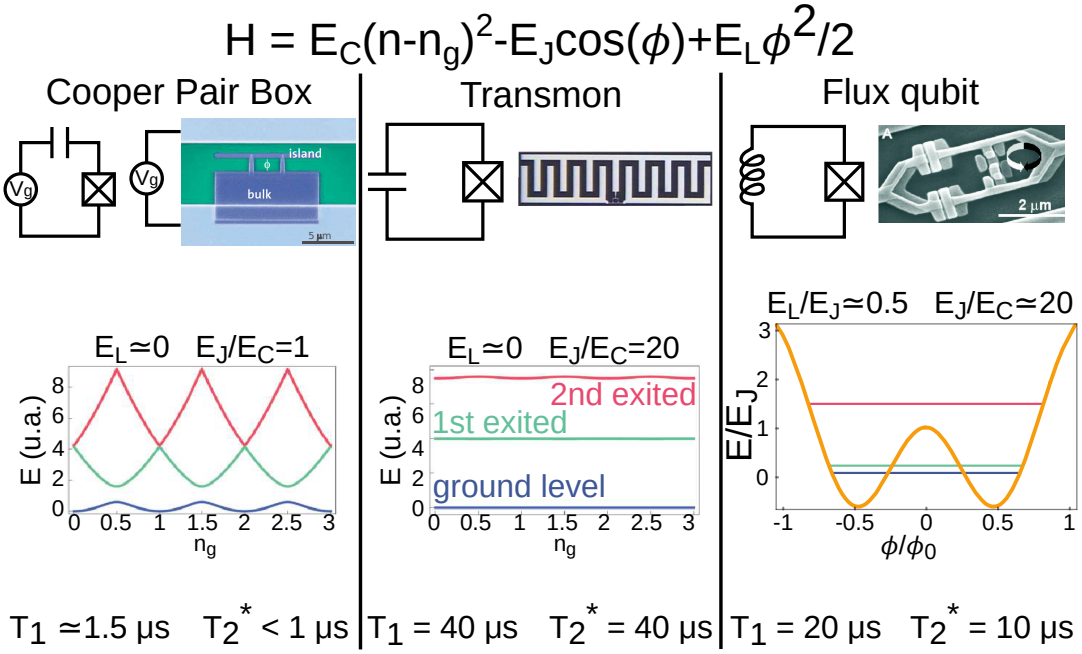

FIGURE 1.5: Superconducting qubits:
Superconducting qubits are all based on the Josephson junction denoted symbolically by a crossed square. One can write a generic Hamiltonian for superconducting qubit by considering three terms:

- the energy E_J stored in the junction which depends in a cosinusoidal way on the phase across the junction (the integral of the voltage).
- the charging energy E_C associated with the circuit capacitance. By adjusting the number of charge on the capacitor plate, one can tune the qubit energy. This can be achieved using a gate voltage.
- the inductive energy E_L which depends quadratically on the magnetic flux enclosed the whole circuit.

By playing on those different terms on can obtain different behavior with respect to charge and flux.

- Cooper pair box : in this design E_J and E_c are of the same order of magnitude allowing to easily tune the system using a gate voltage. However the system is hence very sensitive to charge noise, hence its short lifetime and coherence [40].
- Transmon : here the JJ is shunted by a capacitor in such a way that $E_C \ll E_J$. This reduces the anharmonicity of the circuit but makes it nearly insensitive to charge noise [41]. Transmon qubits have demonstrated the largest coherence time. The values given here corresponds to 2D transmons [42].
- Flux qubit : flux qubits get rid of charge noise by shunting the JJ using a large inductance (often made out of large JJ). They are however quite sensitive to flux noise, which limits their coherence [43].

The lifetime of the qubit can also be increased through a careful geometric design, limiting its coupling to parasitic modes or dissipative elements. A careful fabrication process allows one to reduce the amount of dissipative elements such as resist residue in

close proximity to the qubit.

Thanks both to its long lifetime and coherence and to the possibility of fast operation, the transmon is, at the time being, among the qubits whose state can be manipulated with the highest fidelity. The detailed physics of the transmon will be discussed in Chapter 2, as its simple design and relative use of fabrication makes it very attractive when considering complex sensing schemes such as the one described in section 1.2.2. We have not discussed how to perform the read-out of this qubit, but we will fill this gap in a later section as the read-out of such a qubit is actually performed using an auxiliary bosonic mode.

1.1.1.2 Spin qubits:

When looking for two-levels system susceptible to be used as qubit, there is a candidate much more obvious than superconducting qubits: the electronic spin. The electronic spin is naturally a 2 levels system which is furthermore weakly coupled to its environment, promising long coherence time. The use of the electronic spin as a resource for quantum computation was first proposed in 1998 by D.Loss and P.DiVicenzo in [4]. Their proposal was based on electrons trapped in quantum dots in semiconductor. We will in the following focus on those quantum dots based spin-qubit, which are usually referred to directly as spin-qubits even if some other platforms, such as donors in silicon [44] and defects in diamond [45] or SiC [46] could also be considered as spin qubits.

As already mentioned, the electronic spin is weakly coupled to its environment. This promises long coherence but hinders fast operation. Furthermore, the natural coupling of the electronic spin is to the magnetic field, and one cannot easily generate strong and **local** magnetic fields which is also an issue in term of scalability. This motivated the search for ways to get an electrical control on the spin degree of freedom, which is one of the goal of the work presented here. In general, two main directions have been explored so far:

- in a multiple quantum dots circuits, modulate the exchange interaction between the two electrons in the two dots to manipulate the electronic spin. In such a device, the information is encoded in two of the n possible states of the circuit [17, 47, 48, 49]. This is illustrated in Fig 1.6.

- in a single dot system, made out of a material with an intrinsically strong spin-orbit coupling (SOC) or subject to an inhomogeneous magnetic field, use the electric field to induce oscillation of the electron position that will lead to an effective alternating magnetic field [50, 51, 44]. This is illustrated in Fig 1.7.

In both cases, the underlying idea is to use a charge-spin coupling mechanism to enhance the coupling to the spin degree of freedom. This increases the speed at which the spin state can be manipulated, but it also makes the qubit more sensitive to charge noise. It is hence of paramount importance to ensure that the gain in spin control is more important than the increase in charge noise sensitivity.

The first mechanism has been extensively studied in double quantum dots (DQD) subject to an external magnetic field. Those systems first attracted attention because the exchange interaction allows to perform two-qubit gates when the information is encoded in the electron spin. However when using the DQD state to encode information, the control on the exchange allows to manipulate the qubit on a single axis which is not sufficient to prepare an arbitrary state [17]. This DQD architecture is often referred to as singlet-triplet spin qubit, as the read-out scheme allows one to discriminate between the spin singlet and spin triplet states. To go beyond the limitation imposed by a single axis of control, one can extend the previous architecture to a triple quatum dot where all operation can be performed through exchange coupling [47] or rely on an inhomogeneous magnetic field. In the presence of an inhomogeneous field, the quantization axis is tilted with respect to the exchange axis in the Bloch sphere (see Fig 1.6 b). Modulating the relative strength of the exchange and inhomogeneous field allows to operate on two non-collinear axes. That field can be obtained by polarizing the nuclear spin bath [48] or using a micro-magnet [49].

The second mechanism has been investigated both using natural spin-orbit coupling in InAs nanowires [50] and using inhomogeneous magnetic fields generated using micro-magnets [51]. In InAs nanowires it turns out that the spin-orbit coupling is not the only origin of the coupling: the electric field also modulates the g-factor. This kind of modulation of the g-factor have also been used in Si structure lacking a strong spin-orbit to manipulate the electronic spin [44]. One advantage of the micro-magnet approach is that, being independent of the material properties, one is free to choose an host material

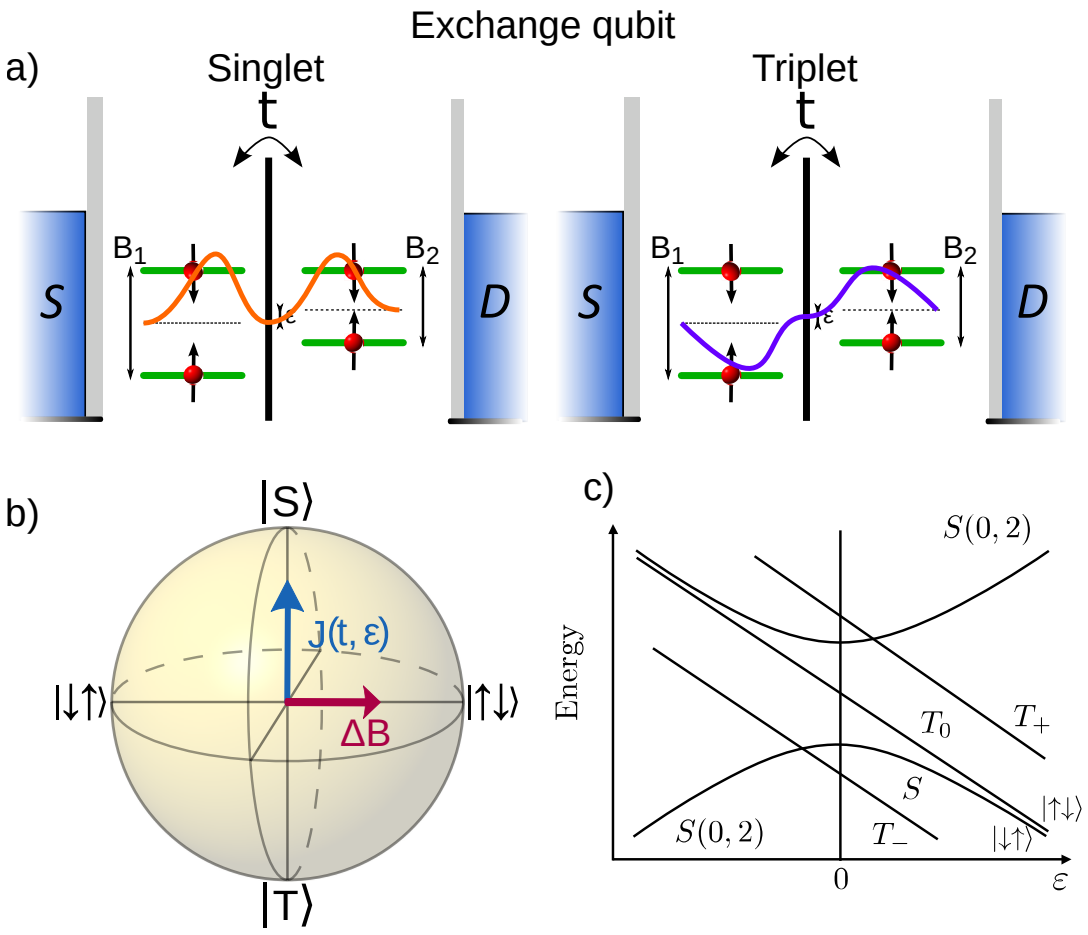

FIGURE 1.6: Exchange based spin manipulation:
A double quantum structure, with two electrons, is similar to a dihydrogen molecule. In particular the tunnel coupling between the two "atoms" gives rise, like in an hydrogen atom, to exchange energy which favors the spin singlet. This interaction is not a magnetic interaction between the spins but arises from the Coulomb interaction. This interaction decreases with decreasing coupling (t) and increasing detuning (ϵ) between the two orbitals. In an inhomogeneous magnetic field however the singlet, favored by the exchange, is in competition with $|\uparrow\downarrow\rangle$ favored by the inhomogeneity. The figure a) illustrates the different energy levels to consider and the symmetry of the wave function for the singlet (orange line) and triplet states (dark purple line). Figure b) summarizes the discussion in term of vectors in the Bloch sphere. Figure c) presents the energy level diagram as a function of ϵ. In the absence of inhomogeneous magnetic field, the qubit is encoded in $|\uparrow\downarrow\rangle$ and $|\downarrow\uparrow\rangle$ at large ϵ. A rotation around the Z axis can be performed by increasing the exchange for a given amount of time. This operation having no phase only a single axis can be addressed. In the presence of an inhomogeneous field the quantization axis is tilted with respect to the z axis. By varying the relative strength of J and ΔB, one can control the direction of the manipulation axis.

free of nuclear spins which can be beneficial to the coherence of the system, which is the main point we will discuss in the following.

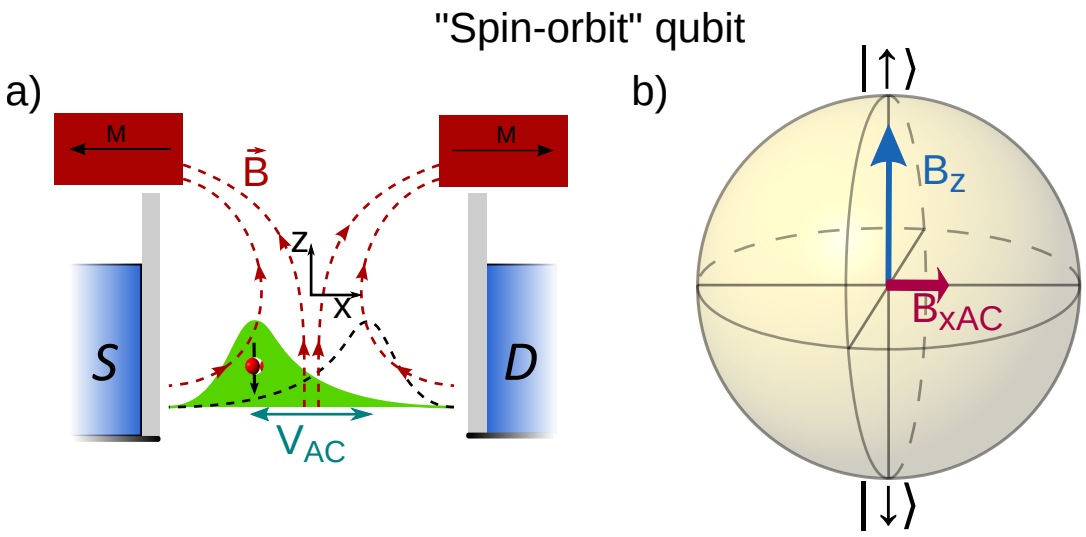

FIGURE 1.7: Spin-orbit based spin manipulation:
The idea of the spin-charge coupling is here illustrated on the case of a micro-magnet setup. The micro-magnet is engineered in such a way as to produce an inhomogeneous field on the scale of the dot. Using gate voltages, one can then displace the wave function inside the dot. In the center of the dot, the field is nearly parallel to z defining the quantization axis. However on the side it has a neat x component as illustrated in figure a. By periodically displacing the wave function using an AC potential, the electron sees an oscillating magnetic orthogonal to its quantization axis as illustrated in b. This field can be used to control electronic spin on two axes by controlling its phase.

Those spin-qubits have three main error channels related to unwanted interactions between the spin and noisy background:

- in system relying on the exchange interaction, charge noise can lead to a noisy term in the exchange term.
- in all systems, spin-orbit coupling (even weak one) couples the spin degree of freedom to both charge noise and the phononic bath.
- in systems in which the host material contains nuclear spins, those spins generate a random magnetic field.

Since the early experiments carried out on GaAs DQD [17], in which a decoherence time of the order of 10ns were observed, many research efforts have focused on understanding in details those mechanisms and mitigates their effects. For example, the gate fidelity was increased in singlet-triplet systems by modulating the tunnel coupling (t) between the two dots rather than the detuning (ϵ) as this mode of operation is far less sensitive

to the charge noise [52]. The issue of the nuclear spin bath has been addressed either in a passive manner by moving to nuclear-spin free materials such as SiGe compounds[53], or in active manner by using dynamical decoupling sequences [54, 55]. Finally, working with holes rather than electron can prove beneficial as they can have a lower coupling to the nuclear field bath [56].

In those systems, the read-out of the qubit state usually relies on the spin-blockade mechanism, which involves two dots and applies to both the schemes presented above. Starting from a situation in which each dot contains one electron, the gate voltage used to define the dot is tuned so that it becomes favorable for both electrons to be in the same dot. In the case of a singlet-triplet qubit, this will only happen if the qubit is in the singlet state because of the Pauli exclusion principle. If the information is encoded in a single spin, then the spin state of one of the dots has to be known, and the tunneling will occur only if the electronic spins are in an anti-parallel configuration. The result of this operation can then be read either through a current measurement by allowing the extra electron to tunnel out, or using a charge sensing scheme. In both cases the read-out is destructive for since there is no way to reload the "right" electron in the empty dot.

The scheme that will be presented in Chapter 4 relies on a DQD architecture but its basic principle is closer to the SO based scheme. We will use as conductor a carbon nanotube (CNT) whose natural spin orbit coupling is actually far too weak to provide an efficient spin-charge conversion. To overcome that issue we will engineer an artificial spin-orbit coupling using non-collinear ferromagnetic contacts. The spin-charge conversion will arise from tunnel coupling between the two dots rather than a simple oscillation of electron position but the rough idea will remain similar. One advantage of using CNT is the naturally low concentration of nuclear spins and the possibility to move to a nuclear spins free environment by using ^{12}C for the growth of the CNT.

So far we have only discussed qubits and hence what could be used for the processor of a quantum computer. But in classical computer, one also finds memory. As presented in the beginning of this section, quantum information is more fragile than classical information and to achieve the precision required to perform quantum computation, it appears unavoidable to rely on error correction algorithm in the hardware. Error correction also exist in classical computer but is reserved to system that need to preserve their state for a very long time such as servers but not in ordinary laptops, whereas

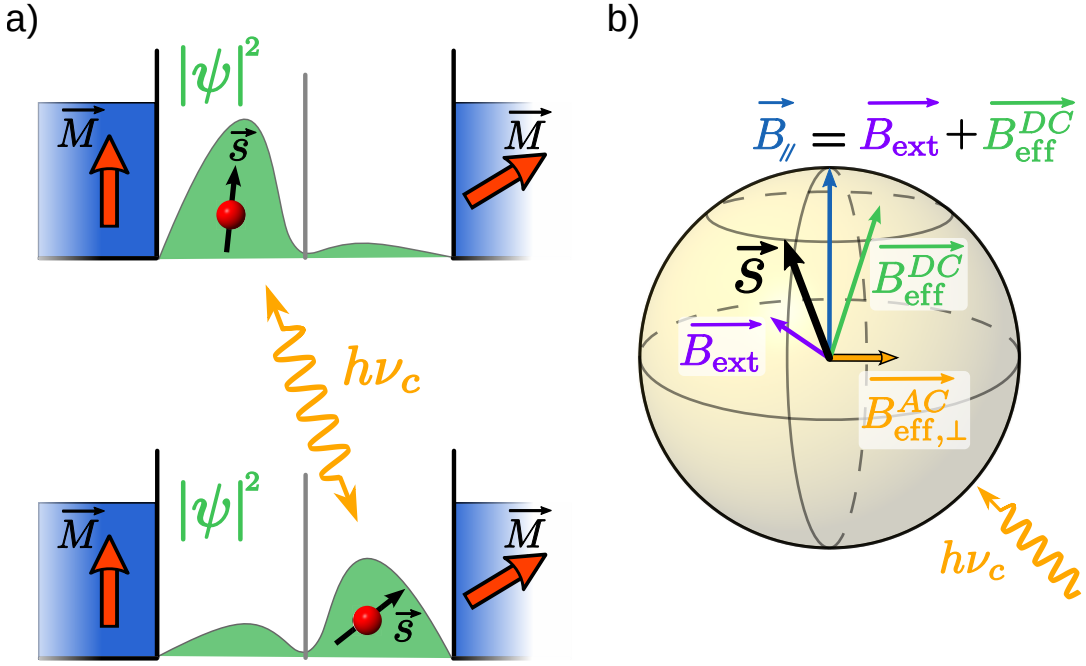

FIGURE 1.8: Artificial spin orbit coupling in a CNT based DQD:
The basic idea underlying this scheme is quite similar to the one already presented above based on spin-orbit coupling. Once again we consider a single electron but in a DQD. Each dot is connected to a ferromagnetic contact inducing a spin polarization of the wave function. However as the ferromagnets magnetizations are not colinear, neither are the quantization axes in each dot, as illustrated in a. Hence by inducing tunneling between the two dots using an electric AC signal, the electron experiences an oscillating magnetic field orthogonal to its quantization axis. Such a field can be used to control the electron spin state (see b).

it appears compulsory in quantum computing. Because of that requirement, it is not obvious to insert a memory-like part that would be different from the rest of the processor in current "design" of quantum computers. This is because transfers to and from the memory should not disturb the error correction operations, and usually a memory is slow because it needs to be very well isolated in order to live long. Nonetheless the idea of having a hardware more resilient to errors when idle remains appealing as it may reduce the cost of error correction. This would require the possibility to either couple or isolate the qubits from the rest of the processor in a fast manner (compared to its lifetime and the error correction cycles). Such an operation might be envisioned in the architecture that will be presented in 4.

In this section we have only focused on single qubit operation however a real quantum computer requires at least two qubit operations. This coupling between two qubits can be achieved in many ways and in the following we will focus on a single one: the use

of an intermediate bosonic mode between the qubits. Coupling our qubit to a single bosonic mode opens more possibilities than just coupling two qubits together, as we will see in the following.

1.1.2 Bosonic mode interface :

Coupling a two level system to a single mode of the electromagnetic field realizes the simplest system to study light-matter interaction. Studying such model systems was one of the goal of the pioneering experiments carried out in cavity quantum electrodynamic. Since then those ideas have been transposed to superconducting circuits with a lot of success, the resulting field is known as circuit quantum electrodynamic (cQED). For example, the strong dispersive regime that will be discussed in Chapter 2 allows to read out in a non destructive manner the state of a transmon qubit with a high precision. Replacing the superconducting qubit used in those circuits by a quantum dot based one gave birth to the field of mesoscopic quantum electrodynamic (mQED). This field has recently achieved the strong coupling [57, 58, 59], that will also be discussed in details in Chapter 2. In the strong coupling regime, an excitation can be exchanged many times between the qubit and the bosonic mode before it is lost. This allows to convert information between two kind of carriers and to transfer information between distant qubits. Those experiments are an important step towards generalizing more complex experiment coming from the field of cQED to mQED.

The idea of using a common bosonic mode to couple two distant qubits is actually quite general and can be applied to many different platforms. Superconducting qubits coupled through microwave photons is obviously one [14]. But experiments trying to couple for example NV-centers in diamond to spin-waves [60] or superconducting qubits to acoustic waves also exist [61], and could open new possibilities for distant qubits coupling. In mQED, interaction between distant single quantum dots (SD) (which are not used as qubit) has also been demonstrated [62].

It should also be noted that the logic can be reversed. The microwave field of a cavity can be used to probe a transmon state, but actually the transmon can also be used to probe the state of the cavity photons [66]. This reverse approach is particularly interesting to probe non classical states of light in a cavity mode. It is also possible to go further and

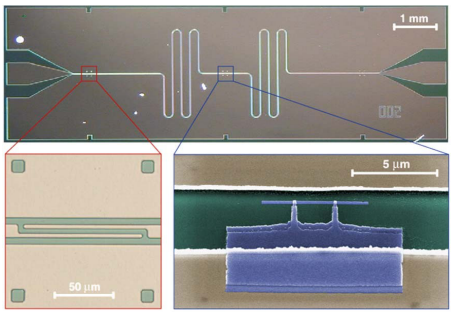

Microwave cavities coupled
to mesoscopic circuits
(superconducting qubit, quantum dots, ...)
ETH, ENS, Yale, Princeton, UCSB, ...

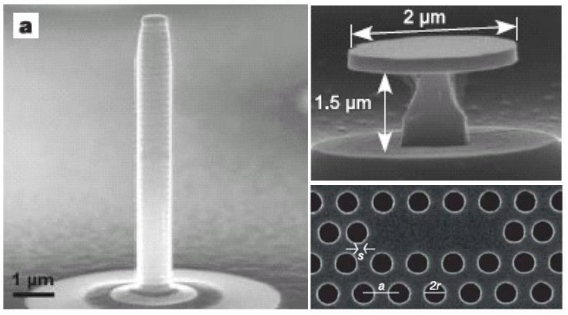

Optical cavities coupled to quantum dots
Wurzburg, ETH, Stanford

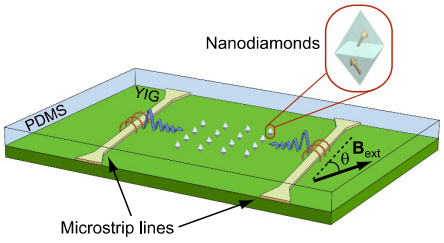

NV centers coupled to spin waves
Chicago

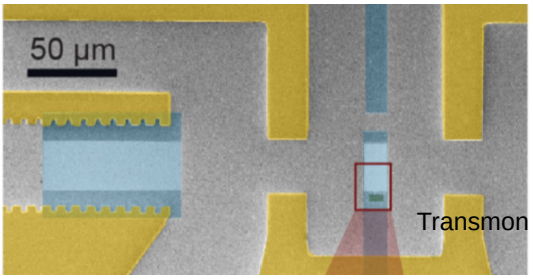

Surface acoustic wave coupled to
superconducting qubits
Chalmers, Boulder

FIGURE 1.9: Experimental realization of coupling to a bosonic mode:
Here we illustrate the variety of bosonic interfaces that can be realized in solid state systems through some experimental realizations:

1. microwave resonators can be used to coupled any mesocopic circuits to microwave light. They are at the base of cQED and mQED [7, 14].
2. micropillars [63], microdisks[64] and photonic crystals [65] can be used to confined infra-red or visible light and enhance the coupling of nano-structure such as optical quantum dots to light.
3. spin wave in ferromagnetic material can be used to carry magnetic excitation in an efficient manner and couple to magnetic systems such as NV centers [60].
4. surface acoustic wave can be generated and confined in piezo-electric materials and coupled to superconducting qubit (as illustrated) or quantum dots [61].

use a single qubit to couple different bosonic modes but this goes outside the scope of this work.

The techniques developed to probe qubits in the context of information processing can provide a very powerful tool to study other systems, such as condensed matter ones. It is those possibilities that we will discuss in the next section.

1.2 Sensing for mesoscopic systems :

The development of more precise measurement techniques has always favored a deeper understanding of the laws of physics. One can, for example, think about the Foucault's pendulum revealing the rotation of the Earth thanks to the very long time during which its oscillation persists. Increasing a measurement precision can usually be achieved by two means:

- increasing the measurement time, to be able to average out more effectively the noise.
- measuring at higher frequencies in order to reduce the sensitivity of the measurement to low frequency noises

Of course, those techniques are not always applicable or without shortcomings: averaging on longer time means we are more sensitive to very low frequency drifts and we lose the possibility to access a system internal dynamics, while increasing the frequencies may not be possible due to some increased system sensitivity to higher frequencies, and hence energy.

In the field of condensed matter, one measurement is of paramount importance: the electric charge. one often needs to measure a current flowing through a system, to determine the number of charge in a structure such as a quantum dot or the charge fluctuations in a system. In this last case, one usually think of the system as a capacitance. Current measurements are usually confined to low frequencies (sub-GHz) due to the constraints on the amplification. Charge sensing on the other hand can reach higher frequencies for example through the use of single electron transistors (RF-SET). In order to filter the noise those system are usually coupled to resonant circuits. Building on this idea, and on the field of cQED, we will see in the next section how superconducting microwave cavities can be used to achieve an unprecedented sensitivity. Finally, once again borrowing from cQED, we will see how the idea of using a two-level ancilla system to perform a measurement can be transposed to condensed matter.

1.2.1 Cavity based sensing :

Microwave cavities thanks both to their high operational frequencies and to their high quality factor are very well suited to the study of condensed matter system. Their high frequency of operation make them naturally less sensitive to low frequency noise. On top of that, their high quality factor makes them extremely sensitive to any perturbation in their environment.

Each mode of those circuits can essentially be described as an ideal LC resonator. In order to preserve their low dissipative nature, they are usually coupled to mesoscopic circuits in a capacitive manner [67, 9, 22]. The mesoscopic circuit response contains both a reactive and a dissipative part, which can both be traced back to the charge susceptibility of the system, i.e. the way the charge responds to a modulation of the chemical potential. The reactive response (capacitive or inductive) can be detected as a shift in the phase of the cavity transmitted signal. Recently this technique has been used to achieve a record measurement of the charge susceptibility of a quantum dot both in the Coulomb blockade regime and the Kondo regime [23]. Both those regimes will be discussed in Chapter 2, but the point here is that this technique has allowed us to achieve an order of magnitude better sensitivity than RF-SET based measurements. So far these measurements have been limited to fixed frequency detection, but the development of variable frequencies resonator [68, 58] may allow to overcome that limitation and allow to probe the frequency response of mesoscopic circuits with unprecedented resolution.

The dissipative part of the mesoscopic circuit answer means it can also use the mode either as a energy provider or dump. If the circuit pumps energy out of the mode, when probing the cavity transmission it will appear as reduction in the transmission, which is a signature of added dissipation. On the other hand if the circuit is driven out of equilibrium the reverse process can occur, with the circuit transferring photons in the resonator in a process known as photo-assisted tunneling. Compared to the situation when no resonator is present, it also leads to an increase in the current. However, because many other processes can allow tunneling (such as coupling to the phonon bath), this photo-current is generally masked by a large background current which can make its detection very challenging. This process can be strengthened by driving the mode (i.e. injecting photons), which can be seen as a stimulated process, hence allowing detection of the current for large drives. On the other hand directly detecting the photons

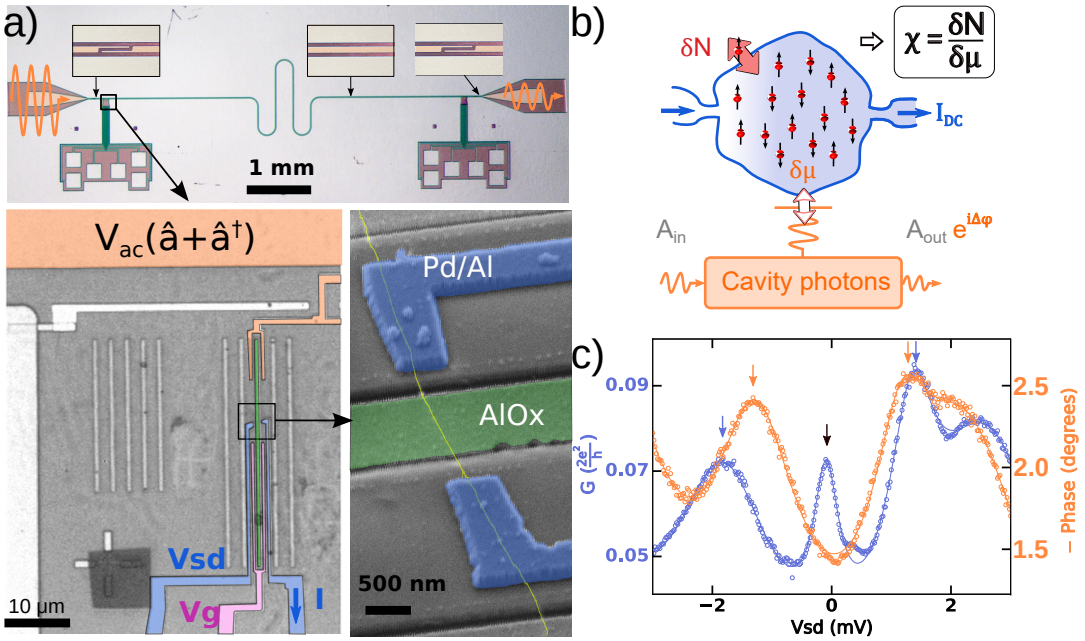

FIGURE 1.10: Zero frequency charge susceptibility of the Kondo cloud: Recently [23], microwave cavities have been used to probe the physics of the Kondo regime in quantum dots. Using the setup presented in a), where a SD made out of a CNT is embedded in a microwave cavity with its bottom gate capacitively coupled to it, we were able to measure simultaneously the conductance of the dot and its charge susceptibility. The exact coupling mechanism is discussed in chapter 2. The basic idea is that the photonic field modulates the chemical potential of the dot, while the phase of the cavity transmission is sensitive to the dot occupation, resulting in a measurement of the charge susceptibility. This is illustrated in b). Figure c) presents those results. While the conductance, in blue, exhibits the zero bias peak characteristic of the Kondo effect, it is completely absent in the susceptibility measurement. Because in that experiment, the cavity frequency was much lower than all the energy scales relevant for the Kondo, this measurement is equivalent to a zero-frequency measurement.

emitted in the cavity can be a much easier task. For example in a recent experiment [22], photons associated with such a process have been detected in a situation where the photo-current would have been of about 0.3 pA and hence unobservable in this experiment. Furthermore, by reducing the losses in the dot circuits, one can reach a regime in which the circuits behave like an amplification medium with sufficient gain to build a MASER [19]. Even if such systems are unlikely to ever reach the performances of conventional electronics in terms of spectral resolution, this experiment may prove seminal in the study of the radiation field emitted by mesoscopic circuits. It has for example been proposed that a Kondo dot coupled to a cavity and driven in and out of the Kondo region at a high frequency (compared to the Kondo temperature) may generate non-classical state of light [69].

It must be pointed out that these techniques are not limited to quantum dot circuits but can be extended for example to Majorana devices as we will see in Chapter 6. In such system, it could allow to go further than the usual conductance measurement and directly probe the self-adjoint property of the Majorana bound states.

Additionally to the sensing schemes discussed above, cavities can have other applications to condensed matter like problems. By providing means to couple different circuit elements as previously discussed, they can be building blocks in quantum simulation systems but also allow to use spin-like systems as probe for mesoscopic circuits. This idea of using ancilla systems to perform high sensitivity measurements will be the focus of the next section.

1.2.2 Pseudo-spin based sensing :

After discussing how the study of a cavity properties can be used to study a mesoscopic system, we are now moving to a different kind of sensing not based on an harmonic oscillator but on a two-level system. The idea here will be that the study of such a two level system coupled to a system of interest can provide many insights in the properties of the studied system. For example in [70], the authors propose to use a superconducting qubit as a spectrometer. More recently, Rydberg atoms have been used as very sensitive electrometer [71], but also to probe the electric field auto-correlation function [72]. To present some of the schemes we are interested in, we will move away from the field of cQED and discuss quickly how NV centers can be used for magnetometry.

NV centers are colored centers in diamond formed by a substitute nitrogen associated with a lattice vacancy. They behave like a trapped molecule inside the diamond matrix. The negatively charged NV centers can be associated with 6 electrons, whose the highest two in energy form a spin 1 system. Due to hyperfine interaction the 0 and ± 1 states are split by ~ 2.8 GHz, which allows to manipulate the spin state using microwave radiation. The spin state can be initialized and read-out by optical means. Its main interest comes from its large coherence at room temperature ($T_2^* > 10\mu s$) which makes it very suitable for magnetometry as we will see, and its small size that makes it a good local probe.

Among the different sensing schemes possible, we will discuss three of them that can be directly applied to mQED systems as we will see in the following. The three schemes are the following :

- to probe DC magnetic field one can measure the energy splitting between the two levels of spin ± 1. This can be achieved either directly through a spectroscopy measurement [73] or through a Ramsey fringes experiment (see Chapter 3 for more details about this kind of measurement).
- to probe random magnetic fields, one can study the relaxation (T_1) of the NV center in presence of the noisy system [74, 75]. This experiment is sensitive to the noise spectral power at the frequency of the transition studied (either $|0\rangle$ and $|-1\rangle$ or $|0\rangle$ and $|+1\rangle$).
- once again to probe random magnetic fields, one can also look at the decoherence (T_2^*)[75]. This experiment is sensitive to the noise at all frequencies. By using more advanced pulse sequences (Hahn-echo, XY4, ...), one can filter out the low frequency component to focus on higher frequencies.

The sensitivity of the first and last technique are limited by the linewidth of the transitions, which is why the large coherence of the NV center makes it interesting for such sensing. The second technique is only sensitive to the lifetime of the system, and a larger lifetime will allow to detect smaller deviations induced by the probed system.

All the above schemes can be adapted to mesoscopic circuits. In Chapter 5, instead of probing the magnetic field, we will be looking at the occupation or charge susceptibility of a single dot which is the simplest model system one can consider. The NV center will be replaced by a superconducting qubit which will act as en effective two level system. The coupling will not be a direct coupling but will mediated by the cavity.

In such a scheme, the mean number of electron in the dot will act as a DC magnetic field and we can expect to shift the qubit frequency. This measurement should for example allow to shed some light on the problem of charge screening in such structure. The fact that the system has a finite charge susceptibility can be translated in a noise in the dot occupation which can be probed through relaxometry and dephasing measurements of the qubit. An added benefit of this scheme is that the qubit could also be used to

probe the cavity state and know precisely the number of state in the cavity which is a quantity which was never precisely measured in previous experiment on single dots [9, 23]. In addition, if the scheme used with Rydberg atoms to measure the electric field auto-correlation can be transposed to the transmon qubit, one may be able to directly probe the electronic auto-correlation function.

Chapter 2

Mesoscopic circuit quantum electrodynamics

Mesoscopic circuit quantum electrodynamics is still a young field of research and because of its hybrid nature it holds a lot of promises. First of all, the mesoscopic circuits themselves through their versatility in the fabrication process and their in-situ tunability, provide access to a large class of physical situations. This point will be partially illustrated in section 2.1 where quantum dots circuits and transmon qubits will be discussed. But more importantly, the ability to couple those circuits to microwave cavities gives access to a broad range of light-matter interaction regimes offering diverse possibilities ranging from the delicate probing of the circuits, to the coherent hybridization between light and matter, or the probing of the trapped microwave light itself and the coupling of distant circuits. How the microwave light trapped in a cavity can be described will be discussed in section 2.2.1, while the different regimes one can reach in those hybrid systems will be treated in the other sections of 2.2.

2.1 Mesoscopic circuits :

In a macroscopic conductor at room temperature, the behavior of electrons can be to a large extent well described by considering the electron as a charged point object. However we know from quantum mechanics that the electron presents a dual particle-wave nature that can be evidenced through interference experiments [76]. When the size

of circuits becomes smaller than the coherence length of the electronic wave function, that dual nature cannot be ignored any longer. This phase coherence length is usually very short but increases at low temperature reaching in some systems few μm below 1 K. Thanks to the advances in nano-lithography, the study of such small circuits boomed in the 90's.

Those circuits, in a sense, combine the best of two worlds: their behavior is quantum in nature just like the one of a single atom but their properties can be engineered and tuned over a wide range in ways impossible for an atom. In the following sections we will focus on two classes of such circuits:

- quantum dots circuits in section 2.1.1 that will be used both as artificial atoms or as model systems for condensed matter problems in this thesis work.
- superconducting qubits and more specifically the transmon qubit in section 2.1.2 that in this work won't be used as a qubit but more as a delicate probe of another part of the hybrid system in which it will be embedded.

2.1.1 Quantum dots :

Quantum dots are zero-dimensional objects in which confined electrons have a discrete energy spectrum reminiscent of an atom. They can be built out of single molecules, carbon nanotubes (CNT), graphene, semi-conducting nanowires or two-dimensional electron gas (2DEG) contacted to metallic electrodes[1]. For 1D materials, the presence of the contact electrode is sufficient to confine the electron gas to 0D while for 2D material an additional electrostatic confinement is required.

The spectrum of such artificial structures can be controlled in several ways:

- the nano-lithography techniques allow to control the geometry of the circuit, allowing to realize single quantum dot or multiple quantum dots. Section 2.1.1.2 will focus on the physics of single quantum dots (SD), while section 2.1.1.3 will deal with double quantum dots (DQD) whose behavior is close to the one of an artificial dihydrogen molecule.

[1] We do not consider here optical quantum dots that do not require metallic electrodes

- the contact electrode material can be used to alter the energy spectrum. The use of ferromagnetic materials can be used to induce a spin-polarization of the spectrum as will be shown in chapter 4. On the other hand, superconducting contact can induce superconducting correlations in the system which will be needed in section 6.

- the use of electrostatic potentials applied using "gate" electrodes can be used to control in-situ the number of electrons in the quantum dot or its coupling to the electrodes.

The coupling of the dot to electrodes allows one to probe its spectrum through transport measurements. This technique simply consists in applying a voltage across the dot and vary the gate voltage to change the internal configuration of the dot. Depending on the number of levels of the dot through which the electron can flow, the current will change allowing to infer the properties of the circuits. At low bias voltage and for well separated energy levels, one can resolve individual level resonances using this technique.

Among the many materials previously mentioned, this thesis work will focus on the CNTs which are of interest notably because of their ability to form contacts with a wide range of metallic electrodes (normal metal, ferromagnetic metals, superconductors). The following sections will hence first discuss their properties (2.1.1.1), before moving to SD (2.1.1.2) and DQD (2.1.1.3). However, as most of the properties of those structures do not depend, at first order, on the host material, properties coming specifically from the CNT will be emphasized to easily separate them from the general properties.

2.1.1.1 Carbon nanotube properties :

Carbon nanotubes are composed of one or multiple concentric cylinder of graphene. For the sake of simplicity, but also because the fabrication technique used in this thesis favors this kind of CNT, we will focus on single wall carbon nanotube (SWCNT), i.e. nanotube consisting of a single graphene cylinder.

CNTs inherit many basic properties from graphene such as a mainly ballistic electronic transport and the valley degree of freedom that will be detailed later. However, folding the graphene sheet is not without consequences. First of all, the folding imposes periodic boundary conditions on the electronic wavefunction, which leads to a quantization of

the circumferential momentum. The energy separation Δ_{band} between two sub-bands with different quantized circumferential momenta is inversely proportional to the CNT radius. For the CNTs considered in this work whose diameter is around 1 nm, the band gap is of the order of 0.7 eV. This implies that, at low temperature, CNT transport properties will be well described by taking into account a single band. Consequently, at low energy, nanotubes can be considered as one-dimensional semi-conductors with a single ballistic conduction channel, and in all the following we will focus on this single conduction channel case.

The quantization of the circumferential momentum also implies that the momentum space is not a plane, as for graphene, but a set of parallel lines (we will denote $k_{\parallel}$ the momentum along those lines, $k_{\perp}$ will be the quantized circumferential momentum). The position, orientation and spacing of those lines depends on the angle between the folding axis and the crystal lattice axis. In momentum space, graphene has six Dirac points at which the conduction and valence bands touch. If the allowed momentum lines fall on the Dirac points, the CNT will have no gap just like graphene and will be considered metallic. On the other hand, if the lines miss the Dirac points, the CNT spectrum will be gapped and the CNT will be referred to as a semiconducting CNT. The energy minima of the dispersion relation will be found for the $k_{\parallel}$ closest to the Dirac point, $k_{\parallel} = 0$ will be defined at this point. This is illustrated in Fig 2.1 extracted from [3].

However, even metallic nanotubes often present a narrow gap induced by curvature or strain in the lattice. These narrow-gap nanotubes happen to be more suitable for electronic transport experiments, as disorder tends to localize massive electrons, found in nanotubes with larger gap [3]. Indeed, the energy dispersion of CNTs can in general be written as :

$$E(k_{\parallel}) = \pm\sqrt{\left(\hbar v_f k_{\parallel}\right)^2 + \Delta_{gap}^2/4} \tag{2.1}$$

This spectrum is bent close to the gap conferring an effective mass to the electron which actually increases with the gap (which justifies the above remark). However for CNTs with many electrons ($E_F \gg E_{gap}$), the dispersion relation can be approximated by a linear dispersion with a constant mean momentum $\langle p \rangle = \pm\hbar k_f$, stemming from the Dirac cones. The Fermi velocity, $v_f \sim 8 \times 10^5 m.s^{-1}$ [3], is one order magnitude larger than in other semiconductors. This high Fermi velocity increases the mean free path and the phase relaxation length of the electrons in the nanotube, as both quantities are

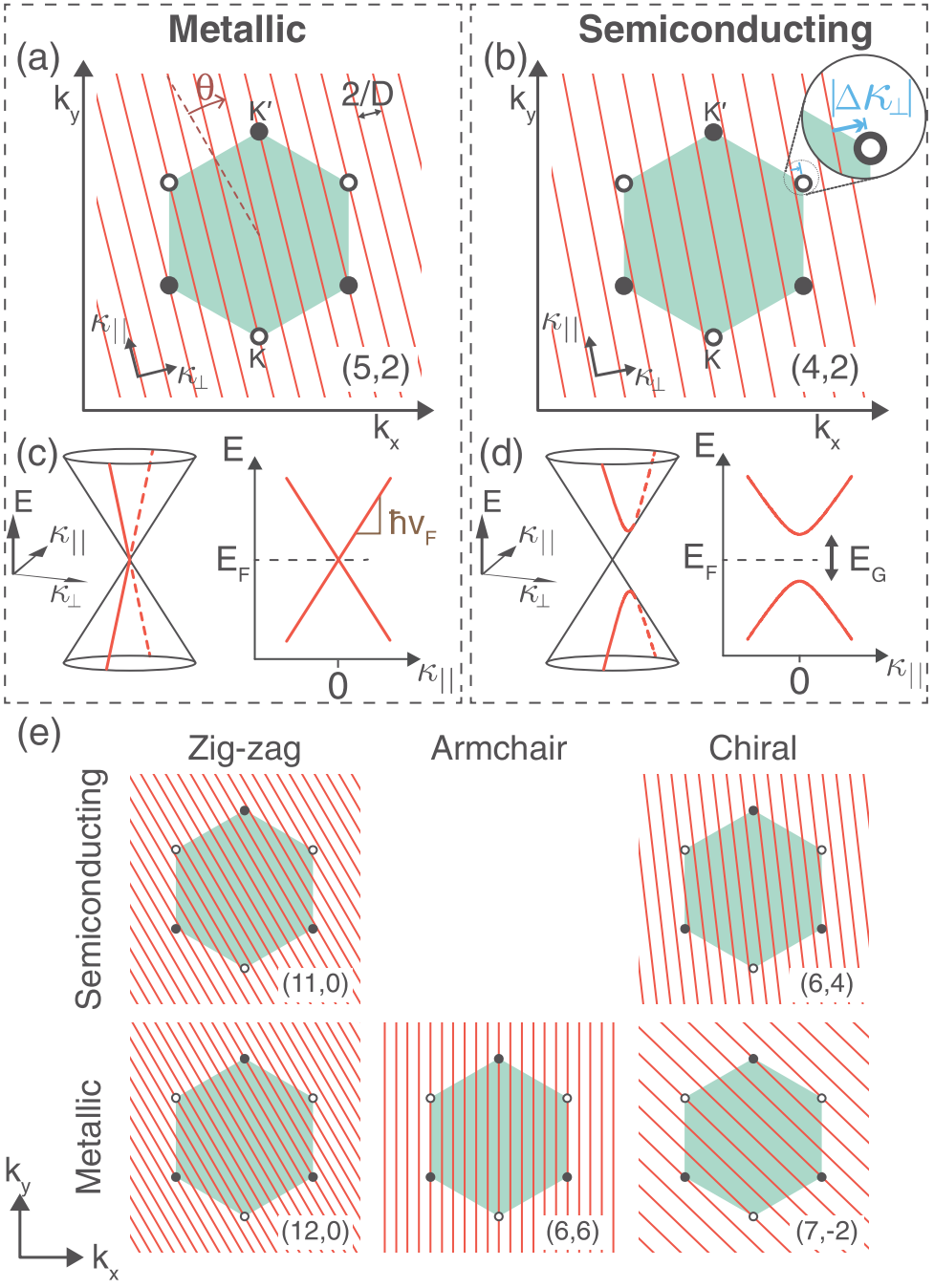

FIGURE 2.1: Carbon nanotube spectrum:
Graphene folding axis can be described by two numbers corresponding to its direction in terms of the two lattice vectors of graphene. This gives rises to different disposition of the carbon atoms referred to as: armchair, zig-zag or chiral. Depending on the folding axis, the allowed wave vectors either fall on or miss the Dirac point leading to metallic or semi-conducting CNTs.[3]

proportional to v_f. It also explains the large band separation as an intuitive argument gives $\Delta_{band} \sim \frac{h v_F}{R}$, with R the radius of the CNT.

Carbon nanotubes also inherit from graphene its K-K' degeneracy[2]. This degeneracy roughly correspond to clockwise/counter-clockwise rotation around the longitudinal axis of the nanotube and adds two differents angular momenta linked to the valley K or K'. The valley index is a priori a good quantum number, as K-K' intervalley scattering would either require breaking time reversal symmetry, or rely on high energy scattering events. Nevertheless, a mixing term $\Delta_{K-K'}$ is empirically relevant for understanding usual experiments (in our experiments it was estimated roughly to be of the order of 100 MHz, cf chapter 4). The lifting of the degeneracy can for example come from short range disorder affecting the honeycomb lattice [3].

2.1.1.2 Single quantum dots :

SDs are formed by connecting a 0D semiconducting island to metallic leads allowing electrons to jump in and out of the island. The structure can hence be biased by applying a voltage (V_{SD}) on one lead and keeping the second one grounded. A gate voltage (V_g)can usually be used to tune the chemical potential of the dot and hence the mean number of electrons on it. As a CNT is already a 1D object, a quantum dot can be simply created by confining the electrons along the length of the CNT. In a semiconducting CNT quantum dot, this confinement directly comes from the metallic electrodes deposited on top of the CNT to contact it. They induce an electrostatic confinement of the electron through two potential barriers, that appear at the interfaces between a semi-conducting and a metallic material. These barriers, named Schottky barriers, appear when adjusting the two work functions of the materials, and can be tuned with the help of the electrostatic potential of a lateral gate.

In order to discuss the physics of SDs one needs to consider mainly four energy scales:

- the single particle level spacing ΔE:

  The confinement of electrons in 0D leads to the quantization of energy, like in an atom. The energy spacing can be related to the size of the structure as it sets the allowed values of momentum. In CNTs, which are already 1D, the confinement sets the allowed values of $k_{\|}$ and the energy spacing is simply given by $\Delta E = hv_f/(2L)$ with L the length of the CNT forming the dot. For 400nm-long carbon nanotubes, $\Delta E \sim 5\text{meV} \sim 60\text{K}$.

[2] A state near the K point has a time-conjugate state near the K' point.

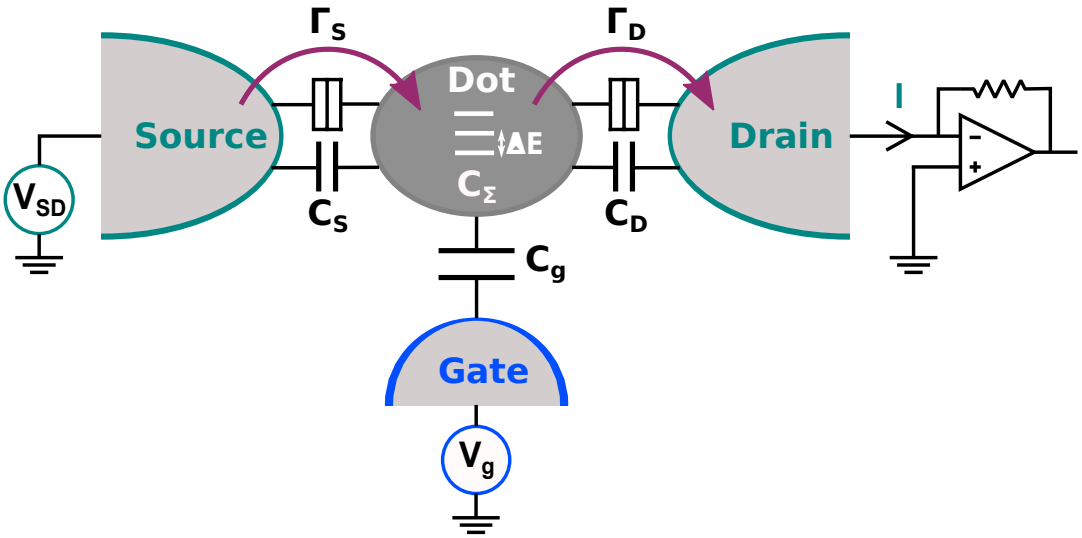

FIGURE 2.2: Single quantum dot:
A quantum dot is a zero-dimensional object (dark grey), which has discrete energy levels, separated by ΔE. In transport experiments, it is contacted to source and drain electrodes. Each contact $i \in (R; L)$ is characterized by a tunneling rate $\Gamma_i/\hbar$ and a capacitance C_i. A gate electrode is capacitively coupled to the dot via the capacitance C_g. The gate voltage V_g enables to tune the position of the energy levels with respect to the reservoirs chemical potential. The ability to charge the dot is basically captured by the dot total capacitance C_Σ, which is the sum of C_L, C_R and C_g. Standard transport measurements are performed by applying a bias voltage V_{SD} to the source electrode, while the current is amplified and measured through the drain electrode.

- the charging energy U:

  Because electrons are confined in a small area, adding an extra electron to an empty orbital of the dot will cost energy due to Coulomb interaction (which is why this energy is sometimes referred to as the Coulomb energy). However, the more the dot is screened by nearby metallic electrodes, the more this energy cost decreases. This result can be recovered in a circuit representation of the dot: adding, or bringing closer metallic electrodes, increases the total capacitance of the island to the ground which decreases the impact of adding a charge. In our CNT devices, this energy is of the order of 10 meV.

- the tunnel rates Γ_S, Γ_D:

  Because the contacts between the metallic electrodes and the dots cannot be perfect, the electrodes, that behaves as electron reservoirs, can only exchange electrons with the dot at a rate $\Gamma/\hbar$. This rate of exchange can be seen as a finite lifetime of the SDs levels. Just like in atom, this means that the levels will be broadened by this parameter. In CNTs, this parameter is not as well controlled as in other

systems (2DEG for example), but it can still be varied on large scale using the gate voltage allowing to explore many different regimes in a single sample.

- the thermal energy $k_B T$:
  The thermal energy of the lead electrons can also contribute to broadening the energy levels.

As all the experiments that will be presented in this thesis have been carried out in a dilution fridge at a base temperature of 35 mK and an electronic temperature below 100 mK, the broadening induced by the temperature will always be much smaller than ΔE and U. We will hence not discuss its impact further but one should keep in mind that if $\Gamma < k_B T$, the temperature will become the dominant source of broadening of the energy levels.

Depending on the relative values of ΔE, Γ and U, different phenomena can be observed in a transport experiment. Their signatures are presented in Fig 2.3 in terms of the differential conductance $G = \frac{dI}{dV_{SD}}$.

- Coulomb blockade regime:
  This regime is achieved when the broadening induced by the leads is much smaller than the charging energy ($\Gamma \ll U$). In this regime, the electrostatic interactions dominate and the number of electron is well defined when no level is aligned with the Fermi seas of the leads. This corresponds to the dark blue area in Fig 2.3 which forms diamonds. Those diamond are outlined by areas of increased conductance where the number of electrons in the dot can fluctuate by one.

- Kondo regime:
  This regime, which is the richest from a physical point of view, corresponds to a Γ which is still smaller than the other two energy scales, but not much smaller than U in practice. This favors some specific virtual tunnel processes which leads, when the electrons on the dots have a net spin, to the formation of a dynamic many-body state involving both the electrons in the leads and the dot electrons. The spectral density of this state is pinned at the Fermi energy and has a finite conductance. It is responsible for the appearance of a Kondo ridge, which is a finite conductance in the middle of a Coulomb diamond which does not disperse in gate voltage, as displayed in Fig 2.3.

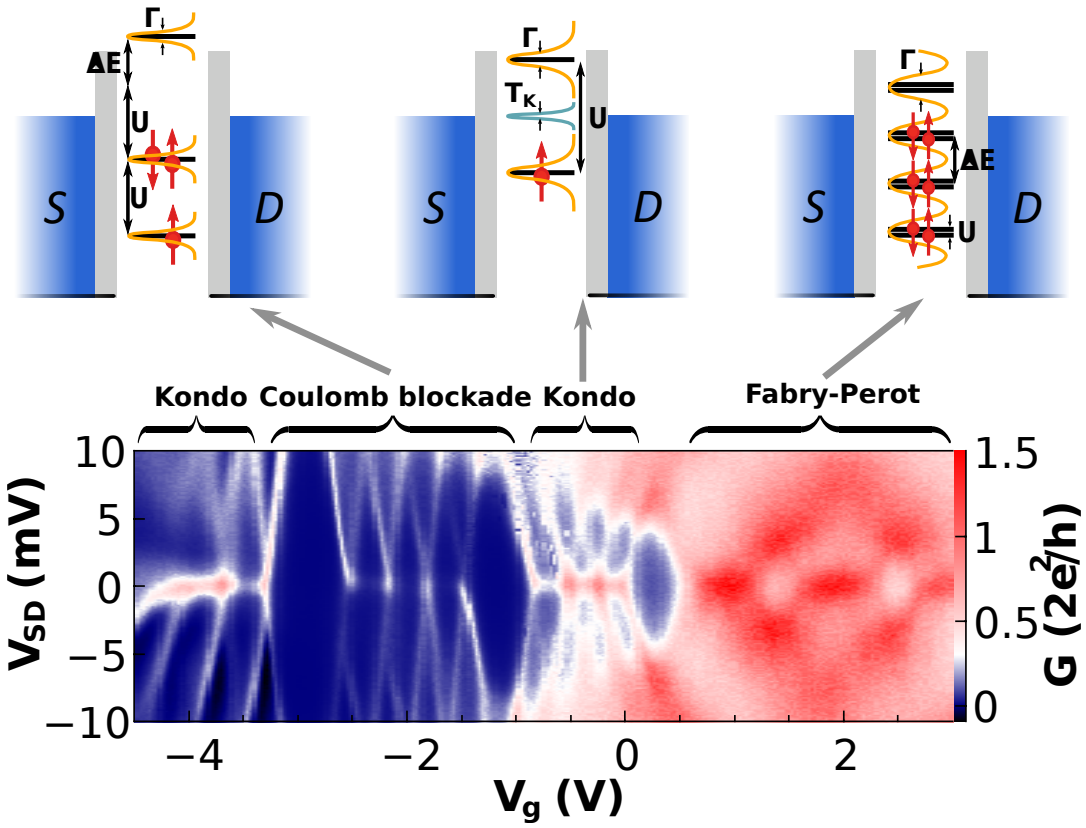

FIGURE 2.3: Transport regimes in a CNT based single dot:
The electronic spectroscopy of the SD often exhibits three regimes of transport : Coulomb blockade, Kondo and Fabry-Perot, because the value of the tunnel rate Γ varies with the gate voltage V_g. The corresponding characteristic features in a conductance colour plot versus gate and bias voltage are respectively : Coulomb diamonds, Kondo ridges and Fabry-Perot checker-board. For each regime a schematics of the QD recalls the relevant parameter hierarchy between the level energy spacing ΔE, the Coulomb energy U and the tunneling energy Γ. The Kondo resonance results in an effective peak in the density of states at zero-bias, whose width defines the Kondo temperature T_K. Here the thermal energy is the smallest energy scale. Extracted from [77]

- Fabry-Perot regime:

  This regime is achieved when the tunneling dominates over the charging energy. In this case, electronic waves interfere just like in a Fabry-Perot interferometer leading to a checker-board pattern in the differential conductance.

In the following we will focus on the Coulomb blockade and the Kondo regime that will be of interest in chapter 5.

Coulomb blockade:

A conductance map, such as the one shown in Fig 2.3, provides a way to estimate the

parameters ΔE, U, Γ and to relate the macroscopic parameters (V_{SD}, V_g) to the dot energy profile. Such a link is essential to understand the experiments.

In the Coulomb blockade regime, because the tunneling rates are the smallest energy scale and hence the levels are well separated, the number of charge on the dot is a good quantum number. Using an electrostatic model of the system, we can, in a first time, explain the shape of the Coulomb diamond in order to extract the charging energy U, the level spacing ΔE and understand how the V_g and V_{SD} influence the dot. We can then relate the shape of the Coulomb peaks, which separates the diamonds at zero bias, to the temperature and tunneling to complete the picture.

Stability diagram: Coulomb diamonds:

In our electrostatic model, we will make the following assumptions (which defines the constant interaction model):

- the single particle spectrum is left unmodified by the interaction. All energy levels have an energy ϵ_i, and for two consecutive levels $\epsilon_{i+1} - \epsilon_i$ is equal either to 0 or ΔE depending on whether or not the levels are degenerate.
- the effect of electron-electron interaction is fully captured by the total capacitance of the system $C_\Sigma = C_g + C_S + C_D$, using the notations of Fig 2.2, with $U = \frac{e^2}{2C_\Sigma}$

In this model, the total energy of the system with N electrons is (we take $e > 0$):

$$E(N) = \sum_i \epsilon_i + U\left(N - \frac{C_g V_g + C_L V_L + C_R V_R}{e}\right)^2 \tag{2.2}$$

The second term is electrostatic and can be computed by considering the energy stored in each capacitor and the work done by the voltage sources.

A given charge configuration will be stable as long as transferring an electron to/from the dot from/to one of the lead is not favorable. This condition gives a set of four inequalities (2 for each lead) defining the Coulomb diamonds in the V_{SD}, V_g plane as illustrated in Fig 2.4. Those inequalities can be written in a compact form by introducing the dot

chemical potential $\mu(N)$:

$$\mu(N) = E(N+1) - E(N) = \epsilon_{i+1} + 2\,U\left(N + 1/2 - \frac{C_g\,V_g + C_S\,V_{SD}}{e}\right) \tag{2.3}$$

$$\begin{cases} \mu(N) + e\,V_{SD} & > 0 \\ -\mu(N-1) - e\,V_{SD} & > 0 \\ \mu(N) & > 0 \\ -\mu(N-1) & > 0 \end{cases} \tag{2.4}$$

As experimentally, we will always bias the dot by applying V_{SD} to the source electrode and keep the drain electrode grounded, the above inequalities are written with that convention in mind.

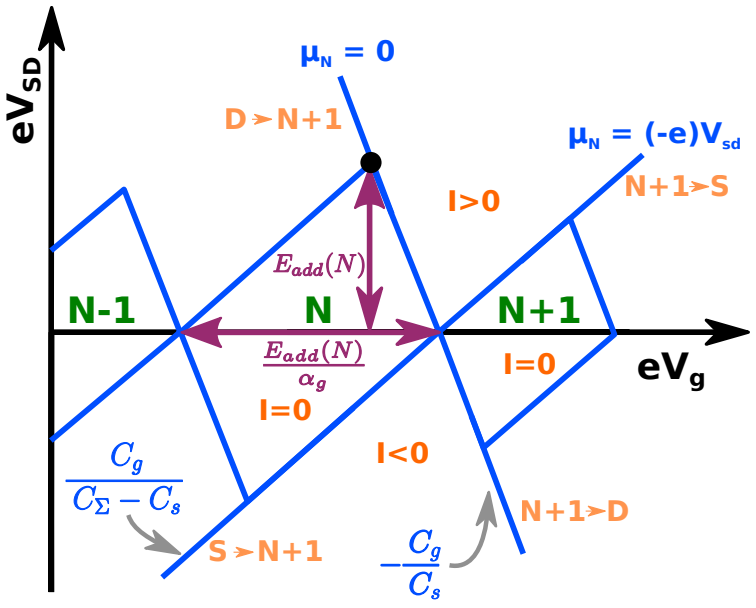

FIGURE 2.4: Charge stability diagram of a single dot for an asymmetric bias voltage $V_S = V_{SD}$ and $V_D = 0$:
The blue lines correspond to the set of conditions ($\mu(N) = -eV_{SD}$, $\mu(N) = 0$) (see equation 2.4). Within a diamond delimited by these lines, the charge in the dot is fixed, and takes an integer value labeled in green. The direction of single-electron transfer is written in orange. It defines the sign of the resulting electronic current.
The positive and negative slopes are respectively $C_g/(C_\Sigma - C_S)$ and $-C_g/C_S$.

The first point of interest in the diagram of Fig 2.4 is the top corner of the Coulomb diamond defined by $\mu(N) = 0$ and $\mu(N-1) = -e\,V_{SD}$ and marked by a black dot. At this specific point, solving the previous equations leads to $e\,V_{SD} = E_{add}(N) = \epsilon_{N+1} - \epsilon_N + U$,

which is nothing else than the energy it costs to add 1 electron to the dot when it already contains N electrons. We can hence directly read that energy from the bias voltage.

A second point of interest is the distance $\Delta V_g(N)$ between the two corners on the $V_{SD} = 0$ line. Those points are defined respectively by $\mu(N-1)|_{V_{SD}=0} = 0$ and $\mu(N)|_{V_{SD}=0} = 0$. Because the chemical potential is zero, electron can freely flow through the quantum dot at those points, which leads to a finite conductance, i.e. a peak in the measured conductance, hence their name of Coulomb peaks. Computing $\Delta V_g(N)$ using the above results yields:

$$\Delta V_g(N) = \frac{1}{e\, C_g/C_\Sigma} \left(\epsilon_{N+1} - \epsilon_N + U\right) \tag{2.5}$$

The ratio $\alpha_g = C_g/C_\Sigma$, often referred to as the gate lever-arm, is an important parameter as it allows to interpret a gate voltage in terms of an effective chemical potential change on the dot. From the above calculation, we see that it can be measured by comparing the width of the Coulomb diamond to its height. Finally the measure of the slope of the diamond allows to recover the last unknown capacitances as the slopes are given by $C_g/(C_\Sigma - C_S)$ and $-C_g/C_S$.

In the plots presented in Fig 2.3, one can notice that the Coulomb diamonds are not of equal width. Three narrow diamonds are followed by a large one. This feature is actually specific to CNT based devices. In CNTs, each energy level is generally four times degenerate. This comes from the combination of the spin-degeneracy (at zero magnetic field), and the valley degeneracy already mentioned in section 2.1.1.1. This means than when adding electrons to a SD made out of a CNT, starting from a completely full level, one has to pay :

- $\Delta E + U$ to add the first electron
- U for each of the next three as the level is degenerate
- $\Delta E + U$ for the fifth and so on

This unequal spacing of the energy levels explain the grouping by four observed in the conductance pattern.

To go further and determine the value of the tunneling, we cannot use any longer only electrostatic arguments and we will introduce the Anderson Hamiltonian to describe the system.

Conductance of a Coulomb peak for $k_B\,T \gg \Gamma$:

Close to a Coulomb peak the charge of the dot is not well defined anymore and can fluctuate on a time scale typically given by the tunnel rates. This gives rise both to a finite conductance and a finite charge susceptibility of the system. To compute those quantities close to zero bias, we will use a simple model. As all the other energy scales are very large, we will consider a single orbital of the dot, so that we can use the Anderson model [78]. For simplicity, we disregard the spin degree of freedom so that the dot can either empty (N=0) or occupied by one electron. Therefore the Coulomb interaction does not come into play. Finally we assume that the tunnel couplings between the dot and the leads does not depend on the wave-vector k of the electrons in the leads.

$$H = \underbrace{\epsilon_d\,\hat{d}^\dagger\hat{d}}_{\hat{H}_{dot}} + \underbrace{\sum_{a\in\{S,D\}}\sum_k \epsilon_{a,k}\hat{c}^\dagger_{a,k}\hat{c}_{a,k}}_{\hat{H}_{leads}} + \underbrace{\sum_{a\in\{S,D\}}\sum_k t_a\,\hat{c}^\dagger_{a,k}\hat{d} + t_a^*\,\hat{d}^\dagger\hat{c}_{a,k}}_{\hat{H}_{tunnel}} \tag{2.6}$$

In this Hamiltonian, $d^\dagger$ (resp $c^\dagger_{a,k}$) creates an electron in the dot (resp in the lead a with a momentum k).

One method to derive the conductance of the system is based on the master equation. Even though it describes only the sequential tunneling limit ($\Gamma \ll k_B\,T$) and is therefore limited to temperatures larger than the tunnel rates in principle, we will present its derivation, as we will use similar derivations numerous times in this work. To establish it, we will compute the evolution of the density matrix up to second order in the tunnel constant (t_a) and trace on the state of the leads. We will work in the interaction representation which is defined as follow:

$$\hat{H}_{int}(t) = e^{i\left(\hat{H}_{dot}+\hat{H}_{leads}\right)t}\hat{H}_{tunnel}e^{-i\left(\hat{H}_{dot}+\hat{H}_{leads}\right)t} \tag{2.7}$$

$$\tilde{\rho}(t) = e^{i\left(\hat{H}_{dot}+\hat{H}_{leads}\right)t}\rho e^{-i\left(\hat{H}_{dot}+\hat{H}_{leads}\right)t} \tag{2.8}$$

$$\hat{c}_{a,k}(t) = e^{-i\,\epsilon_{a,k}t/\hbar}\hat{c}_{a,k} \tag{2.9}$$

$$\hat{d}(t) = e^{-i\,\epsilon_d t/\hbar}\hat{c}_{a,k} \tag{2.10}$$

$$i\hbar\frac{d\tilde{\rho}}{dt} = \left[\hat{H}_{int},\tilde{\rho}\right] \tag{2.11}$$

with ρ the density matrix of the system in Schrodinger representation.

We can integrate formally equation 2.11:

$$\tilde{\rho}(t) = \tilde{\rho}(t_0) + \frac{1}{i\,\hbar}\int_{t_0}^{t}\left[\hat{H}_{tunnel}(t'), \tilde{\rho}(t')\right] dt' \tag{2.12}$$

and re-inject the result in the same equation to get a second order equation in the tunneling [79].

$$\frac{d\tilde{\rho}}{dt} = \underbrace{\frac{1}{i\,\hbar}\left[\hat{H}_{tunnel}(t), \tilde{\rho}(t_0)\right]}_{=0\ \rho \text{ is factorized at } t_0} - \frac{1}{\hbar^2}\int_0^{t-t_0}\left[\hat{H}_{tunnel}(t), \left[\hat{H}_{tunnel}(t-\tau), \tilde{\rho}(t-\tau)\right]\right] d\tau \tag{2.13}$$

In this equation we can eliminate the first order term by considering an initial state in which the density matrix is factorized.

We can now take the partial trace on the state of the leads. However if the two systems become entangled there is no easy way to perform that computation. We would hence like to neglect any correlations between the dot and the leads and assume that the density matrix can be factored into a product of the dot and the leads density matrices at all times. Can we do it ? Correlations between the dot and the leads build up because of the tunneling (t_a), and we are interested in a perturbative regime in which t_a is small. However as time grows, so should the correlations which would prevent any perturbative treatment at it would fail at long time. Nonetheless, we can perform such an approximation because the bath itself has a finite coherence time, a finite memory. The electronic correlations in the leads are essentially short lived ($\hbar/k_B\,T < 1$ns), so our perturbative treatment will remain valid as long as $t_a/(k_B T) \ll 1$. This approximation is known as the decorrelation approximation. In addition, based on a similar argument, we will neglect any correlation between the two leads, such that $\langle \hat{c}^{\dagger}_{a,k}\hat{c}_{a',k}\rangle$ is zero if $a \neq a'$. Those approximations, and the fact that the leads are at equilibrium, imply that the only mean values involving the leads operators that are non-zero are $\langle \hat{c}^{\dagger}_{a,k}\hat{c}_{a,k}\rangle = f(\epsilon_{a,k})$ and $\langle c_{a,k}c^{\dagger}_{a,k}\rangle = 1 - f(\epsilon_{a,k}) = f(-\epsilon_{a,k})$, with $f(\epsilon)$ the Fermi distribution. Under those hypotheses we get:

$$\frac{d\,Tr(\tilde{\rho})_{leads}}{dt} = -\frac{1}{\hbar^2}\int_0^{t-t_0} Tr\left(\left[\hat{H}_{tunnel}(t),\left[\hat{H}_{tunnel}(t-\tau),\tilde{\rho}(t-\tau)\right]\right)\right]d\tau \tag{2.14}$$

$$= -\frac{1}{\hbar^2}\int_0^{t-t_0}\sum_{a,k} e^{i(\epsilon_d-\epsilon_{k,a})\tau/\hbar}|t_a|^2 Tr\left(\left[\hat{c}^\dagger_{a,k}\,\hat{d},\left[\hat{d}^\dagger\,\hat{c}_{a,k},\tilde{\rho}(t-\tau)\right]\right]\right) + e^{-i(\epsilon_d-\epsilon_{a,k})\tau/\hbar}|t_a|^2 Tr\left(\left[\hat{d}^\dagger\,\hat{c}_{a,k},\left[\hat{c}^\dagger_{a,k}\,\hat{d},\tilde{\rho}(t-\tau)\right]\right]\right)d\tau \tag{2.15}$$

At this stage we will have a convolution product which is cumbersome to treat. But, because the density matrix evolves only because of the tunneling and because the correlations of the bath dies quickly selecting a short time window, we can approximate $\tilde{\rho}(t-\tau)$ by $\tilde{\rho}(t)$ as the difference is of order $t_a/(k_BT)$. Furthermore, such a treatment can only be valid when we are interested in times long compared to the correlation time of the bath. We can hence simplify the computation by considering that the duration $t-t_0$ is infinite. Furthermore, we will replace the discrete sum over the wave-vectors by an integral over energy (with a constant density of state ν) and, assume that the tunnel barrier does not depend on energy which is a very reasonable approximation for CNTs, leading to:

$$\frac{dTr(\tilde{\rho})_{leads}}{dt} = -\frac{\pi}{\hbar^2}\sum_{a,k}\delta(\epsilon_d-\epsilon_{a,k})|t_a|^2 Tr\left(\left[\hat{c}^\dagger_{a,k}\,\hat{d},\left[\hat{d}^\dagger\,\hat{c}_{a,k},\tilde{\rho}(t)\right]\right]+\left[\hat{d}^\dagger\,\hat{c}_{a,k},\left[\hat{c}^\dagger_{a,k}\,\hat{d},\tilde{\rho}(t)\right]\right]\right) \tag{2.16}$$

$$= \frac{\pi\,\nu}{\hbar^2}\sum_a |t_a|^2 f(\epsilon_d + e\,V_a)\left(2\hat{d}^\dagger\tilde{\rho}(t)\hat{d} - \hat{d}\hat{d}^\dagger\tilde{\rho} - \tilde{\rho}\hat{d}\hat{d}^\dagger\right) + f(-(\epsilon_d+e\,V_a))\left(2\hat{d}^\dagger\tilde{\rho}(t)\hat{d} - \hat{d}\hat{d}^\dagger\tilde{\rho} - \tilde{\rho}\hat{d}\hat{d}^\dagger\right) \tag{2.17}$$

By projecting on the empty and occupied state of the orbital, we obtain a master equation for the probability for the dot to be empty (P_0) or occupied (P_1). We could have derived the same set of equation from probabilistic consideration and obtained the rates using the Fermi golden rule $\Gamma_a^\pm = \frac{2\,\pi\,\nu}{\hbar^2}|t_a|^2 f(\pm(\epsilon_d + e\,V_a))$:

$$\frac{dP_0}{dt} = \sum_{a\in\{S,D\}} \Gamma_a^-\,P_1 - \Gamma_a^+\,P_0 \tag{2.18}$$

$$\frac{dP_1}{dt} = \sum_{a\in\{S,D\}} \Gamma_a^+\,P_0 - \Gamma_a^-\,P_1 \tag{2.19}$$

The above approximations lead to an evolution of the density matrix controlled by the Γs and in which the typical time for the leads is given by the temperature. It is hence common to rephrase the above validity condition under the form $\Gamma = \frac{\pi\nu}{\hbar^2}|t|^2 \ll k_B T$. This formulation is more correct when considering the approximation $\tilde{\rho}(t-\tau) = \tilde{\rho}(t)$ as densely packed levels would induce a non-negligible evolution. However in the decorrelation approximation it is really t_a that matters.

Using those equation we can then compute the mean occupation of the dot, using the conservation of the probabilities, and the current through a simple balance performed either on the source or drain contact ($P_0 + P_1 = 1$ and $\frac{dP_{0/1}}{dt} = 0$).

$$P_0 = \frac{\sum_a \Gamma_a^-}{\sum_a \Gamma_a^- + \Gamma_a^+} \qquad P_1 = \frac{\sum_a \Gamma_a^+}{\sum_a \Gamma_a^- + \Gamma_a^+} \tag{2.20}$$

$$I = \frac{e}{\hbar}\left(\Gamma_S^+ P_0 - \Gamma_S^- P_1\right) = \frac{e}{\hbar}\frac{\Gamma_S^+\Gamma_D^- - \Gamma_D^+\Gamma_S^-}{\sum_a \Gamma_a^- + \Gamma_a^+} \tag{2.21}$$

In this regime the only energy scale leading to a broadening of the features is the thermal energy, the mean occupation n of the dot is given by P_1 and is equal to:

$$n = N + f(\epsilon_d) = N + \frac{1}{2} - \frac{1}{2}\tanh\left(\frac{\epsilon_d}{2k_bT}\right) \tag{2.22}$$

For our case of interest where $V_S = V_{SD}$ and $V_D = 0$, we get the following the current :

$$I = \frac{e}{h}\frac{\Gamma_S\Gamma_D}{\Gamma_S + \Gamma_D}\left(f\left(\epsilon_d + eV_{SD}\right) - f\left(\epsilon_d\right)\right) \tag{2.23}$$

In the low bias regime $V_{SD} \ll k_B T$, the current through the dot writes $I = GV$ with the low-bias conductance :

$$G = \frac{e^2}{h}\frac{\Gamma_S\Gamma_D}{\Gamma_S + \Gamma_D}\frac{1}{4k_BT\cosh^2\left(\frac{\epsilon_d}{2k_BT}\right)} \tag{2.24}$$

This corresponds to a symmetric peak centered on $\epsilon_d = 0$. Its maximum is a fraction of the conductance quantum $G_Q = \frac{e^2}{h}$, which is equal to $\frac{1}{16}\frac{\Gamma}{k_BT}$ for symmetric tunneling

energies $\Gamma = \Gamma_L + \Gamma_R$. The Full Width at Half Maximum (FWHM) in energy units is $4k_BT \operatorname{arccosh}\left(\sqrt{2}\right) \approx 3.5\, k_BT$.

In practice, our experiments are mostly in the regime $k_BT \lesssim \Gamma$. Equation 2.24 for the conductance remains interesting in that it can give an upper bound for the electron temperature. However this motivates a more detailed treatment of this model as, given that the lifetime of an electron in the dot is limited by Γ, we would expect to find Γ in the linewidth of the level.

Conductance of a Coulomb peak for $k_B\,T \ll \Gamma$:

The approach we will present now aims at taking into account the fact the tunneling can be a coherent process when $k_B\,T < \Gamma$. The systematic approach to derive the properties of the system would be to use Green's functions. We will however use a less general method based on Heisenberg picture for the sake of simplicity.

We start by deriving the evolution of the dot and leads operators in the Heisenberg picture:

$$\frac{d\,\hat{c}_{a,k}}{dt} = \frac{i}{\hbar}[\hat{H}, \hat{c}_{a,k}] \tag{2.25}$$

$$= -i\frac{\epsilon_{a,k}}{\hbar}\,\hat{c}_{a,k}(t) - i\,\frac{t_a^*}{\hbar}\,d(t) \tag{2.26}$$

$$\frac{d\,\hat{d}}{dt} = -i\left(\frac{\epsilon_d}{\hbar} + i\sum_{a\in\{S,D\}}\sum_k \frac{t_a}{\hbar}\,\hat{c}_{a,k}(t)\right) \tag{2.27}$$

At this stage we can formally integrate the equation on $\hat{c}_{a,k}(t)$ and re-inject it in the equation of $d(t)$.

$$\hat{c}_{a,k}(t) = e^{-i\,\epsilon_{a,k}(t-t_0)/\hbar}\,\hat{c}_{a,k}(t_0) - i\,\frac{t_a^*}{\hbar}\int_{t_0}^{t} e^{-i\,\epsilon_{a,k}(t-\tau)/\hbar}\,\hat{d}(\tau)\,d\tau \tag{2.28}$$

$$\begin{aligned}\frac{d\,\hat{d}}{dt} =& -i\frac{\tilde{\epsilon}_d}{\hbar}\hat{d}(t) + i\sum_{a\in\{S,D\}}\sum_k \frac{t_a}{\hbar}\,e^{-i\,\epsilon_{a,k}(t-t_0)/\hbar}\hat{c}_{a,k}(t_0)\\ &- \sum_{a\in\{S,D\}}\sum_k \frac{|t_a|^2}{\hbar^2}\int_{t_0}^{t} e^{-i\,\epsilon_{a,k}(t-\tau)/\hbar}\,d(\tau)\,d\tau\end{aligned} \tag{2.29}$$

To simplify this expression further, we will express $d(t)$ at zeroth order in tunneling and re-inject the result under the time integral. By integrating formally, the time evolution of $d(t)$ dropping the tunneling we get $d(t) = e^{-i\,\epsilon_d\,(t-t_0)/\hbar} d(t_0)$. We are now left to compute $A = \sum_{a\in\{S,D\}} \sum_k \frac{|t_a|^2}{\hbar^2} \int_{t_0}^{t} e^{-i\,\epsilon_{a,k}(t-\tau)/\hbar}\, \hat{d}(\tau)\, d\tau$

In order to do so, we introduce a regularization in the exponential (describing the fact that in the distant past the dot and the leads have not interacted) and we perform the change of variable $u = t - \tau$, we also note $\delta_k = (\epsilon_{a,k} - \epsilon_d - i\,0^+)/\hbar$. We express $\hat{d}(t-u)$ as a function of $d(t)$ such that A becomes:

$$A = \sum_{a\in\{S,D\}} \sum_k \frac{|t_a|^2}{\hbar^2} \int_0^{t-t_0} e^{-i\,\epsilon_{a,k} u/\hbar}\, \hat{d}(t-u)\, du \tag{2.30}$$

$$= \hat{d}(t) \sum_{a\in\{S,D\}} \sum_k \frac{|t_a|^2}{\hbar^2} \int_0^{t-t_0} e^{-i\,\delta_k u} du \tag{2.31}$$

$$= \hat{d}(t) \sum_{a\in\{S,D\}} \sum_k \frac{|t_a|^2}{\hbar^2} \left(\frac{1 - e^{-i\,\delta_k (t-t_0)}}{i\,\delta_k} \right) \tag{2.32}$$

Next we need to perform the summation on k. To do so, we will assume a constant density of state and large (infinite) and symmetric bandwidth[3] , such that $\sum_k \to \int_{-\infty}^{\infty} \rho d\epsilon$ and we relabel ϵ_k in ϵ (and hence δ_k in δ). Furthermore we finally set the time t_0 to 0 which allows to simplify the expression of A:

$$A = \hat{d}(t) \sum_{a\in\{S,D\}} \int_{-\infty}^{\infty} \rho \frac{|t_a|^2}{\hbar} d\delta \frac{1 - e^{-i\delta\, t}}{i\,\delta} \quad = \hat{d}(t) \sum_{a\in\{S,D\}} \pi\, \rho \frac{|t_a|^2}{\hbar} = \hat{d}(t) \frac{\Gamma_S + \Gamma_D}{2} \tag{2.33}$$

We can now integrate formally the equation to obtain $\hat{d}(t)$, to which A gives a finite lifetime. To get slightly more compact equation we will write $\Gamma = \Gamma_S + \Gamma_D$.

[3] If the density of state was not symmetric, A would contribute an imaginary term depending on ϵ_d, however this term would be slowly varying for a smooth density of state and would only renormalize ϵ_d.

$$\frac{d\,\hat{d}}{dt} = -i\frac{\tilde{\epsilon}_d}{\hbar}\hat{d}(t) - \frac{\Gamma}{2}\,\hat{d}(t) + i\sum_{a\in\{S,D\}}\sum_k \frac{t_a}{\hbar}\,e^{-i\,\epsilon_{a,k}t/\hbar}\,\hat{c}_{a,k}(0) \tag{2.34}$$

$$\hat{d}(t) = \int_0^t e^{-\left(i\,\epsilon_d/\hbar+\frac{\Gamma}{2}\right)(t-\tau)}\sum_{a\in\{S,D\}}\sum_k \frac{t_a}{\hbar}\,e^{-i\,\epsilon_k\,\tau/\hbar}\,\hat{c}_{a,k}(0)d\tau + e^{-\left(i\,\epsilon_d/\hbar+\frac{\Gamma}{2}\right)(t)}\hat{d}(0) \tag{2.35}$$

The expression we obtain is non-perturbative in $|t_a|$ which may seem surprising. What is actually hidden in that derivation is that we have resummed all the processes involving $|t_a|$ to second order. This is equivalent to computing the self-energy to second order in the Green's function formalism.

As before we will compute the static properties, i.e. the long time limit. This means that when computing mean values, we will discard all terms involving a decreasing exponential in time. To simplify the notations we will drop the t_0 argument of the c operators and remember that it corresponds to a time where the dot did not yet interact with the leads. Hence we can compute the lead mean values based on equilibrium properties, in particular $\langle c_\epsilon^\dagger c_\epsilon\rangle = f(\epsilon)$ and we can use Wick's theorem. Under this hypothesis we get:

$$\hat{d}(t) = \sum_{a\in\{S,D\}} \sum_{k} \frac{t_a}{\hbar} \frac{e^{-i\,\epsilon_k\,t/\hbar}}{i(\epsilon_d - \epsilon_k)/\hbar + \Gamma/2} \hat{c}_{a,k} \tag{2.36}$$

$$n(t) = \sum_{a',a\in\{S,D\}} \sum_{k,k'} \frac{|t_a|^2}{\hbar^2} \frac{e^{i(\epsilon_k - \epsilon_{k'})t/\hbar}}{(i(\epsilon_d - \epsilon_k)/\hbar + \Gamma/2)\,(-i(\epsilon_d - \epsilon_{k'})/\hbar + \Gamma/2)} \hat{c}^{\dagger}_{a,k}\,\hat{c}_{a',k'} \tag{2.37}$$

$$\langle n(t)\rangle = \int \frac{\mathrm{d}\epsilon}{\pi\,\hbar} \frac{\Gamma/2}{(\epsilon - \epsilon_d)^2/\hbar^2 + (\Gamma/2)^2} f(\epsilon) \tag{2.38}$$

$$\begin{aligned}
\langle n(t)n(t-\tau)\rangle &= \langle d^{\dagger}(t)d(t)d^{\dagger}(t-\tau)d(t-\tau)\rangle \\
&= \sum_{a_1,a_2,a_3,a_4\in\{S,D\}} \sum_{k_1,k_2,k_3,k_4} \frac{t^*_{a_1}\,t_{a_2}\,t^*_{a_3}\,t_{a_4}}{\hbar^4} \langle \hat{c}^{\dagger}_{a_1,k_1}\,\hat{c}_{a_2,k_2}\hat{c}^{\dagger}_{a_3,k_3}\,\hat{c}_{a_4,k_4}\rangle \\
&\qquad \frac{e^{i(\epsilon_{k_1} - \epsilon_{k_2})t/\hbar} e^{i(\epsilon_{k_3} - \epsilon_{k_4})(t-\tau)/\hbar}}{\prod_{k\in\{k_1,k_3\}} \prod_{k'\in\{k_2,k_4\}} (i(\epsilon_d - \epsilon_k)/\hbar + \Gamma/2)\,(-i(\epsilon_d - \epsilon_{k'})/\hbar + \Gamma/2)}
\end{aligned} \tag{2.39}$$

$$= \int\int d\epsilon d\epsilon' \frac{\Gamma^2}{4\,\pi^2\,\hbar^2} \frac{f(\epsilon)f(\epsilon') + f(\epsilon)f(-\epsilon')\,e^{-i(\epsilon' - \epsilon)\tau/\hbar}}{\prod_{\xi\in\{\epsilon,\epsilon'\}} ((\epsilon_d - \xi)^2/\hbar^2 + \Gamma^2/4)} \tag{2.40}$$

$$\tag{2.41}$$

We recover as expected a Lorentzian shape in energy for our level with a lifetime Γ. And we can also compute the charge correlation directly. This quantity will be of interest when coupling the system to a cavity and in chapter 5. The differential conductance $\frac{\partial I}{\partial V_{sd}}$ corresponds, at zero bias, to the transmission through this orbital state, and can be considered as a Breit-Wigner resonance across the quantum dot with a finite lifetime Γ and transition rates in and out Γ_S, Γ_D:

$$G = \frac{e^2}{h} \frac{4\Gamma_S\Gamma_D}{\Gamma^2 + 4\epsilon_d^2} \tag{2.42}$$

The maximum conductance is a fraction of the conductance quantum, which is set by the asymmetry between source and drain tunnel energies. In the fully symmetric case, the conductance reaches $\dfrac{e^2}{h}$. For degenerate levels where interactions come into play, Coulomb peaks qualitatively have the same features : $G_{max} \sim \dfrac{e^2}{h}$ and $FWHM \sim \Gamma$. The conductance cannot be calculated exactly by analytical methods in this many-body situation. Numerous theoretical approaches are currently used to treat many-body problems approximately. In practice, experimental Coulomb peaks are often fit

by a Lorentzian, knowing that height and width are renormalized by interactions. The Lorentzian shape assumption is convenient, and it is a rather good approximation, if the peaks are well separated, which is an hypothesis in our single non-degenerate level approximation.

However when the tunneling rates becomes similar to the charging energy, this approximation cannot remain valid and new physical processes can appear such as cotunneling and Kondo physics. Both processes lead to unexpected charge transfers through the dot in areas where the charging energy should prevent it. Quantum mechanics allows short-lived virtual states associated with non-energy conserving transitions whose lifetime is related to the energy conservation violation by Heisenberg relations : $\Delta E\,\Delta t \geq \hbar/2$. In the case of a dot, tunneling leads to the temporary addition of an electron to the dot which costs U. If the tunneling rates are large enough, the electron can exit the dot, which leads to a neat current. This process is however weak and cannot explain the high conductance ($G \sim e^2/h$) observed on a Kondo ridge, which we will briefly discuss in the next paragraph.

Kondo regime:

The Kondo effect is not specific to quantum dots circuits. It was first observed in 1930's in metal containing dilute magnetic impurities [80], as an increase of the resistance when the temperature decreases below a critical temperature (~ 10 K). This fact was puzzling as all the scattering phenomena (electron-electron, electron-phonon) are suppressed when the temperature decreases. It is only in the 1960's that a theoretical explanation was proposed by Kondo [81]. He related the increase in resistance to an anti-ferromagnetic interaction between the magnetic impurities and the conduction electrons leading to the formation of a localized many-body state around the magnetic impurity. The conduction electrons being involved in those states were not anymore available to carry a current hence leading to the observed increase in resistance.

The same kind of phenomenon can be uncovered in any system in which an isolated spin is coupled to a fermionic reservoir. In particular in quantum dots, when the last available orbital hosts a single electron, and the chemical potential is tuned in a Coulomb diamond, we do have a single spin 1/2 coupled to fermionic reservoirs through the tunnel coupling. The advantage of quantum dots is, once again, their tunability which allows to explore situations not accessible in bulk materials and make them interesting model

systems to study condensed matter problems. One can also consider more exotic systems such as Kondo related to spin 1 [82], or to a pseudo-spin related to an orbital degeneracy [83]. In the following, we will give a brief description of how one can relate the Anderson model to the Kondo problem.

Anderson Hamiltonian and the Kondo problem:

In order to describe the Kondo physics, we will now include the spin degree of freedom in the Anderson Hamiltonian and the charging energy. We will index the spin using σ and we introduce $n = \sum_\sigma \hat{d}_\sigma^\dagger \hat{d}_\sigma$ the total number of electron on the dot (0, 1, 2 in this case). We will note the energy associated to each occupation E_n with n the occupation. We consider a situation without magnetic field such that the spin states are degenerate and with spin independent barriers . The Hamiltonian reads:

$$H = \sum_\sigma \epsilon_d \, \hat{d}_\sigma^\dagger \hat{d}_\sigma + \frac{U}{2} n(n-1) + \sum_{a\in\{S,D\}} \sum_{k,\sigma} \epsilon_{a,k} \hat{c}_{a,k,\sigma}^\dagger \hat{c}_{a,k,\sigma} + \sum_{a\in\{S,D\}} \sum_{k,\sigma} \epsilon_{a,k} t_{a,k} \, \hat{c}_{a,k,\sigma}^\dagger \hat{d}_\sigma + t_{a,k}^* \, \hat{d}_\sigma^\dagger \hat{c}_{a,k,\sigma} \tag{2.43}$$

We consider a situation in which ϵ_d is tuned in such a way that $\langle n \rangle = 1$. Specifically, we focus on $E_1 = \epsilon_d = -U/2$. In this case, the closest states in energy (empty or doubly occupied) are both distant of $U/2$ ($E_0 = E_2 = 0$). However, as mentioned in the above discussion about co-tunneling, transitions involving virtual states exist. Those come in two flavors: one inducing spin-flips (presented in Fig 2.5) and the other conserving the spin of the electron on the dot.

In order to describe that system, it is interesting to derive an effective Hamiltonian, limited to the single occupation subspace at it is the most relevant here, and treat the impact of the other dot occupancy in a perturbative manner. Schrieffer and Wolf [84] proposed a general method to derive such Hamiltonians based on a canonical transformation $H_{eff} = e^{iS} H e^{-iS}$. The matrix S is chosen hermitic (to make the transformation unitary) and such as to cancel the first order terms in the tunneling when expanding the transformation using the Baker–Campbell–Hausdorff formula. The transformation is then truncated to second order in the tunneling to obtain the effective Hamiltonian. Applying this method to the Anderson Hamiltonian yields :

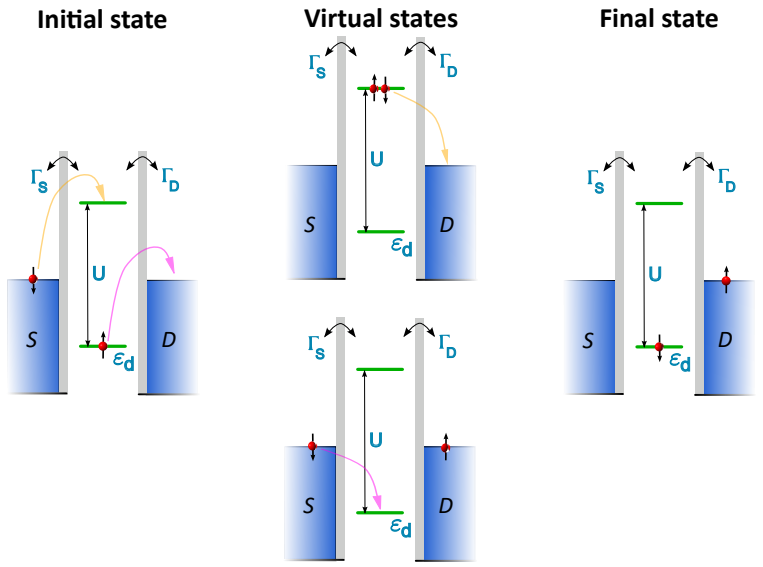

FIGURE 2.5: Spin-flip processes leading to the Kondo cloud formation: Starting from a dot singly occupied, two processes can lead to a spin flip through two tunneling events. First (depicted in yellow), an extra electron can enter the dot leading to a virtual state with an energy higher by U compared to the initial state. The electron that was on the dot first can then exit. In the second process (depicted in pink), the electron in the dot, first, leaves the dot and is replaced by an electron from a lead. Are depicted here only the process involving both leads and inducing a spin-flip, however equivalent processes involving a single lead and/or no spin-flip exist but only spin-flip processes contribute to the anti-ferromagnetic interaction which results in the Kondo effect.

$$H_{\text{eff}} = H_d + H_{leads} + H_{scattering} \tag{2.44}$$

with :

$$H_{scattering} = \sum_{aa' \in \{S,D\}} J_{a,a'} \left(\overrightarrow{\hat{s}}_{a,a'} . \overrightarrow{\hat{S}} \right) + \sum_{kk',aa',\sigma} W_{aa'} \, \hat{c}^{\dagger}_{a,k,\sigma} \hat{c}_{a',k',\sigma} \tag{2.45}$$

This Hamiltonian involves the dot spin $\frac{1}{2} \overrightarrow{\hat{S}}$ and the local spin density of itinerant electron $\overrightarrow{\hat{s}}_{a,a'} = \sum_{k,k',\sigma,\sigma'} c^{\dagger}_{a,k,\sigma} \frac{\overrightarrow{\hat{\sigma}}_{\sigma\sigma'}}{2} c_{a',k',\sigma'}$. Both its terms come from second-order tunneling involving empty and doubly-occupied virtual states, as illustrated by the expressions for the scattering energies :

$$J_{a,a'} = 2 \left(\frac{t_a t_{a'}}{E_2 - E_1} + \frac{t_a t_{a'}}{E_0 - E_1} \right) = \frac{2U t_a t_{a'}}{(\epsilon_d + U)(-\epsilon_d)} > 0 \tag{2.46}$$

and

$$W_{a,a'} = -\frac{1}{2}\left(\frac{t_a t_{a'}}{E_2 - E_1} + \frac{t_a t_{a'}}{E_1 - E_0}\right) = \frac{(2\epsilon_d + U)\, t_a t_{a'}}{2\,(\epsilon_d + U)\,(-\epsilon_d)} > 0 \tag{2.47}$$

However the two terms account for different scattering processes depending on whether or not they induce a spin flip. The first term of (2.45) is called the Kondo Hamiltonian and expresses an anti-ferromagnetic spin-spin interaction between the dot spin and the local spin density of itinerant electron. It involves joint dot and lead electron spin-flips, while the second term is independent of spin and acts as a potential scattering. At $\epsilon_d = -U/2$, only the anti-ferromagnetic term survives and we are left a single spin coupled to leads. The coupling term favors the emergence of a singlet state at low temperature which, because it is delocalized across both leads, can very efficiently carry a current.

Current flowing through the device is related to tunneling rates between reservoirs, which can be calculated perturbatively with respect to $H_{scattering}$. To first order in $H_{scattering}$, the tunneling amplitude is given by the standard co-tunneling formula. However, when computing the tunneling amplitude to second order in $H_{scattering}$ (fourth order in tunneling matrix elements), the spin-flip scattering term causes a divergence below a certain energy $k_B T_K = D e^{-1\frac{\pi\,(U+\epsilon_d)\,(-\epsilon_d)}{\Gamma\, U}}$, defining the Kondo temperature T_K. In this last expression, D is the bandwidth on which the DOS is assumed constant. Since we do not know D, we cannot predict a priori the Kondo temperature of our system. This low-energy divergence is caused by the spin-flip scattering term.

This temperature is the only relevant energy scale to the Kondo physics and dictates the width of Kondo ridge with respect to bias voltage, its behavior in temperature and also at what energy scale charge fluctuations are susceptible to appear. The divergence encountered in the computation of the conductance is actually quite general and prevents one from treating the Kondo in a perturbative manner most of the time. However numerical techniques, based on the renormalisation group developed by Wilson [85], allow to properly take into account all energy scales and computes both the conductance and the charge susceptibility of the Kondo cloud.

2.1.1.3 Double quantum dots :

A double quantum dot (DQD) consists in two quantum dots tunnel coupled to each other. They are usually in series with the leads to which they are contacted, meaning that one lead is contacted to one dot and the other lead to the second dot[86], even if one finds cases where each dot is contacted to both leads [87] or to different drains [88]. In the following, we will focus only on the usual series version and label our dots either L or R (see Fig. 2.6 c).

Each dot chemical potential can be tuned using a local gate voltage $V_{g(L/R)}$ and is characterized by its coupling to its lead $\Gamma_{L/R}$ and its on-site charging energy $U_{L/R}$. To describe the coupling between the two dots we need to introduce two additional parameters :

- U_m: the mutual charging energy describing the Coulomb interaction between electrons trapped in different dots.
- t: the tunneling between the two dots which will hybridize the orbitals to form an artificial molecule.

When each dot can be considered in the Coulomb blockade regime and when the tunneling between the dots is negligible, one can determine the charge stability diagram as a function of the gate voltage using electrostatic arguments similar to the one used for the single dot case. This yields a honey-comb pattern as presented in Fig 2.6. In each cell, the number of electron in each dot is fixed and no current can flow through the device. On the lines separating two stable areas, one level of one dot is aligned with the Fermi seas of the leads (at small bias) which allows current to flow through co-tunneling processes. In such a situation, the current is limited by the coupling between the resonant level and the (far/near) lead. The asymmetry in conductance between the horizontal and vertical lines allows to estimate the asymmetry between the tunnel couplings. Finally, close to the area where four areas should join, one can notice a splitting related to the mutual charging preventing to the states (N, M) and (N+1, M+1) to be degenerate. The two resulting corners are distant of U_m and are called triple points because, at the lowest point in the diagram, the states (N, M), (N+1, M), (N, M+1) (respectively (N+1, M+1), (N+1, M), (N, M+1) for the other point) are degenerate in

energy allowing energy conserving processes to carry current. As a consequence, it is at the triple points that one observes the highest conductance at low bias. When working close to the triple points area, we will prefer, to the natural gate voltage axes, the axes ϵ_Σ and ϵ_δ defined, respectively, along the line joining the triple points and orthogonal to it as illustrated in Fig. 2.6b.

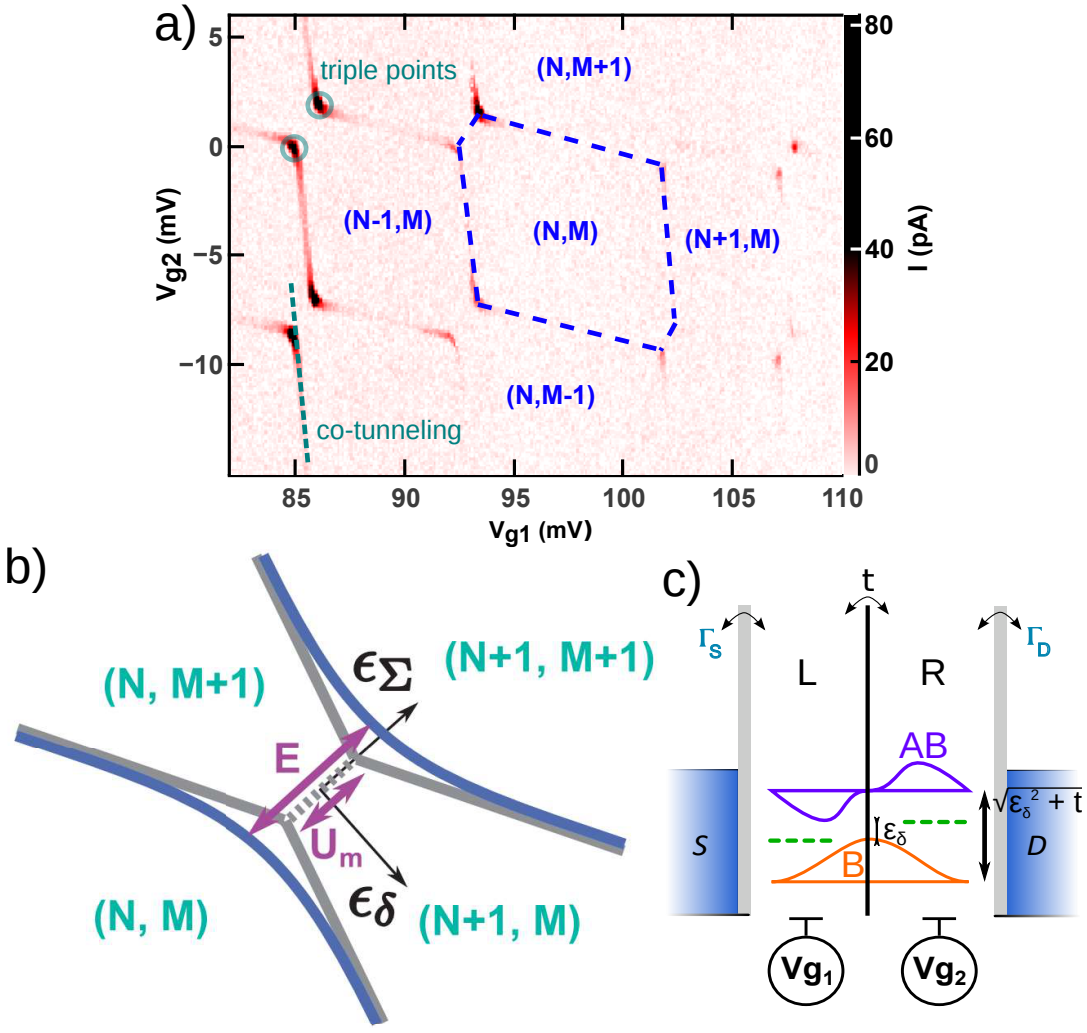

FIGURE 2.6: Double quantum dot stability diagram:
a) Experimental double dot stability diagram measured by tunnel spectroscopy. The stable charge numbers are indicated in blue, the triple points and co-tunneling lines discussed in the main text in green. b) Zoom on the triple point area illustrating the impact of the tunneling and defining the axes ϵ_δ and ϵ_Σ used to describe the charge qubit. c) Schematic of the DQD levels in the area of the triple points in the coherent regime.

When the tunneling t becomes larger than the thermal energy, one cannot neglect anymore its impact. In this regime called coherent regime, the tunneling will hybridize the orbitals of the single dots to give rise to molecular orbitals. This effect will be stronger

the closer in energy the single dot orbitals are. Hence, the area of the triple points will be the more strongly modified. The co-tunneling lines will actually bend and their splitting will become $E = U_m + \sqrt{\epsilon_\delta^2 + t^2}$ in the ϵ_Σ direction. If we focus only on the area between the triple points, the total number of charge in the DQD is frozen. The hybridization, resulting from the tunneling, leads to the formation of molecular bonding (B) and anti-bonding (AB) orbitals in the DQD, with an energy splitting $\sqrt{\epsilon_\delta^2 + t^2}$. Those two states can be used as qubit, coding the logical 0 in the bonding orbital and the 1 in the anti-bonding orbital.

This qubit, often referred to as charge qubit, can be manipulated using the gate voltage used to control the DQD. For a t in the GHz range, applying a resonant modulation on the ϵ_δ axis allows two-axis manipulation of the qubit by varying the phase of the micro-wave signal. Its state can then be read either through DC current measurement, or charge sensing.

However, in all experimental realizations of such qubits, the observed coherence time T_2^* was always of the order of few ns (GaAS [89, 90, 91]; Si [92], CNTs [13]). In all these experiments, which differ by their host material and device implementation, the common limiting factor is the charge noise. The charge noise arises from local electronic jumps between defects leading to uncontrolled fluctuations of the gate potential and hence of the parameter ϵ_d at low frequency. The charge noise spectrum is in $1/f$ with an associated density of about $10^{-4}e/\sqrt{\text{Hz}}$ at 1 Hz in most materials. To improve the coherence time, one can try to find a sweet spot at which the first order contribution of the noise vanishes. In the charge qubit, it corresponds $\epsilon_\delta = 0$. However, the previous values were obtained at this point showing that the charge noise impact is still very large and make qubits with low coherence of those systems.

2.1.2 Superconducting circuits :

Superconducting circuits built on non-dissipative elements such as capacitance, inductance and Josephson junction (JJ) can be used to realize many functions such as high-quality resonators (that will be discussed in section 2.2.1), parametric amplifiers (JPA [93, 94], JPC[95]), and qubits. The goal of this section is to introduce the Josephson junction (JJ) and the transmon qubit which will be used in chapter 5 as probe.

2.1.2.1 Josephson junction :

The JJ is a superconducting-insulator-superconducting junction with a thin enough insulating layer as to allow Cooper pair to tunnel through it. The tunneling of Cooper pair gives rise to a supercurrent depending on the superconducting phase difference ($\phi(t)$) across the junction [96] :

$$I = I_0 \sin(\phi(t)) \tag{2.48}$$

where I_0 is the junction Josephson current. In the presence of a voltage V across the junction the phase evolves according to:

$$\hbar \frac{d\phi}{dt} = 2\,e\,V \tag{2.49}$$

Taking the derivative of equation 2.48 and using 2.49 we get the equation for the AC Josephson effect and deduce the inductance of the junction from Faraday's law ($V = L\,\dot{I}$):

$$\dot{I} = \frac{2\,e\,V\,I_0}{\hbar} \cos(\phi) \tag{2.50}$$

$$L_J = \frac{\phi_0}{2\,\pi\,I_0\,\cos(\phi)} \tag{2.51}$$

with $\phi_0 = e/h$ the magnetic flux quantum.

This non-linear inductance is the key element needed to build anharmonic oscillators out of superconducting circuits. One should also note that because of its shape, the JJ also possesses an intrinsic capacitance.

One last very interesting property from the experimental point of view is the existence of a simple relation between the room temperature resistance of the JJ and its Josephson current. This relation, derived in 1963 by V. Ambegaokar and A. Baratoff [97], can be written as follows for a junction with two identical superconductors:

$$I_0 = \frac{\pi\,\Delta}{2\,R_n} \tag{2.52}$$

with Δ the superconductor gap in V, and R_n the junction resistance in the normal state.

This relation allows, through a simple measurement at room temperature, to determine the inductance of the junction. With this value, one can predict the frequency of the qubits we will build using it. It is also a key ingredient in tuning the fabrication process parameters, that will be presented in 3.

2.1.2.2 Transmon qubit :

The transmon qubit is a superconducting qubit whose design derive from the Cooper pair box (CPB). It was first introduced in 2007 in [41]. Some of its general properties have already been discussed in chapter 1 (see Fig 1.5), here we will go in more details and provide the required background to the discussions of chapter 5.

The main drawback of the CPB that the transmon design overcomes is its large sensitivity to charge noise. Both designs share the same Hamiltonian but operate in different regimes :

$$H = 4\,E_C(\hat{n} - n_g)^2 - E_J\,\cos\left(\hat{\phi}\right) \tag{2.53}$$

with $E_C = e^2/2\,C$ the charging energy of the system determined by its total capacitance C to the ground, $\hat{n}$ is the number of Cooper-pair operator while n_g is a charge offset that can be tuned using a gate voltage in the CPB. The Josephson energy, E_J, is directly linked to the Josephson current of the JJ $E_J = I_0\,\phi_0/2\,\pi$ and ϕ is the phase across the junction.

In order to reduce the sensitivity to charge noise, the transmon design abandons the charge offset tuning and reduces the charging energy by increasing the system capacitance such that $E_C \ll E_J$. The impact of varying this ratio on the first levels energy dispersion is recalled in Fig 2.7.

The flattening of the dispersion relation with respect to the charge number means that charge fluctuations does not induce anymore fluctuations in the qubit energy hence

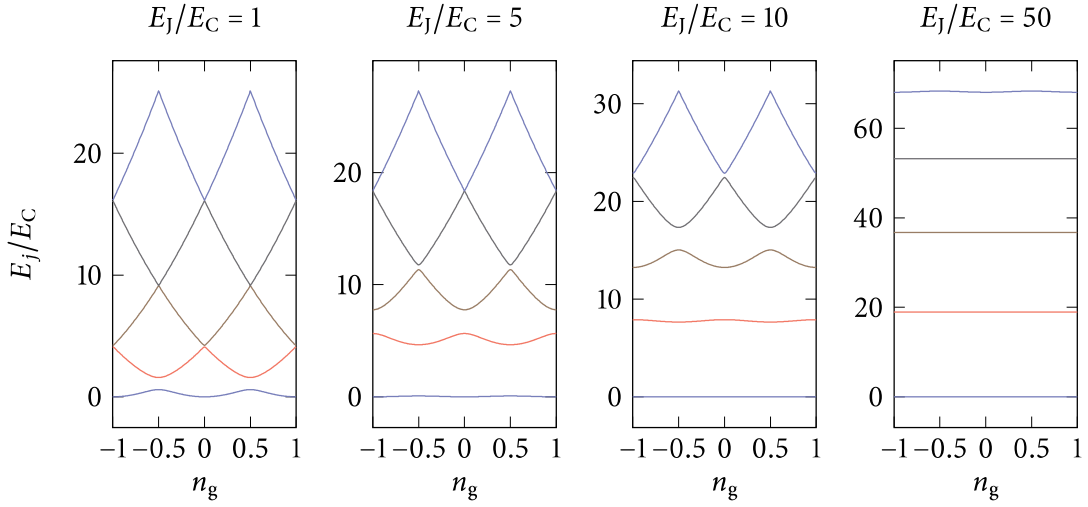

FIGURE 2.7: Charge qubit dispersion as a function of E_J/E_C: The energies of the lowest 5 levels of the charge qubit Hamiltonian 2.53, in units of the charging energy E_C. For low E_J/E_C ratio, we are in the Cooper pair box regime, and the energies are parabolic functions of the offset charge n_g, with avoided crossings. As the ratio of E_J/E_C is increased the levels become exponentially flatter, as we enter the transmon regime. Figure reproduced from [41].

preventing decoherence. This problem can be treated in a fully analytic fashion by decomposing the system on the charge states using Mathieu's functions. This allows to compute the full spectra presented in Fig. 2.7 [98]. This treatment allows to show that the charge sensitivity decreases in an exponential fashion with the ratio E_J/E_C. The cost to pay, to benefit from this reduced sensitivity to charge noise, is a reduced system anharmonicity. The anharmonicity can be deduced from the analytic treatment but, this treatment is cumbersome and yields results that are not straightforward to discuss, because of the special functions it involves. In the following, we will prefer a perturbative treatment that gives very good results in the transmon regime $E_C \ll E_J$, and will make further discussion easier.

In the large Josephson energy limit, phase fluctuation are energetically unfavorable. This allows to consider a development of the cosine term of equation 2.53 to the lowest non-linear order to describe the transmon. Rewriting $\hat{n} = -i\left(\frac{E_J}{8\,E_C}\right)^{1/4}\frac{1}{\sqrt{2}}(\hat{b}-\hat{b}^\dagger)$ and $\hat{\phi} = \left(\frac{8\,E_C}{E_J}\right)^{1/4}\frac{1}{\sqrt{2}}(\hat{b}+\hat{b}^\dagger)$, the Hamiltonian then takes the form of a Duffing oscillator:

$$\hat{H} = \sqrt{8\,E_J\,E_C}(\hat{b}^\dagger\hat{b}+1/2) - E_J - \frac{E_C}{12}\left(\hat{b}^\dagger+\hat{b}\right)^4 \tag{2.54}$$

where b is the annihilation operator for the harmonic oscillator diagonalizing the quadratic part of the Hamiltonian.

Using perturbation theory and considering only the quartic terms of the form $(b^\dagger b)^2$, one can compute the energy of the n^{th} level of the transmon (E_n) and from here deduce the transition frequencies ($\omega_{n,n+1}$) and the anharmonicity of the qubit (α):

$$E_n = -E_J + \sqrt{8\,E_J\,E_C}\,(n+1/2) - \frac{E_C}{12}\left(6\,n^2 + 6\,n + 3\right) \tag{2.55}$$

$$\hbar\,\omega_{n,n+1} = E_{n+1} - E_n = \sqrt{8\,E_J\,E_C} - (n+1)\,E_C \tag{2.56}$$

$$\alpha = \omega_{n+1,n+2} - \omega_{n,n+1} = -E_C/\hbar \tag{2.57}$$

From this, we see that the anharmonicity of the qubit only decreases linearly with respect to E_C, while the charge noise sensitivity decreases in an exponential fashion. This difference of scaling allows to choose parameters in which the charge noise contribution will not be dominant while retaining a sufficient anharmonicity to allow single transition addressing.

The transmon qubit, because of its size, has a naturally large electric dipole that can be coupled to an electric field to manipulate its state. One can model this coupling by adding in the Hamiltonian an AC electric potential $V(t) = V_0\cos(\omega\,t)$ coupled to the electric charge degree of freedom:

$$\hat{H} = \sqrt{8\,E_J\,E_C}(\hat{b}^\dagger\hat{b} + 1/2) - E_J - \frac{E_C}{12}\left(\hat{b}^\dagger + \hat{b}\right)^4 + 2\beta\,e\,\hat{n}\,V_0\cos(\omega\,t) \tag{2.58}$$

with β the ratio between the coupling capacitance and the total capacitance of the transmon.

In the limit $E_J \gg E_C$, we can approximate $\hat{n}$ using the raising and lowering operator of the transmon ($\hat{q}$ and $\hat{q}^\dagger$) (rather than the harmonic oscillator ones) and compute the coupling between the field and two transmon levels:

$$g_{i,j} = \sqrt{2}\frac{e\,V_0}{\hbar}\beta\left(\frac{E_J}{8\,E_C}\right)^{1/4}\langle i|\hat{q}-\hat{q}^\dagger|j\rangle \tag{2.59}$$

$$g_{i,i+1} = \frac{e\,V_0}{\hbar}\beta\sqrt{2(i+1)}\left(\frac{E_J}{8\,E_C}\right)^{1/4} \tag{2.60}$$

The coupling term we find is transverse which means it allows to drive transitions between levels of the transmon, using a resonant signal. Looking at the transmon as a qubit, whose state is encoded in the lowest levels, this is equivalent to a coupling in the xy plane whose axis is actually controlled by the phase of the external drive. We hence have two orthogonal manipulation axes allowing arbitrary control of the qubit state.

Furthermore, from the expression of the coupling, one can notice that single processes cannot induce transition between the state 0 and 2. However two photon processes can induce such transition, involving photons with a pulsation $\frac{\omega_{i,i+2}}{2}$, and we will use them when characterizing our transmons in chapter 5.

So far we have not discussed the transmon relaxation and coherence time. As will be discussed in 2.2.3 the coupling to a cavity limits the lifetime of an atom, and it can be the main channel relaxation of a transmon. It will actually be the situation we will be most interested in chapter 5. The coherence on the other hand, while being ultimately limited by the relaxation, is quite sensitive to any noise affecting the flux across the junction. This is why we will have to magnetically shield our samples as explained in 3. It is also why we will not use flux tunable transmons which are intrinsically more sensitive to flux noise. In those transmon, the JJ is replaced by a SQUID (two JJ in parallel), which allows to tune the Josephson energy and hence the qubit frequency. However the tuning range ($\sim 1GHz$) is too limited to be of interest in the experiments presented in chapter 5, which is why we will not use them given their potentially shorter coherence times.

Now that all the mesoscopic circuits, that will be used in this work have been presented, we will move to the description of the microwave resonator and their coupling to mesoscopic circuits that we will use in our hybrid devices.

2.2 Hybrid systems :

As already pointed out in chapter 1, microwave cavities can be used as extremely sensitively probes of quantum systems, thanks to their combined high frequency and high finesse. They have been first used in the field of cavity QED and coupled to Rydberg atoms. Microwave radiation are centimeter scale waves which, compared to the size of an atom, even in a Rydberg's state, justify perfectly the dipole approximation. The coupling can hence be written as:

$$H_{dip} = -\overrightarrow{D}.\overrightarrow{E} \tag{2.61}$$

with $\overrightarrow{D}$ the atom electric dipole and $\overrightarrow{E}$ the electric field which is considered uniform on the scale of the atom.

However in circuit QED architecture things are not that simple due to the screening of the electric field by metallic electrodes. For those circuits, the confinement of the electric field to scale much smaller than the wavelength can have a large impact on the physical properties probed by the microwave light. The description of this coupling will be the subject of section 2.2.2, following the theoretical model used to describe microwave cavities presented in 2.2.1. We will then distinguish two broad families of hybrid systems:

- one in which the mesoscopic circuit can be seen as closed system and behave like an atom with a discrete set of levels.
- one in which the mesoscopic circuit is open, in that its coupling to the fermionic leads cannot be ignored. Such circuits can model condensed matter phenomena.

The different regimes that can be reached in the case of atom like circuits will presented in section 2.2.3. In this section we will see how the relative strength of the coupling between the atom and the cavity, the dissipation and the energy mismatch between the atomic transitions and the cavity frequency can lead to very different physical phenomena. In section 2.2.4, we will focus on the type of information that can be retrieved from cavity transmission in the case of open circuits.

2.2.1 Microwave cavities :

The most straightforward way to design a cavity consists in having two mirrors facing each other. The resulting system will then have quantized energy modes defined by the length of the cavity. The width of those levels will then be related to the lifetime of the trapped photons. These photons can either escape the cavity, because the reflectivity of the mirrors is not perfect for example, or be absorbed by defects (either in the mirrors or in the propagation medium). This kind of setup finds its origin in the optical domain with the Fabry-Perot cavity.

Going from the optical domain to the microwave domain, one can build a cavity on chip by interrupting the transmission line, which serves as propagation medium, in two points as illustrated in Fig 2.8 for the case of a coplanar waveguide (CPW). In the CPW case, the resulting capacitance between the two sides of the central conductor acts as a mirror in the microwave domain. In such a configuration, the allowed wavelength are multiple of the half-wavelength and the lowest mode electric field is concentrated in the areas close to the capacitances.

Looking at this design from an electronic viewpoint, we can model this cavity as a distributed LC resonator. Such a model allows to extract key parameters of the resonator from easily computed or simulated parameters (see 3 for a discussion on those computations). For example, if we consider only the first harmonic of the resonator, we can relate the electric potential associated with quantum fluctuations in the ground state to the total capacitance and inductance. Starting from the Hamiltonian of an LC resonator of pulsation $\omega_c = \sqrt{1/(LC)}$, expressed in term of flux and charge:

$$\hat{H} = \frac{\hat{\phi}^2}{2\,L} + \frac{\hat{q}^2}{2\,C} \tag{2.62}$$

One can directly derive the charge operator and deduce from it a voltage operator $\hat{V}$:

$$\hat{V} = \frac{\hat{q}}{C} = \sqrt{\frac{\hbar\omega_c^2}{2}\sqrt{\frac{L}{C}}}\left(\hat{a} + \hat{a}^\dagger\right) = V_{ZPF}\left(\hat{a} + \hat{a}^\dagger\right) \tag{2.63}$$

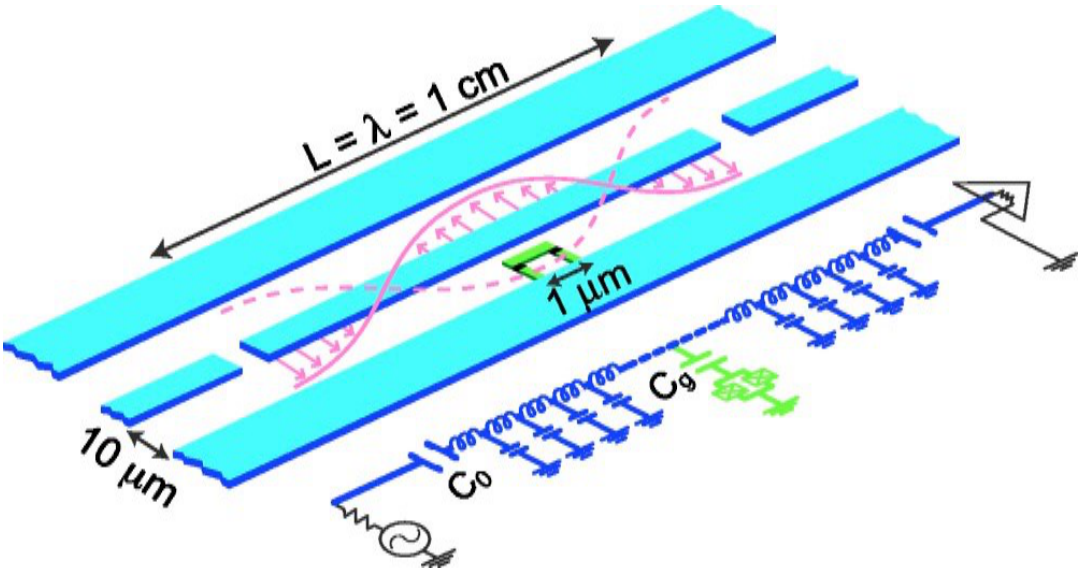

FIGURE 2.8: Schematic layout and equivalent lumped circuit representation of a CPW cavity:
The mode depicted here, in pink, is the second harmonic of the cavity. A qubit is placed in the CPW gap and is hence capacitively coupled to the center conductor at a maximum of the voltage standing wave, yielding a strong electric dipole interaction between the qubit and a single photon in the cavity. Input and output signals, travelling in 50 Ω transmission lines, are coupled to the resonator, via the capacitive gaps in the center line, which allow measurements of the amplitude and phase of the signal transmitted by the cavity. Source [99]

Following [100], we can relate the total capacitance and inductance used in the previous calculation to the inductance L_l and capacitance C_l per unit length that can be computed for a CPW, giving V_{ZPF}:

$$Z_c = \sqrt{\frac{L_l}{C_l}} = \frac{\pi}{2}\sqrt{\frac{L}{C}} \tag{2.64}$$

$$V_{ZPF} = \sqrt{\frac{\hbar\,\omega_c^2\,Z_c}{\pi}} \tag{2.65}$$

As we will see in section 2.2.2, the relevant coupling between a cavity and a circuit is electric by nature. So the larger the pre-factor found in $\hat{V}$ the larger the coupling between our systems is likely to be. We see here that one way to increase the coupling between our systems would then be to use high-inductance resonators. Those can be distributed as in [58] or made out lumped inductance and capacitance [101].

The circuit model can be used to compute the coupling between the resonator and the mesoscopic circuits, and it gives results that agrees well with experiments for transmon qubits. However for quantum dots circuits, one has to be very careful in the modeling of the system in term of circuits, which is why we will mostly avoid it in the following discussion.

As before, we will focus only on the first harmonic, as all other modes will be high enough in energy to have a negligible impact. Under this hypothesis the cavity can be modeled by a single harmonic oscillator. In order to observe the phenomena which will be described in section 2.2.3, such as the vacuum Rabi splitting, the mode needs to be in the ground state or at least to contain very few excitations ($\hbar\omega \gg k_B T$). Bringing an oscillator in its ground state can be challenging if its resonance is at low frequency. However microwave light can reach quantum regime at temperature routinely achievable with commercial dilution refrigerator, since $7GHz \sim 30\mu eV \sim 300mK$. So in the following, we will mostly disregard thermal excitations in the microwave field.

Starting from the Hamiltonian of an harmonic oscillator, one can describe the interaction of the system with propagating modes at the ports of the cavity and also the dissipation, by modeling each one as a bath of harmonic oscillator using the Caldeira-Legget model first introduced in [102]. In the following, we will focus on transmission measurements, so we consider two ports 1 and 2 connected to the outside world and a port L describing internal dissipation. The starting Hamiltonian is the following:

$$\begin{aligned}\hat{H} = \hbar\omega_c\,\hat{a}^\dagger\hat{a} + \sum_{m\in\{1,2,L\}}\sum_{\mu}\hbar\,\omega_{m,\mu}\,\hat{b}^\dagger_{m,\mu}\hat{b}_{m,\mu} + \\ \sum_{m\in\{in,out,L\}}\sum_{\mu}\hbar\,(\hat{a}+\hat{a}^\dagger)(g_{m,\mu}\,\hat{b}_{m,\mu} + g^*_{m,\mu}\,\hat{b}^\dagger_{m,\mu})\end{aligned} \tag{2.66}$$

Using a similar technique to the one used to derive the single dot dynamics in the coherent regime, presented in 2.1.1.2, one can derive an equation of motion for a (see also supplementary materials of [103]). The approximations involved in this calculation are the following:

- the product between the coupling to each bath and its correlation time is small allowing to perform the Markov approximation

- as a consequence the bathes are supposed uncorrelated
- the density of state of the modes in the bathes and their couplings are assumed constant.

This allows to write:

$$\frac{d}{dt}\hat{a}(t) = -i\,\omega_c\hat{a}(t) - \frac{\kappa}{2}\hat{a}(t) - \sum_{m\in\{1,2,L\}}\sum_{\mu} g_m e^{-i\,\omega_{m,\mu}(t-t_0)}\hat{b}_{m,\mu}(t_0) \tag{2.67}$$

with t_0 a time in the distant past at which the bathes have not interacted with the cavity yet, and $\kappa = \kappa_1 + \kappa_2 + \kappa_L$ with $\kappa_m = 2\,\pi\,\rho_m\,|g_m|^2$ where ρ_m is the density of states in the bath m.

The superposition of mode from the bathes can be seen as a mode propagating towards the cavity. By defining $b_{m,in} = \frac{1}{\sqrt{2\,\pi}}\sum_\mu e^{-i\,\omega_{m,\mu}(t-t_0)}b_{m,\mu}(t_0)$, we can rewrite equation 2.67 as:

$$\frac{d}{dt}\hat{a}(t) = -i\,\omega_c\hat{a}(t) - \frac{\kappa}{2}\hat{a} - \sum_m \sqrt{\kappa_m}\hat{b}_{m,in}(t) \tag{2.68}$$

It is important to notice that $b_{m,in}$ does not have the same dimensionality as $b_{m,\mu}$, as it does not represent a photon but a photon flux. Given that the cavity is leaky, we expect some outgoing photon flux too. To compute it, we can choose an initial condition far in the future (t_1) and define $\hat{b}_{m,out} = \frac{1}{\sqrt{2\,\pi}}\sum_\mu e^{-i\,\omega_{m,\mu}(t-t_1)}\hat{b}_{m,\mu}(t_1)$. By doing so one port at a time and computing the difference between the evolution of a we obtain in each case, we can deduce the output field:

$$\hat{b}_{m,out}(t) = \hat{b}_{m,in}(t) + \sqrt{\kappa_m}\hat{a}(t) \tag{2.69}$$

The whole cavity dynamics can hence be described in a simpler fashion, as sketched in Fig. 2.9, by considering two modes at each port: one input mode and one output mode, which is why this description of a cavity is referred to as input-output formalism.

In the following we will mostly be interested in the cavity transmission from port 1, at which there is an input field, to port 2, where there is none. For a cavity without

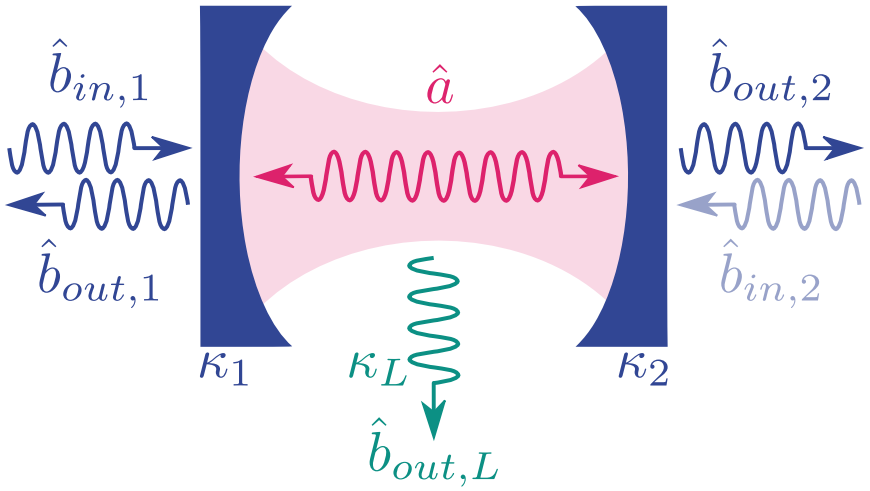

FIGURE 2.9: Input-output formalism:
A single mode cavity associated to an operator $\hat{a}$ is coupled to two ports: 1 and 2. To each port we can associate an in going and out going mode describing the photon flux and a coupling constant $\kappa_{1/2}$. The internal losses of the cavity can be described by a third port with only an outgoing mode and coupling κ_L.

any embedded circuit, we can easily compute the mean transmission in the frequency domain by performing a Fourier transform on the mean value of equation 2.68.

$$i\,\omega\,\langle\hat{a}\rangle = -i\,\omega_c\,\langle\hat{a}\rangle - \frac{\kappa}{2}\langle\hat{a}\rangle - \sqrt{\kappa_1}\langle\hat{b}_{1,in}\rangle \tag{2.70}$$

$$\Rightarrow S_{21} = \frac{\langle\hat{b}_{2,out}\rangle}{\langle\hat{b}_{1,in}\rangle} = \frac{\sqrt{\kappa_1\,\kappa_2}}{i(\omega_c-\omega)+\kappa/2} \tag{2.71}$$

We recover the expected Lorentzian line shape for a Fabry-Perot cavity. We can notice that, by measuring the spectral response of the cavity as a function of the input signal pulsation, we can determine both the central frequency and the linewidth, which appear in (2.71). However in order to determine fully the coupling parameters of the three ports, a transmission measurement is not sufficient and one also needs to look at the reflection properties.

Finally, one can note that in transmission, contrary to what happens in reflection, the phase shift when going from low to high excitation frequencies is always π no matter the ratio between the different couplings. However in this thesis work, it will happen to find lower phase shifts and non-Lorentzian line shape for the transmission of the cavity. To explain those phenomena, we will have to consider the existence of parasitic transmission

channels that can interfere with the cavity mode. In the presence of a single parasitic mode with a small transmission $\sqrt{T}e^{i\zeta}$, we can sum the contributions of the cavity and the mode to the transmission (coupled temporal modes theory [104]). The transmission hence reads:

$$S_{21} \simeq -i\sqrt{T}e^{i\zeta} + \frac{\sqrt{\kappa_1\,\kappa_2}}{i(\omega_c - \omega) + \kappa/2} \tag{2.72}$$

Depending on its transmission and relative phase, one can observe the signatures presented in Fig 2.10. However a single mode model does not explain the data that will be presented in chapter 4, which suggest that multiple channels exist in this setup. But from a single transmission measurement, we do not have sufficient data to actually fully characterize all those modes which will hinder the analyze of those data. In addition, those modes can couple to our circuits in uncontrolled way and it is hence very desirable to eliminate them. The experimental origin of those parasitic modes and how to eliminate them will be discussed chapter 3.

2.2.2 Coupling mechanisms :

With a clear description of the cavity physics in place, we now move to the description of the coupling between the cavity and the mesoscopic circuits embedded in it. We will start with the case of the transmon qubit as it is simpler to treat than quantum dot circuits.

The transmon qubit, apart from its rather small anharmonicity, is very similar to an atom. In particular, when subject to an external electric field, the charge density will be modified and an electric dipole will appear. However, one key difference is that, in the case of an atom, the boundary conditions imposed on the electric field are very far from the atom (on the mirrors basically) compared to its size. This allows to consider the electric field homogeneous and leads to the well-known dipolar Hamiltonian $H_{dip} = -\overrightarrow{d}.\overrightarrow{E}$. For a transmon, on the contrary, the ground plane is very close. However, because we are only coupling the microwave light to macroscopic superconconducting state, the electric potential can be considered rather homogeneous inside the metallic islands while having sharp variations at its edges. This situation allows to use a circuit model, as we have already done to describe the transmon, and to derive the coupling

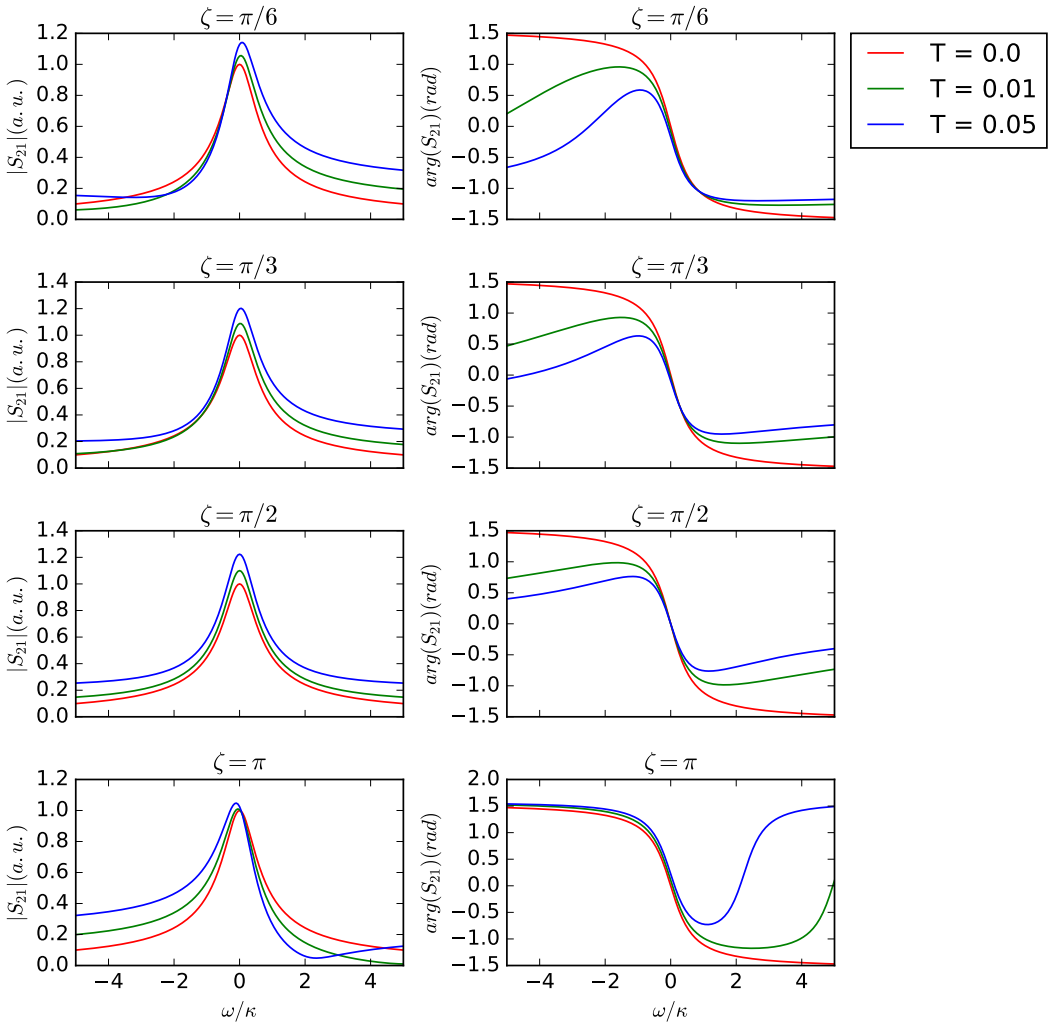

FIGURE 2.10: Fano line shape for a single parasitic mode:
The transmission of the cavity is normalized and the transmission of the parasitic (T) is given in unit of the cavity transmission. We observe that a parasitic mode can induce asymmetric resonances and reduced phase shift across the resonance

of the transmon qubit to the cavity in term of capacitance ratio, as already exposed in 2.1.2.2 when considering the coupling to an electric field.

When moving to quantum dot circuits (see Fig. 2.11), the size based argument does not change (it actually should be even more relevant). However the presence of non-superconducting elements requires a more detailed description of the electrons behavior.

To do so, one can write the coupling in the following formal manner involving a scalar photonic pseudo-potential (cf [105] for a full derivation):

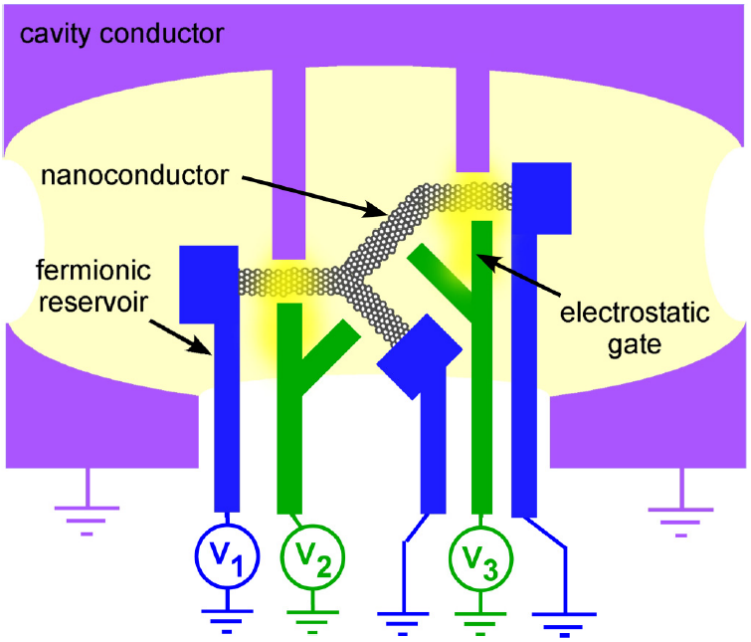

FIGURE 2.11: Electric coupling between a mesoscopic circuit and a cavity: This sketch depicts a mesoscocpic circuit based on a nanoconductor (black) contacted to reservoirs (blue) and whose properties can be controlled by local gate voltages (green). The cavity (purple) has protrusions which shapes the electric potential over the circuit. The electric field strength is encoded in yellow tones, with darker yellow area being associated to higher field.

$$H_{e-ph} = -e \int d^3r \quad \underbrace{\hat{\Psi}^\dagger(\overrightarrow{r})\hat{\Psi}(\overrightarrow{r})}_{\text{tunneling electron density}} \quad \underbrace{V_\perp(\overrightarrow{r})(\hat{a}+\hat{a}^\dagger)}_{\text{photonic pseudo-potential}} \tag{2.73}$$

where the field operator $\hat{\Psi}(\overrightarrow{r})$ includes all tunneling charges in the circuit and $\hat{a}$ is the single cavity mode annihilation operator. The field screening related to the gate and contact electrodes can lead to a strong spatial dependence of the scalar photonic pseudo-potential $V_\perp(\overrightarrow{r})$ over the circuit length.

This coupling Hamiltonian 2.73 is valid under two assumptions:

- the plasmon dynamics in the electrodes and their biasing circuit is much faster than the tunneling dynamics in the mesoscopic circuit and the dynamics of the cavity. This means that the plasmons rebalance immediately the charge locally after tunneling events, and that the currents which screen the excess charge induced by tunneling do not need to be treated explicitly. It is this approximation that allows to consider only the tunneling electrons in the coupling and forget any direct

coupling to the plasmons. This hypothesis is however not valid if, for example, the circuit exhibits dynamical Coulomb blockade [106].

- there is no closed loop in the electronic circuit, disregarding Aharonov-Bohm-like effect, and consequently disregarding coupling mechanisms relying on the magnetic flux.

To gain further insight on the impact of the coupling on the circuit, we will consider a situation in which the tunneling is weak enough so that we can decompose the field $\widehat{\Psi}(\overrightarrow{r})$ onto the local states describing the different circuit elements.

$$\widehat{\Psi}(\overrightarrow{r}) = \sum_{i,o} \phi_{i,o}(\overrightarrow{r}) c_{i,o} \tag{2.74}$$

where i indexes the circuit element being considered (lead electrode, dot) and o indexes the state (a given wave-vector in a lead, a particular orbital in a quantum dot), which can be described by an annihilation operator $c_{i,o}$ and an associated wavefunction density $\phi_{i,o}$.

Using the decomposition of the tunneling density on the orbitals of the nanocircuit, the coupling Hamiltonian reads :

$$H_{e-ph} = h_{int}(\widehat{a} + \widehat{a}^{\dagger}) \tag{2.75}$$

with :

$$h_{int} = \sum_{i,o} g_{i,o} \hat{c}^{\dagger}_{i,o} \hat{c}_{i,o} + \sum_{oj \neq o' i'} \left(\gamma_{i,o,i',o'} \hat{c}^{\dagger}_{i,o} \hat{c}_{i',o'} + h.c. \right) \tag{2.76}$$

and :

$$\hbar g_{i,o} = -e \int d^3 r |\phi_{i,o}(\overrightarrow{r})|^2 V_{\perp}(\overrightarrow{r}) \tag{2.77}$$

$$\gamma_{i,o,i',o'} = -e \int d^3 r \phi^*_{i,o}(\overrightarrow{r}) \phi_{i',o'}(\overrightarrow{r}) V_{\perp}(\overrightarrow{r}) \tag{2.78}$$

Two different coupling mechanisms appear as illustrated on Fig 2.12 both in the case of a single and double quantum dot:

- The term $g_{i,o}$ couples the photons to the charge on an orbital $\hat{n}_{i,o} = \hat{c}^{\dagger}_{i,o}\hat{c}_{i,o}$. Looking at the full Hamiltonian, we can interpret it as a modulation of the energy level $\epsilon_{i,o}\hat{n}_{i,o}$.

- The term $\gamma_{i,o,i',o'}$ describes a modulation of the tunnel coupling term between two orbitals $t_{o,i,o',i'}\hat{c}^{\dagger}_{i,o}\hat{c}_{i',o'}$. It is much smaller than the modulation of the energy levels as it is proportional to the tunnel matrix elements between two different orbitals.

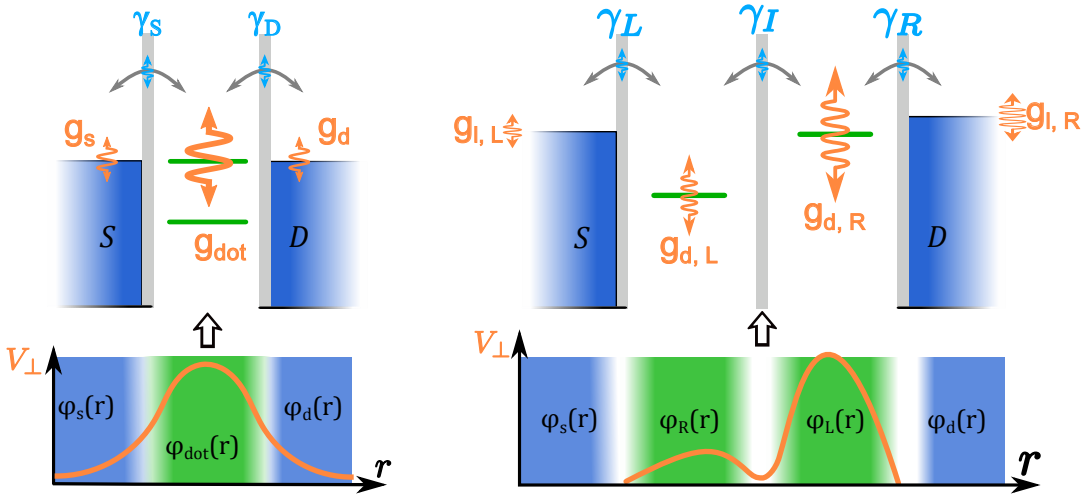

FIGURE 2.12: Cavity induced modulations of quantum dot circuits properties: The electric field of cavity photons can modulate two kinds of properties of quantum dots:

- the chemical potential of electrons sitting either in a quantum dot or in a lead electrode.
- the tunnel coupling between different elements.

It should be noted that the second type on modulation is in general much weaker and can most of the time be ignored.

In the following we will focus on the energy modulation term and forget about the tunneling renormalization. The first thing we can remark is that, for an homogeneous modulation, the field will not lead to any 'real' coupling as the state of the circuit will not be modified by a global change of the energy of all its component. We will hence need to engineer the proper asymmetry in the energy modulation to get a coupling.

As mentioned previously, the above formalism is not appropriate to describe any kind of magnetic coupling between the circuit and the cavity. We will not discuss those couplings because they are in practice much weaker than electric couplings. Although many advances have been made in increasing the coupling strength in such hybrid systems [101], the magnetic coupling to a single spin remains elusive.

We will now focus on two limits of mesoscopic circuits: closed or atomic systems and open systems and describe how we will engineer the coupling in both cases and describe the resulting regimes depending on the coupling strength and dissipation in the system.

2.2.3 Atomic limit :

We have shown in section 2.1.1.3, that a DQD can be used as qubit by encoding information in its B/AB states. Following the work done in cQED on superconducting qubit, we would like to be able to read-out the state of such a qubit using the cavity and manipulate it using fields injected in the cavity. For that purpose, we need a transverse coupling to the cavity field which can be obtained for instance if the cavity modulates the detuning ϵ between the left and right orbitals. Furthermore, we want to keep our electrons inside the DQD so we should avoid strong modulation of the leads energies. To achieve this, one needs to strongly confine the electric potential on one of the two dots. How we can do that in practice will be discussed in chapter 4 as the proposed spin-qubit will use the exact same kind of coupling.

Both the transmon and DQD can behave as qubits, in which case the full Hamiltonian of the system can be mapped on the Jaynes-Cuming Hamiltonian, under the hypothesis that the rotating wave approximation (RWA) is valid :

$$H = \hbar \frac{\omega_q}{2} \hat{\sigma}_z + \hbar \omega_c \hat{a}^\dagger \hat{a} + \hbar g \left(\hat{\sigma}_+ \hat{a} + \hat{a}^\dagger \hat{\sigma}_- \right) \tag{2.79}$$

where ω_q is the qubit frequency, ω_c the cavity frequency, g the coupling between the qubit and the cavity, and $\sigma_\pm$ the raising and lowering operators of the qubit (going from $|g\rangle$ to $|e\rangle$ and respectively). The levels are considered are depicted on Fig 2.13 b.

Disregarding dissipation for a time, we can identify two distinct regimes of this Hamiltonian (without breaking any assumption we made):

- the resonant regime : $\Delta_{qc} = \omega_q - \omega_c \ll g$.
  In this regime, the atom and the cavity states are fully hybridized and we can identify doublets of conserved total excitations in the system. This is depicted in Fig 2.13 c.

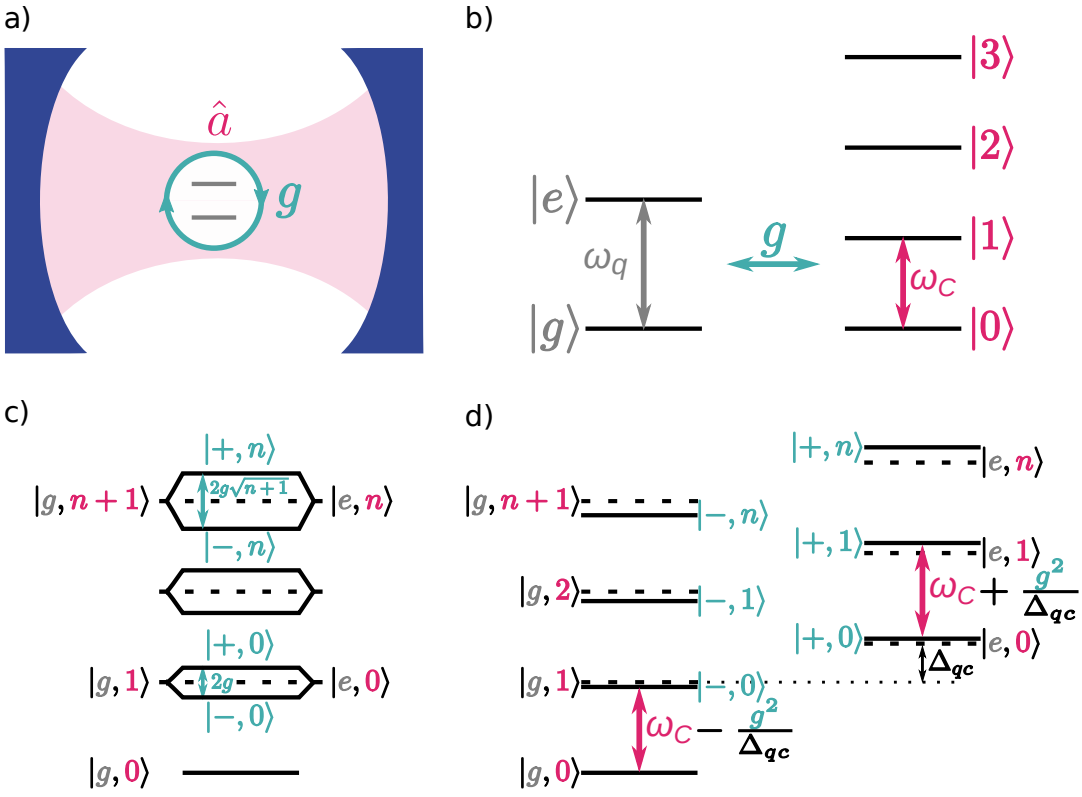

FIGURE 2.13: Non-dissipative qubit-cavity system spectrum:

a) Sketch of a qubit (grey) coupled to the cavity field (pink) with coupling strength g (turquoise blue)

b) Level diagrams (in pulsation unit) of bare qubit (grey) and bare cavity (pink) coupled by g

c) Energy level diagrams (in pulsation unit) in the resonant regime ($\Delta_{qc} = 0$). In this regime, the atom and photon states are fully hybridized and the spectrum can be described in terms of subspaces of constant excitation numbers.

d) Energy level diagrams (in pulsation unit) in the dispersive regime ($\Delta_{q[a)]c} \gg g$). In this regime, the states are weakly hybridized and the main effect of the coupling is to renormalize the spectrum of the cavity based on the atom state (and reciprocally).

Uncoupled states are recalled with dashed lines and grey/pink labels on the sides. Dressed states are represented with plain lines and labeled in blue

- the dispersive regime : $\Delta_{qc} \gg g$.

  In this regime, the energy mismatch is too large to allow energy exchanges between the atom and the photonic field. However, virtual transitions renormalize the energy states leading to a photon number dependent qubit frequency and conversely an atom state dependent cavity frequency. This is depicted in Fig 2.13 d.

Relaxation and dephasing in both systems will broaden the levels as we see them by

spectroscopy. As a consequence, the effect of the coupling as described above will be hidden if decoherence rates are larger than the coupling, as basically both systems will relax faster than they interact.

2.2.3.1 Strong coupling regime:

In the case of the resonant regime, when the coupling is larger than the losses in both the atom and the cavity, we reach the so-called strong coupling regime. In this regime, an excitation can be exchanged several times between the atom and the cavity before being lost. This has a quite striking signature in the spectrum of the cavity: the cavity transmission peak is split in two peaks distant of $\sim 2\,g$, in the single-photon limit. We can recover this result by diagonilizing the system Hamiltonian in the absence of dissipation. We can also go further and compute the cavity transmission using the input output formalism, as presented below.

We start from the Jaynes-Cumming Hamiltonian but we now add dissipation to the cavity (κ) along with a classical drive (ϵ_{in}) and dissipation and dephasing to the qubit (γ, Γ_ϕ). The evolution of the operator mean values is given by the Ehrenfest equations:

$$\frac{d}{dt}\langle a\rangle = -i\,\omega_c\,\langle a\rangle - \frac{\kappa}{2}\langle a\rangle - i\,\epsilon_{in} - i\,g\,\langle\sigma_-\rangle \tag{2.80}$$

$$\frac{d}{dt}\langle\sigma_-\rangle = -i\,\omega_q\,\langle\sigma_-\rangle - \left(\frac{\gamma}{2} + \Gamma_\phi\right)/2\langle\sigma_-\rangle + i\,g\,\langle a\,\sigma_z\rangle \tag{2.81}$$

$$\frac{d}{dt}\langle\sigma_z\rangle = -\gamma\,(\langle\sigma_z\rangle + 1) - 4\,i\,g\mathrm{Im}\left(\langle a^\dagger\sigma_-\rangle\right) \tag{2.82}$$

At this stage, we can either use the semi-classical approximation and write $\langle a\,\sigma_z\rangle \sim \langle a\rangle\langle\sigma_z\rangle$ or compute the evolution of $\langle a\,\sigma_z\rangle$ and truncate later as there is no fully analytic treatment of this problem. The semi-classical approximation does not consider the correlation between the atom state and the photonic field and is hence valid when the photonic fields contains a large number of photons (> 10). However in order to probe the strong coupling regime, one needs to use a low number of photons as otherwise the field saturates the atom ($\langle\sigma_z\rangle \sim 0$) which leads to the disappearance of the splitting (this can be seen as induced transparency in a sense). Those a priori incompatible

approximations yield nonetheless correct insights for the cavity transmission spectrum, which can be validated using numerical methods which are free of that approximation.

$$S_{21} = \frac{\langle b_{out} \rangle}{\epsilon_{in}} = \frac{-i}{i\,\Delta_{cd} + \kappa/2 + i\,g^2 \dfrac{\langle \sigma_z \rangle}{\Delta_{qd} - i\,\Gamma_2/2}} \tag{2.83}$$

where we introduced $\Delta_{cd} = \omega_c - \omega_d$ and $\Delta_{qd} = \omega_q - \omega_d$, with ω_d the pulsation of the field used to probe the cavity and $\Gamma_2 = \gamma/2 + \Gamma_\phi$.

If the cavity is probed with a very low power, such that the mean number of photon is small, the states which will contribute more strongly to the transmission will be the lowest doublet corresponding to a single excitation in the system, as described in Fig 2.13 c. In this situation, we can consider to a good approximation that the atom remains in its ground state and that $\langle \sigma_z \rangle = -1$. We expect to find nonetheless two lines as both hybrid states have a finite weight on the $|g, 1\rangle$ state. Before plotting the full dependency of the transmission, we can compare the transmission at resonance and the bare transmission to identify a key quantity: the cooperativity.

$$\frac{\lim_{\Delta_{qd}\to\infty} |S_{21}||_{\Delta_{qd}=0}}{|S_{21}|}\Big|_{\Delta_{cd}=0} = 1 + \frac{4\,g^2}{\kappa\,\Gamma_2} \tag{2.84}$$

The cooperativity $C = \dfrac{4\,g^2}{\kappa\,\Gamma_2}$ can be used to distinguish between what can be called a coherent regime ($C > 1$) and an incoherent one ($C < 1$). In Fig 2.14, we plot the cavity transmission as a function of the probe frequency and the cavity-atom detuning and the position of the maximum transmission. We also plot a cut at zero detuning between the atom and the cavity.

The color plots in Fig 2.14 display the expected anti-crossing expected for the strong coupling regime. We can also quickly check, on the line plots, that the cooperativity does give us the reduction of the transmission at resonance: it is particularly easy for $C = 1$. One should, however, be careful when associating the strong coupling regime to the split resonance. The visibility of the splitting is not only controlled by the cooperativity but also by the ratio Γ_2/κ as illustrated in Fig 2.15.

The width of the hybrid states is controlled both by the atom and by the cavity, hence, if one is much wider than the other, the cooperativity can be large but the states will

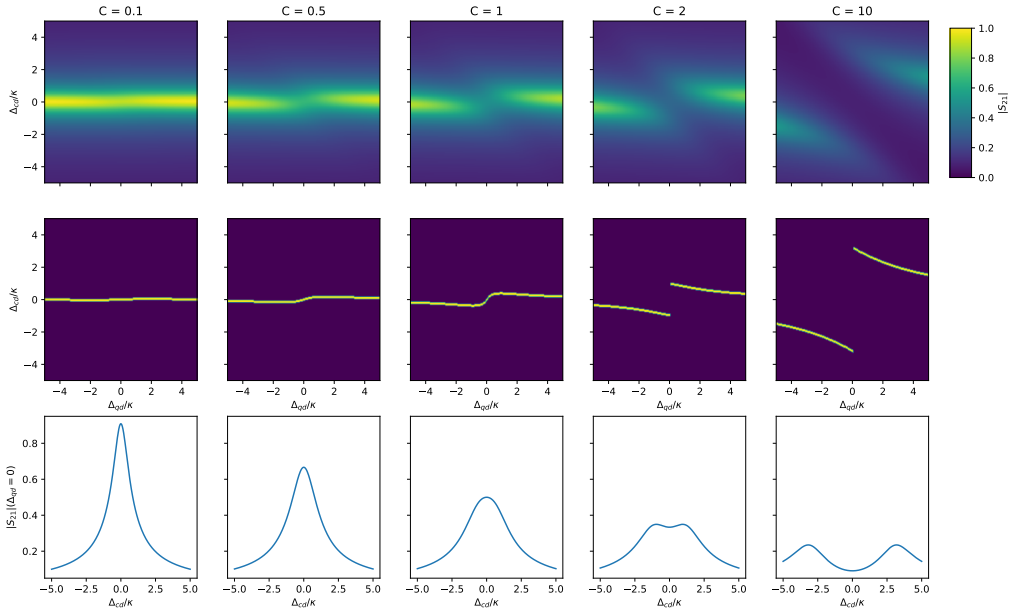

FIGURE 2.14: Cavity transmission around the strong coupling regime: The first line presents the cavity transmission as a function of the detuning between the qubit and cavity (x axis) and the detuning between the probe field and the cavity for different values of C (and $\Gamma_2/\kappa = 4$). The second line plots the points at which the transmission is maximal. The third line presents a cut of the cavity transmission at $\Delta_{cq} = 0$. For cooperativity larger than unity, we observe a splitting of the transmission typical of the strong coupling regime.

still be wider than the splitting of $2\,g$. This leads to the kind of S shaped distortion of the cavity transmission that we see in the position of the maximum in Fig 2.15 for $\Gamma_2/\kappa = 4$. That situation of a bad atom coupled to a good cavity is unusual nowadays in cQED but we will encounter it in chapter 4.

The strong coupling can be interesting to swap an excitation between the photonic field and the atom, however it is not adapted to read out the qubit (or the photonic) state in a non-destructive manner. In order to do so we need to forbid direct energy exchange between the two systems, which can be done by increasing the detuning between the cavity and the atom. We will now present how to describe this regime that will be of paramount importance when describing experiments involving the transmon qubit.

2.2.3.2 Dispersive regime :

The dispersive regime is defined by $g \ll |\Delta_{dc}|$, such that the two systems cannot exchange energy in a direct manner. Simply looking at the equation 2.83 derived in the previous

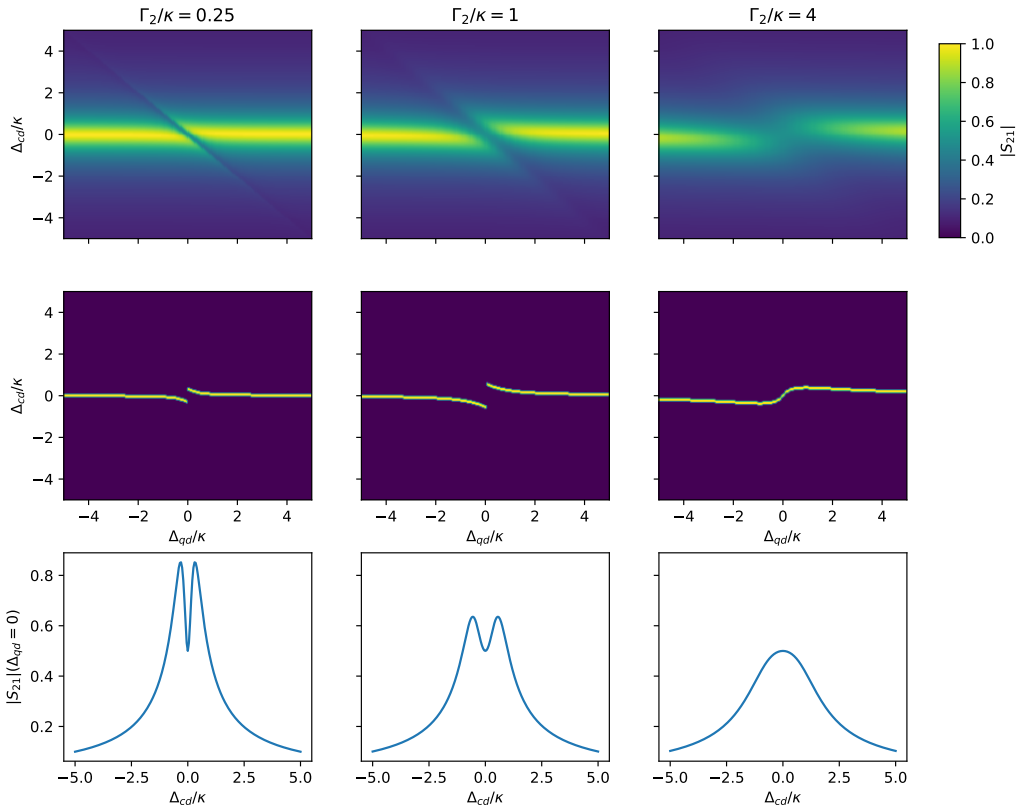

FIGURE 2.15: Impact of the atom linewidth on cavity transmission in the strong coupling regime:
The plots are similar to the ones of Fig 2.14. Here, they have been obtained for a cooperativity of 1 and a varying Γ_2/κ ratio. We notice that as this ratio increase, we go from a situation in which we can resolve two peaks to a situation in which the transmission merely presents an S shape.

section, and that is also valid here, we can notice that the cavity frequency shift induced by the atom depends on the atom state and can hence be used to read the state of the atom. In order to get a more precise description and in particular to see if there is any reverse effect of the photons on the atom, we will derive an approximate Hamiltonian for the system.

As we did in section 2.1.1.2, the idea here is to eliminate the first order processes that do not conserve energy and keep only the second order ones. As before we can get the effective Hamiltonian using the Schrieffer-Wolf transformation. The unitary operator to use here is:

$$U = e^{\frac{g}{\Delta_{qc}}(\hat{a}\,\hat{\sigma}_+ - \hat{a}^\dagger\,\hat{\sigma}_-)} \tag{2.85}$$

And the effective Hamiltonian at second order in g/Δ_{qc} is :

$$H_{eff} = \hbar\left(\omega_c + \frac{g^2}{\Delta_{qc}}\hat{\sigma}_z\right)\hat{a}^\dagger\hat{a} + \frac{\hbar}{2}\left(\omega_q + \frac{g^2}{\Delta_{qc}}\right)\hat{\sigma}_z \tag{2.86}$$

Written this way, we can see that the atom state will shift the resonance frequency of the cavity by $\chi = \frac{g^2}{\Delta_{qc}}$ as we had already inferred. If we want a strong measurement (i.e. projective measure) of the qubit state, we need the pull induced by the atom state to lead to two well separated transmission peaks in the cavity signal. We hence need $2\chi > \kappa$. This condition defines the "strong dispersive regime". As one can see this condition is harder than the one associated with the strong coupling regime as $\frac{g}{\Delta_{qc}} \ll 1$. This regime will not be reached with quantum dots circuits in this work, it is however the usual regime for the transmon qubit.

As explained in section 2.1.2.2, the transmon is not a real two level system but an anharmonic oscillator. And it turns out that when computing χ, we must not only consider the contribution of the transition between the states 0 and 1 but also the transition between the states 1 and 2. This leads to a renormalisation of χ:

$$\chi_{transmon} = \chi_{01} - \frac{\chi_{12}}{2} \simeq -\frac{g^2}{\Delta}\frac{\alpha}{\Delta - \alpha} \tag{2.87}$$

where Δ is the detuning between the cavity and the first transition and α is the transmon anharmonicity.

The interesting thing about equation 2.86 is that we can use it to look at the back action of the photons in the cavity on the atom spectrum. In order to do so it is simpler to rewrite it like follows:

$$H_{eff} = \hbar\omega_c a^\dagger a + \frac{\hbar}{2}\left(\omega_q + \frac{g^2}{\Delta_{qc}} + \frac{g^2}{\Delta_{qc}}a^\dagger a\right)\sigma_z \tag{2.88}$$

Written like this, we see that each photon in the cavity causes a shift of the qubit frequency by an amount of χ. This is the situation illustrated in Fig 2.13 d. If χ is larger than Γ_2 and κ, it means that we will be able to resolve a spectroscopic line for each number of photon in the cavity at illustrated in Fig 2.16. The weight (area) of each peak is related to the probability of finding the associated number of photon in

the cavity. For a coherent state, that distribution is Poissonian allowing to determine precisely the mean number of photon in the cavity [66]. In this regime, often referred to as photon number resolved, one can also perform operations on the qubit conditioned on the number of photons in the cavity by sending a pulse at the proper frequency [107].

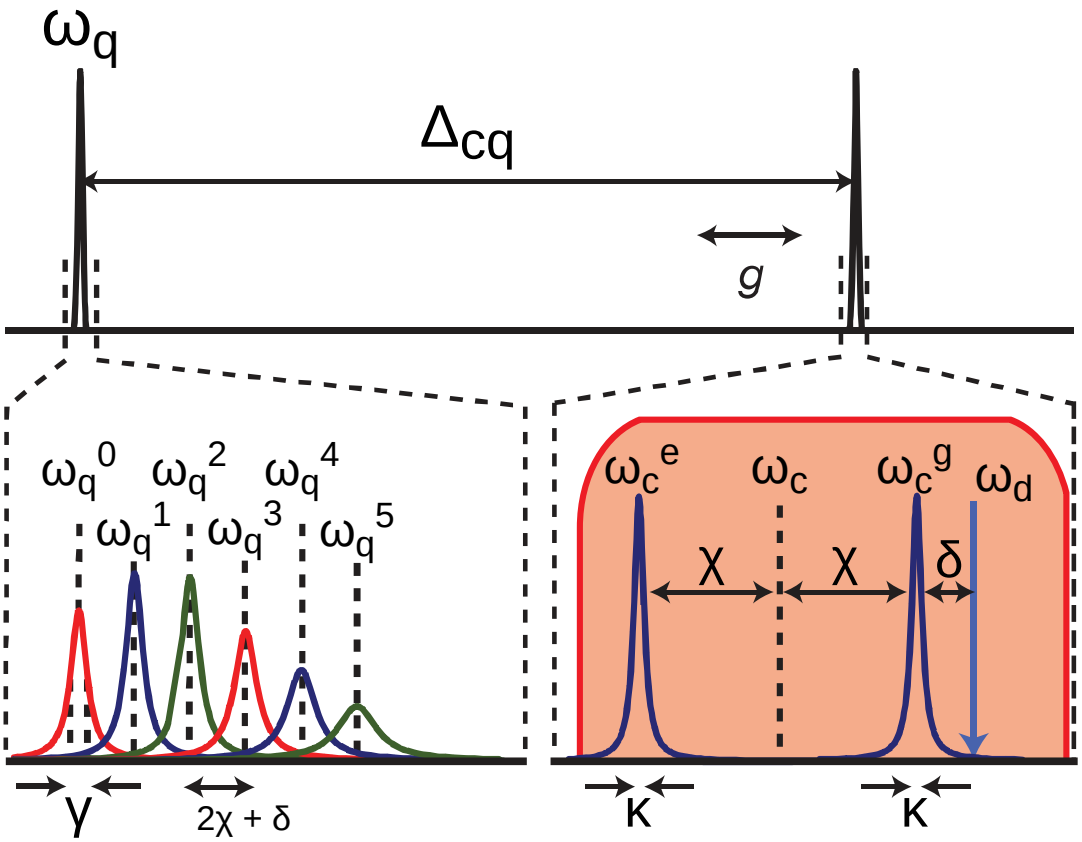

FIGURE 2.16: Strong dispersive and photon number resolved regime: The zoom on the left peak depicts what can be observed in the spectroscopy of a qubit in the photon number resolved regime. Rather than a single peak corresponding to the qubit transition we observe a peak for each possible number of photon in the cavity. The area of the peak n is proportional to the probability to find n photons in the cavity. The zoom on the right peak, which corresponds to the cavity spectroscopy, displays two sub-peaks which appear at well separated frequencies corresponding to the two possible states of the qubit. By probing the cavity transmision at one of those frequencies, one can perform an efficient read-out of the qubit state. Figure adapted from [66].

Another interest of the method we used to obtain equation 2.86 is that it can also be applied when taking into account the bath modeling the cavity decay. We start again from the Jaynes-Cumming Hamiltonian and add a single Caldeira-Legget bath as introduced in equation 2.66:

$$\hat{H} = \hbar \frac{\omega_q}{2} \hat{\sigma}_z + \hbar \omega_c \hat{a}^\dagger \hat{a} + \hbar g \left(\hat{\sigma}_+ \hat{a} + \hat{a}^\dagger \hat{\sigma}_- \right) + \sum_\mu \hbar \omega_\mu \hat{b}_\mu^\dagger \hat{b}_\mu + \tag{2.89}$$

$$\sum_\mu \hbar (\hat{a} + \hat{a}^\dagger)(g_\mu \hat{b}_\mu + g_\mu^* \hat{b}_\mu^\dagger) \tag{2.90}$$

To deduce the impact of the cavity loss on the qubit, we may use the same Schrieffer-Wolf transformation (or adiabatic elimination) and additionally project the resulting Hamiltonian in the subspace where the cavity is empty. We absorb the qubit frequency renormalisation and write $\tilde{\omega}_q$ the renormalized frequency. The resulting effective Hamiltonian is:

$$\hat{H}_{eff} = \frac{\hbar}{2} \tilde{\omega}_q \sigma_z + \sum_\mu \hbar \omega_\mu b_\mu^\dagger b_\mu + \sum_\mu \hbar \frac{g}{\Delta_{qc}} (g_\mu b_\mu + g_\mu {}^* b_\mu^\dagger) \sigma_x \tag{2.91}$$

Using the same method as presented to derive the evolution of the cavity in section 2.2.1, we can compute the induced decay of the qubit. We find that the population of the qubit decay with a rate:

$$\Gamma_p = \frac{g^2}{\Delta_{qc}^2} \kappa \tag{2.92}$$

This rate can be identified with the decay rate of an atom in cavity as predicted by the Purcell effect. It can also be interpreted as the decay of the residual photonic part of the qubit dressed states.

For dots circuits, the coupling will be small enough and the natural lifetime also to allow us to neglect this term. However for the transmon, it can be large and we will engineer our system such that it is the main decay channel. The reasons behind this choice will be explained in chapter 5.

2.2.4 Open systems :

In this section, we will focus on single dots as open quantum system. Contrary to their closed counterpart, we cannot, here, think in terms of coupling the microwave light to a discrete transition as such transitions in SD are in the THz range. In our system, the microwave light can only induce modulation of three different chemical potentials: the

one of the dot and the ones of each lead. As already mentioned, a global modulation of the chemical potential will not have any effect on the system, we are then left with two possible coupling schemes:

- induce asymmetric oscillations of the chemical potential of the leads. This would be in a sense similar to a measure of differential conductance but carried out at high frequency.
- induce symmetric oscillations of the leads chemical potential with respect to the dot one. This can be achieved either by modulating the leads chemical potential, or more directly by inducing modulation only of the dot chemical potential.

The general form of the coupling Hamiltonian is hence:

$$H_{e-ph} = \hbar \left(g\hat{n}_{qd} + g_s\hat{n}_s + g_d\hat{n}_d \right) \left(\hat{a} + \hat{a}^\dagger \right) \tag{2.93}$$

Let us introduce the symmetric and anti-symmetric part of $\hat{n}_s$, $\hat{n}_d$: $\hat{n}_\pm = \hat{n}_s \pm \hat{n}_d$. Charge conservation imposes that $\hat{n}_+ + \hat{n}_{qd}$ is constant. Omitting this constant term in the coupling Hamiltonian, the coupling Hamiltonian can be rewritten as :

$$H_{e-ph} = \hbar \left(g_{qd}\hat{n}_{qd} + g_-\hat{n}_- \right) \left(\widehat{a} + \widehat{a}^\dagger \right) \tag{2.94}$$

where $g_{qd} = g - \frac{g_s+g_d}{2}$ and $g_- = \frac{g_s-g_d}{2}$.

In order to derive the cavity response, we will once again adopt a semi-classical point of view and use $\langle \hat{a}(t) \rangle = \bar{a} e^{-i\,\omega_d\,t}$. The equation of the evolution of $\bar{a}$ can then be written :

$$-\,i\,\omega_d\,\bar{a} = -i\,\omega_c\,\bar{a} - \frac{\kappa}{2}\bar{a} - i\,\left(g_{qd}\hat{n}_{qd}(t) + g_-\hat{n}_-(t) \right) e^{i\,\omega_d\,t} \tag{2.95}$$

To go further we need the dynamics of the quantum dot circuit. If we can assume the modulations induced by the cavity to remain small compared to all other energy scales in the system, we can express it in term of the charge susceptibility of the system to the perturbation of a chemical potential ($\chi(t) = -i\theta(t)\langle[\hat{n}(t), \hat{n}(0)]\rangle$):

$$\langle \hat{n}_i(t) \rangle = \langle \hat{n} \rangle_0 + \frac{1}{\hbar} \sum_{j \in \{qd,-\}} \int \mathrm{d}t' \chi_{i,j}(t-t') g_j \left(\bar{a} e^{-i\omega_d t'} + \bar{a}^* e^{i\omega_d t'} \right) \tag{2.96}$$

Injecting this formula, in the previous equation for the evolution of the cavity field, gives a result similar to equation 2.83 in which it was the qubit charge susceptibility that was involved :

$$\bar{a} = \frac{-i\,\epsilon_{in}}{i(\omega_c - \omega_d) + \frac{\kappa}{2} + i\sum_{i,j} g_i\, g_j\, \chi_{i,j}(\omega_d)} \tag{2.97}$$

From this equation, we can see that the shift in frequency and change in width of the cavity will encode the real and imaginary part of the sum of four different susceptibilities in the case of a single dot. This is not ideal as it may be hard to trace each signal back to its original cause. It is why in all experiment the coupling will be engineered in such a way as to eliminate any coupling to n_-, leaving only the dot susceptibility $\chi_{qd,qd}$ in the response.

We can compute the charge susceptibility of a single dot in the Coulomb blockade regime starting from equation 2.40, which gives the spectral density $S_{nn}(\omega)$:

$$S_{nn}(\omega) = \langle n(t)n(t-\tau)\rangle - \langle n\rangle^2 \tag{2.98}$$

$$= \int_{-\infty}^{\infty} d\tau e^{i\,\omega\,\tau} \int\int d\epsilon d\epsilon' \frac{\Gamma^2}{4\,\pi^2\,\hbar^2} \frac{f(\epsilon)f(-\epsilon')\,e^{-i(\epsilon'-\epsilon)\tau/\hbar}}{\prod_{\xi\in\{\epsilon,\epsilon'\}}((\epsilon_d-\xi)^2/\hbar^2+\Gamma^2/4)} \tag{2.99}$$

$$= \int d\omega' \frac{\Gamma^2}{2\,\pi} \frac{f(\hbar(\omega'-\omega))f(-\hbar\,\omega')}{((\omega'-\epsilon_d/\hbar)^2+\Gamma^2/4)\,((\omega'-\epsilon_d/\hbar-\omega)^2+\Gamma^2/4)} \tag{2.100}$$

We can then use the fluctuation-dissipation theorem to compute the imaginary part of susceptibility:

$$Im\chi(\omega) = \frac{1-e^{-\beta\,\hbar\,\omega}}{2\,\hbar} S_{nn}(\omega) \tag{2.101}$$

$$= \frac{1}{\hbar}\int \frac{d\omega'}{2\,\pi} \frac{\Gamma^2\Big(f(\hbar\,\omega') - f(\hbar(\omega'-\omega))\Big)}{((\omega'-\epsilon_d/\hbar)^2+\Gamma^2/4)\,((\omega'-\omega-\epsilon_d/\hbar)^2+\Gamma^2/4)} \tag{2.102}$$

Finally, we can use the Kramers–Kronig relations[4] to compute the real part which gives the final result:

[4] $Re(\chi)(\omega) = \frac{1}{\pi}\mathcal{P}\int_{-\infty}^{\infty}\frac{Im(\chi)(\omega')}{\omega'-\omega}d\omega'$ and $Im(\chi)(\omega) = \frac{1}{\pi}\mathcal{P}\int_{-\infty}^{\infty}\frac{Re(\chi)(\omega')}{\omega'-\omega}d\omega'$

$$\chi(\omega) = \frac{1}{\hbar}\int \frac{d\omega'}{\pi\,\omega}\frac{f(\hbar\,\omega') - f(\hbar(\omega'-\omega))}{(\omega' - \epsilon_d/\hbar - i\,\Gamma/2)\,(\omega' - \omega - \epsilon_d/\hbar + i\,\Gamma/2)} \tag{2.103}$$

We find that the charge susceptibility only depends on the tunnel coupling to the leads which can be determined through transport measurement. Hence, if we know precisely the number of photons in the cavity, we can use this result to determine the electron-photon coupling strength.

In the Coulomb blockade regime, the conductance and the charge susceptibility give equivalent information on the quantum dot properties, but it is not always so. For example in the case of the Kondo regime described in section 2.1.1.2, a finite conductance exists only because the electrons tunnel through a virtual state. One should not be able to observe such a state, which means that the number of electron in the dot should appear frozen. The system charge susceptibility should vanish. The corresponding experiment was carried out in the lab and indeed revealed that absence of charge susceptibility of the Kondo cloud, whereas it displays a finite conductance [23].

Now that the theoretical basis needed to describe the experiments presented in this thesis have been introduced, we will focus on the sample design, fabrication and measurement in the next chapter.

Chapter 3

Experimental techniques

The goal of this chapter is to present the different techniques involved in designing, fabricating and measuring the samples under study in this work. The order of the following sections reflects a kind of idealized work flow, even if in practice due to time constraints, previously unknown issues or not yet developed techniques, it has not really been the work flow of this thesis, save close to its end.

3.1 Sample design :

When considering a new experiment, involving a new kind of sample, the first step is to design the sample. This step is obviously crucial as it will impact all further work. In particular when working in the microwave domain, one should pay special attention to the sample layout to avoid parasitic microwave modes that can lead to Fano shaped cavity transmission spectrum as discussed in chapter 2, or degrade the properties of the mesoscopic circuits we want to study. As all circuit parts have to interact properly

together, it is not easy to design each component in a completely separated manner, so that the following presentation may seem a bit artificial.

3.1.1 Substrate choice :

The first choice to be made is the choice of the substrate as it will influence largely the properties of the microwave related parts of the device, through its dielectric constant . The constraints on this choice are the following:

- it should have low losses in the microwave frequency range, as otherwise our cavity will have high internal losses which will limit the quality factor.
- it should be insulating as otherwise we are likely to observe leaks between the gate used to tune the dot circuits.
- it should induce a low charge noise in the devices to preserve coherence, which means it should have a low number of charge trapping defects.

The superconducting community is mostly using, nowadays, either sapphire or high-resistivity silicon from which the natural oxide layer has been removed. We cannot use high-resistivity silicon without oxide as we would have short between our DC gates. Sapphire on the other hand is an insulator but e-beam fabrication processes on it tend to be more complex and there is little experience in the lab about those processes. As a compromise, we will be using thermal silicon oxide (500 nm) on high-resistivity silicon ($10k\Omega.cm$) even if we know that the silicon oxide layer will contain charge trapping defects.

3.1.2 Cavity design :

The cavities used in this work are made out of coplanar wave guide (CPW) as already mentioned in chapter 2. Fig 3.1 presents the profile of a CPW:

The aspect ratio of the CPW s/w will influence two properties of the cavity: first the impedance of the resonator and second the losses related to surface defects [108]. As explained in the section 2.2, the higher the impedance the higher the coupling we

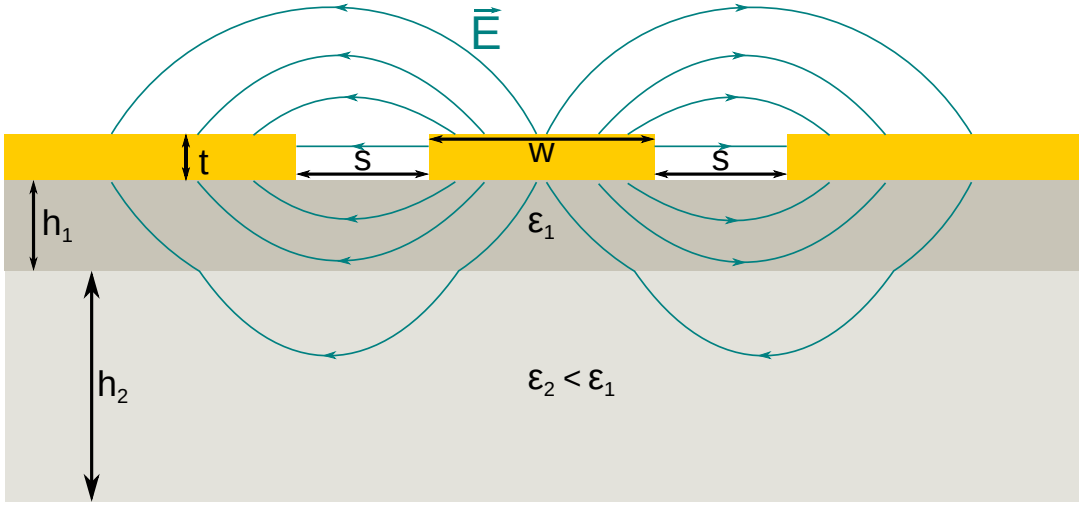

FIGURE 3.1: Coplanar waveguide profile:
A CPW profile is mainly characterized by the width w of the central conductor and the gap s between it and the ground planes. The smaller the gap the more strongly the field is confined close to the surface, increasing losses related to surface defects as well as decreasing the importance of the substrate bottom layer. The thickness t of the metallic layer is usually negligible compared to the substrate thickness $(h_1 + h_2)$, and we will model it as a bi-dimensional sheet, save when determining the impedance of the CPW.

can expect between the photons and our nano-circuit. However in a CPW geometry, it is actually hard to reach characteristic impedances higher than 200Ω while keeping reasonable dimensions. As the feeding and collecting CPWs need to be 50Ω to avoid parasitic reflections going from them to the coaxial cables in the fridge, we will use a 50Ω CPW also for the cavity, for the sake of simplicity.

When increasing the gap of the CPW, the electric field between the central conductor and the ground plane diminishes in magnitude and becomes less vertically confined. Both those facts lead to a smaller coupling to dissipative defects such as resist residue. Given the large number of steps in the fabrication process, many resist residues are likely to be left behind so increasing the gap seems appealing, if we can properly engineer the coupling to not suffer from the reduced electric field. We will discuss that second point later.

The impact of surface defects is hard to model, however looking at the literature [108], it appears sensible to target a gap of the order of $30\mu m$, which leaves us with the determination of the central conductor width in order to get the proper impedance. Analytic formula exists to relate the impedance of a CPW to its dimension but only for

a single layer of underlying dielectrics. While it is possible to experimentally determine an effective dielectric constant for the stack, that value is sensitive to the CPW gap width as it depends on the penetration of the electric field in the different layers. The CPW for the cavity has a fixed width along its length, however it is not the case of the feeding and collection CPWs. Those CPWs match the dimensions of the cavity CPW at one end. At their other end, to avoid any parasitic reflections, they must be close to the dimensions of the CPW to which they will be micro-bonded when the sample is mounted in the sample holder. The gap of the CPW of the sample holder is close to the thickness of the oxide layer, which means that when designing a CPW on the sample with similar dimensions the electric field will reach into the silicon layer. On the contrary at the cavity end, the gap is much smaller and the electric field is strongly confined in the oxide layer. The fact that the confinement of the field varies prevent us to use an effective electric constant. To circumvent this difficulty, we used finite element modeling solvers to determine the aspect ratio of the CPW giving a constant impedance. In this thesis work, we used HFSS, to perform simulations on such slices and also full 3D modeling of the samples. For slices, the thickness of the metallic layer ($\sim 100 - 150$nm) is taken into account while in 3D models it is approximated by a 2D plane. Fig 3.2 shows the computed gap of the CPW needed to preserve an impedance of 50Ω with a gap width varying linearly from 5 to 400 μm.

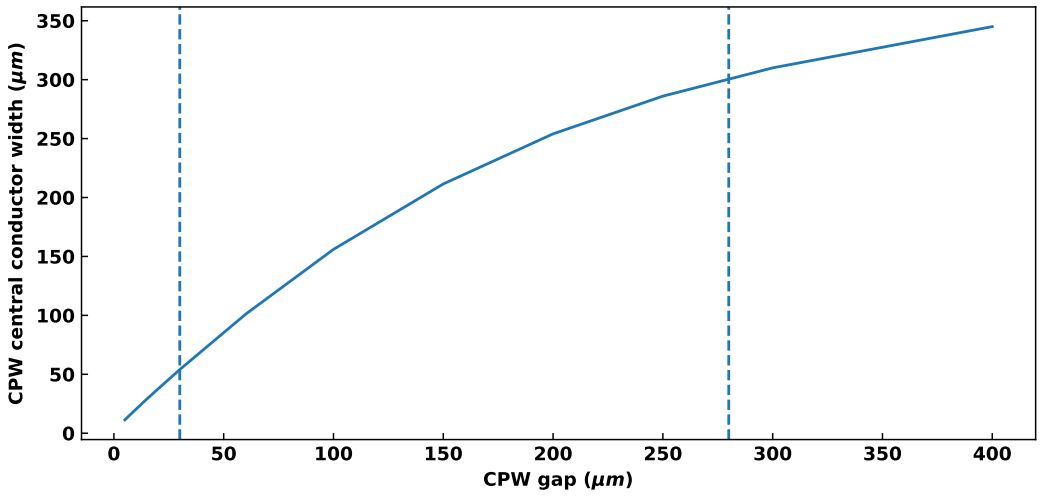

FIGURE 3.2: 50Ω CPW aspect ratio:
The width of the central conductor is optimized as a function of the CPW gap to have a 50 Ω CPW on our substrates. The simulation are carried out using HFSS. The vertical lines corresponds to the cavity gap (30 μm) and the bonding pad gap (280 μm)

Once the aspect ratio is fixed, we can choose the cavity length to get the proper frequency. The frequency choice depends on the cavity role in the setup and on the experimental constraints on the detection chain and sample holder as will be discussed in section 3.3.1. Those constraints led us to work in the 6 to 8 GHz band. From the previous determination of the impedance, we can extract an effective dielectric constant corresponding to the CPW line and link the frequency f_c to the length L of the cavity :

$$L = \frac{c\, f_c}{2\sqrt{\epsilon_{eff}}} \tag{3.1}$$

In theory, we should take into account the kinetic inductance of the superconductor to get the exact value off the resonance frequency. The kinetic inductance of a superconducting wire is given by [109]:

$$L_K = \mu_0\, \lambda_L\, \frac{l}{A} \tag{3.2}$$

with λ_L the London penetration length, l the length of the superconductor and A the cross-section of the wire.

In the case of niobium that we will be using, the London penetration length is about 400 Å [110] for $T \ll T_c$. Combined with the typical dimensions of the cavity CPW, this gives:

$$\frac{L}{L_K} \sim 1000 \tag{3.3}$$

which explains why we can get nearly quantitative result from HFSS simulations even neglecting the kinetic inductance.

Once the cavity designed, we can, using HFSS, analyze the electromagnetic eigen-modes in order to validate the frequency of the resonator. The system can have several eigen modes but we can identify the CPW mode by looking at the mode field geometry. We can also look at other unwanted modes that may appear but we will come back to that in section 3.1.5.

At this stage, we need to adjust the coupling of the cavity to the feeding and collecting lines used to carry out the transmission measurements we will be interested in. The main concern driving these choices are the following :

- if the coupling to the external lines is very strong, the cavity will have a very large linewidth and will not be very sensitive (as the linewidth set the minimal detectable susceptibility).
- if the internal losses are very large compared to the coupling to the outgoing line, the signal to noise ratio will be very low as most of the photons which interacted with the system will never be detected.
- similarly if the input line is more coupled than the outgoing line the photons will exit by the wrong end of the cavity and the measured signal will be weak.

We would hence like to have the following hierarchy between the different couplings:

$$\kappa_{in} \ll \kappa_{loss} \lesssim \kappa_{out} \tag{3.4}$$

The fact that κ_{in} is very low is in practice not an issue as we have a lot of margin on the input power we can apply.

The coupling rates are directly related to the capacitances between the central conductor of the CPW cavity and the central conductors of external CPWs. Those can either be a simple cut in the central conductor or inter-digitated capacitances. Using HFSS, one can simulate the scattering matrix of the sample (ie transmission and reflection coefficients between both ports as a function of the frequency) which allows to extract separately all the previously mentioned rates, using a Lorentzian model such as the one presented in section 2.2.1. This allows to choose the proper length for the inter-digitated capacitances at input and output as illustrated in Fig 3.3. Of course, the extracted κ_{loss} only reflects the radiation losses and the losses related to the natural losses of the substrate and is hence, in general, widely underestimated. However, it can be estimated from previous experiment carried out in the lab on samples with smaller gaps to be of the order of 500kHz to 1 MHz.

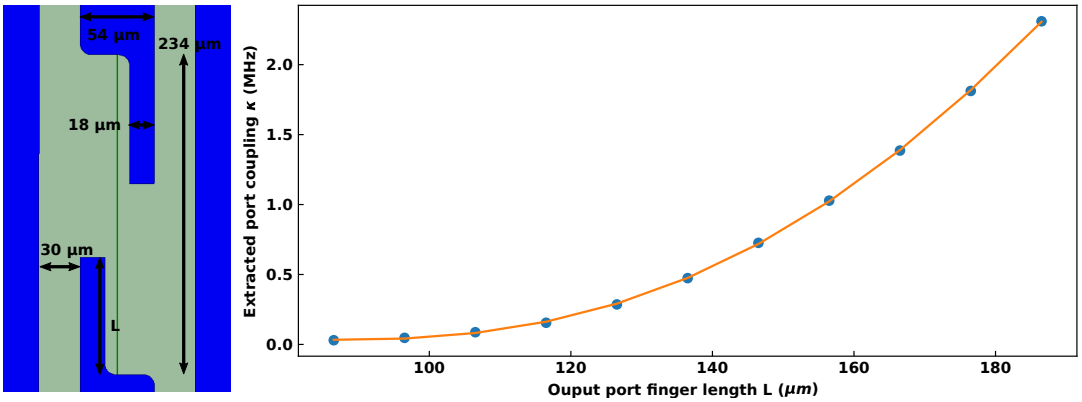

FIGURE 3.3: Port coupling function of the capacitance fingers length: The left picture explicit the dimensions used in the simulation for the output port of the cavity. The plot on the right displays the extracted coupling rates for different lengths of the capacitor fingers. The simulation data points can be fitted to a quartic model (orange) with very good agreement.

3.1.3 Transmon design :

Because the transmon is very well modeled in term of electric lumped elements and because in the transmon design the capacitance of the Josephson junction (JJ) can be neglected compared to the geometrical capacitance, it can be very well simulated using HFSS, simply including discrete lumped linear inductance. For the transmon presented in this thesis work, the design is inspired from work in the IBM group [42] in which losses are reduced by replacing the inter-digitated capacitance by a large planar capacitance.

To determine the parameters of the transmon, such as its capacitance, coupling and the value of the JJ inductance, we need to get the right qubit frequency, we proceed as follow. We determine the frequencies of the system eigen modes as a function of the JJ inductance. We can identify the modes by looking at the geometry of the field. When the transmon and the cavity are nearly resonant, we will observe an anti-crossing as illustrated in Fig 3.4. The distance between the two branches give directly the coupling between the modes. The capacitance can be extracted either directly from the transmon frequency (ie neglecting the inductive behavior of the other part of the circuit) or by fitting the frequency dependence on the JJ inductance. Usually both methods agree rather well.

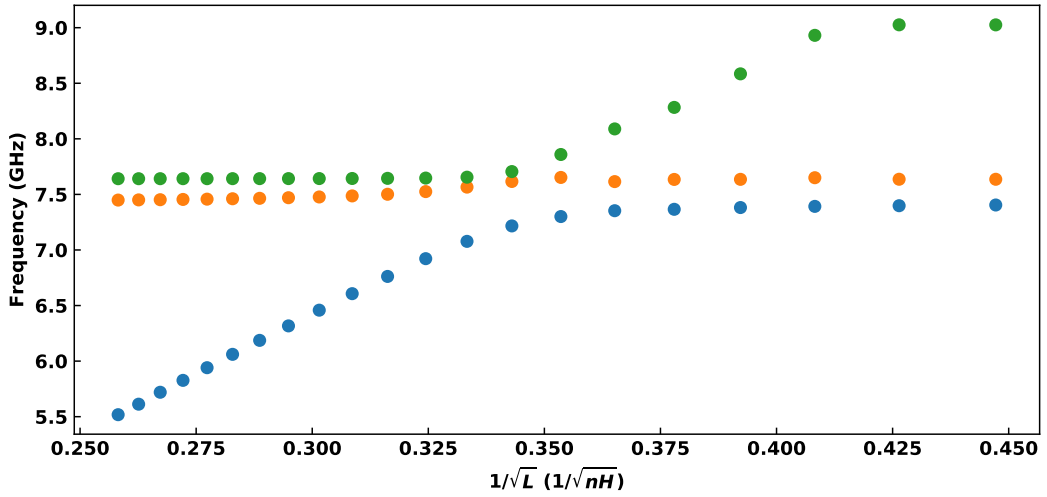

FIGURE 3.4: Transmon properties simulations:
By simulating the eigenmodes of the design for varying values of the transmon inductance, we get its dispersion from which we can extract the target value of the JJ inductance and the transmon capacitance as discussed in the main text. For large value of the inductance ($1/\sqrt{L}$ small), the transmon mode is the blue one and the cavity mode the orange one. The green one is a parasitic mode.

3.1.4 Dot coupling :

The first attempts made in the lab to couple quantum dots circuits to a microwave cavity relied on either simply placing the QD circuit close to the CPW central conductor or using a DC gate capacitively coupled to the central conductor. To maximize the coupling this was done at an anti-node of the electric field. This is illustrated in Fig 3.5 a and b. Both techniques are, however, not ideal. In the first case, the asymmetry in the couplings to the different circuit elements is small leading to a small modulationof the dot chemical potential. In the second case, the gate coupled to the cavity has a large capacitance to the ground and so we can expect a non-negligible AC potential drop between the CPW and the electrode. In order to avoid those issues, we are now using a floating top gate galvanically connected to the central conductor resonator. This prevents the electric potential drops related to capacitive coupling and also lead to a larger inhomogeneity as one dot is directly below the electrode while other dots/electrodes only have a capacitive coupling. Those "optimizations" were made only based on rough assumptions as the appropriate numerical simulation tools were not available at the time. However, the results that were obtained using the different geometries (capacitive [13] $g \sim 3 - 10$

MHz, galvanic [21] $g \sim 40 - 50$MHz) show that we have been moving in the right direction.

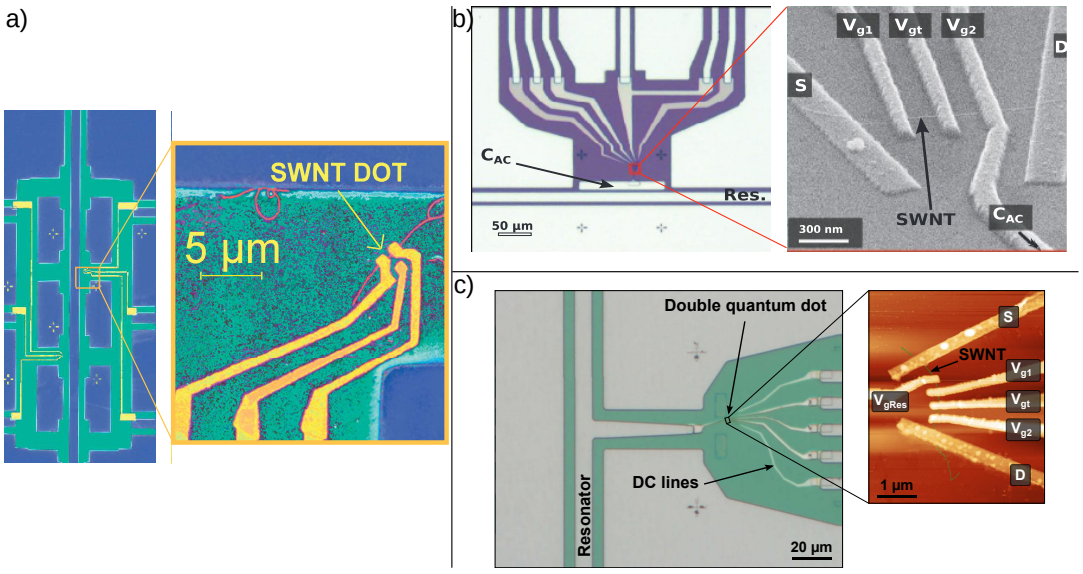

FIGURE 3.5: Dot-cavity coupling geometries:
The geometries presented here are the ones that been used in the group in the last years. Other groups use geometries similar to c nowadays.

a) The first attempt to couple a quantum dot circuit to a CPW simply consisted in placing the QD close by the central conductor of the CPW.

b) An improved design used a top gate capacitively coupled to the central conductor. This improves the asymmetry but the electric potential drop between the central conductor and the gate limits the coupling. Furthermore, the other electrodes are not shielded from the cavity field. [13]

c) The design used for the samples presented in chapter 4, also relies on a top gate but which is galvanically connected to the central conductor and left floating in DC. This design maximizes the collection of the resonator potential by eliminating the capacitance and improves a bit the shielding by partially closing the ground plane around the top gate.

We cannot hope to get a stronger electric potential than by using a galvanic connection (for a given resonator impedance). So in order to increase the coupling, we are left with no other direction than to improve the screening of the part of the circuit that should not be coupled. Using HFSS, we have studied the impact of prolonging the ground plane of the CPW as close as possible to quantum dots circuits. All electrodes are modeled as perfect conductor with negligible thickness. The hope here is that the protrusions of the ground plane may be able to shield efficiently the electric field. Some results of that study are presented in Fig 3.6 on a single dot geometry. In this case, we have no experimental data on which to base an estimate of the absolute coupling we can hope to

reach using such a shielding, because the galvanic coupling scheme has not been tested with SD. However, comparing the maximal potential on the central gate, it appears that this "trick" could allow to increase the coupling by about 30%. In addition, the leads appear less influenced in the presence of shielding which should reduce parasitic effects.

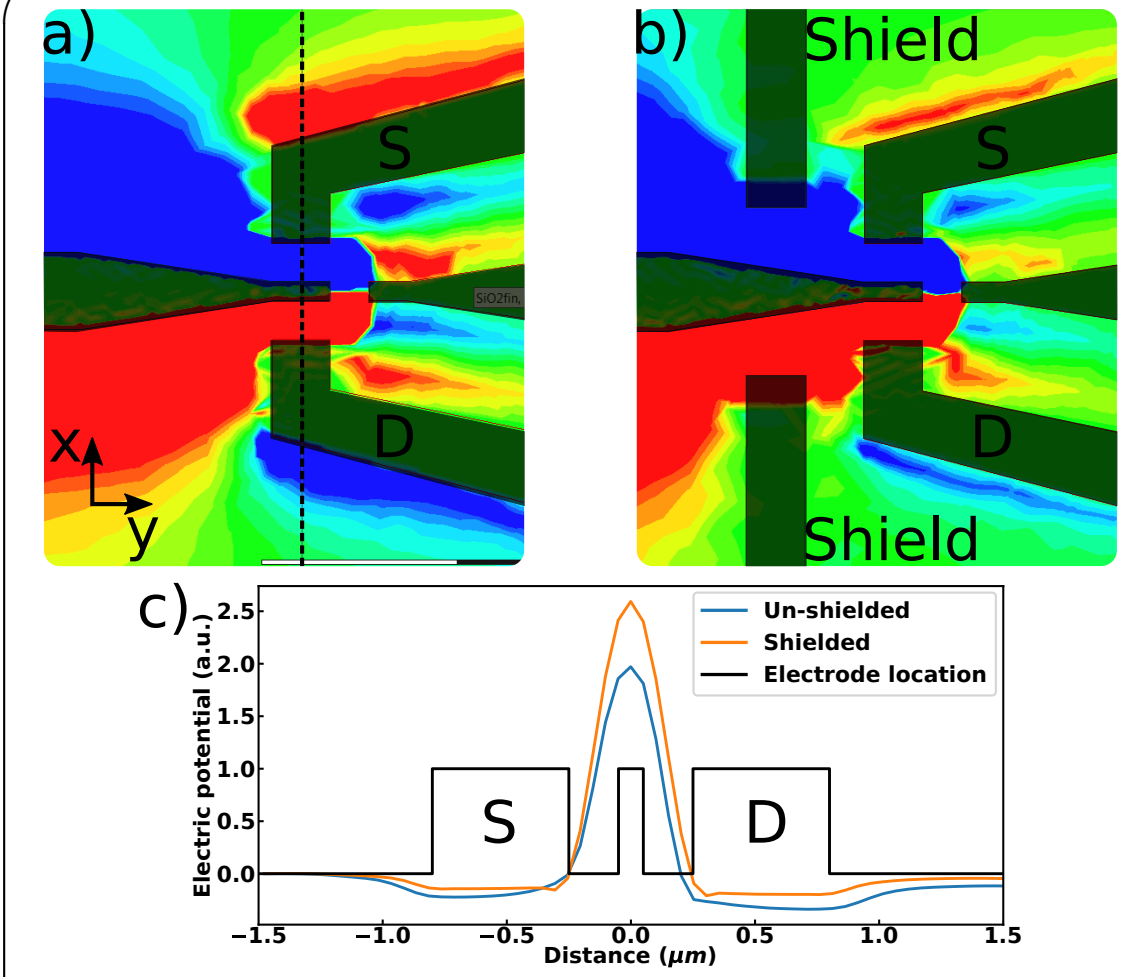

FIGURE 3.6: Single dot screening:

a), b) Simulation of the electric field (x component) both in un-shielded geometry (a) and a shielded one (b). The grey regions delineate the location of the metallic electrodes. The colorscale is the same in both cases but is clipped for large value to help the reader identify the differences in the geometry of the field. In the presence of shielding, the field in the vicinity of the contacts is reduced.

c) Plot of the electric potential (integral of the field) along the dashed line of figure a. The origin of the potential is taken on the left of the plot which is not perfectly accurate as we can see from the non-zero value for large x. One can notice that the potential appears higher in the shielded case (by about 30%) and that the contacts are also slightly less affected.

Because of the vast difference in scale between the resonator and the quantum dots

circuits, performing those simulations requires some care. In particular, one cannot simply rely on the automatic meshing of the structure to obtain an accurate description, as the small structure tend to be overlooked. The mesh must be manually refined in those areas. In HFSS, this was done by dividing the substrate in different parts and imposing different meshing constraints on each area.

A final point we can consider in designing the dot circuit is the geometry of the control lines. Two parameters can enter the discussion:

- the need to filter the DC signal used for bias and gate voltages in order to reduce the noise and lower the electronic temperature.
- the necessity to sometimes add an AC electric signal to the DC part used to tune the dot. This AC component can for example be used to perform qubit rotation or fast tuning of the system properties.

Both problems are complex and have not been studied in details in this work. The filtering has always been done off-chip and will be discussed in 3.3.2, however following [57], adding on chip filters may prove beneficial. The AC/DC mixing has been done on chip at one time but was moved off-chip to avoid issue with the filtering circuit, and its properties has never been studied using numerical simulation.

Now that all parts have been designed in more or less separated ways, we will discuss how to optimize the sample geometry.

3.1.5 Chip optimization :

Our main concern in this section will be to eliminate or at least push to high frequencies the modes other than the fundamental mode of the CPW cavity. We have already mentioned two motivations to do so:

- those modes can lead to a parasitic transmission leading a Fano shaped resonance that hinders the proper exploitation of the data.
- the coupling of those parasitic modes to our mesoscopic circuits can lead to reduced coherence and more noisy behaviors.

There are two main kinds of parasitic modes:

- CPW modes can exist in the input and output lines of the cavity or in the DC lines of the dot circuit.
- slot line modes in which two ground planes oscillates in phase opposition.

The first modes can be pushed to higher frequencies by minimizing the length of the lines, but this usually means to use longer bonding wires which also has drawbacks. As a consequence, we mostly focus on making sure those modes were above the cavity frequency and associated with weak fields in the area of the transmon and dot.

The slot line modes are harder to eliminate only through the chip design as CPW naturally support such modes. In order to avoid having too many such modes on chip, it is important to minimize the number of ground plane discontinuity as any such discontinuity can allow oscillations between the two parts. In our sample we cannot have less than one discontinuity because of the dot circuit connection to the cavity always introduce one. Furthermore, the two ground planes of our CPW are disconnected and the long DC lines, embedded in the ground planes, are CPWs and can support slot line modes. Those modes can be pushed to higher frequencies by connecting the two ground planes. For simple CPW cavity, the field of the slot line mode is concentrated in the center of the design as illustrated in 3.7, and connecting the ground planes in this area is effective to push this mode to higher frequencies as discussed in [111].

Connecting the ground planes can be done either using nano-fabrication techniques to make bridges or using wire-bonding. Nano-fabricated bridges allow for shorter and hence less inductive connections than wire-bond and are more effective to suppress the slot-line modes. However, as the fabrication techniques required to make such bridges are not mastered in the lab, we used superconducting wire-bonds.

Realistic wire bonds can be added to HFSS simulations, to determine their impact and how many bonds are required to push the parasitic modes high enough in frequency (typically > 10 GHz). However as those simulation are time-consuming, we tend to simulate many bonds at once rather than adding them in an incremental fashion. Fig 3.7 presents the same design both with and without wire-bonds and the frequencies of the main parasitic modes.

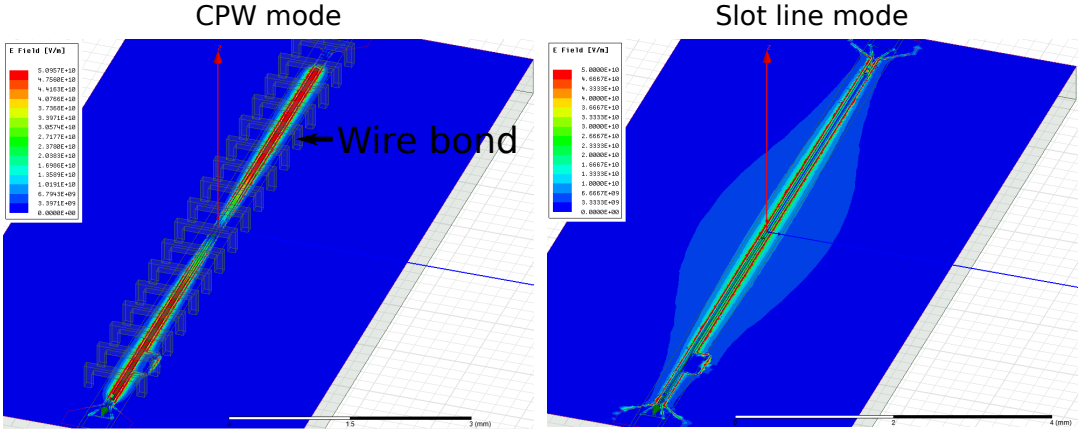

FIGURE 3.7: Bonds impact on slot line modes:
The left picture presents the electric field magnitude for the CPW mode. The bonds can be seen as semi-transparent arches. The right picture presents the electric field magnitude for the first slot line mode in the absence of bonds (bonds strongly reduce the field intensity). The impact of the bonds on the three first modes of the design (the cavity mode and two slot line modes) is summarized below (all frequencies are given in GHz):

	Cavity	First slot line mode	Second slot line mode
Without bonds	7.45	8.92	9.72
With bonds	7.47	9.72	12.2

Once the design of the sample is completed, it is time to move to the fabrication process.

3.2 Sample fabrication :

Because of the hybrid nature of the sample we are interested in, the fabrication process can prove tricky as otherwise perfectly mastered techniques can prove incompatible with previously fabricated elements. We will illustrate the fabrication on a sample used in chapter 5, as only those samples incorporate a transmon. A typical sample design is presented in figure 3.8

After giving a brief overview of the clean-room techniques used, we will describe the fabrication of each elements of our sample and point out what incompatibilities between the processes force us to choose a particular order of fabrication.

All samples have been fabricated in the ENS clean room. And the detailed recipes of the processes can be found in annex A.

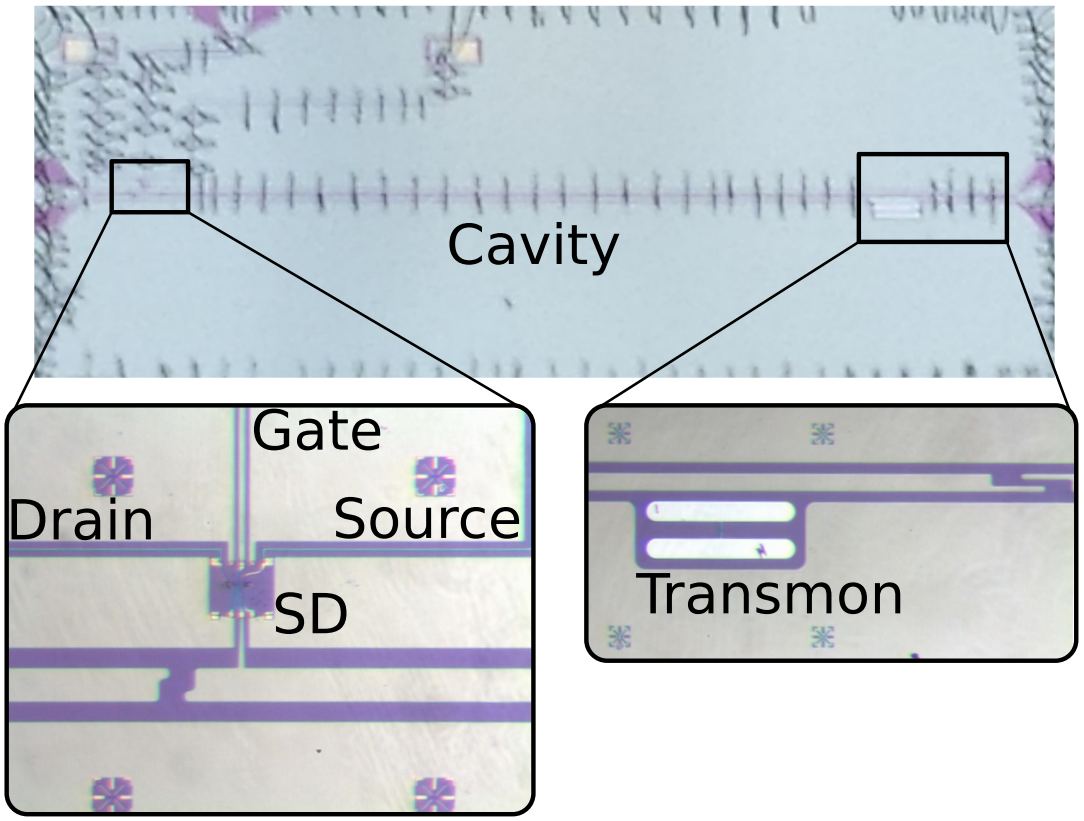

FIGURE 3.8: Sample layout:
The large view features a sample after adding the micro-bonds. The two insets focus on the dot part of the circuit on which the fine structure used to contact the CNT can be seen and on the transmon part of the circuit. One can also see the input and output capacitances of the microwave cavity. The marks that one can see on the transmon are the marks left by the probe station tips used to check the resistance of the transmon JJ.

3.2.1 Fabrication techniques :

In order to fabricate our samples, we need to be able to:

- define patterns in order to expose or protect different areas of the sample. This is done by lithography.
- deposit metallic layers, such as the ones of the cavity, the transmon or the contacts on the CNT.
- etch materials to define trenches 3.2.2 or pillars 3.2.4

Lithography : The principle of nano-lithography is presented in Fig 3.9. First an electro (or photo) sensitive resist is deposited on the substrate. The deposition is done

using spin-coating to guarantee an homogeneous and reproducible coating of the sample. The resist is then selectively degraded using an electron-beam (UV light). The degraded resist can then be removed using a developer and hence exposing the substrate. The remaining resist acts as a mask protecting the underlying substrate. This allows to coat with a metallic layer, or to etch, only the exposed areas. The protective resist layer can be then removed at a later step (lift-off step in the case of a metallic deposition, cleaning for an etching).

Such a lithography, in which the insulated areas are removed by the developing step, is qualified of positive. One can also perform negative lithography in which only the exposed areas will remain. In this work we will only use positive lithography.

No matter the type of lithography, in order to obtain the proper pattern without having resist residue at the bottom of the trenches, one to needs to adjust the exposition (amount of electron/UV light per unit of area) and the development time. This tuning requires to perform a number of blank lithographies (known as dose tests). To get more meaningful results, one should test close to reality patterns and when possible perform the metallic deposition. Using realistic patterns is crucial, as two structures can influence each other. This is particularly relevant in electronic lithography, in which proximity effect can lead to strong over-estimation of the proper exposure doses in some cases.

The choice of using electronic or optic lithography depends mostly on the resolution in the lithographed patterns one requires and on the alignment with respect to pre-existing structures. Using electronic lithography, we routinely achieve re-alignment within 10 nm and structures with a width of about 100 nm. On the other hand, optical lithography allows re-alignment within 1μm and a resolution of about 1μm. Optical lithography is much faster than its electronic counterpart and is hence preferred for large structures. However, it requires a mask, which in order to properly align on structure patterned using electronic lithography (100μm fields distant by several mm), need to be patterned using the same scanning electronic microscope (SEM). This lithography takes a lot of time, and has a rather low success rate. Furthermore the need for this mask limits the evolution of the design (due to the constraint of making new masks) and so it was sometimes preferred to do all lithography using the SEM. In the future the use of a laser masker could allow to combine the flexibility of the electronic process to the speed of the optical process for the large structures.

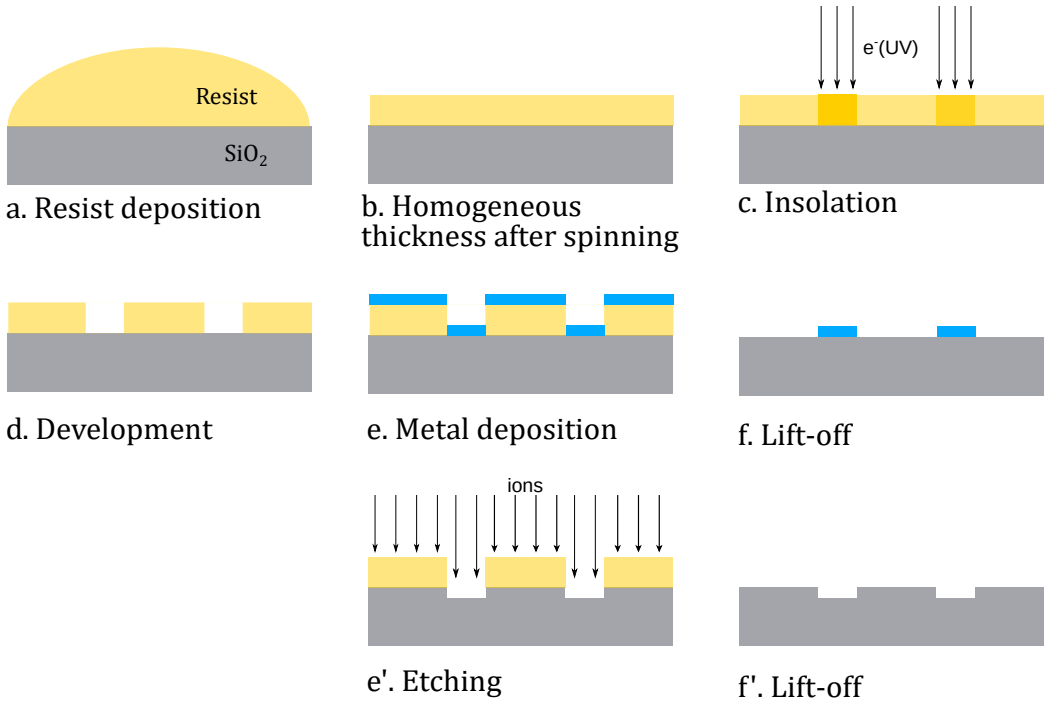

FIGURE 3.9: Lithography principle:

a and b To obtain a reproducible layer of resist with an homogeneous thickness, the resist is spin-coated on the sample.

c The resist is then insulated according to the pattern to write, using either accelerated electrons or UV light.

d The insulated resist is then removed using a dedicated chemical. Alternatively the resist that has not been insulated can be removed, the lithography is then considered negative (the previous process is qualified of positive) and is not described here.

e One can then deposit a thin metallic layer using either a Joule or e-beam evaporator. The metallic layer should be thinner than the resist as otherwise one will not be able to remove the metal deposited on top of the resist in the next step.

e' Alternatively one can use the resist as a protection layer and etch selectively the desired part of the substrate. The etching can be performed either using an etching solution or reactive plasma.

f and f' After the metallic deposition or the etching, the residual resist is removed during the lift-off step, leaving either metallic mesas or trenches.

Electronic lithography was performed on Polymethyl methacrylate (PMMA). The thickness of the coating was reduced by diluting it with anisole for one critical step, but otherwise undiluted PMMA 950 was used (giving a thickness of about 450 nm for the spinning parameters used). It is indeed preferable to use a layer thickness comparable

to the smallest characteristic size of the pattern in order to avoid collapsing of the resist related to a too deep and narrow trench. Development is performed using methyl isobutyl ketone (MIBK) diluted in isopropanol (IPA). The removal of the resist can be done in acetone.

Optical lithography were performed on AZ5214 coating which can be removed in acetone and developed in AZ 726 MIF.

Metallic coating :

All metallic layer deposition have been performed in an ultra high vacuum (UHV) electron-gun machine whose base pressure is around 5.10^{-10}mbar. Such low pressures ensure ballistic trajectories of the atoms after evaporation and very clean metallic thin films. This machine has two chambers: one load-lock allowing fast cycling of the samples and the main evaporation chamber.

Electron gun evaporation is performed by focusing a beam of accelerated electrons on a crucible containing metal ingots. The current is increased until the metal temperature exceeds the sublimation point, thus creating a jet of metallic atoms. The evaporation rate and total thickness are monitored using a mechanical quartz resonator, whose frequency is extremely sensitive to the amount of metal deposited on top. As mentioned above, in order to ensure the quality of the evaporated film, it is crucial for the evaporation to be done in high vacuum. This can prove challenging for metals such as Niobium whose sublimation temperature is about 3000 °C. The UHV system, we used, is fitted with cryogenic panels which can be filled with liquid nitrogen. Under those conditions Nb can be evaporated at 10Å/s at about $1e^{-8}$mbar. At different stages (JJ fabrication 3.2.3, dot top gate deposition 3.2.4), we will need to oxidize an aluminum layer to get an isolating layer of alumina. This is done under a pure oxygen atmosphere in the load-lock of the evaporator to avoid exposing the metals, in their crucible, to the oxygen.

Etching:

Etchings processes are crucial for creating mesas or holes on substrates, cleaning substrates, removing intermediate auxiliary metal layers, or defining clean patterns on chips entirely covered with metals such as niobium. One can use chemical wet etching

solution such as KOH to remove aluminum, or reactive ion etching (RIE), that consists in a dry chemical and/or physical etching using plasmas.

Dry etching is used in two steps of the fabrication process (see 3.2.2 and 3.2.4). Dry etching is preferred in those cases over wet etching, because we are interested in strongly directional etching whereas wet etching is a nearly isotropic process.

Dry etching steps are done in a reactive ion etching machine (Corial 200R), allowing to use SF_6, CHF_3, O_2 and Ar as etching agents.

3.2.2 Cavity fabrication :

As described in 3.1.1, our samples are fabricated on 500μm thick high-resistivity silicon substrate with a top layer of 500 nm of SiO_2. We work on 10×10 mm pieces obtained by dicing a wafer. In order to protect the wafer during the dicing operation, the wafer is coated with a protective layer of resist which is removed at the very beginning of the fabrication process. On each chip, we will pattern two cavities. We proceed in this way as it allows more homogeneous resist coating than working with 5×10mm samples. However it means we will have to split each sample in two at the end of the fabrication process.

Before patterning the cavity, the first step in the fabrication consists in patterning alignment marks that will be used in all further steps and pre-contacts. Because we will need to re-align very precisely on the areas in which the dots circuit fine structure will be defined, this step is realized in electronic lithography. In addition to the alignment marks in the vicinity of the dot circuit(s), we also pattern large scale alignment marks and numbers to identify the sample. After the development, we deposit a thin layer of titanium (5nm), which plays the role of sticking layer, then 45 nm of gold. Gold gives a large contrast in SEM imaging which will facilitate the alignment in the following steps and additionally will not oxidize hence ensuring a good contact between the niobium used for the large structure and the small scale contacts of the CNT. The use of those pre-contacts is mandatory as the niobium oxidizes which prevents a direct contact between it and the contacts of the CNT, which are realized at a later stage.

The cavities of the first samples were made using aluminum (Al). However, the experiment presented in chapter 4 requires to apply an external magnetic field to unveil some

of the system properties. Even though this field is in the plane of the cavity it still affects the superconductor. The low critical field of Al prevented us to go to fields higher than 15 mT as the quality factor of the cavity was decreasing too much at higher field. This motivated the use of niobium which has a higher critical field.

However as previously mentioned niobium has a high sublimation temperature which makes its deposition on resist mask tricky as the resist is baked by the radiation. This is why we use an etching process to fabricate our samples. Given how delicate both the CNTs and the JJs are, we cannot perform the etch with them already on the substrate which is why we pattern the cavity first. The fabrication begins with the deposition of a 150 nm (or 100 nm) thick film of niobium on the whole sample. We then spin-coat resist and pattern in it the cavity, the ground plane opening in which the transmon will sit, and the DC line of the dot circuits. This step can be done using either optical or electronic lithography to expose the parts corresponding to the gap of the CPW. The niobium film is then etched using an SF_6 based RIE etching. The etching is monitored by reflectometry on the niobium surface.

Once the etch is complete, the residual resist is removed in acetone. This step can prove tricky as the resist usually hardens during the etching. In extreme cases the sample needs to be scrubbed with clean room paper to remove large patches of resist. The final step in the cleaning always consist in a low power O_2 plasma etching to remove the smallest resist residue. This step can be carried out for more than 10 minutes without causing any degradation of the resonator quality factor.

With the resonator complete, we can move to the fabrication of the mesoscopic circuits. When both a transmon qubit and a CNT dot circuit need to be fabricated, it is not obvious which should be made first. In both cases, we would prefer to avoid any unnecessary exposure to resist to avoid the deposition of more residues. We will first present the fabrication of the transmon qubit but both route have been explored.

3.2.3 Transmon fabrication :

The fabrication of a transmon qubit requires to make a JJ as discussed in section 2.1.2.2, which requires to deposit two superconducting layers separated by a thin insulator. This

can be done either in two lithography steps or in a single one. We will prefer the single step process as it is easier and already known in the lab.

This process, illustrated in Fig 3.10, relies on two-angle evaporation of aluminum and on a free standing bridge of resist (Dolan bridge) to provide a shadow mask. The sample is mounted in the evaporator in such a way that the bridge is aligned with the rotational axis of the sample holder. First a layer of aluminum is evaporated and then partially oxidized to form alumina that will serve as the insulator in the junction. The second evaporation is performed at an angle in order to have a partial covering of the first layer on one side of the bridge by the second coming from the other side. This leads a small overlap between the metallic layers on each side of the bridge, whose size depends on the evaporation angle and the bridge width.

In practice, the bridge is made using three layers of resist: two layers of MMA-MAA which is a light copolymer and a top layer of PMMA. The transmon is lithographed in an opening of the CPW ground plane and a thin bridge of PMMA, between the two protrusions of the capacitor plates, is not insulated . The following development step is quite critical as the developer will attack the insulated PMMA and copolymer but also the little insulated copolymer further away from the main pattern. This will lead to the formation of a free standing bridge of PMMA. The development time should be long enough so that no copolymer remains below the bridge which will prevent the formation of the junction. On the other hand if it is too long, the copolymer will recess too far away and the bridge will break, in which case the junction will be shorted.

After the development, the sample is placed in the UHV system. Because this system is not fitted with a plasma cleaner allowing to remove the resist residues, we let the sample under vacuum for at least 14 hours (a night) under vacuum before proceeding with the metal deposition. The presence of resist residues can have a drastic effect on the JJ as between a sample left overnight and one evaporated right away, we observed a factor of 2 in the critical current.

During the first evaporation, performed at 0° (displayed -4°), 30 nm of aluminum are deposited. The sample is then taken back to the load-lock and oxidized during 5 minutes under a pressure of 5 mbar of O_2. At the end of this step, the load-lock is re-pumped and the samples sent back to main chamber for a second evaporation of 30 nm of aluminum

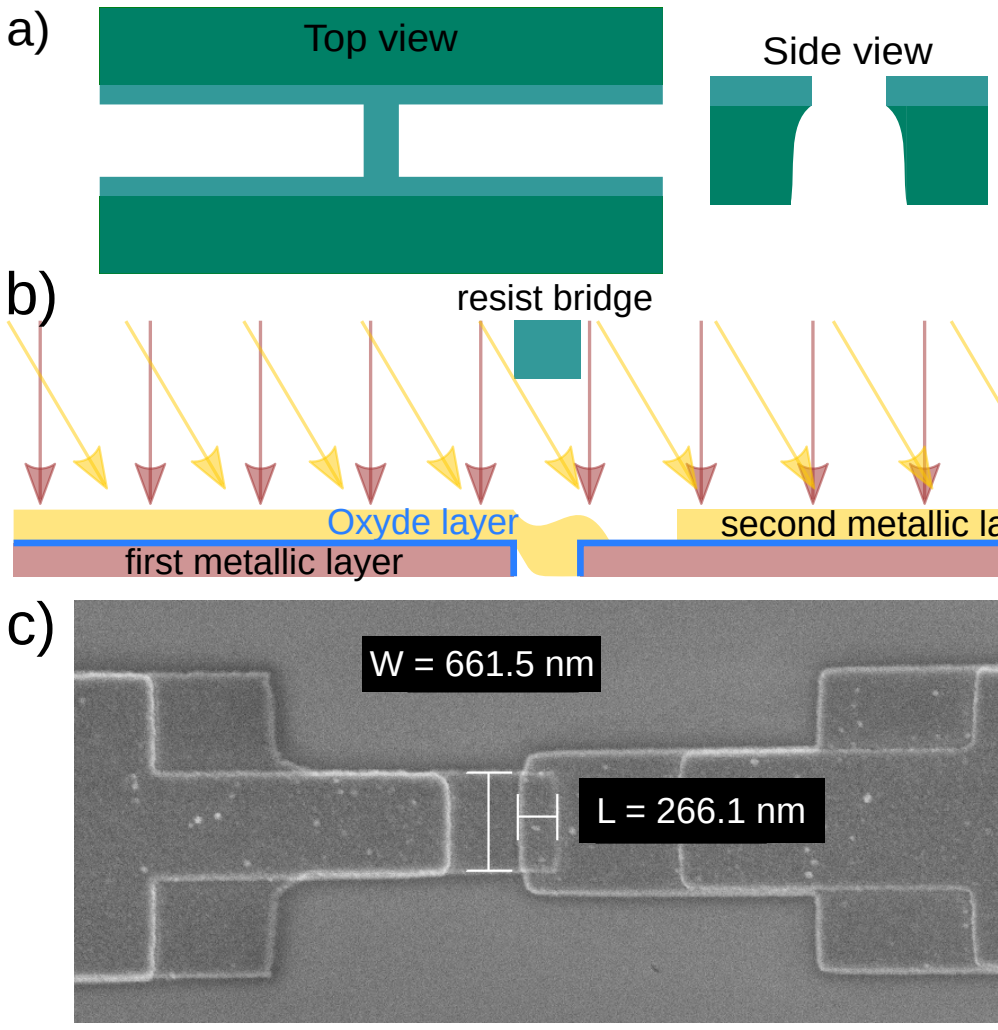

FIGURE 3.10: Josephson junction fabrication:
One common technique to fabricate JJ relies on shadow mask evaporation. First one deposits two layers of resist, choosing for the bottom layer a resist more sensitive to the exposition/development. During the lithography, two trenches are patterned in such a way that the development will remove the bottom layer of resist under the border area between the two trenches (see color code in a). This lead to the formation of a bridge. One then performs two metallic depositions of aluminum at different angles and an oxidation step in between. This leads to the situation illustrated in b, where the active part of the JJ is on the right of the bridge. Figure c is an SEM image of a typical junction fabricated during this work.

but at -40° (displayed 324°) this time. The angle chosen here is constrained by several factors:

- a too small angle is sensitive to errors, and will lead to small overlaps whose areas are not very reproducible

- a too large angle will lead to the deposition of the aluminum against the wall of copolymer. In such a situation, the lift-off step can actually tear off the metallic layer which is of course to be avoided.

Once the lift-off step is completed, the transmon is complete and the junction resistance can be measured. The JJ resistance can be related to the critical current using equation (2.52), which fixes the qubit frequency. This quantity is inversely proportional to the JJ area and its value can be used to finely tune the fabrication process to get the targeted value. Before fabricating a transmon, many junctions have been fabricated in order to finely tune the lithography dose, the development time and the oxidation parameters. As the JJs are quite sensitive objects and can easily be destroyed by electrostatic chocs, the protection circuit presented in Fig 3.11 a) was used. The relation between the resistance of the junction and the inverse of its surface (deduced from SEM imaging after the measurement) presented in Fig 3.11 b) is linear and can be used to determine the target value when making a qubit. However as the exact size of the junction depends on the lithography parameters it is usually reasonable to perform additional tests on the target design to check the area. The typical size of the junctions used in our transmons is about 1 μm^2.

The presented fabrication technique works well but has one pitfall. Because the oxide layer formed during the oxidation step is not stoechiometric (alumina stoechiometry is Al_2O_3), the oxide layer ages, i.e. it thickness evolves with time. This leads to a change in the junction critical current. In our process we have routinely observed changes by a factor of 2 in the junction resistance. This has to be taken into account when designing the junction. Under ambient condition this aging takes about a week. If the sample is baked (for example because the transmon was made before the dot circuit), the aging stops after the first baking and reach similar values as the one obtained after one week under ambient conditions. So it does not impact the processing order.

3.2.4 Dots fabrication :

As we are mainly interested in the low energy spectrum of the CNTs, we need high quality CNTs with a low number of defects. This imposes to growth the CNT by CVD (Chemical Vapours Deposition) as commercially available CNTs spend a lot of time in sonic bathes

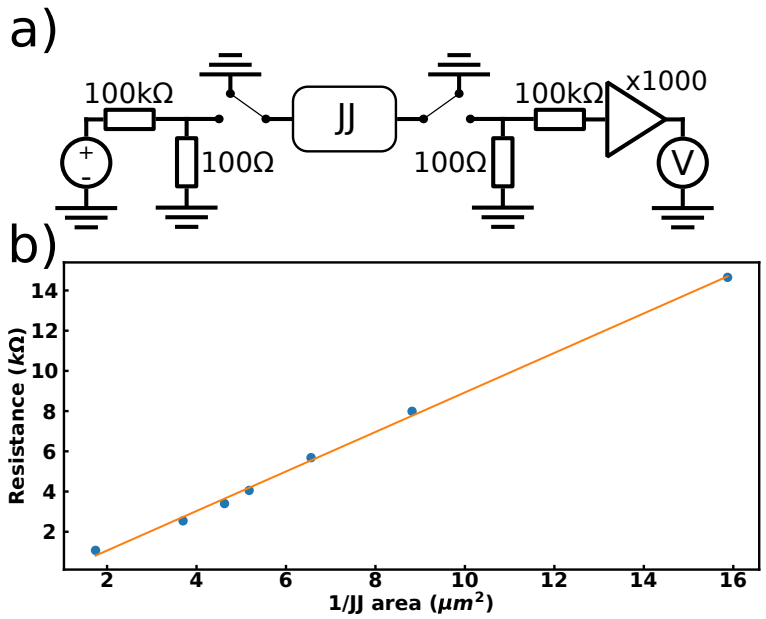

FIGURE 3.11: Room-temperature JJ characterization:

a) Circuit used to measure the room temperature resistance of the junction. The junction is tested in a probe station. Before the probe station tips make contact with it, the test line are grounded. During the test, the switches are commuted and a DC bias is applied through a voltage divider. The voltage on the output resistance is amplified and then measured. The second voltage divider protects the sample from any input voltage drift of the amplifier.

b) JJ resistance as a function of the inverse of its surface. Those two quantities are linearly linked.

which are known to induce defects altering the low-energy spectrum. However this growth is strongly incompatible with the realization of high quality microwave resonator because of two consequences of the growth:

- first the high temperature involved in the growth process ($\simeq$ 900 °C), can induce migration in the substrate leading to increased losses in the microwave domain.
- second during the growth, which is done in presence of methane, in addition to the growth of the CNT amorphous carbon is deposited on the substrate. This amorphous carbon will also increase the losses.

Previous attempts in the lab to perform the growth on the cavity substrate have shown that the total losses induced by the growth limits the cavity factor to about 40.

To circumvent those issues, a dry transfer technique of the CNTs was developped by J.J.Viennot [112]. This technique relies on the use of an auxiliary 1 cm^2 quartz chip

on which the CNT's are grown before being transferred on the sample substrate as illustrated in Fig 3.12

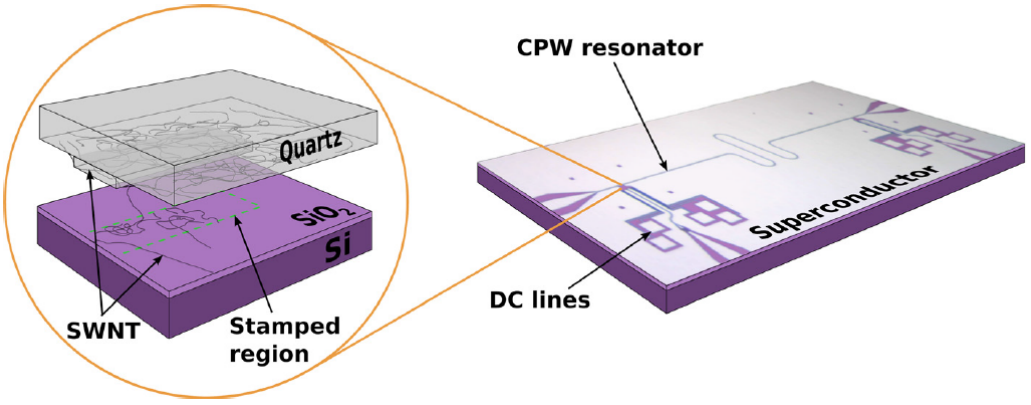

FIGURE 3.12: Stamping principle :
The CNTs are first grown on a quartz substrate on which mesas have been patterned as illustrated in the zoom on the left of the figure. The CNTs are then stamped by pressing the mesas on the sample chip on which the cavity has already been patterned. CNTs and carbonated materials are transferred only in a limited area around the contact area, if the quartz is free of parasitic mesas and the two chips are well parallel.

3.2.4.1 Stamps fabrication :

In order to transfer carbonated materials only in the area of interest and avoid to transfer more dissipative amorphous carbon than necessary, we pattern mesas on the quartz substrate before the growth. Patterning those mesas is a three step process:

- first we lithograph small pairs of openings (5×12 μm^2 each) in a double layer of PMMA. Those will become the mesas that will use as stamps. Because quartz is an insulator, the top layer of resist need to be coated with a 15 nm layer of aluminum to avoid charge accumulation. This layer is etched in KOH before the development.

- second a layer of 250 nm of nickel is deposited using the electron beam evaporator. Because nickel does not stick very well on quartz, the development step must be followed by a one minute long low power oxygen plasma to remove all resist residue from the bottom of the trenches.

- after the lift-off, the sample is etched in a CHF_3 and O_2 plasma. The nickel plays the role of protective mask. Because it is etched much more slowly than SiO_2 and because the RIE gives a directional etching we can get mesas high of 4 μm. The residual nickel is then removed using a wet etching (iron-perchlorure).

The above process differs from the one presented in [112] which uses aluminum as a masking layer. Nickel has the advantage to withstand better the etching process allowing to use thinner layer. This leads to less frequent maintenance on the UHV system, while getting higher mesas which makes the stamping procedure less sensitive to small angles between the sample and the quartz stamp.

Because we will stamp the CNT's after the cavity fabrication, we have to pay a lot of attention to the presence of unwanted mesas. If such defects are present, they will touch the top of the niobium layer and prevent the mesas in the proper place to touch the silicon dioxide surface 150 nm below. Those spurious mesas can be eliminated at three steps. First by protecting the edges of the quartz during the evaporation (and any other areas that may not be covered by resist), one reduces efficiently the number of defects on the edges which are among the most problematic. In our fabrication process this is done using mechanical masks made out of tungsten. Next, thoroughly cleaning the quartz after the lift-off of the nickel layer, one avoids that residual nickel or dust serve as mask during the etching. Second after the etching, one can mechanically remove any spurious mesas. Both steps can be done using a needle under a binocular lens. This technique allows to remove even large spurious mesas, and it has been seen that the metal of the needle that can get transferred on the quartz does not alter the CNT's growth.

Once the mesas patterned on the quartz, the next step consists in growing the CNTs as described in the next section.

3.2.4.2 Carbon nanotube growth :

The nanotubes are grown using a CVD growth process in a home made oven. The growth is activated by an iron based catalyst prepared in solution[1]. Before deposition, the catalyst solution is sonicated for 1 hour in order to break apart any clusters, then left to decant for 45 min. Two drops of solution, taken from the top of the solution,

[1] 39 mg $Fe(NO_3)3-9H_2O$, 7.9mg MoO_2 and 32 mg of Al_2O_3 nanoparticles, diluted in 30 ml of IPA

are then deposited on the quartz and immediately dried using a nitrogen flow. This method works most of the time but does not allow a fine control on the concentration of deposited catalyst, which can however play a critical role. A too low concentration will not lead to any CNT growth, whereas a high concentration leads to the formation of bundles of nanotubes. Using catalyst nano-particles obtained by evaporation, may lead to a more reproducible deposition but attempts with palladium, which is known to catalyze CNT growth, proved to be inconclusive and no evaporator in the clean room could evaporate a sufficiently thin layer of iron.

The standard growth procedure is a methane-dihydrogen based process carried out at 900°C. It was optimized to produce single wall CNTs, but has no preferential direction. CNTs growing in between the two mesas are of particular interest since they can be placed close to the cavity. Following the work presented in [113], we tried to reduce the flows of methane and dihydrogen (CH_4 from 1140 sccm to 100 sccm, H_2 flux from 200 sscm to 50 sscm) and increase the growth temperature. We observed directional growths, as shown in 3.13, but TEM imaging done by J. Palomo showed that most CNTs were double walls CNTs, which cannot be used in our experiments. This process was actually even more sensitive to catalyst concentration and the above results were obtained only deposing catalyst on the edge of the quartz.

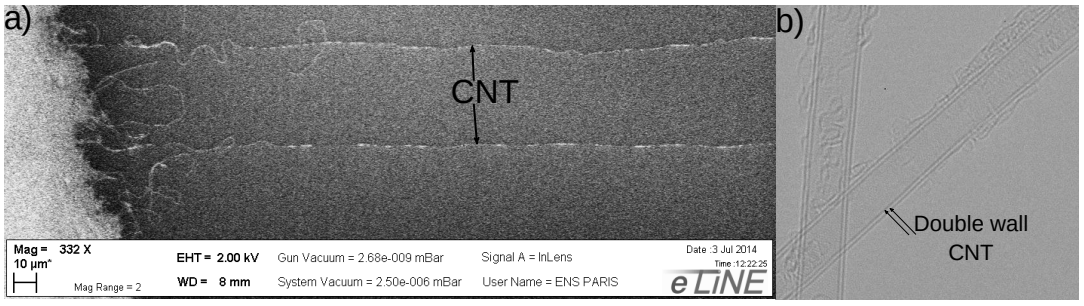

FIGURE 3.13: Directional growth of CNTs:
Using a variant of the growth recipe previously used in the lab, in which the gas flows are reduced to reach a laminar flow in the oven, directional CNTs have been obtained. However further characterizations using transmission electron microscopy evidenced a pre-dominance of double wall CNTs which are not suitable for the envisioned experiments.

To avoid damaging the CNTs, the mesas are not imaged after the growth but directly stamped as described in next section.

3.2.4.3 Stamping and localization :

The stamping operation is performed using the same optical masker (MJB4) used for optical lithography. The quartz is glued on a glass which is used as a mask. In [112], the quartz was glued using a drop of PMMA. In recent processes, we have replaced the PMMA in favor of double sided tape, which provides a flatter surface and is still plastic enough to tolerate minor flatness issues. Furthermore it yields much more reproducible results.

Depending on the samples, either a single area (samples of chapter 5) or two (samples of chapter 4) were stamped at a time. Stamping one area at a time is much more tolerant with respect to alignment and flatness issues. When stamping two areas at once, it happened multiple times that only the mesas of one area touched. At first, we preferred stamping two areas at once to avoid a contact between the edge of the quartz and the sample chip, as this would deposited dust on the middle of the cavity. However, with high mesas close to the quartz corner it turned out not to be a problem and so we stamped one area at a time.

During the stamping, the quartz substrate is lowered progressively towards to the silicon sample. First the mesas are aligned with the opening of the ground plane, in which the quantum dot circuit will be patterned. As the two chips are brought closer together, the alignment can be improved and usually the mesas are slightly deported towards the protrusion of the CPW central conductor as illustrated in 3.14. When the mesas touch the silicon dioxide, interference pattern can be observed inside the mesa corresponding to the compression of the tape directly above the mesas. The pressure is then increased till the interference color stops changing (and potentially even a bit more after that) or till the quart mesas start breaking into pieces. In this case, the quartz chip must be brought back up quickly to avoid depositing to many quartz pieces.

After the stamping steps, the CNTs must be localized in order to pattern the electrodes on top it. This is done using the SEM at a low acceleration voltage (2 kV). The image are positioned with respect to the gold crosses in the four corners of the area, to allow later re-alignment. To limit the damages done to the CNTs the number of image per CNT is kept to a minimum with a 100×100 μm^2 scan corresponding to the full area and then non overlapping zoomed images.

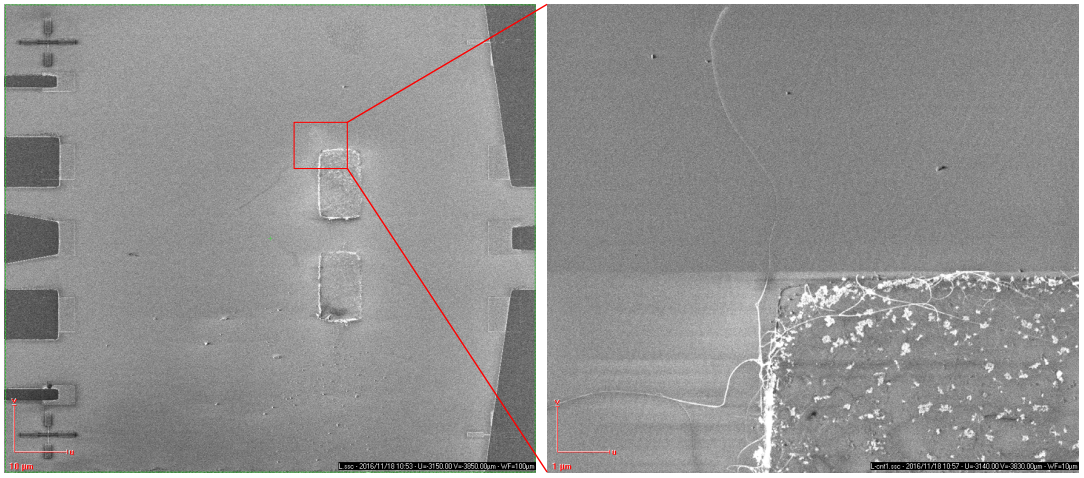

FIGURE 3.14: CNTs localization:
Once stamped, CNTs needs to be localized in order to be contacted. The localization step is done in a SEM at low acceleration voltage. First the write field of the SEM is aligned on the four crosses that can be seen in the left picture. The full field ($100 \times 100\mu$m) is then imaged once (left image). This allows to check whether the stamping left any marks on the substrate (their absence usually means that there was no contact) and to localize the largest pieces of quartz that one will try to avoid when designing the electrodes. More detailed images ($10 \times 10\mu$m or $5 \times 5\mu$m), such as the one shown of the right, are then acquired. During that step, the same area is never scanned more than once to avoid damaging the CNTs.

3.2.4.4 Electrode deposition :

Once the CNTs are localized, we can pattern the circuits on top of it. For the circuits presented in this thesis, this always implies two lithography steps: one to pattern the grids and one to pattern contacts. For both types of samples (chapters 4, 5), the gates electrodes are made using a stack of alumina, aluminum and palladium. The alumina layer is formed in three successive depositions of 1.5 nm each, followed by a 10 minutes oxidation step (1 mbar of O_2). We then deposited 40 nm of aluminum and 20 nm of palladium. The contacts of samples presented in chapter 4 are made out of a palladium nickel alloy. For magnetic reasons explained in 4, those electrodes must be thin and narrow, which is why we used a diluted PMMA giving a coating of about 250 nm. The electrodes are about 170 nm wide and formed of about 30 nm of alloy covered by 5 nm of palladium. For the samples presented in 5, the contacts are made out of titanium and gold (5 nm/45 nm). Originally those contacts were made out of palladium, but we found that those were torn off when lifting resist used in the transmon process. As the experiment we have in mind requires contacts with a low-transparency we moved to Ti/Au. During the second lithography step, we also deposit patches to contact the gate

electrodes to the gold pre-contacts. This is necessary as even if the gates are deposited on top of the pre-contacts the alumina layer prevents a good contact to form.

Following each metallic deposition, one must be careful during the lift-off process to remove all unwanted metallic patches that may short the resonator.

On the whole the fabrication of those samples is very delicate and requires a lot of fine adjustments, in particular in the lithography process. Furthermore statistically only one dot circuit out of 2 is connected (which does not presume of the quality of the low-energy spectrum). As a consequence, a lot of samples have been fabricated with only a fraction being completed and an even smaller number being connected and finally measured.

3.3 Measurements :

This section will focus on the practical details involved in characterizing the samples whose fabrication has just been presented. First we will describe the mounting of the sample and how we can eliminate 3D box modes, which will echo the discussion about the parasitic modes in 3.1.5. The next section will focus on the fridge and fridge wiring that allow not only to cool the sample itself but also the radiation reaching the cavity and the electrodes. Finally the last two sections, will focus on the measurement techniques used to characterize the samples.

3.3.1 Sample mounting :

As mentioned at the beginning of section 3.2.2, our samples are fabricated by pair on 10×10 substrates and need to be split before being mounted. This is done using a cleaving machine with a diamond tip, with a high rate of success (during this thesis only 3 half chip were accidentally broken). The sample is then glued (using PMMA) and micro-bonded to a printed circuit board (PCB) as illustrated in Fig 3.15.

The PCB board is fitted with SMA connectors whose pins are soldered on both faces, in such a way as to provide a continuous contact between the pins and the ground planes. This avoids parasitic reflections. The DC pins are soldered on the back face of the PCB. We use a multi-layer PCB that was designed by A. Denis and L. Contamin, in which the DC lines are on a different layer than the microwave CPW lines and are isolated from

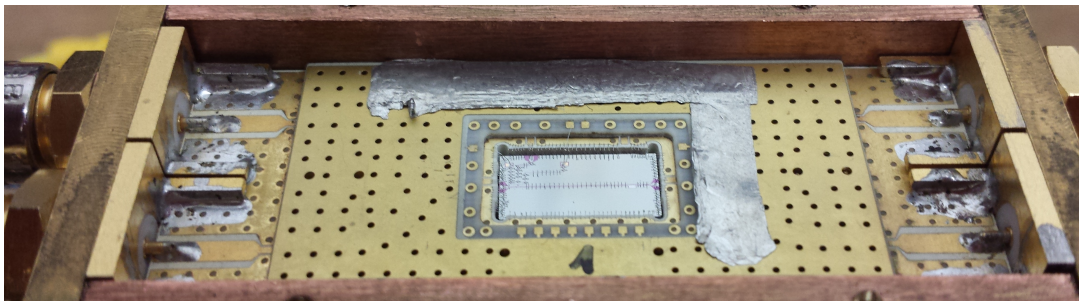

FIGURE 3.15: Micro-bonded sample:
Samples are glued, using PMMA, on a copper protrusion of the sample holder ensuring its proper thermalization. They are then micro-bonded to a multi-layer PCB board. The microwave line are on the lower layer and connected to the outside world using soldered SMA connectors. DC lines are on an intermediate layer and are brought from the back through a filtering circuit. Finally the top layer is a ground plane (connected to all other ground planes through via holes) which allows to put a copper cover on top of it, hence enclosing the sample in a small box. To ensure the electric contact between the cover and the PCB, a thin indium foil is used from which two pieces can be seen. When micro-bonding, the micro-wave parts are connected first, then one adds the wire bonds playing the role of air bridges and finally the DC lines are connected. It should be noted that the DC lines are grounded during this operation.

them by a ground plane layer in between. This allows to reduce cross-talk between the lines. Furthermore all lines are buried and the top layer is a ground plane. This is of paramount importance as it allows to put a cover on top of the sample, which is then enclosed in a box of 1cm×5mm×5mm[2], which does not allow any 3D box mode below 9 GHz. We want to eliminate such modes as just like 2D modes they can create Fano resonances and couple in unwanted way to our circuits. Using this cover we measure perfectly lorentzian transmissions for our cavities with a background isolation of about 40 dB. However this improvement is recent and the experiment presented in chapter 4 has been done with an older PCB which did not allow to enclose the sample and presented many modes as low as 4 GHz.

On Fig 3.15, one can also observe that we use multiple wire bond to connect the central conductors of the CPW and to define the ground plane. This is done to counter balance the natural inductance of the wire bonds. One can also observe the bonds connecting the two ground planes discussed in 3.1.5, whose goal is to push to higher frequencies the slot line modes in which the ground planes oscillate which respect to one another.

[2]The presence of many via holes between the different layer of the PCB effectively prevents the field to extend into the dielectric

3.3.2 Fridge wiring and operation :

All experiments presented in this work, have been carried out in a wet dilution cryostat with a base temperature of 35 mK. The wiring of the cryostat has been carried out by J. Viennot [114] and was left untouched given how little room remains.

We recall it in Fig 3.16 to discuss how it may impact our measurements and for future discussion of what may need to be improved in the future.

For AC and DC wiring, the key idea is to prevent the transmission of 300 K noise down to the sample. For the DC lines, this is achieved by thermalizing the lines at two stages (4 K and 35 mK) and by filtering the microwave noise using homemade filters (Manganese wires in Eccosorb MF 117) and the low frequency noise using low pass π-RC filters with a cutting frequency of 1 MHz on a PCB board at the back of the sample holder. In addition all gate lines are filtered at room temperature using again low pass π-RC filters with cutting frequencies at either 1 kHz or 0.1 kHz.

The thermalization of the microwave lines is more complex and different for input and output lines. For input lines, we find at each stage of the fridge (4 K, 1.5 K, 100 mK and 35 mK) both a clamp thermalizing the outer conductor of the microwave cable and thermalized attenuator whose role is to ensure that the noise after the attenuators is dominated by thermal noise at the temperature of the stage. Additionally low-pass filters are used to filter out components at frequencies higher than 20 GHz. For the output line, we isolate the system from the noise of the amplifier at 4 K using two circulators. The cable used between the amplifier and the 35 mK plate is made of NbTi, which is superconducting when the fridge is running, providing enough thermal isolation between the 4 K and the 35 mK that no clamping is required.

Only two changes have been introduced with respect to the original setup for the experiment presented in chapter 5. First, because the transmon is sensitive to magnetic noise, the sample has been covered with a magnetic shield made out of multiple layers of Metglas® amorphous Co-based alloy 2714A glued using white stycast. Second, because we need to send both AC and DC signals on the gate of the SD that we will use, and because previous experiments relying on on-chip bias-tee proved disappointing, we used a commercial bias-tee mounter on top of the sample holder. To preserve the filtering of the DC line, we connect the bias-tee to one output of the filtering PCB.

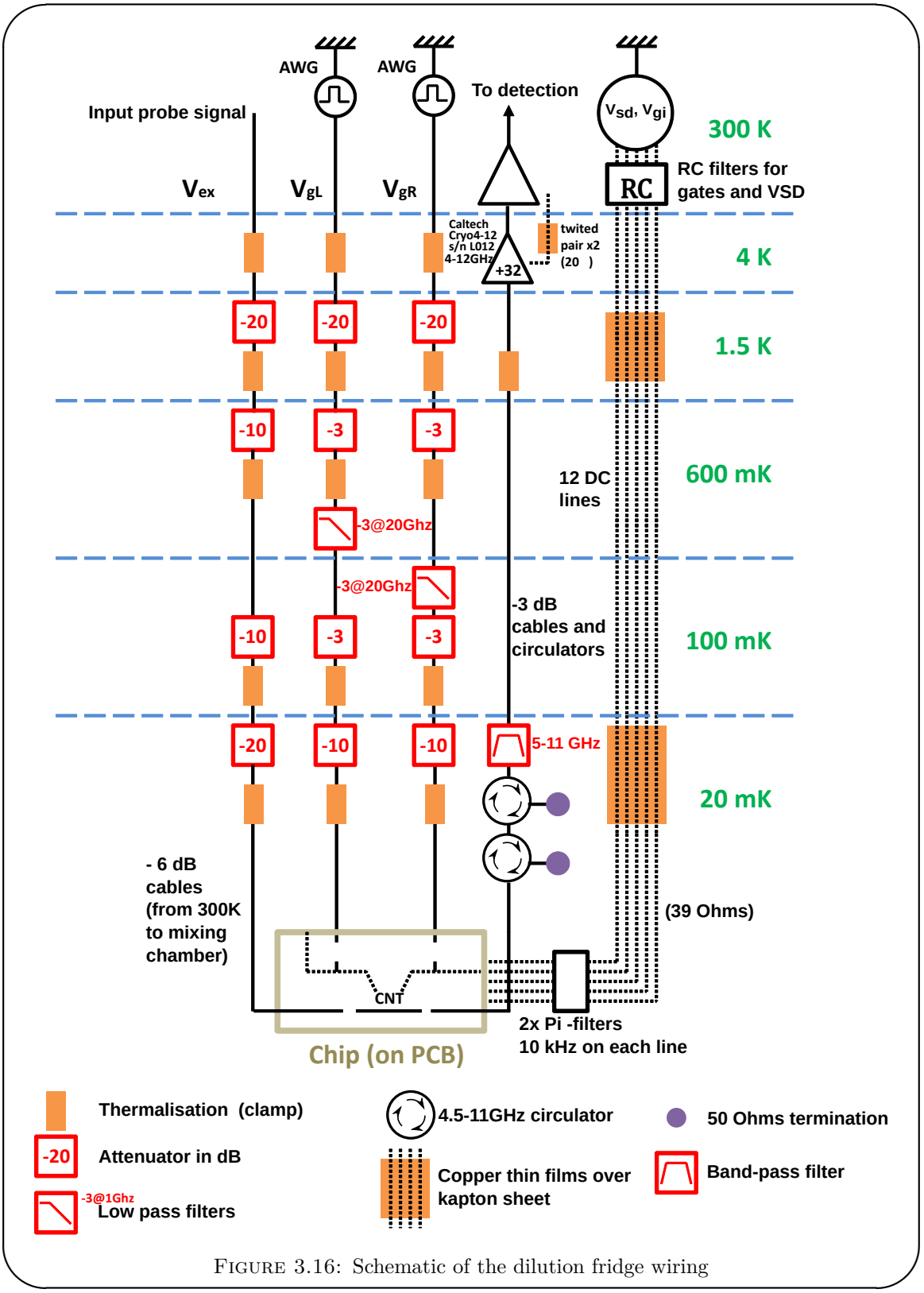

FIGURE 3.16: Schematic of the dilution fridge wiring

As discussed in 3.1.4, in the future we may want to incorporate on chip microwave filters to reduce the noise on the DC lines. Furthermore, the measurement carried out on the transmon qubit hint at the presence of residual thermal photons in the cavity. As those

are damageable to the transmon properties, we may want to add additional filters on the microwave lines.

3.3.3 DC measurements :

The DC measurements carried on the dot circuits are limited to current measurement. Once again to reduce noise, the bias circuit relies on a voltage divider setup (with a division factor of 1000 (1 MΩ/1 kΩ)). We used as voltage source a Yokogawa GS200 for the bias voltage line and one for each gate line. The current from the sample is then converted to a voltage using a commercial trans-impedance amplifier (Femto LCA-400k-10M) with a gain of 10^7 and a bandwidth of 400 kHz. The output voltage is measured using a Keithley 2000.

Usually to study such nano-circuits, one prefers to measure the differential conductance using a low-frequency modulation of the bias voltage and using a frequency locked measure (using a lock-in amplifier). This was not done in this work because, for yet unknown reasons, the fridge wiring appears to work poorly with such measurements, even if all cut-off frequencies are much higher than the one used in the detection. This is mostly damageable to experiments that will be presented in chapter 5 in which the conductance needs to be measured to characterize the system. For experiments presented in chapter 4 this is much less bothering, since at the working point of the experiment the sample has no conductance.

3.3.4 AC measurements :

Most of the measurements carried out in this work focused on measuring the cavity transmission and how it depends on the system control parameters such as the dot circuits gate voltages, the externally applied magnetic field or the frequency or power of an applied microwave tone. After discussing how such measurements were performed with a continuous wave excitation of the cavity, we will move to time domain experiments that are key in characterizing qubits.

3.3.4.1 Continuous measurements :

The general principle of the cavity transmission measurement can be described as follow:

- a microwave tone at the probe frequency is sent down the fridge and into the cavity.
- the output signal is then amplified inside the fridge using a low-noise amplifier (see Fig 3.16) and further amplified and filtered at room temperature.
- finally the signal is down-converted in frequency before being measured. That down conversion must of course preserve the phase of the signal.

Over the course of my thesis, four different setups have been used. They are presented in Fig 3.17 (not necessarily in chronological order).

The setup A is in sense the simplest one. It relies on a vector network analyzer (VNA) to perform both the generation of the probe signal and analysis of the transmitted signal. The VNA handles internally both the down-conversion and the measurement. Among the four setups, this one has the largest range in term of input signal power and is very well adapted to perform fast frequency characterization of the cavity transmission (much faster than what has been achieved with the other setups). This proved instrumental for the measurements under magnetic field presented in chapter 4. The applied magnetic field shifts the cavity frequency, which needs to be determined for each value of the field.

The setup B was the one existing when I started my work. It relies on a low frequency modulation (kHz) of the probe signal created using a double balanced mixer. A mixer uses a diode ring to realize a multiplication operation between a high-frequency and high-power reference signal (LO) and a low frequency signal (IF). The output signal is present at the RF port of the mixer and contains two frequencies: the sum of the input frequencies and their difference. The output signal is then down converted once again using mixers by multiplying the LO and RF signal. In this scheme, an IQ mixer is used to extract both quadrature of the signal at low frequency. To achieve this, an IQ mixer contains two mixers and a $\pi/2$ phase shifter. Both the LO and RF signals are split in two, one part is sent to one mixer and gives the I component, while in the other arm, the RF signal is phase shifted before the mixing operation which gives the Q part of

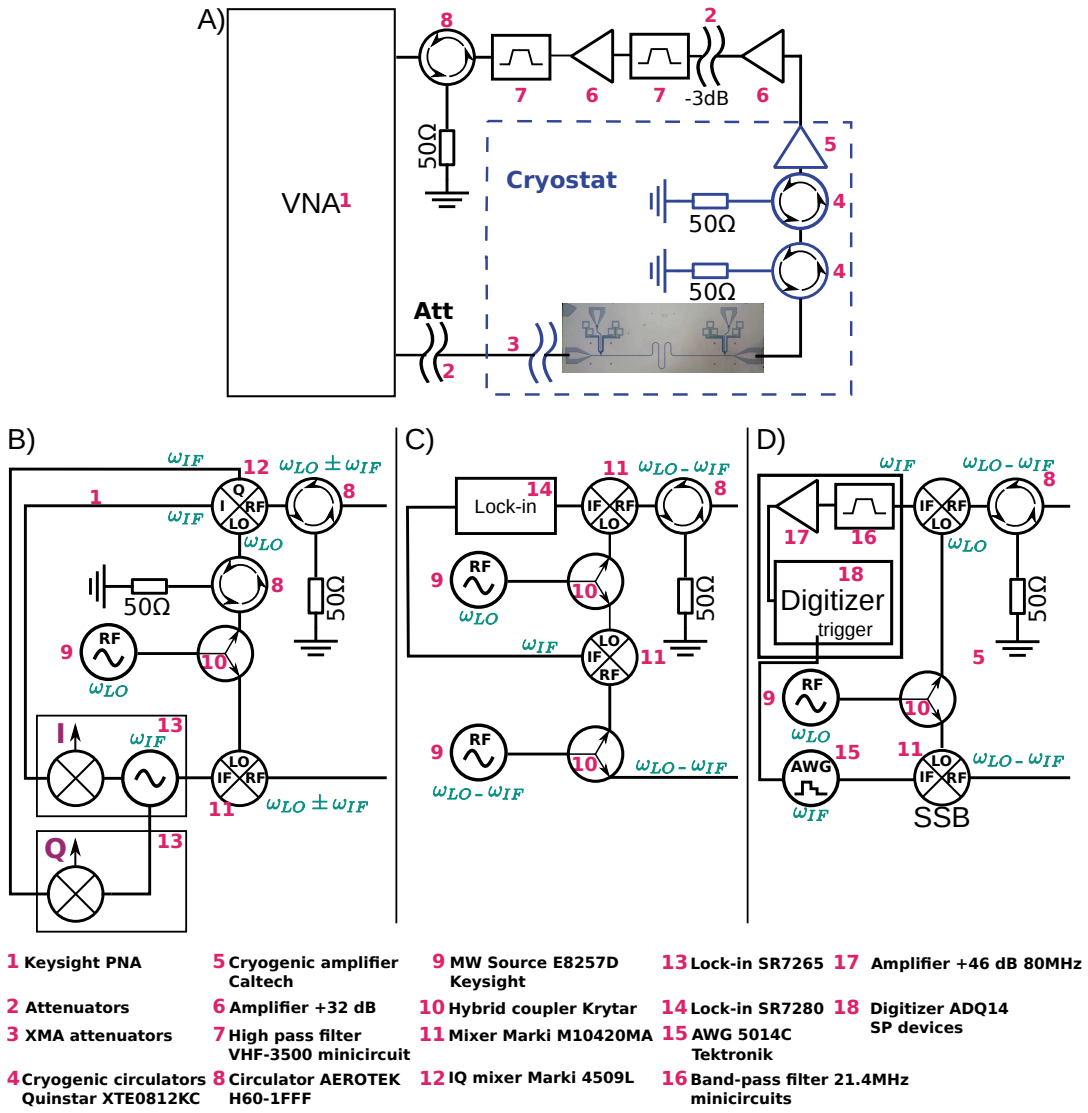

1 Keysight PNA
2 Attenuators
3 XMA attenuators
4 Cryogenic circulators Quinstar XTE0812KC
5 Cryogenic amplifier Caltech
6 Amplifier +32 dB
7 High pass filter VHF-3500 minicircuit
8 Circulator AEROTEK H60-1FFF
9 MW Source E8257D Keysight
10 Hybrid coupler Krytar
11 Mixer Marki M10420MA
12 IQ mixer Marki 4509L
13 Lock-in SR7265
14 Lock-in SR7280
15 AWG 5014C Tektronik
16 Band-pass filter 21.4MHz minicircuits
17 Amplifier +46 dB 80MHz
18 Digitizer ADQ14 SP devices

FIGURE 3.17: Microwave measure setups:
The four setups used to probe the cavity during this work are presented here. For each of them the amplification at the output of the fridge is the same and has been depicted only in case a, in the other cases simply replace the VNA by the depicted circuit. Note that the schematics do not always include all filters and attenuators.

A Simplest setup as the VNA handle both the signal generation and detection internally.

B Oldest setup, it relies on a kHz modulation of the probe tone coupled to an IQ demodulation and lock-in amplifiers to perform the detection.

C This setup relies on two microwaves sources, one used to probe the cavity and the other to down convert the signal usually in the megahertz range.

D Only setup adapted to time domain measurements, it generates the probe tone using a single-side band mixer driven by an arbitrary waveform generator (allowing for short pulses). The detection relies on a digitizer whose acquisition can be triggered.

the signal. Finally lock-in amplifiers, working at the modulation frequency, are used to measure the amplitude of each component. The main drawback of this design is that the signal sent into the cavity is not spectrally pure, which could produce inter-modulations.

The third setup, setup C, was suggested to us by Vlad Manucharyan. Its main advantage is that it allows to work with a spectrally pure probe tone. In order to do so, it requires two microwave sources sharing a common phase reference (typically at 10 MHz) and generating signals at two frequencies whose difference corresponds to the frequency at which the detection is to be carried out. The signal of one source is used unmodified to probe the cavity, while the signal of the other source is used to perform the down conversion using a simple mixer. The resulting low frequency signal (in the MHz or 10 MHz range typically) carries both amplitude and phase information and can be analyzed using a high frequency lock-in to which a reference frequency is provided by mixing the two microwave signals. Using this setup, one can choose the demodulation frequency. As already discussed, to reduce the sensitivity to low frequency noise it is interesting to use higher frequencies, however we were in that case limited by the lock-in capabilities at 2 MHz (SR 7280).

Finally the setup D was realized to perform time domain experiments as the detection scheme of none of the other allows them. It generates the probe signal by driving a single sideband mixer with an arbitrary waveform generator (AWG) and a microwave source. The single sideband mixer is a mixer specifically designed to output only one frequency (either sum or difference of LO and IF). The suppression of the second sideband is not perfect, neither is the isolation with respect to the LO, which means that our probe signal is no longer spectrally pure. However, as we will work with much higher frequencies (20 MHz), the leaking signals will be far from the cavity frequency when probing it transmission. The demodulation is performed using the LO signal, which gives a low frequency signal at the AWG generator frequency. This signal is then digitalized using a digitizer (ADQ14 from SP devices) and the extraction of the amplitude and phase is performed on the control computer. The advantage of this setup is that, using the AWG generator, we can generate short excitations and trigger the digitizer to acquire the signal only when pertinent allowing to do time resolved experiments. To properly trigger the digitizer one must first measure the propagation time of the signal inside the cables. This can be done, for example, by looking at the digitizer trace as a function of the delay in the triggering.

In order to determine the frequency of our qubits, we can also perform spectroscopy measurements involving a second microwave tone. When this second tone is at resonance with the qubit, it will drive its state away from $\langle\sigma_z\rangle = -1$, which will show in the cavity transmission as shown in equation 2.83 which is recalled below:

$$S_{21} = \frac{\langle a\rangle}{\epsilon_{in}} = \frac{-i}{i\,\Delta_{cd} + \kappa/2 + i\,g^2 \dfrac{\langle\sigma_z\rangle}{\Delta_{qd} - i\,\Gamma_2/2}} \tag{3.5}$$

When performing such measurements, the power of the second tone is crucial. If it is too low it will have no impact on the qubit, on the other hand if it is too high, it will make the qubit appear wider in frequency that it really is.

The width of the spectroscopy peak can also be increased by the photons present inside the cavity. Indeed in the weak dispersive regime (see section 2.2.3.2) the peaks corresponding to each photon number will be merged together and will give a wider peak. When a peak is wider, it also tends to be smaller making its detection more delicate. This is why it is often preferable to perform spectroscopy by separating temporally the qubit excitation and the cavity probing. However this can be done only if the qubit lifetime is not much smaller than the cavity rise time as otherwise the qubit will have relaxed before we probed the cavity state. This is why in practice one usually starts with continuous wave measurements. Using similar methods we can also measure the cavity-qubit dispersive shift in the strong dispersive regime by driving the qubit out of $\langle\sigma_z\rangle = -1$ and measuring the cavity transmission that presents in that case two peaks, whose weight match the probability to find the qubit in each state.

Once we know the frequency of our qubit we can manipulate its state in time resolved measurements as presented in the next section.

3.3.4.2 Time resolved measurements :

The first challenge in time domain experiments performed with a system whose lifetime is not much longer than the cavity lifetime is the measurement. Because of the finite coupling to the input/output line, it takes a finite time for photons to actually enter the cavity and then start leaking out. If the system relaxes in a non-negligible fashion during that time the contrast of the measurement will be strongly reduced. To counter-balance

that effect one can start feeding the cavity before the end of the manipulation on the qubit. Furthermore the qubit can relax during the measurement itself. Hence one must find a compromise between the measurement time and the number of repetition allowing to perform the measurements.

The first quantity, we typically measured in time resolved experiment, is the frequency at which we can induce oscillations between the two states of the qubit. This frequency, known as the Rabi frequency, is measured using the pulse sequence presented in Fig 3.18 a.

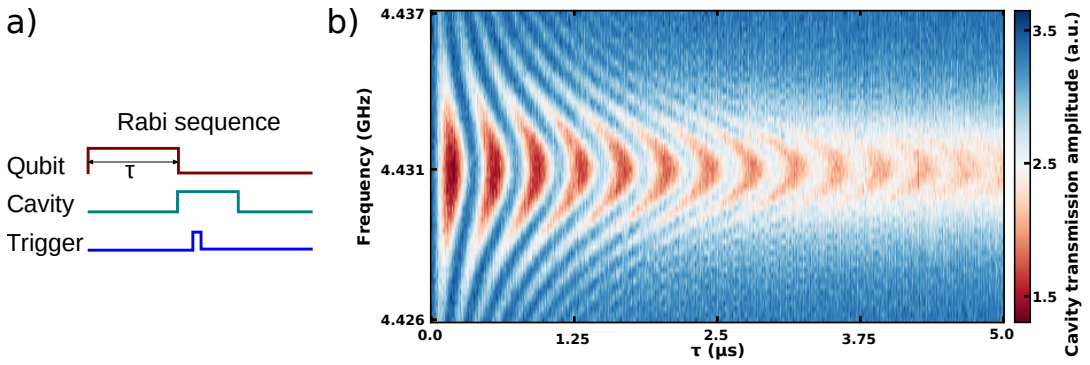

FIGURE 3.18: Rabi pulse sequence :
Figure a presents the sequence of pulses played by the AWG when measuring Rabi oscillations. First the qubit (here a transmon qubit) is driven for a time τ, then the qubit population is measured through the cavity transmission. The trigger starting the data acquisition is delayed compared to the beginning of the cavity feeding to account for the propagation and the finite bandwidth of the cavity. Figure b is a typical measurement of Rabi chevrons. The x axis is the time τ, the y axis the frequency of the manipulation tone and the color code maps the cavity transmission and hence the qubit population.

In a Rabi experiment, the qubit is driven by a pulse of frequency f_d and of duration τ then its state is inferred from the cavity transmission. We then wait for both the cavity and the qubit to relax before starting over. The sequence is then repeated many times for each value of f_d and τ. Plotting the probability of finding the qubit in the exited state as a function of f_d and τ we obtain chevrons like pattern, whose tip is centered on the qubit frequency. From the periodicity of the oscillation we can deduce the Rabi frequency.

We can further characterize our qubit by measuring its relaxation time and dephasing time using the pulses sequences presented in Fig 3.19.

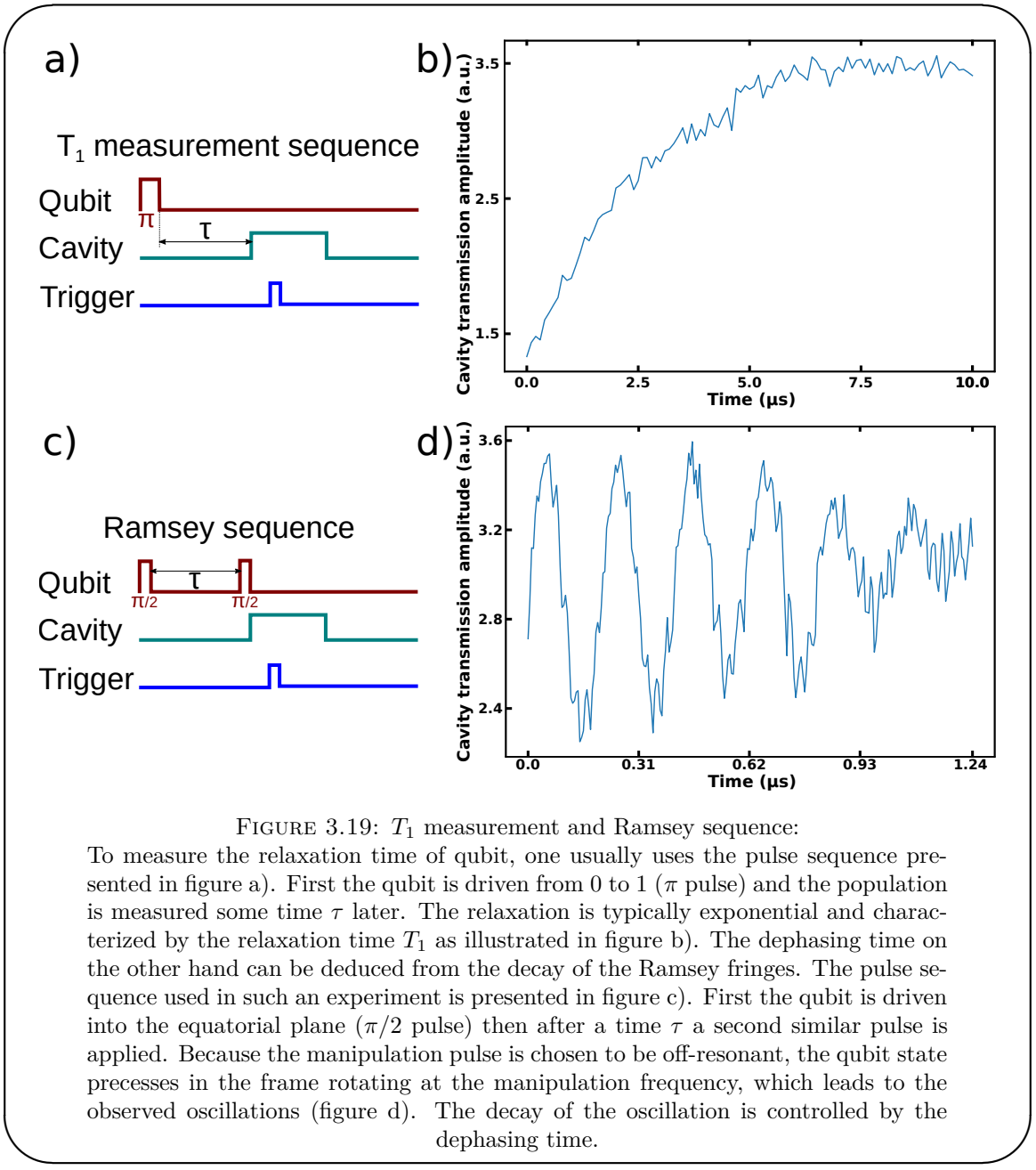

FIGURE 3.19: T_1 measurement and Ramsey sequence:
To measure the relaxation time of qubit, one usually uses the pulse sequence presented in figure a). First the qubit is driven from 0 to 1 (π pulse) and the population is measured some time τ later. The relaxation is typically exponential and characterized by the relaxation time T_1 as illustrated in figure b). The dephasing time on the other hand can be deduced from the decay of the Ramsey fringes. The pulse sequence used in such an experiment is presented in figure c). First the qubit is driven into the equatorial plane ($\pi/2$ pulse) then after a time τ a second similar pulse is applied. Because the manipulation pulse is chosen to be off-resonant, the qubit state precesses in the frame rotating at the manipulation frequency, which leads to the observed oscillations (figure d). The decay of the oscillation is controlled by the dephasing time.

To measure the relaxation time, we first apply a π pulse on the qubit driving it from its ground state to its exited state and we then vary the time we wait before measuring its state, as illustrated in Fig 3.19 a. Plotting $\langle\sigma_z\rangle$ against the waiting time, we obtain a decreasing curve that we can fit to an exponential in the simple case of the transmon (Fig 3.19 b).

To measure the dephasing time, we perform a Ramsey fringes experiment. First we choose a drive frequency slightly detuned from the qubit frequency, such that in the

frame rotating at the drive frequency the qubit state precesses at difference of the frequencies around the z-axis. Then the sequence consists in two $\pi/2$ pulses followed by the measurement of $\langle\sigma_z\rangle$ (Fig 3.19 c). The first pulse prepares the qubit on $|+X\rangle$. During the waiting time, the state will precess in a deterministic fashion due to the frequency mismatch and in a random fashion due to the noise to which the qubit is subject. When the second pulse is applied it will have a varying impact depending on the accumulated phase. In the absence of relaxation and dephasing, we expect oscillations at the frequency mismatch. In the presence of dephasing, will get damped oscillation as shown in Fig 3.19 d. From those, we can extract the dephasing time, and the qubit frequency with greater precision.

3.4 Computer interface:

Running all the measurements presented in the above section requires the instruments to be interfaced to a computer given the large amount of data they require. Before the work done during this thesis, the interfacing and the on fly data visualization was done using Labview. This solution was problematic for visualizing large data and also required to often create new programs for specific measurements that were only marginally different from existing measurements.

During my internship in the lab I developed a simple data visualization software in Python, that outperformed the existing Labview visualization software. Even though, this program could use many improvements, it proved very useful, and convinced the lab that using Python for running the experiments was a viable option. The data acquisition software went through several phases during my thesis, as I became aware of new tools and learned more about proper software design following the development of other open source projects. This software have been used for the experiments carried out in the lab since Fall 2013.

In the last years, Python driven experiment control systems have boomed. The Martinis group system, LabRad, which started in 2007, uses Python and other languages to implement a distributed acquisition, processing and storing data system. More recently, projects like Qudi [115], focused on quantum optics, and QCoDeS, supported by Microsoft in Copenhagen, Delft and Sydney have been made public. Using them was,

at the start, not an option either because they did not exist yet or because of the complexity in setting them up (LabRad). Furthermore, coming from a Labview background, a graphical interface was more appealing to the people in the lab than a script based system.

After a brief presentation of the key ideas underlying the current state of the data acquisition software (the reader is free to consult the documentation for more details), I will discuss a bit a yet unfinished work on improving the interfacing with the hardware. And, finally, describe what may be future perspective for this work.

3.4.1 Ecpy: experiment control in python

The data acquisition software, named Ecpy, is designed to be flexible and extensible. It focuses only on data acquisition and does not deal at all with live data plotting. This is because live plotting of increasing amount of data can cause memory issues and also leads to unexpected crashes as GUI components are not always extremely stable, which is why it should not be the responsibility of the program in charge of handling the data acquisition. For the same reasons, the measurement execution is isolated from the main GUI component and cannot be altered in a live fashion (although it can be paused, resumed and stopped).

It is extensible because one cannot, ever, hope to provide all the capabilities a user may need. To achieve this goal, it is designed around the notion of plugins where each plugin provides some specific capabilities such as the description and compilation to hardware compatible representations of pulse sequences. In order to add new plugins or add capabilities to an existing plugin one does not need to edit directly the sources of the application but can simply create an additional Python package that the application will load at start-up. This also allows to split the applications in smaller more manageable packages rather than dealing with a gigantic project. Of course such an architecture has a cost in term of complexity but I believe it is nonetheless a better choice in a long term vision. As a consequence, the basic application does not know how to talk to any instrument but simply installing the ecpy_hqc_legacy package allows to access all the currently used tasks and instruments driver in the HQC lab at the time being.

It is flexible in the way in which it represents a measurement as it allows to combine different actions in any hierarchical way needed to describe the experiment and allows tasks to do computations on the values provided by others as input, allowing a great flexibility inside the GUI. The tree can include logical tasks such as loops, and conditions. Furthermore even if the tree is executed in an essentially sequential manner, one can very simply execute different tasks in parallel if needed and synchronize when necessary. Contrary to what is attempted in other packages, the user is responsible for choosing the data that should be saved, as in complex measurements this can be a complex problem.

Fig 3.20 shows a screenshot of the main window when used to edit a measurement.

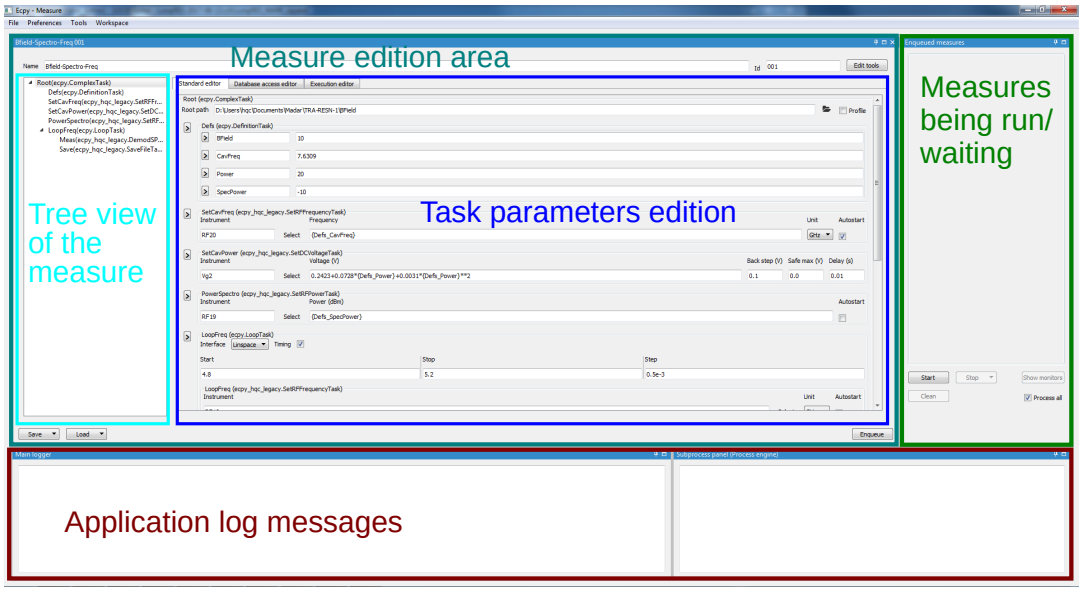

FIGURE 3.20: Ecpy main window:
This is the main window of the application which can be used to edit and run measures. It features three main panels that can be freely re-ordered:

- A log panel in which the application will display messages about the performed actions and potential errors (even if most of them are reported through pop-up windows).
- A queue of completed, running(only one at a time), or waiting measures. Those can be re-ordered and re-edited while not running. The running measure can be paused, stopped and resumed.
- A panel dedicated to the edition of measures with a tree editor on the left featuring the structure of the measure in term of tasks and allowing to modify it using drag and drop, and more specialized editors on the right.

Finally, because a lack of those can be a main issue in that kind of software, the code is thoroughly tested to avoid regressions when changed are made (coverage $> 95\%$) and inline documented. In addition, the documentation (`http://ecpy.readthedocs.io/`

en/latest/) attempts to cover how to use the application and all the possible ways to extend it. Finally to ease the installation, it is packaged using conda (to use with the Anaconda distribution) and easily installable on both Python 2 and 3. In order to know more one can read the docs or get in touch on Github (https://github.com/Ecpy/ecpy)

3.4.2 I3py: instrument interfacing in python

One key point in handling the computer interfacing of an experiment is the proper interfacing of the dedicated hardware (VNA, AWG, DC sources, microwave sources, etc ...). While the problem appears simple at first, it quickly becomes nightmarish to handle the different modes incompatibilities, the limits on the different parameters and to do so in a manner that avoids to duplicate too much code (this is a source for bugs and hinder code maintenance). Overcoming those difficulties is not easy as hardware components are full of "exceptional" behaviors. Furthermore, in order to easily swap similar hardware in an experiment, one needs them to have similar interfaces. Designing such interfaces can prove complicated while retaining access to the full capabilities of the hardware.

Quite quickly this appeared to be an issue with the initial design of the hardware interfacing in the first version of the data acquisition program. I spend quite some time trying to improve this design, which led to several draft implementations. In particular, one attempt at establishing a collaboration between several developers on Github was quite motivating but failed due to a lack of time/interest from the other involved parties. The current implementation can be found under the I3py project https://github.com/Ecpy/i3py. It is nearly complete but lack proper documentation and use on concrete hardware.

The key ideas behind this project are the following:

- reduce as much as possible the code needed to write a driver while providing a lot of flexibility to handle corner cases.
- allow to organize a driver in a hierarchical fashion using sub-systems
- easily handle instruments with multiple channels

- avoid unnecessary communication with the instrument by properly caching the instrument state
- allow to discover the capabilities of an instrument without the need to communicate with it (as much as possible), in such a way that building a GUI, providing a remote interface or performing automatic tests can be automated

This last requirement stems from the fact that a most desired feature is the possibility to integrate Ecpy with a front panel for the instrument.

I truly hope to be able to achieve before leaving the lab and possibly during my post-doc.

3.4.3 Future directions

Such a project cannot ever reach an end, and the number of future features that could be added is large. I will only discuss four points here that have already surfaced in the lab.

The first, and most ambitious one, is to provide a remote interface both to the hardware and for data storing in such a fashion that multiple programs can use a single resource. The two main applications are

- providing update about the hardware state during a measurement to an hypothetical control panel
- feeding new data to a plotting program. While the need for such a protocol is not needed for simple text based files, it becomes mandatory for binary storage (such as HDF5) that cannot be opened by two programs at the same time.

This would represent a very large amount of work, which is why the Quantum circuits group, which also uses Ecpy and involved me in the candidature, attempted to hire a computer science engineer through a partnership with the INRIA.

The second and third consist in two improvements to Ecpy. The first would consist in adding a plugin tracking some global variables related to an experiment (such as the qubit frequency) and allow to parametrize measurements with respect to them. This feature has already been discussed in the lab and has a clear roadmap. The other would

the possibility to create templates, representing an often done sequence of tasks in an experiment, which could be directly embedded inside a measurement to simplify it.

Finally, a rejuvenation of the plotting program written at the beginning of my thesis would be desirable.

Of course, trying to develop a versatile software with proper testing takes time and requires an effort from the people participating. Even if it is not physics, given the complexity of recent experiments, it is not possible to completely skip such developments.

Chapter 4

Coherent spin-photon coupling in a cQED architecture:

Chapter 1 has motivated the interest in encoding quantum information in spin qubits and of coupling qubits to microwave cavities, which is at the core of the experiment presented in this chapter. To reach the strong coupling regime, we need the coupling between the cavity and the spin to be larger than the losses in either system. The natural magnetic coupling is very weak ($\sim 10Hz$) compared to the cavity lifetime, and enhancing the magnetic field of a cavity to overcome this is very challenging. On the other hand, inducing a charge-spin hybridization to enable a coupling to the cavity electric field must be done very carefully as any such hybridization will make the spin qubit sensitive to charge noise. The key challenge is hence to increase the coupling while preserving the coherence of the electronic spin.

As mentioned in chapter 1, the spin-qubit we used is unusual as, while relying on a DQD architecture like exchange based spin qubits, its basic principle is closer to a spin-orbit based scheme. After a more detailed presentation of the system from a theoretical point of view in 4.1, I will describe in section 4.2 the samples used in this experiment and how they were tuned in the regime of interest. The work presented in the following section 4.3 will closely follow the article [21] which describes the main results. I will then move to some additional results about the influence of the double dot occupation on the spectrum of the system, in section 4.4, and conclude with some perspective about this experiment in section 4.5.

4.1 Principle of the ferro-magnetic spin qubit:

The spin-qubit architecture developed in this work, was first introduced in [20] and has been designed from the start to be embedded in a microwave cavity. The key idea, of the spin-charge coupling, is to engineer a spin-orbit like interaction limited to the two sites of a double quantum dot, such that oscillations of the charge between the two sites induce a spin precession. The coupling to the cavity arises then from interaction between the large electric dipole of the double quantum dot and the electric field of the cavity. By combining those two ingredients one can hope to achieve a spin-photon coupling. Those ideas are sketched in Fig 4.1, that were already presented in chapter 1.

However, such qualitative arguments do not give any clue about the decoherence mechanisms that will affect the spin as a result of its hybridization to the charge. Indeed, if the spin dephasing coming from the charge noise contribution increases faster than the coupling, one will end up with something quite similar to charge qubits which, up to recent results [57, 58], have a dephasing rate much larger than their coupling. To pinpoint the link between the charge qubit properties and the spin-qubit ones, we will need to introduce a more detailed description of the system. This will be done in section 4.1.2, just after discussing the origin of the spectrum polarization by the ferromagnetic contact.

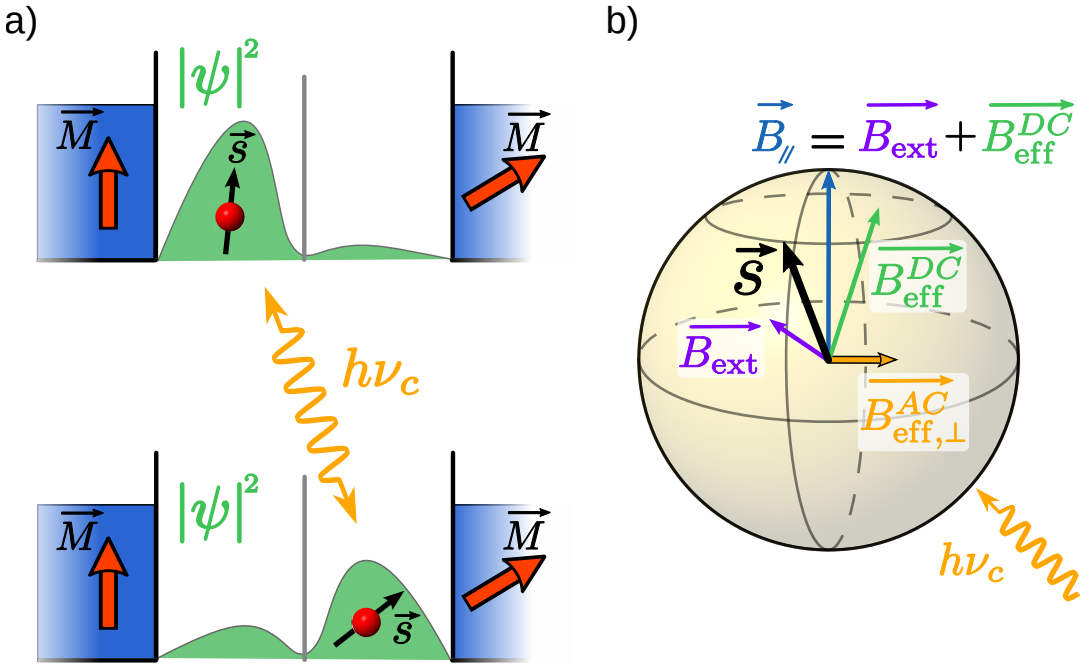

FIGURE 4.1: Artificial spin orbit coupling in a CNT based DQD: We consider a single electron with spin $\vec{s}$ in a DQD. We represents its charge probability density $|\psi|^2$ in green. Each dot is connected to a ferromagnetic contact, whose magnetization is noted $\vec{M}$. This induces a spin polarization of the wave function. However, as the ferromagnets magnetization are not colinear, neither are the quantification axes in each dot, as illustrated in a. Hence by inducing tunneling between the two dots using an electric AC signal, at frequency ν_c, the electron experiences an AC magnetic field orthogonal to its quantization axis ($\vec{B}^{AC}_{eff,\perp}$) that can be used to control the electron spin state (see b). The quantification axis is defined by the effective field induced by the ferromagnets $\vec{B}^{DC}_{eff}$ and the externally applied DC field B_{ext}

4.1.1 Ferromagnetic contact induced Zeeman splitting:

The first, and most obvious, mechanism through which a ferromagnet is susceptible to induce a polarization of the spectrum of a nearby quantum dot is through the stray fields it generates.

In addition, just like superconductivity can be induced by proximity effect, a ferromagnetic interface can induce a spin polarization in a conductor to which it is connected. In a non interacting picture, one can use the scattering matrix formalism to compute the spectrum of a confined portion of coherent conductor connected to a ferromagnet via a barrier with transmission (t^{σ}_{lead}) and reflection (r^{σ}_{lead}) probabilities which are spin dependent, as depicted in Fig 4.2.

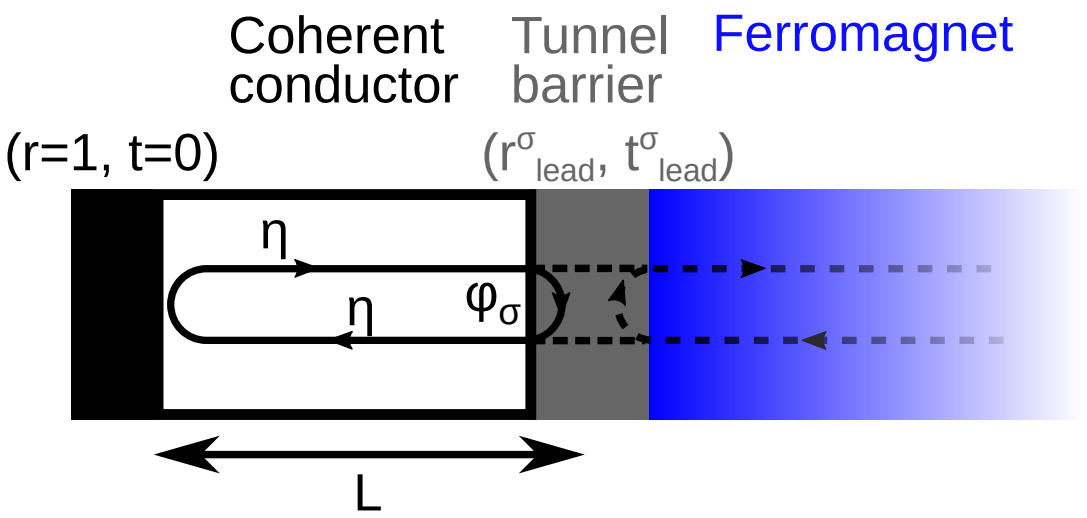

FIGURE 4.2: Principle of the confinement-induced exchange field: When tunnel coupling a coherent conductor to a ferromagnetic lead, a spin-dependent interfacial phase shift φ_σ appears for electron reflecting the ferromagnetic interface. This combines with the phase η acquired by the electronic wavefunction when propagating through the coherent conductor over a length L and create a spin dependent quantification condition which gives rise to a spin polarized spectrum.

The spin dependence of the spectrum in the dot can arise from both the transmission probability and the phase of the reflection coefficient. If the transmission probability is spin dependent, and non-zero, it means that the electronic wave-function is "leaking" into the ferromagnet (through an evanescent part). The wave-function is hence hybridized to the first atomic layers of the ferromagnetic lead, which naturally leads to spin polarization of the total quantum state. This mechanism can be referred to as tunneling exchange field. Its strength strongly depends on the amplitude of the transmission probability and vanishes for a totally reflecting barrier ($t_{\text{lead}} = 0$). It has been observed in quantum dot spin valves [116, 117] and studied as a function of lead coupling $\Gamma_{\text{lead}} \propto |t_{\text{lead}}|^2$ on a Kondo resonance [118].

However, a spin dependent phase at the reflection can also induce a similar polarization of the spectrum. Such a spin-dependent phase can arise from a spin dependent barrier potential landscape, as it could happen for a connection to a ferromagnetic insulator for example. In the non-interacting picture considered here, this confinement-induced exchange field yields an effective Zeeman splitting [119]:

$$2\delta = E_{ex} = \frac{\hbar\, v_F}{2\, L}\,(\varphi_\uparrow - \varphi_\downarrow) \tag{4.1}$$

where v_F is the Fermi velocity, L is the length of the dot and $\phi_{\uparrow(\downarrow)}$ is a spin-dependent interfacial phase shift.

Gate voltages can in principle be used to tune the coupling between the dot and the ferromagnetic lead, which means that it should be possible to control the exchange field using gate voltages.

In the perspective of making a long lived qubit, the first and last mechanism are more interesting than the second as the finite t_{lead} in the second one is likely to strongly limit the lifetime. However in our experiments, we will not be able to actually pinpoint the physical origin of the induced Zeeman splitting, although it is likely the third mechanism which is dominant.

4.1.2 System properties:

As we aim at implementing a long-lived two level system, the double quantum dot will be tuned in between the triple points where transitions to the leads are forbidden for both dots (see chapter 2). In this regime of parameter, the total number of electron in the structure is fixed and only internal transitions between the molecular orbitals can occur. We will hence describe the system by taking into account a single orbital in each dot. Those two orbitals are subject to a Zeeman field along different axes (δ_L, δ_R) and tunnel coupled (t) as illustrated in Fig 4.3. We will denote by θ the angle between the two axes. For the sake of clarity, we will introduce the valley degree of freedom present in CNT, only later, to properly describe the experimental results presented in section 4.3.

The system Hamiltonian, for a single electron in the structure, can then be written:

$$H_{SQB} = \epsilon\,\tau_z + t\,\tau_x + \delta_L\,\sigma_z\,\frac{1+\tau_z}{2} + \delta_R\,\left(\sigma_z\,\cos\left(\theta\right) + \sigma_x\,\sin\left(\theta\right)\right)\frac{1-\tau_z}{2} \tag{4.2}$$

with τ acting on the orbital degree of freedom ($\tau_z = |L\rangle\langle L| - |R\rangle\langle R|$, with L and R the left and right orbitals), and σ acting on the spin degree of freedom for which the axis is chosen to be the left dot quantification axis. This Hamiltonian is similar to the one presented in [120].

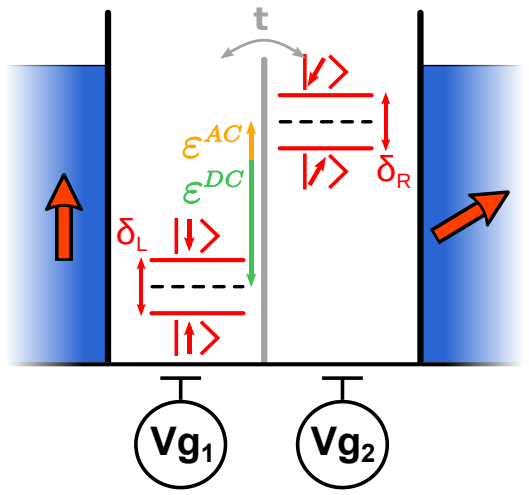

FIGURE 4.3: Spin qubit level schematic:
Simplistic scheme of a double quantum dot connected to non-collinear ferromagnets. Interface exchange fields induce effective Zeeman splittings in both dots with tilted quantification axes and different magnitudes (δ_L, δ_R). The coherent delocalization of the charge probability density $|\psi|^2$ is controlled via the inter-dot detuning ϵ which can tuned in DC, using the gates V_{g1} and V_{g2}, and modulated in AC by the cavity field.

Diagonalizing this Hamiltonian allows us to study the spectrum of the spin qubit. Furthermore, we can compute its coupling to the cavity: the cavity field induces oscillations of ϵ which implies that the coupling is proportional to $|\langle i|\tau_z|j\rangle|^2$. Finally, we can extract the sensitivity of the qubit to charge noise at first order by computing the derivative of the transition frequency f_{ij} with respect to ϵ.

From there the goal, is to find a compromise between the coupling and the dephasing due to charge noise, while preserving the system anharmonicity. In order to obtain sufficiently mixed states the different energy scales cannot be too different. In Fig 4.4, we present the spectrum, and the coupling and dephasing of the three transitions from the ground state for parameters close to the ones we will use in section 4.3.1.

Looking at Fig 4.4, one can follow two paths to get a low dephasing while keeping a finite coupling. One can either work in the large ϵ limit where the 0 and 1 states becomes asymptotically parallel with respect to ϵ and hence insensitive to charge noise. This transition is interesting as it is a nearly pure spin transition. Furthermore, its coupling can easily be turned off by increasing ϵ while leaving the transition frequency nearly unchanged. Such an operation scheme could allow to use this device both as a qubit and a quantum register. The other course consist at working very close to $\epsilon = 0$ but

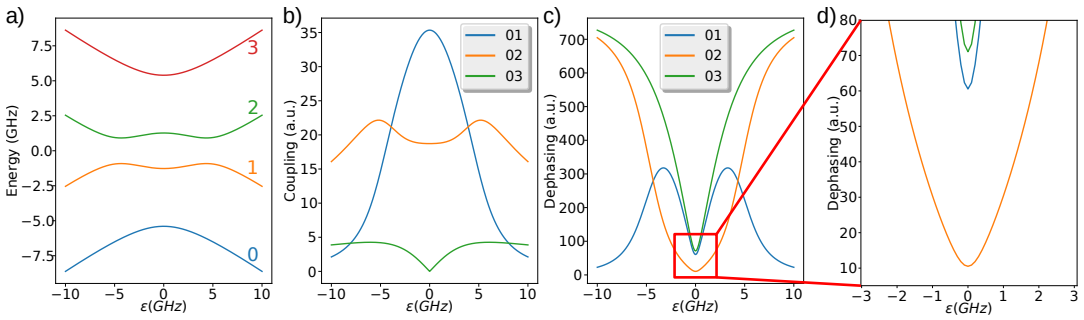

FIGURE 4.4: Spin qubit properties:

a) Spectrum of the spin qubit for parameters similar to the one used in Fig. 4.10.

b) Coupling between the ground state and the exited state. At zero detuning the 01 transition is the more strongly coupled but its coupling decreases quite quickly with the detuning as apposed to the 02 transition.

c) Charge noise induced dephasing rate for each transition. All transitions have a sweet spot at zero detuning and the 01 transition has an asymptotic sweet spot at large detuning but also a vanishing coupling.

d) Zoom of the sweet spot for the charge noise induced dephasing. One can notice that all transitions are not equal with respect to charge noise suppression at zero detuning and in particular the 02 transition has an increased coherence compared to the other two.

on the $0 \rightarrow 2$ transitions. Naively one could think it is a pure charge transition but actually at $\epsilon = 0$, the mixing is maximal and it can be associated with a strong spin-flip (cf 4.3.1). One can notice that it has a much stronger coupling and a "very sweet spot" with respect to charge noise, which is why it is the transition whose signature will be dominant in section 4.3. However it lacks the possibility to use the system as a register as one cannot go to large detuning to protect the state without largely modulating the transition frequency and going through an anti-crossing.

4.2 Sample:

The experimental results that are presented in this chapter have been all obtained on a single sample, but the main ones concerning the spin-photon coupling have all been reproduced on another one (not shown here). The case of that sample will not be discussed as the results were very similar at first and because a power breakdown destroyed it before more results could be obtained. This section will focus on the peculiarities in the design and fabrication of the devices and on the first measurement required to tune

the system into the right range of parameters. The spin-photon coupling will be the subject of the next section.

4.2.1 Geometry and fabrication:

The main specificity, as far as the fabrication of those devices is concerned, is the deposition of the ferro-magnetic contacts. We require to have two ferromagnetic contacts with a controlled magnetization orientation and which forms not too transparent contacts on CNTs. In theory, we can work with opaque contacts as already explained in the previous section. However transport is the only method we have to control at room temperature the quality of the sample and given that the fabrication is not extremely reliable such tests allow to save a lot of time.

PdNi alloy can form good contacts with CNT's[116, 117] and thin films magnetization direction can be systematically controlled by the shape of the electrode. Indeed, Chauleau et al. [121] have shown that for thin $Pd_{0.2}Ni_{0.8}$ layer (30 nm), electrodes narrower than 500nm systematically present a transverse magnetisation, see Fig. 4.5.

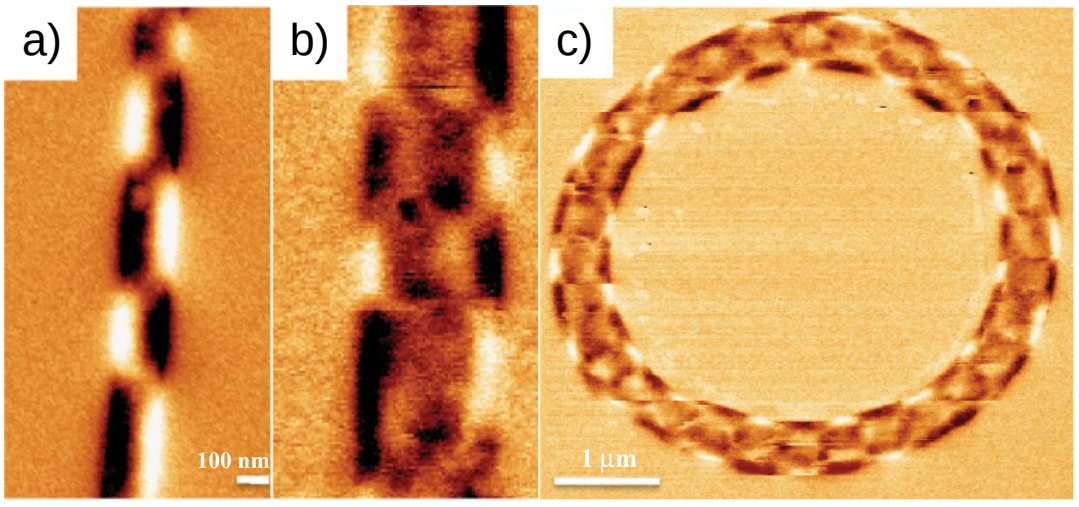

FIGURE 4.5: MFM images of PdNi nanostructures:
Each structure was patterned in a 30nm thick film. (a) 150nm-wide and (b) 450nm-wide nanostrip. (c) nanoring with 500nm width and 5μm diameter. Source: [121]

The alternating dark and light regions of magnetic force microscopy (MFM) images show magnetic domains of opposite orientation demonstrating a magnetization perpendicular to the axis of the electrode. For 150 nm wide electrodes, the strip presents clear magnetic domains with orientation orthogonal to the longitudinal direction that minimizes the

magnetostatic energy. Taking advantage of this knowledge, we can therefore define the magnetization direction of our electrodes at the lithography step. Fig. 4.6 shows a topography (AFM) and magnetic map (MFM) of a CNT-based double quantum dot connected to non collinear PdNi electrodes, similar to the ones shown in Fig. 4.5. In this case the ferromagnetic contacts were tilted with an angle $\theta = \pi/4$ with respect to each other. This angle was chosen because previous experiment carried out with an angle of $\pi/6$ did not exhibit any spin-photon coupling.

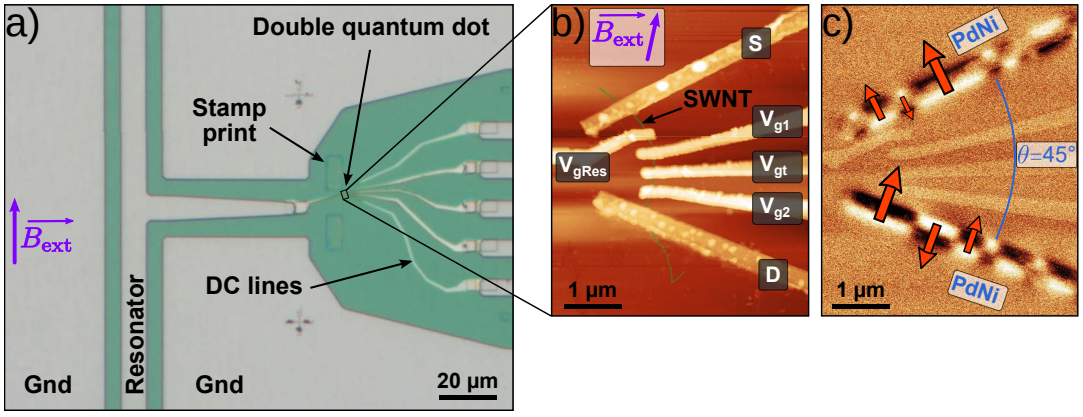

FIGURE 4.6: Spin-qubit sample:

a Optical micrograph image of the studied sample zoomed into the area of the DQD. One can recognize the stamp marks left by the quartz mesas as well as the six electrodes deposited on the CNT.

b Atomic force microscopy image of the sample on which the CNT appears in false colors.

c Magnetic force microscopy image of the sample. The magnetization of the source and drain electrodes appear in the checker board pattern, in which black and white area correspond to the North and South poles of the magnetization.

On the MFM image, one can notice that the magnetic domains can be quite small. In practice, this causes no issue for the contact induced spin-polarization as the domains remain much larger than the CNTs diameter ($\sim$ 1 nm), however it means that the net stray fields are going to be very small and are not likely to be the main phenomenon involved in the polarization of the spectrum.

Previous experiments carried out in the group had demonstrated that on such samples side gates were not effective in tuning the system properties, which is why we chose a geometry using only top gates to define our DQD. As shown in Fig. 4.6, our DQD circuit is composed of the two ferromagnetic contacts and of four top gates. Among those four top gates three are connected to DC voltage sources and used to tune the DQD

properties. The fourth one is only connected to the central conductor of the resonator. As discussed in chapter 3, this allows to maximize the coupling to the microwave photons. This gate is as far as possible of the "center" of the DQD to maximize the asymmetry of the field. At this point, it is worth mentioning that our systems are far less controlled than DQD in GaAs for example:

- the top gate allow to tune the chemical potential in the dots but the tunnel barrier between the dots is mainly controlled by disorder.
- the location of the dots remains uncertain as is their filling. Contrary to what can be done in GaAs it is impossible to drive the system at charge neutrality and work with a single electron in the DQD (although this has been demonstrated is ultra-clean CNT devices [122])
- the disorder and defects distort the honeycomb pattern one expects to find in a DQD. As a consequence, this pattern appears only in small gate voltage ranges.

Finally it should be mentioned that two such DQD were embedded in the same cavity.

4.2.2 Sample tuning:

After cooling down the sample, we need to tune the gate voltage so that the sample behaves in the proper fashion. Given the experiments we are interested in, the sample should have the following properties once properly tuned:

- it should display the honeycomb pattern specific to a DQD, similar to Fig. 2.6.
- its conductance on the triple points should be very low ($G \simeq 10^{-6} - 10^{-5}$ S), as otherwise the coupling to the leads will be too strong and the qubit will not be very coherent.
- we should be able to bring the internal transitions in the area of the triple points into resonance with the cavity. We also need a low dephasing rate, as we hope to observe the strong coupling regime.

During that tuning step, we used only two top gates (Vg_1 and Vg_2) to explore the stability diagram, Vg_t was tuned later on but had a limited impact in the studied sample. As

always, we can measure both the current and the cavity response. As discussed in chapter 2.2, the cavity response is mainly dominated by the susceptibilities of internal transitions ($\chi_{n,m}$ between levels n and m) and can be described, in the semi-classical regime, by :

$$S_{21} = \frac{-i}{i\,\Delta_{cd} + \kappa/2 + i\sum_{n,mn<m}\chi_{n,m}\left(\langle|m\rangle\langle m|\rangle - \langle|n\rangle\langle n|\rangle\right)} \tag{4.3}$$

with $\chi_{n,m} = \dfrac{g_{n,m}^2}{\Delta_{n,m} - i\,\Gamma_{2,n,m}/2}$

In most cases, we can get a qualitative understanding of the signal by considering a single transition with a dispersion similar to the one of a DQD $\Delta = \sqrt{\epsilon^2 + 4\,t^2} - \omega_d$. In the regime of weak coupling, we can map the phase response to the real part of the system susceptibility and the amplitude response to the imaginary part. Fig 4.7 illustrates the typical answer one can expect.

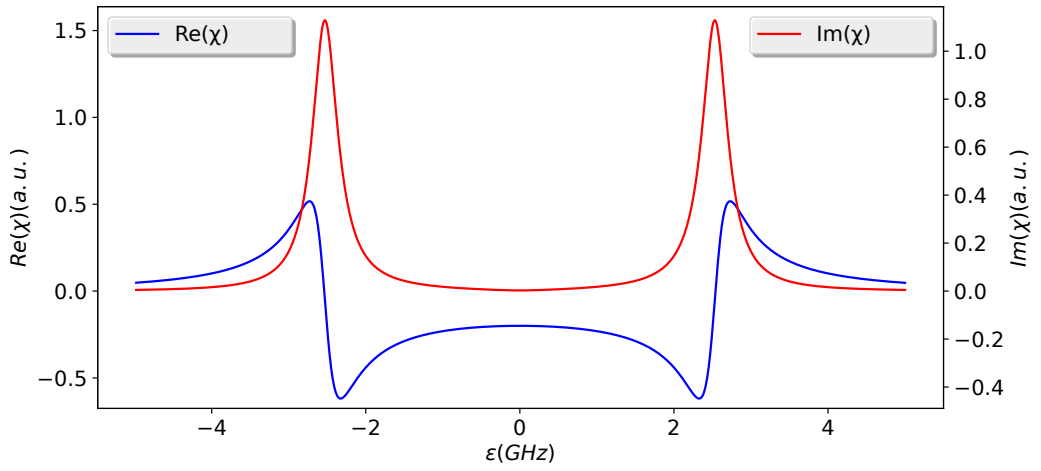

FIGURE 4.7: DQD charge susceptibility for $t = 3.1$ GHz and $\omega = 6.7$ GHz: The imaginary part of the susceptibility displays two peaks matching the resonance condition $\omega_{cav} = \sqrt{4\,t^2 + \epsilon^2}$. In between those two peaks the transition frequency for the qubit is smaller than the cavity frequency which gives a negative real part which will lead to a positive phase shift. If the dephasing rate was much larger, we would not resolve the two peaks in the imaginary part. On the other hand if $2\,t$ was larger than the cavity frequency we would not observe a sign change in the real part .

The susceptibility remains finite and detectable only close to the degeneracy line ($\epsilon = 0$), on a scale of the order of $2\,t$. As we are interested in cases where the system can be brought into resonance, it means that we should have $2\,t < \omega_{cav} = 6.73\text{GHz} \sim 25\mu\text{V}$.

This implies that we will need to perform quite detailed gate scan to resolve those features. To avoid losing too much time by performing very detailed maps of the whole stability diagram, it is usually relevant to first do a coarse mapping using a large bias voltage ($\sim 500\mu$V) which will broaden all transport signatures. This allows to identify areas fulfilling the first two conditions. Those can then be mapped more in details to identify areas fulfilling the last criterion.

As shown in Fig. 4.7, the cavity response shape allows to quite quickly identify resonant areas as they will display a sign change in the phase response. Furthermore, a qualitative difference in the shape of the response exists depending on the dephasing rates: at low dephasing rates one can resolve the two dips in the transmission matching the two conditions of resonance between the DQD transition and the cavity. The typical experimental signature one can expect is presented in Fig. 4.8.

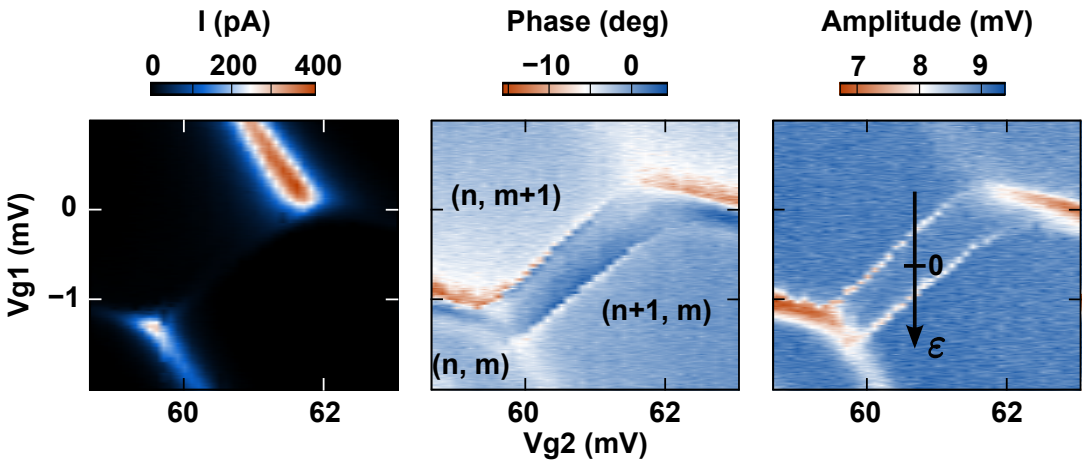

FIGURE 4.8: Spin qubit in the triple points area:
The current measurement, presented in the left panel, only shows the two triple points and one co-tunneling lines. The phase and amplitude response are on the other hand richer. We can see the other set of co-tunneling lines because of the finite charge susceptibility of the system in those areas and in between the triple points the response of the internal transitions. The fact that we resolve very well the two dips in the amplitude suggest a rather low dephasing. Please note that in the following ϵ will not denote the detuning measured as the distance to the degeneracy line but merely one gate voltage as indicated in the amplitude measurement. This does not change the interpretation of the results however. The sample conductance and cavity transmission are measured simultaneously.

In theory, one can calibrate the gate voltage action in term of energy, which would allow to determine the lowest frequency of the internal transition and give an estimate of the dephasing. In practice, this is very hard as the full calibration requires a regular cell of the honeycomb pattern and the possibility to observe the usual broadening of

the triple points into triangles when the bias voltage in increased [86]. However in our samples the disorder usually prevents one to observe a full cell of the honeycomb (this will be illustrated in section 4.4) and because we are interested in areas with a very low conductance the triangle measurement is usually challenging. One could think of performing the calibration in another area, however this does not work well as the properties of the DQD change between different areas.

This lack of calibration prevents a quantitative study of the system susceptibility. However even if such a calibration was possible, such measurements would not allow to discriminate between a simple charge qubit and our spin qubit as the expected response are, in the range of parameters explored here, quite similar. How to go further and unveil the spin-photon coupling is the topic of the next section.

4.3 Coherent spin-photon interface:

So far the data presented could perfectly have been obtained on a simple, rather coherent, charge qubit. To go further, we would like to prove that the state coupled to the cavity are actually hybrid spin-charge states. To do so we will first apply an external magnetic field. In order to preserve the cavity high finesse, the magnetic field will be applied in plane as indicated in Fig. 4.6. If our transition are spin-full, we should observe that they actually disperse not only with respect the gate voltage but also with respect to this field. This will actually allow us to fine tune our system in a sweet spot for the charge noise at which it is at resonance with the cavity. For those parameters, we will be close to the strong coupling regime, which will allow us to extract the spin-photon coupling strength and the coherence of our qubit. Finally, as the spectrum is strongly controlled by the behavior of the ferromagnetic contacts we will look for a signature of their impact in the hysteresis of the system.

4.3.1 Levels dispersion:

The usual way to map the dispersion of the energy levels of a qubit consists in performing a spectroscopy as described in section 3.3.4.1. However so far such measurements have never been very conclusive on this system, as discussed later. Here we will rely on the measurement of the cavity transmission versus the applied gate voltage and magnetic

field. As we have seen in Fig. 4.7, when a transition becomes resonant with the cavity it leads to an increase in the dissipation and hence a dip in the transmission which allows to identify the resonance condition location. We can hence map the dispersion of the transition at the frequency of the cavity in the magnetic field (B_{ext})-gate voltage (ϵ) plane. Such a map is presented in Fig. 4.9.

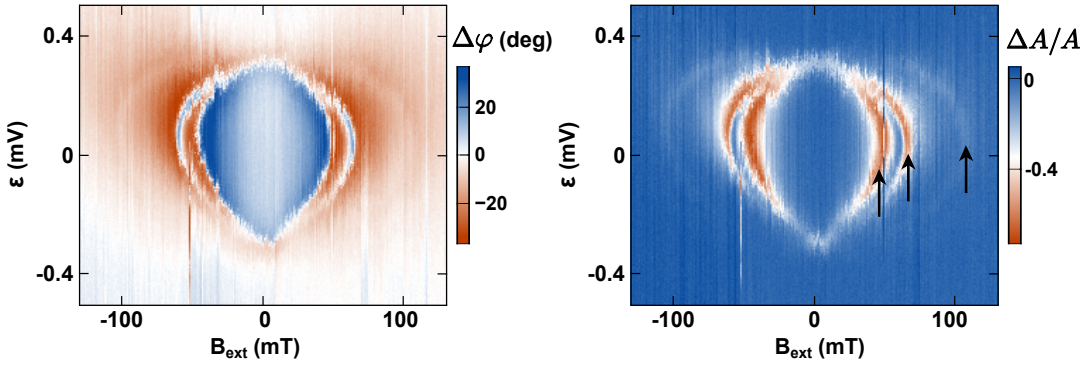

FIGURE 4.9: Spin qubit dispersion as a function of ϵ and B_{ext}:
The map of the cavity transmission displays three dips corresponding to three transitions brought into resonance with the cavity. Those three transitions disperse both with respect to the gate voltage and the magnetic field. In addition the phase contrast increases at finite field for the two main transitions, which can be related to an increase in the coupling or a reduce decoherence.

When a magnetic field is applied, the resonances, we observed at B = 0 T, split. We can identify three distinct transitions, that can be brought into resonance with the cavity as indicated by the black arrows in Fig. 4.9. The third one is much fainter which may indicate a weaker coupling or larger dephasing rate. All three transitions disperse both with respect to the gate voltage and the magnetic field, which suggest that they are related to mixed charge-spin transitions. Furthermore, for the two main transitions, the phase contrast increases at finite field which may be due to an increase in the coupling or decrease in the dephasing.

To conclude about the origin of the increased contrast at finite magnetic field, we will use a model similar to the one presented in section 4.1.2 to reproduce those results. We cannot use the exact same model because such a model can only reproduce one of the two main transitions. To actually have both transitions we need to take into account the valley degree of freedom of the CNT. We assume that there can be a small disorder induced valley mixing which we include in the usual way with a phenomenological parameter $\Delta_{KK'}$. We furthermore use different induced Zeeman splittings between the left and right dots (and between the valleys): $\delta_{L,K}$, $\delta_{L,K'}$, $\delta_{R,K}$, $\delta_{R,K'}$. We also introduce

a phenomenological orbital Lande factor α_{orb} and phenomenological electronic Lande factors $\alpha_{spin}^{L(R)}$, which are distinct in the left and right dots. The spectrum we obtain is similar to the one presented in Fig. 4.4, but each level is doubled, with a different dispersion in magnetic field for each level of the doublet. We will refer to the levels as $0, 0', 1, 1', 2, 2', 3, 3'$, following the notations of Fig. 4.4.

Another phenomenon, that we need to model, is the behavior of the ferromagnetic contacts in the applied magnetic field. At zero magnetic field the magnetization direction is controlled by magneto-strictive effects, at high magnetic field we expect the magnetization to align with the external field. No detailed experimental studies of the behavior of those thin magnetic stripes have been carried out describing how one goes from one situation to the other, so we have used phenomenological models. First we tried to model those electrodes as mono-domain easy-axis magnet obeying the Stoner-Wohlfarth equation which describes the switching of the magnetization of such magnets. However, we did not get a very good agreement between our data and the calculations. We then turned to an empirical exponential alignment law that gave better results. The typical field on which the magnetization align with the external field is noted B_0. The angle between the field direction and the magnetizations of the left and right electrodes at zero field are noted $\theta_{L(R)}^0$. We considered that the external field only affects the orientation of the induced Zeeman term but not its strength.

For each values of ϵ and B_{ext}, we have first numerically diagonalized the Hamiltonian to get the eigenenergies and eigenvectors. The eigenvectors are then used to compute the coupling to the cavity modeled as a modulation of the detuning between the left and right dot. The dephasing is deduced from the derivatives of the transition frequencies. To get reasonable result even on the sweet spots we compute both first and second order contribution of charge noise to dephasing and combine them by computing the square root of the sum of each term squared. This combination is an ansatz, which has the proper limit behavior and avoids to underestimate the charge noise contribution on a sweet spot. We also assumed a constant relaxation rate Γ_1. Having computed, the frequencies, couplings and dephasing rates we can deduce the cavity response. Because in our case, we found $\Delta_{K,K'}$ to be much smaller than the temperature, we considered the two lower states to be occupied. Using the following parameters, we reproduced quite accurately our experimental results as shown in Fig. 4.10.

ω_{cav} = 6735 MHz	t = 2380 MHz	$\delta_{L,K}$ = 3135 MHz
$\delta_{L,K'}$ = 3095 MHz	$\delta_{R,K}$ = 3145 MHz	$\delta_{R,K'}$ = 3100 MHz
$\alpha^L_{spin}\mu_B$ = 2700 MHz/T	$\alpha^L_{spin}\mu_B$ = 1300 MHz/T	$\alpha_{orb}\mu_B$ = 300 MHz/T
$\Delta_{K,K'}$ = 45 MHz	Γ_1 = 1 MHz	B_0 = 1.5 T
θ^0_L = -0.17 rad	$\theta^0_R = \theta^0_L + \pi/4$	

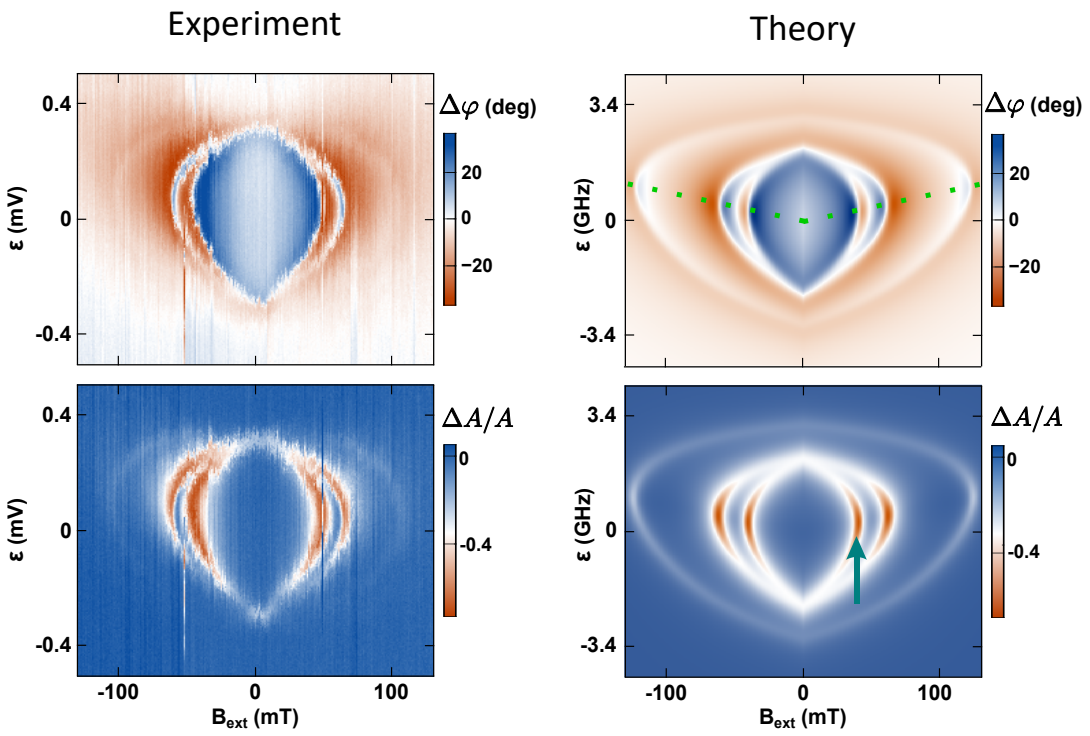

FIGURE 4.10: Spin qubit dispersion theoretical model: Diagonalizing the full Hamiltonian of our spin qubit, we can reproduce the data presented in Fig. 4.9. A weak asymetry between the contact induced Zeeman fields is required but this is not surprising. More surprising is the need for an effective Lande factors and a small intervalley coupling. The valley coupling can arise from disorder and given the fact that on a large scale our DQD spectrum is quite irregular we could have expected a larger inter-valley coupling. The Lande factor renormalization may be induced by the ferromagnetic contacts but we do not have enough control on the system to investigate this further.

The overall agreement we get is good for the two main transitions which corresponds to $0 \rightarrow 1$ and $0' \rightarrow 1'$, while the third one $0' \rightarrow 1$ is predicted at a slightly higher field than observed which we can impute to our model of the ferromagnetic electrodes. Looking at the dephasing rate, we can identify a sweet line for the charge noise as indicated by the green dots which explain the increase of the phase contrast in that area.

Finally, from the eigenvectors, we can identify the nature of the transition between levels i and j. To do so, we decompose the σ_y operator associated to the degree of freedom of

interest (the spin) on the four possible combination of the other two degree of freedom (charge and valley so LK, LK', RK, RK'). We then consider the following quantity:

$$C_{spin}^{ij} = \sum_{u \in \{LK, LK', RK, RK'} |\langle i|\sigma_y^u|j\rangle|^2 \tag{4.4}$$

This quantity is bounded between 0 (identical state) and 1(opposite state). We can use similar definitions for the charge and valley degree of freedom. Using this characterization, we find that the two main transitions are mainly valley conserving (30%), while having a neat spin flip component (75%) and a 50 % charge flip. The third transition is closer to a valley flip transition which may explain its larger dephasing as the valley degree of freedom is expected to be less coherent than the spin one.

Going to higher fields may allow to align the ferromagnetic contacts magnetization and recover a simple charge qubit whose characterization may allow to access the bare coupling and charge noise induced dephasing. However the magnetic field range for such measurements is limited by the degradation of the quality factor of the cavity in presence of the magnetic field. On the range chosen here, the quality factor is divided by 2 between zero field and the highest field, as illustrated in Fig. 4.16. At higher fields, the degradation is much faster which prevents such a characterization. On the practical side, the resonance frequency is also affected by the magnetic field and vary by about 10 MHz in such a measurement, as illustrated in Fig. 4.16. This is more than ten times the cavity linewidth, which means that the resonance frequency needs to be determined for each field and the probing tone frequency adjusted accordingly as otherwise we would quickly lose the signal. To avoid creating artifacts, this determination of the cavity frequency is carried out at large detuning such that the dot circuit does not affect the cavity. In the data presented above, we plot the difference between the measured signal and the amplitude and phase measured at resonance during this calibration measurement for each field.

We will now focus on the area in which the system appears to be the most coherent and in which we reach a phase contrast of more than 50°. Such a large phase contrast should be related to strong distortion of the cavity transmission, from which we may learn more directly about the dephasing rate and the coupling.

4.3.2 Approaching the strong coupling:

We now work at fixed $\epsilon = 50\mu$eV which is the value at which we get the largest phase contrast at finite field and measure the cavity transmission as function of the probe frequency and the applied external magnetic field. In Fig. 4.11, we present the raw measurement with an absolute frequency axis. The impact of the external magnetic field on the cavity resonance is quite striking and mask any information.

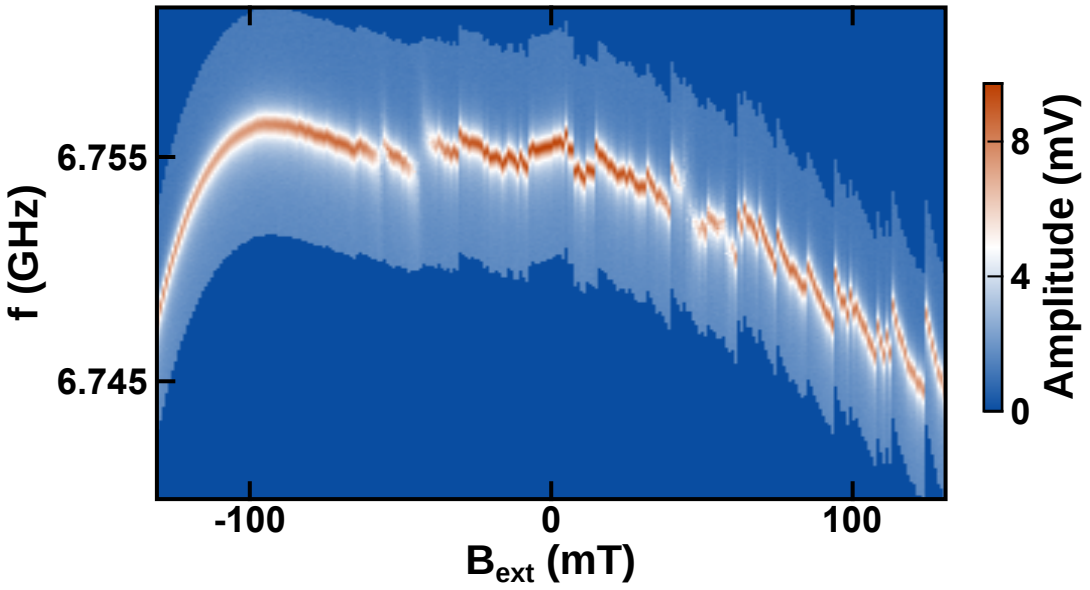

FIGURE 4.11: Cavity transmission vs B:
The frequency shift induced by the magnetic field on the cavity frequency are much larger than the cavity linewidth and prevent the direct observation of the impact of the coupling to the dot.

However, as we did for the B-Vg maps, we can determine the cavity resonance frequency at each field when the dot circuit is far detuned ($\epsilon \simeq 1$mV). We can then plot the same data but this time centering each column around the cavity resonance frequency. The result is presented in Fig. 4.12.

We observe four strong distortions of the cavity transmission which results from the hybridisation between the cavity and the dot circuit levels. Those correspond to the four main dips we identified in 4.9 and associated to two transitions symmetric in magnetic field. At first, those distortions look like anti-crossings. However looking at the cuts, we never resolve two peaks but we see a weak peak in the middle which is reminiscent of the situation presented in section 2.2.3.1 when one has a cooperativity larger than one but a dephasing of the atom stronger then the coupling. In this section, we discussed

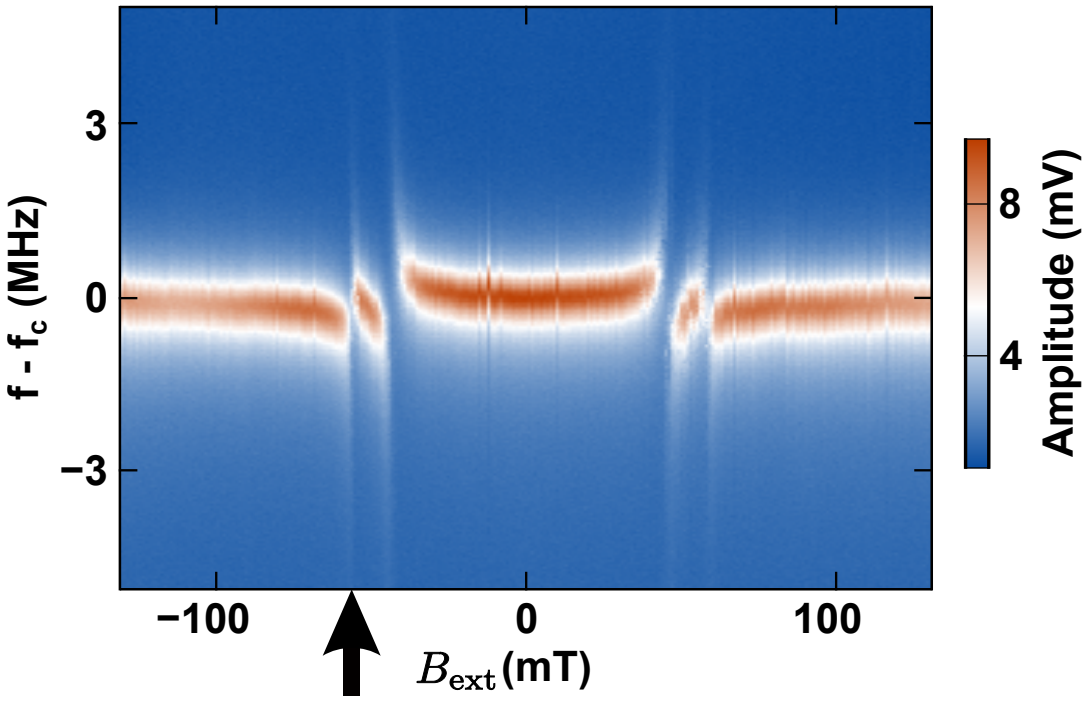

FIGURE 4.12: Cavity transmission vs B: re-centered:
The raw measurement of the cavity transmission did not allow to identify the signature of the interaction between the cavity and the spin qubit. Centering each cavity transmission trace around the cavity frequency measured when the qubit is detuned, we clearly observe two near-anticrossings for each of the two main transitions. We cannot talk here about anti-crossings as we do not resolve two peaks, however the cavity transmission is strongly distorted. The black arrow indicates the area on which the following analysis will focus.

how to model this regime very close to the strong coupling regime and we will now use those results to extract both our spin-photon coupling strength and the coherence of our qubit.

We will focus on the resonance at -67 mT, but the exact same treatment can be done on the other resonance. First, we can estimate the cooperativity C by comparing the transmission amplitude when the system is detuned and when it is tuned as $A_{detuned}/A_{tuned} = 1 + C$. To identify the field at which the dot circuit is perfectly tuned, we look at the cavity resonance frequency and search for the point at which it is not modified when tuning the system. Indeed, if the cavity frequency is unmodified, it means that the response of the dot circuit is purely imaginary which according to 2.83 can only occur when the detuning between the dot circuit and the cavity is zero. This simple comparison yields a cooperativity of about 2, which means that our interface is coherent.

To go further and extract separately the coupling and the dephasing rate, we can fit the transmission using the following formula derived in chapter 2:

$$S_{21} = \frac{\alpha}{i\,\Delta_{cd} - i\,\kappa/2 - \dfrac{g^2}{\Delta_{qd} - i\,\Gamma_2/2}} - i\sqrt{T}e^{-\zeta} \tag{4.5}$$

One can clearly see on Fig. 4.13 that the transmission is not symmetric but displays a Fano lineshape. The induced distortion is strong enough to prevent a simple Lorentzian fit, which is why we include the term $i\sqrt{T}e^{-\zeta}$. First, we can determine all the cavity parameters $(\alpha, \kappa, \omega_{cav}, T, \zeta)$ by fitting the transmission at large detuning. We are then left with three parameters for the dot circuit. In theory, they can all be extracted from a single fit, the broadening of the resonance, its shifting and the change in amplitude should be enough to determine the three unknowns. However, in practice the data are too noisy to make such a fit reliable. To circumvent that issue, we fitted multiple traces at different cavity-qubit detuning assuming a constant coupling and dephasing. This is an approximation as the coupling and dephasing depends on the applied field, but it allowed us to precisely pinpoint a trace with a detuning (14 kHz) much smaller than the dephasing (MHz range). We could then only focus on that trace and perform the fit with a zero detuning, as illustrated in Fig. 4.13. This procedure yields a coupling $g = 2\,\pi\,1.3$MHz and a dephasing rate of $\Gamma_2^* = 5$MHz. Importantly, this gives a cooperativity of 2.3 which agrees well with the comparison of the transmitted amplitudes.

.

As mentioned earlier, we cannot fit at the same time the transmitted amplitude and phase. This makes in particular the determination of the parasitic mode parameters (T, ζ) a bit uncertain. However, whereas the Fano line shape is important to obtain a quantitative fit of the resonances both tuned and detuned, letting T to zero does not give markedly different cooperativies and decoherence rates (in this case one has to correct for the background of the data)

A similar analysis, on the neighboring transition at – 43 mT, yields $C \simeq 3.3$. However this does not come from a weaker decoherence but rather a higher coupling.

Those results allow us to give a lower bound for the spin decoherence time in carbon nanotubes $T_2^* > 60$ ns ($T_2^* = 2/\Gamma_2^*$). This is already almost one order of magnitude larger

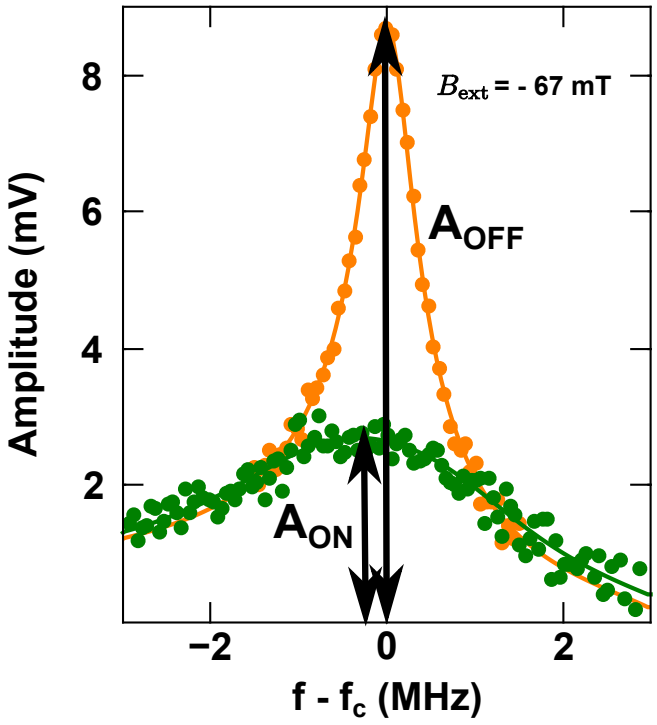

FIGURE 4.13: Cavity transmission fitting:
The orange curve corresponds to the cavity transmission when the qubit is far detuned, while the green one corresponds to the situation in which the qubit is tuned. By comparing the maximum transmission we can estimate the cooperativity of the system which reaches about 2 in this case. We can also go further and extract independently g and Γ_2 by fitting the curves as explained in the main text. The fits allows to disentangle the two quantities as they exploit the extra information encoded in the broadening of the cavity resonance.

than the previous measurements in CNTs based charge DQD [123], but we believe that it could be improved further by optimizing the spin-charge hybridization.

So far, we have not made a direct proof of the impact of the ferromagnetic contacts on the system, apart from the fact that according to previous experiments we cannot have such a low decoherence rate in a charge qubit. In the next section, we will address that question by studying the hysteretic behavior of our sample.

4.3.3 Hysteretic behavior:

The magnetization of ferromagnetic materials with an easy axis of magnetization usually presents a hysteretic behavior when subject to an external magnetic field. This comes from the competition between the anisotropy energy of the ferromagnets and the interaction with the external field:

- at high positive field the magnetization is aligned with the external field
- when the field is decreased, the magnetization rotates towards the easy axis.
- when the field change sign, the anisotropy energy and the interaction are now competing: the anisotropy prevents a rotation of the magnetization while the interaction favors a magnetization reversal.
- when the field overcomes the anisotropy the magnetization flips. This happens at $-H_C$

The reverse cycle leads to the same kind of behavior but with a reversal at $+H_C$.

In the case of our system, we have two such magnets however and we can expect to see two switchings. The expected behavior is depicted in Fig. 4.14.

Because our electrodes are not single-domain magnets, we cannot really model the energy of the ferromagnet as a simple double well function only of the angle between the magnetization and the easy-axis. The existence of multiple domains gives the system many more degree of freedom which leads in general to the existence of low energy paths allowing the reversal of a particular domain. The existence of those low energy paths can mask the existence of the hysteresis if the magnetic field is varied slowly, as thermal energy will be sufficient to allow the magnetization reversal before H_C is reached. In particular, we cannot observe the hysteresis on the large B-Vg maps because those were too long to acquire. We will hence only focus on line scan in the following.

The first signal, in which we can hope to observe a hysteretic signature, is the current flowing through the device. Indeed, the geometry of our device is close to a spin valve, which means that we should observe an increase in the sample resistance when the contacts magnetization are "anti-aligned". This results from the fact that we will inject mainly electrons with spin "up" while we can only receive electron with spin "down". As our electrodes are non-collinear, the effect will not be huge, as the spin filtering will never be perfect ("up" and "down" not being defined with respect to the same axis). Fig. 4.15 a) presents a measurement of the current flowing through the device on a triple point. We observe a decrease in the current for an external field of about 10 mT, which we can attribute to the switching of the first electrode, most likely the one whose magnetization

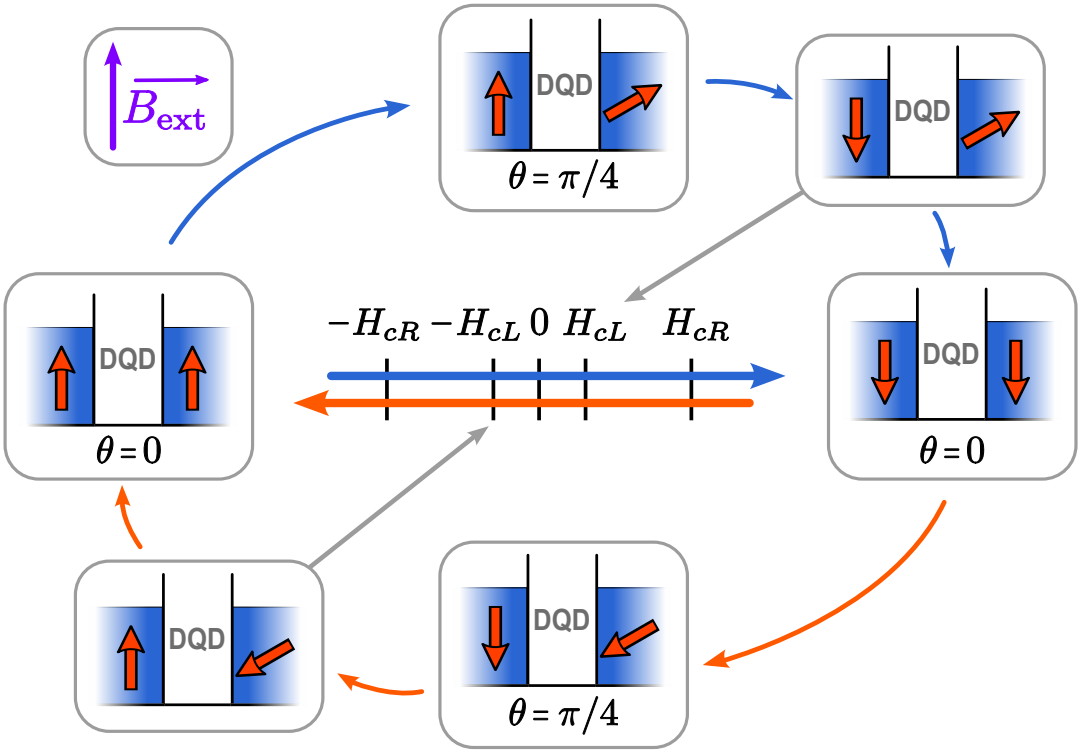

FIGURE 4.14: Hysteresis measurement principle:
Starting from a very strong negative magnetic field, the field is first reduced towards zero. At first both electrodes magnetizations are aligned with the magnetic field, as the field decreases both electrode magnetizations rotates towards the easy axis. Going to positive fields, at first the magnetization remains unchanged as the magnetization switching is protected by a high energy barrier. Then a first electrode switch. At a higher field the second switches too. The differences between the fields at which the switching occurs can be related either to the internal properties of the electrode or the misalignement of one electrode with respect to the field. Going the other way round, the switching will now occur at negative fields. This lack of symmetry gives rise to the hysteretic signal.

is aligned with external field. There is no second jump but rather a smooth recovery and at high field we get the same decreasing behavior[1]

Knowing that the ferromagnetic contacts do impact the system through a current measurement is interesting, but a stronger indication would come from a direct hysteresis of the cavity signal that we could related to the spin qubit spectrum. Fig. 4.15 b) presents a measurement very similar to the one presented in a but on the transmitted phase. As for all other measurements carried out on the cavity signal the probe tone is adjusted at

[1]This decreasing behavior is not understood but may be related to magneto-Coulomb effect [124]. This effect can convert a magnetic field change in a gate voltage change, and could detune the system from the initial working point. The existence of magneto-Coulomb in the device does not however void our previous results as alone it cannot explain the increased coherence of the device.

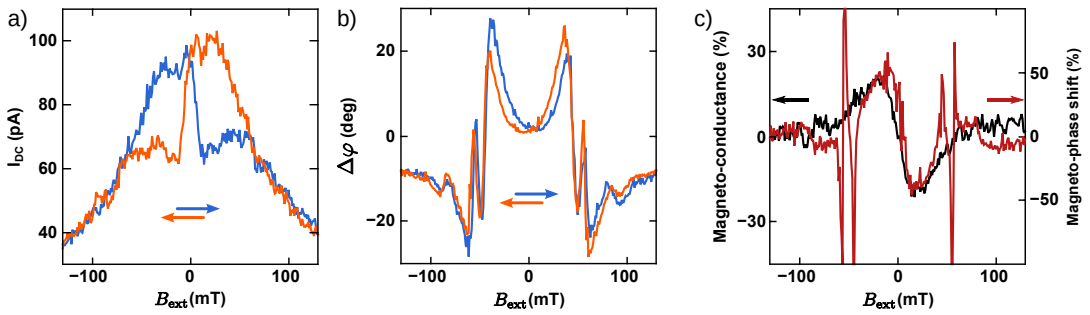

FIGURE 4.15: Current and phase hysteresis:

a) Current hysteresis measured on a triple point, the blue(orange) curve corresponds to increasing(decreasing) magnetic field. One can clearly see a sharp reduction of the conductance around zero field followed by a plateau and then a slow decrease. This sharp switching can be associated to the switching of one electrode magnetization. No second switching can be clearly identified but it may due to the fact that one electrode is not aligned with the field. Finally the slow decrease may be due to magneto-Coulomb effect as discussed in the footnote.

b) Phase shift hysteresis measured in the area studied so far, around $\epsilon = 0$. The phase shift is as before measured with respect to a reference acquired at resonance for each field. Here too we observe a clear hysteresis in the signal.

c) Magneto-current $\Delta_M\sigma$ and magneto-phase $\Delta_M\phi$ as defined in the main text. Both responses evolves on the same scale of magnetic field, which strongly suggests that they are governed by the same underlying mechanisms.

each field to match the cavity frequency. We observe also in this signal a net hysteretic component.

In order to compare more easily those two responses, we plot in Fig 4.15 c) the magneto-conductance $\Delta_M\sigma$ and the magneto-phase shift $\Delta_M\phi$ defined as follows:

$$\Delta_M\sigma = \frac{I_{forward} - I_{backward}}{I_{forward} + I_{backward}} \qquad \Delta_M\phi = \frac{\Delta\phi_{forward} - \Delta\phi_{backward}}{|\Delta\phi_{forward}| + |\Delta\phi_{backward}|} \tag{4.6}$$

The absolute values in the definitions of $\Delta_M\phi$ are required as contrary to the current the phase shift takes both signs.

Up to the absolute scale both signals are very similar: the s shape characteristic of a magneto-conductance measurement appears in both on the same characteristic magnetic field. The sharp peaks appearing in the magneto-phase shift simply marks the position of the resonance between the cavity and the spin qubit levels, which is why they do not

appear in the current. Overall, the combination of those two measurements appears to show that the spectrum is genuinely affected by the ferromagnets.

There is however one thing that needs to be checked here before concluding. We have seen that the cavity is affected by the external magnetic field and phenomena such as vortex trapping can induce hysteretic behavior in superconductors subject to a magnetic field. We must hence check that the signature in the cavity hysteresis cannot explain the hysteresis in the phase signal we observed. Fig. 4.16 presents the cavity frequency, linewidth and phase slope as measured during the acquisition of the magneto-phase shift data but at a point at which the qubit is far detuned. Along the raw data, the equivalent magnetic dependence of each quantity is also plotted.

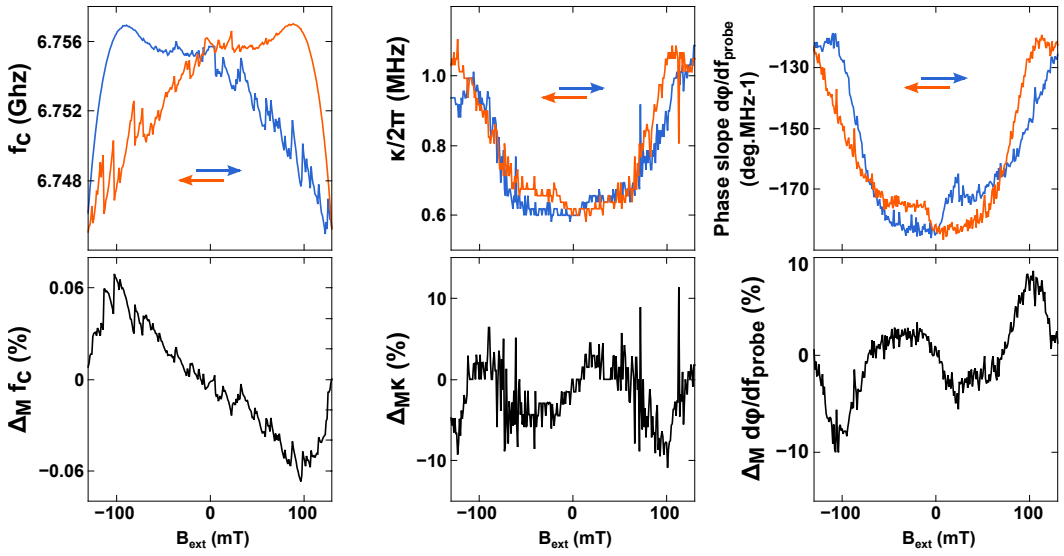

FIGURE 4.16: Cavity hysteresis:
The cavity also displays an hysteretic behavior, which may find its origin in vortices trapped in the superconductor. To evidence it, we plot the magneto-frequency $\Delta_M f_c$, magneto-linewidth $\Delta_M \kappa$ and magneto-phase slope $\Delta_M \frac{d\phi}{df_{probe}}$. The slope of the phase versus the probe frequency around the resonance, whose hysteresis could explain the previous observations, is hysteretic but much less that the phase shift and cannot explain alone the observed signal that hence does encode an hysteresis in the spin-qubit susceptibility.

We do observe that the cavity presents an hysteretic behavior. However looking at the magneto phase slope, the hysteresis in the signal barely reaches 10 % while the signal observed for phase shift signal on the spin qubit is more than 50 %. As a consequence the hysteresis of the cavity cannot explain the observed hysteresis in the behavior of

the spin qubit, and our previous conclusion holds: the ferromagnetic contacts genuinely influence the system spectrum.

In this section we have focused on the demonstration of the coherence of our spin interface and validated its basic principle. The cooperativity and decoherence rates achieved place our system at the strong coupling threshold. Owing to the general principle used here, this method could be applied to many host materials for spin quantum bits. However, we are far from having explored in details the possibility of our devices.

4.4 Impact of the occupation parity:

So far our model has focused on a single electron picture, but the total number of electrons in our structure is unknown. Changing the parity of the total number of electrons in the dots should drastically change the spectrum by moving from a single electron picture to a singlet-triplet like system. We investigate in details these features in this section.

In order to study the impact of the occupation parity on the system spectrum , we performed cavity transmission measurements with respect to the external applied magnetic field and the gate voltage similarly to what was done in 4.3.1. We cannot know the number of electrons, however we know that by moving from one set of triple points to the next the parity of this number changes. In the following sections, we will present measurements performed on four adjacent areas along the axis set by one of the gate and another area along the other gate axis. The four areas are presented in Fig. 4.17. The previously studied area is not shown here. On a larger map it would appear as the second area on the right hand side of area 1.

In the following, we will refer to odd and even areas. This denomination comes from the fact that our single electron model can describe the so-called odd area.

4.4.1 Odd areas:

The dispersion maps associated with area 1 and 3, identified as odds by comparison to the model, are presented in Fig. 4.18.

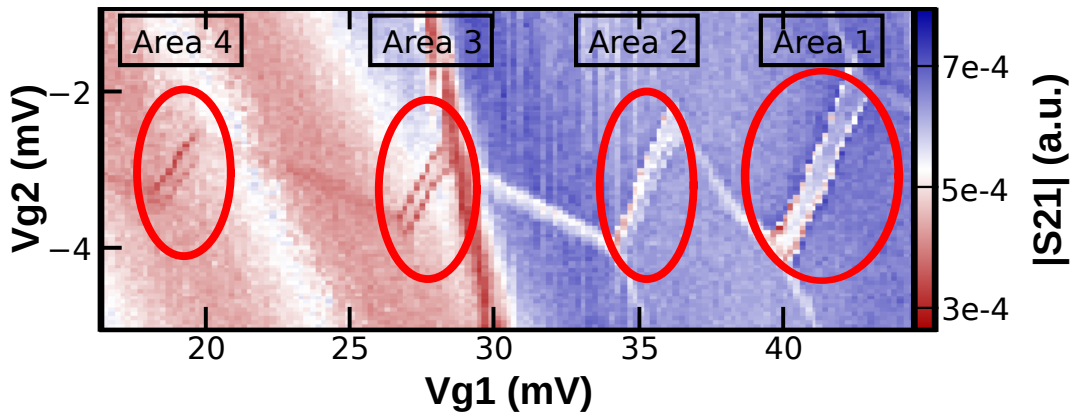

FIGURE 4.17: Gate-gate map of the cavity transmission in the area of the parity study:
The four areas indicated are the four main area in which the impact of the parity was studied. Area 1 and 3 will be identified as odd area and 2 and 4 as even area.

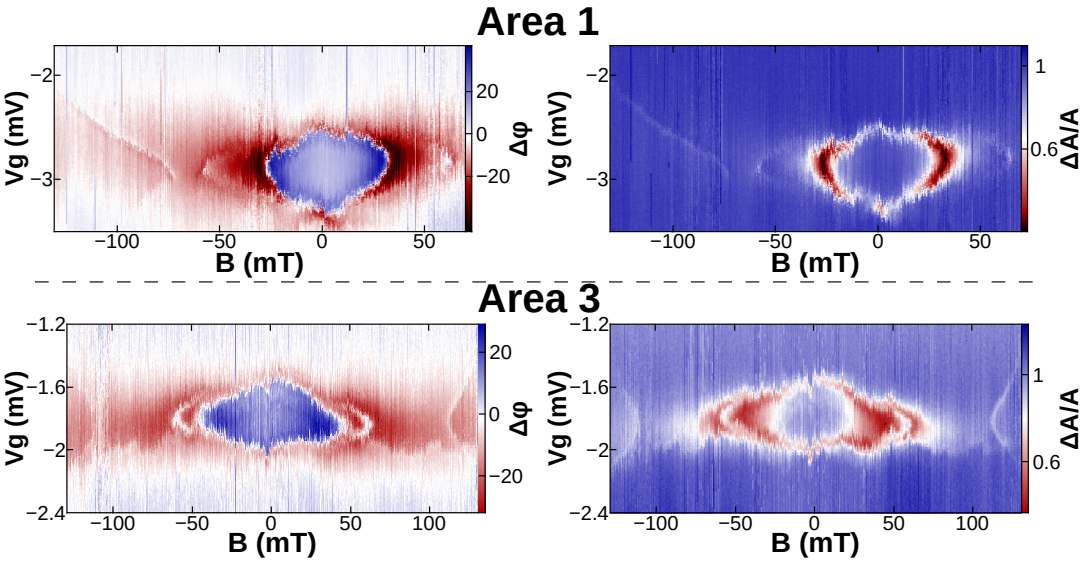

FIGURE 4.18: Parity study: odd areas

Area 1 This area is very similar to the area discussed in the previous section except that we do not resolve the transitions from the two valleys and that we see an additional transition with an unexpected dispersion: it requires a higher detuning to be resonant at higher field as opposed to all the other observed transitions.

Area 3 This area is similar to the previous one but with a different asymmetry with respect to $\epsilon = 0$, which can be attributed to a reversed asymmetry in the Zeeman terms between the two dots.

Those areas remain quite similar to the data described above and a change in the asymmetry of the model parameters can explain the inverted dependence in ϵ. However, one

feature that remain unexplained is the line found at higher field whose dispersion is unexpected as it requires a higher detuning to be resonant at higher field, which means that the two levels are moving closer together when the field increases. This is unexpected and may be related to a change in the interface with the ferromagnetic contacts.

The fifth area that has not been presented in Fig. 4.17, has a quite different dispersion which is presented along simulations in Fig. 4.19. The stability diagram deformations could be misleading about the parity but the simulation and the map of a neighboring area quite similar to area 4 suggest that is indeed an odd area.

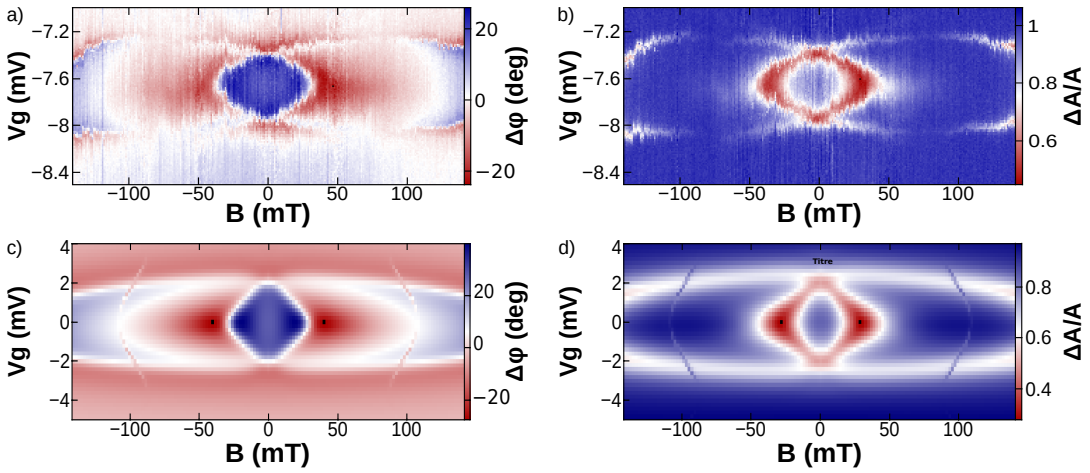

FIGURE 4.19: Parity study: fifth area
This third odd area displays a very different dispersion with respect to the external filed and the gate voltage. We can explain it using our single electron model by introducing an orbital Lande factor about 30 times larger than the one used to fit the previous data. This change is quite surprising and once again would require a more detailed investigation.

The parameters used to reproduce the experimental data are given below. The most striking change is the very strong increase in the orbital Lande factor.

ω_{cav} = 6735 MHz	t = 2590 MHz	$\delta_{L,K}$ = 2900 MHz
$\delta_{L,K'}$ = 3040 MHz	$\delta_{R,K}$ = 2900 MHz	$\delta_{R,K'}$ = 3040 MHz
$\alpha^L_{spin}\mu_B$ = 1500 MHz/T	$\alpha^L_{spin}\mu_B$ = 1500 MHz/T	$\alpha_{orb}\mu_B$ = 10000 MHz/T
$\Delta_{K,K'}$ = 150 MHz	Γ_1 = 1 MHz	B_0 = 1.5 T
θ^0_L = -0.17 rad	$\theta^0_R = \theta^0_L + \pi/4$	

This is not understood and would require a more detailed and careful analysis than this sample actually allowed.

4.4.2 Even areas:

While the features of two of the three odd areas are quite close to the previously presented results, the maps of the even areas, shown in Fig. 4.20, look completely different.

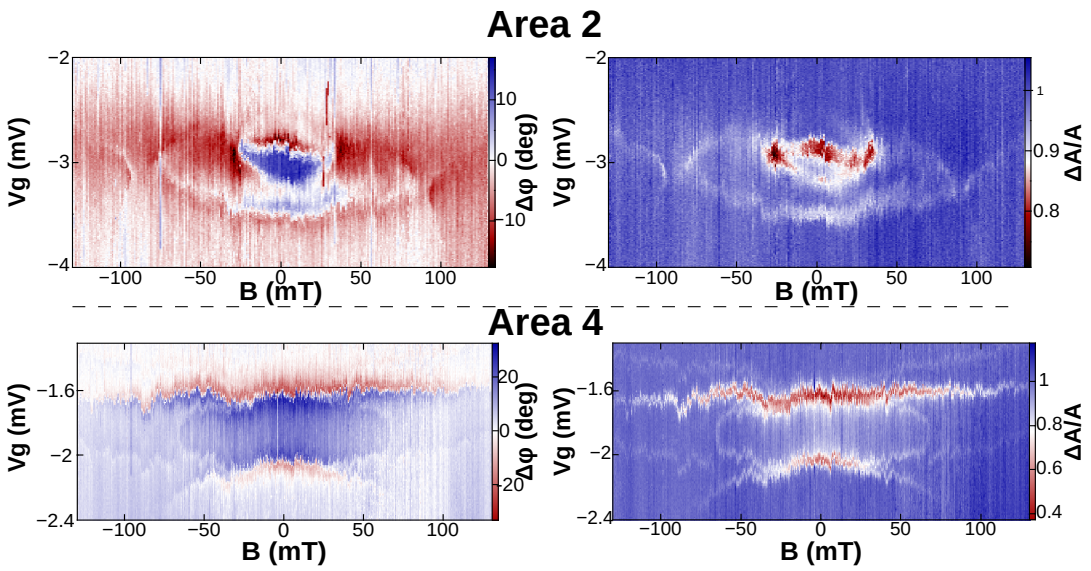

FIGURE 4.20: Parity study: even areas

Area 2 This area presents a very distinct and surprising feature: three visible dips in the transmitted amplitude signaling three resonant level at zero field. The phase signal does not change sign in between the two main crossings, showing that the level crossing in the middle has a very small susceptibility outside of the resonance condition.

Area 4 This area display many more levels than seen usually with very different dispersion with respect to the magnetic field, with two transition that disperse very little, two transitions for which the resonance condition is associated to increasing detuning and one which requires decreasing detuning similarly to what we observed in the odd regime.

This spectrum is very rich and our models did not manage to reproduce those data.

The first thing, one can notice about area 2, is the presence of three visible dips in the transmission at zero magnetic field. If there is indeed no masked fourth dip and that each dip corresponds to one level at resonance, it is a striking signature of an even number of electron as in the odd case it is impossible for a transition to cross a single time the cavity frequency. Area 4 has no such clear signature of its even nature but present a large number of transitions with dispersion unlike the ones presents in the odd case such as line either not dispersing in magnetic field or requiring a larger detuning to be resonant when the field is increased rather than a smaller one. Once again, this reminds us of some properties of a singlet triplet spectrum in which the singlet and the

triplet of spin -1 get closer in energy when the field in increased or the singlet and the triplet of spin 0 which do not disperse in magnetic field. Finally, one can notice that those areas are not as coherent or as coupled as the odd areas presented in section 4.3.

To model this system we need to consider many more levels than in the one electron picture, because, contrary to the usual case in which the spin is the only degree of freedom to consider to build the singlet, here we have both the spin and valley which yields six singlet state for the situation in which one dot is doubly occupied. The total number of state is then 22. This does not only make the computation more cumbersome but also make the spectrum more complex to explore and even more sensitive than before to small changes in the parameters.

This model was actually derived and studied but never yielded results which matched the experimental data as well as the ones for the single electron case. The reason for this remains unclear. However the fact that all parameters appear to be able to change quite a lot between two neighboring areas, associated to the fact that we do not have a separate determination of the model parameters, is de facto one of the main issue when trying to model those data.

The parity study then remains an open topic and would benefit from improvement in the setups, such as the possibility to perform a microwave spectroscopy that would give more constraints about the level dispersion.

4.5 Perspectives:

The system presented in this chapter is very rich and the present work has only begun to explore its possibilities. So far we have demonstrated an hybrid coupling to the spin that is five orders of magnitude larger than the natural magnetic coupling and a dephasing rate much lower than what one would expect in a charge qubit. We have also shown that the parity of the number of electrons in the device strongly affects its spectrum.

One interesting comparison point missing so far is a comparison between the bare properties of the charge qubit and the properties of our spin qubit. In particular, a direct comparison of the coupling and dephasing in both cases would allow to say for sure whether or not this scheme suppress more efficiently charge noise than it reduces the

coupling to the cavity. From our previous experiments and from the literature, in such systems, the coupling can range from 20 to 50 MHz while the dephasing can go from 450 MHz to 3 GHz, which does not really allow us to conclude.

In the next sections, I will discuss some key improvements which may be beneficial to the study of this system.

4.5.1 Microwave spectroscopy:

In the lab, microwave spectroscopy of our devices remains a challenge. At first, the sample holder and the sample geometry were suspected to be the main issue. As exposed in chapter 3, we are now using a multilayer PCB which allows to enclose the sample is a small box and eliminate all parasitic modes below 9 GHz, however at the time at which the experiments presented here were carried out, this PCB did not exist yet and numerous mode existed as low as 4 GHz. In addition, because of the geometry of the sample, the DC wire bonds had to cross above the cavity as illustrated in Fig. 4.21, which made them likely to couple to 3D modes. As the coupling of the device transition to microwave light is very sensitive to the field geometry, the 3D modes, whose geometry is not controlled, are likely to couple to the device in different fashions. This may blur the spectroscopy.

To resolve the issue caused by the long wire bonds, the geometry presented in Fig. 4.22, in which the dot is on the same side of the cavity as the DC contacts, was designed. However, this design suffered a slightly Fano transmission, even in the sample holder in which the box modes were absent. The origin of the parasitic mode was understood only later when we started to use HFSS to design our samples. As illustrated in Fig. 4.22, the sample support a slotline mode on the whole distance between the bonding pads. This mode can be expected to have a low quality factor and as it sits at only 500 MHz above the cpw mode it can contribute the parasitic transmission involved in the Fano. Given the geometry of the CPW it is not easy to add bonds in the middle of the cavity where they would most efficiently suppress this parasitic mode.

As a consequence no sample was ever measured in a truly optimal situation. However numerous attempts have been made to perform a spectroscopy: attempting to tune the excitation power, trying to work close to resonance with the cavity in an area in which

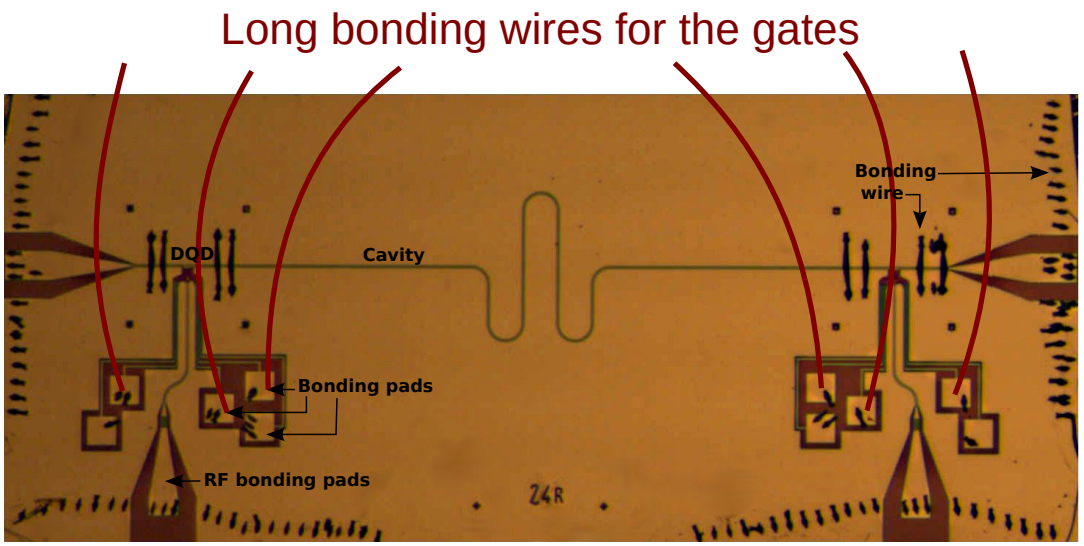

FIGURE 4.21: Spin-qubit sample bonding:
The geometry of the sample discussed in this section required to proceed to long bonding to connect the DC gates. Those long wires could have easily coupled to box modes which may not be coupled to the device in the same way as the cavity and drive different transitions.

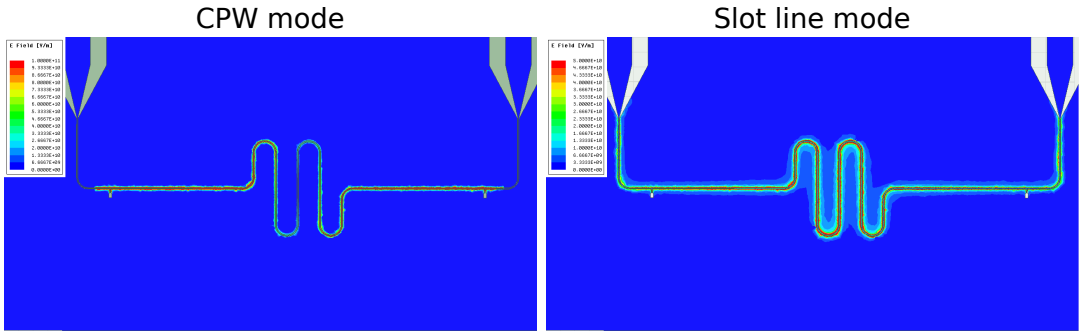

FIGURE 4.22: Spin-qubit U-shaped cavity design:
In this design, the DC bonding pads that have been removed for the simulation are all on the same side (opposite to the cavity bonding pads and allow for short DC bonds. The CPW mode is found at 6.52 GHz, while the slot line mode is found at 7 GHz. The slot line mode field is weaker (the color scales start at 0 for both and stop at 10^{11} V/m and $5\,10^{10}$ V/m for the CPW mode and slot line mode respectively.

the frequency of the qubit is more or less known, etc. None gave any result worth discussing here and this in turn prevented a time domain study of the system which may have a provided a more direct measurement of the coherence time of the spin in our device.

Currently this experiment is in pause, waiting for more improvement in the fabrication process that should make it more reliable as so far the number of good sample is rather low compared to the number of sample fabricated. But when restarting it, the first step

will be to re-design a cavity in which the parasitic modes are less problematic while allowing to have the DC bonding pads close by the pads on the PCB.

4.5.2 Increasing the coupling, reducing the noise:

One key development from which this experiment could benefit is the optimization of the coupling of the dot transition to the cavity field. HFSS simulations could prove instrumental in improving the design. We have done some simulations in that direction. We simulated two designs: one very similar to the one of the experiment we carried out and another in which the ground plane was prolonged and finally used to screen the dot from the field radiated by the gate. The simulation corresponding to both geometries are presented in Fig. 4.24.

One can notice in Fig. 4.24 c that the potential reached is higher in the shielded case but also stronger in the area of the second gate starting from the right. However its value around the two left most gates is nearly unchanged. This means that, if the dots are properly localized towards the most distant gates, shielding can increase the coupling to the charge. By comparing the peak values of the computed potential, it appears that we can expect a 75% increase compared to the unshielded case.

Of course reducing the charge noise impact on the device would also be a key improvement. Adding on-chip microwave filters on the DC lines, similar to what was done in [57], would probably be one of the first possible improvements. Another one would be to find a way to reduce the charging energy of the device similarly to what was done in [59]. In this experiment, the two dots are connected in a symmetric fashion to the cavity which provides a large capacitance between the two dots and strongly reduces the charging energy. The coupling is achieved through a modulation of the tunnel coupling between the dots, engineered by the use of a superconducting contact between the two dots. The electrode pattern used there is not directly applicable as it leads to a symmetric coupling. So we would need either to find another way to decrease the device charging energy, following in a sense the path leading from the CPB to the transmon qubit, or use the same coupling scheme and add a superconducting contact to our geometry.

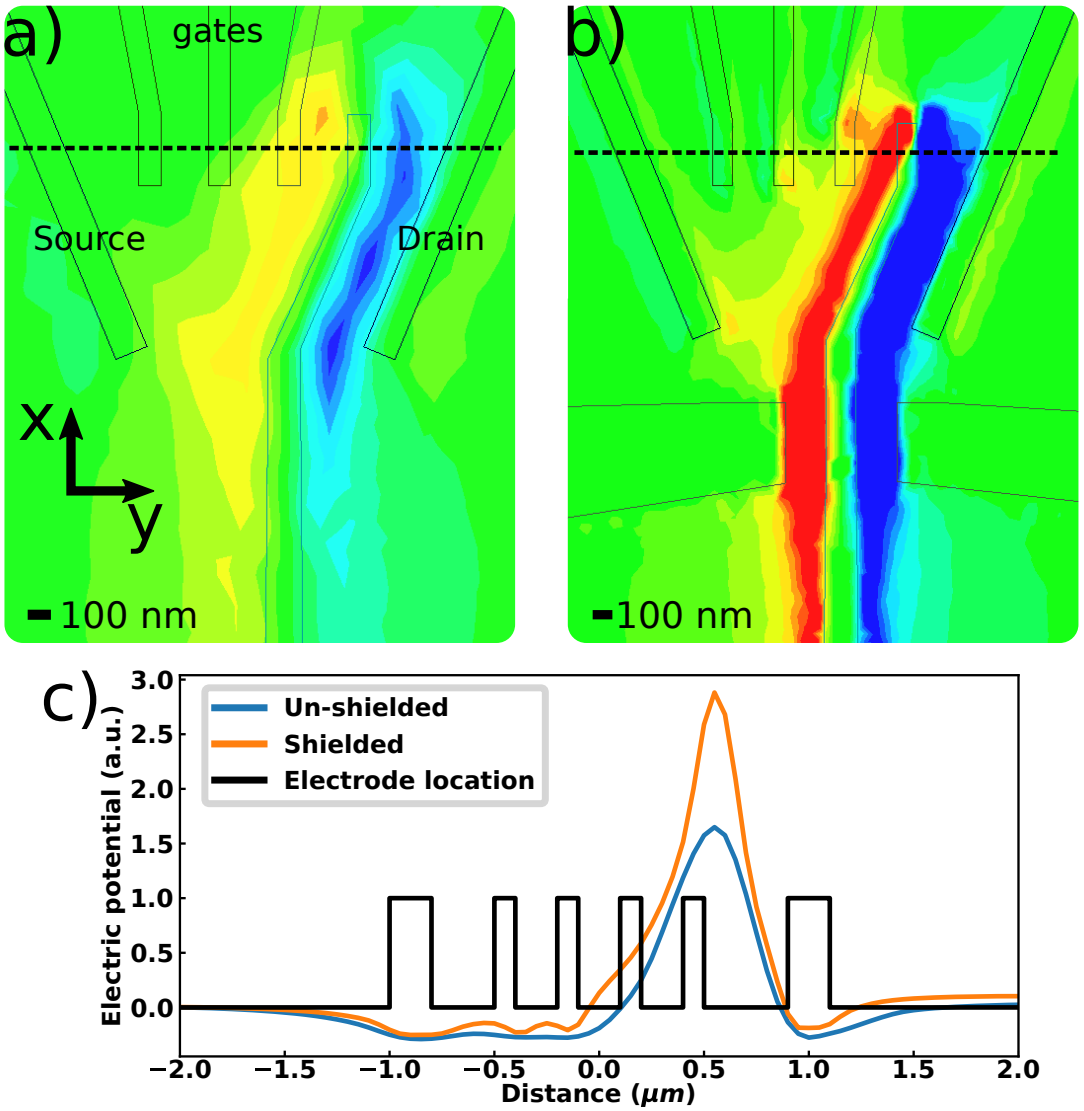

FIGURE 4.23: Impact of shielding on a DQD:

a), b) We plot the field along the y direction with the same color scale in both cases a) unshielded b) shielded. In the shielded case, the field appears to be stronger.

c) By integrating the computed field, we compute the electrical potential along the dashed line. The blue line correspond to figure a and the orange one to figure b. The black line indicates the position of the gates and contacts.

4.5.3 Ultra-clean nanotubes:

One strongly limiting factor in that experiment is the limited control we have on the CNTs spectrum which is dominated by disorder. The use of suspended CNTs transferred at the very end of the process and hence not exposed to any chemical process may prove to be instrumental in getting a more detailed understanding of our system. Such devices

have been made in other groups and displayed a remarkable tunability [122, 125]. In particular if we could, as is done in other quantum dot architectures, control the tunnel rate using electrostatic potentials we may be able to control the induced Zeeman splitting using an electric knob.

This perspective is very attractive and the development of this kind of CNT transfer is actively pursued in the lab. With that application in mind, during my thesis, I participated in trying to optimize the growth recipe to get a directional growth as presented in chapter 3. Furthermore, as this kind of transfer of the CNT on the metallic electrodes require very clean electrode surfaces, we designed a vacuum transfer chamber, shown in Fig 4.24, that may allow in the, hopefully, near future to work with ultra-clean carbon nanotubes.

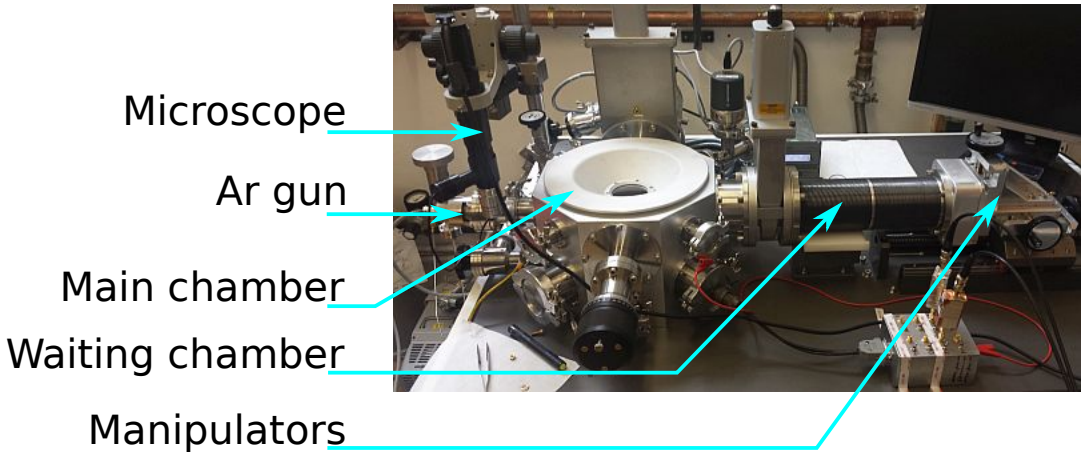

FIGURE 4.24: Ultra-clean CNTs transfer chamber:
The transfer chamber consists of a main chamber in which the sample holder with the chip on which to transfer the CNT can be mounted and electrically connected. A Ar ion canon which can be used to remove adsorbed materials from the contacts and hence improve their transparency. A waiting chamber allows to isolate the CNTs during the plasma cleaning and a manipulation arm can be used to position the forks on which the CNTs are grown. At the tip of this arm, Attocube positioning modules can be used for the last part of the transfer procedure.

Chapter 5

Probing single dot dynamics using a transmon qubit

The previous chapter focused on a usual theme of quantum information processing: the realization and characterization of a qubit. In this chapter, the goal will be notably different since we will attempt to use quantum information processing techniques, namely a qubit, to probe a condensed matter model system.

This idea is not new in the context of mesoscopic circuits. However previous experiments focused on using a resonant circuit [126, 127] or equivalently a cavity [23] to access the internal dynamics of mesoscopic circuits. In other cases, a Josephson junction was also used as a quantum detector [128, 129]. Here, we propose something different and, closer in its spirit, to magnetometry using an NV center as already explained in chapter 1. The central idea here will be to couple a single quantum dot, that will play the role of model system under study, to a superconducting qubit, that will play the role of probe. In the following we will focus on the case of a transmon qubit coupled to the SD via a microwave cavity, but it is not the only coupling one can envision. This setup presents also the interest to add a very delicate photon probe to a system in which previously the accurate determination of the photon number in the cavity, while crucial, could not be performed. As hinted in chapter 1, it could also be used to probe the photon field statistic, which may be influenced by the dot. The first section will focus on the theoretical description of the system and try to give some ideas about what we can expect. The second one will be dedicated to the experimental side on which so far the results are slim, mainly due to fabrication issues.

5.1 Theoretical description:

By combining, a single dot, a transmon qubit and a microwave cavity we obtain a system which is potentially very rich. We cannot hope to treat all regimes here, so we will focus on the simple case in which the cavity is not externally driven, the SD is not voltage biased and only the dot chemical potential is modulated. In such a situation, the SD will act as a source of electric noise for the transmon. One natural approximation would be to treat the transmon qubit as a two-level system. However, as discussed in chapter 2, the transmon qubit is not a real two-level system but an anharmonic oscillator. Furthermore, we know that in the Coulomb blockade regime, which will be the easier

regime to describe for the SD, the SD occupation will fluctuate on a time-scale given by Γ, the coupling to the leads. The spectral distribution of this noise will also be of width Γ as shown in chapter 2. We can expect the transmon to be most sensitive when the SD fluctuations will be close to its fundamental frequency so $\Gamma \sim \omega_t$. Consequently, since the transmon anharmonicity $\alpha \ll \omega_t$, the SD is likely to excite many levels of the transmon which means that we cannot treat it as a simple two level system, but as a full anharmonic oscillator.

We will be interested in two main impacts of the dot on the transmon:

- the possible change in frequency of the transmon induced by the dot.
- the impact of the dot on the lifetime of the transmon

To treat this problem, we will start by deriving an effective Hamiltonian for the SD and the transmon by eliminating the cavity. This will make the dot-transmon interaction appear as an instantaneous interaction while it is not. This may yield incorrect results in certain cases. In particular, we will not discuss the transmon dephasing but focus only on the relaxation. The basic idea behind this restriction is that cavity photons induces a frequency shift of the transmon and that the phase accumulated by the transmon will depend on the interaction time.

Next to gain some insight about what may happen for reasonable values of the parameters, we will treat the transmon as a two level system and the dot in the sequential regime. Finally, we will use a more general approach to overcome some of the limitations of the sequential tunneling treatment.

5.1.1 System effective Hamiltonian:

We start from the following very general Hamiltonian :

$$\begin{aligned}\hat{H} =&\hat{H}_{cavity} + \hat{H}_{transmon} + \hat{H}_{dot} + \hat{H}_{contacts} + \hat{H}_{tunnel} + \hat{H}_{bath} + \\ &\hat{H}_{cavity<->bath} + \hat{H}_{cavity<->transmon} + \hat{H}_{cavity<->dot}\end{aligned} \tag{5.1}$$

with :

$$\hat{H}_{cavity} = \hbar\,\omega_{cav}\hat{a}^\dagger\,\hat{a} \tag{5.2}$$

$$\hat{H}_{transmon} = \hbar\,\omega_t\,\hat{q}^\dagger\hat{q} - \hbar\,\frac{\alpha}{12}(\hat{q}^\dagger + \hat{q})^4 \tag{5.3}$$

$$\hat{H}_{dot} = \epsilon\,\hat{n} + \frac{U}{2}\,\hat{n}\,(\hat{n}-1) \tag{5.4}$$

$$\hat{H}_{contacts} = \sum_{a=L,R}\sum_{k,\sigma}\xi_{k,\sigma}\hat{c}^\dagger_{a,k,\sigma}\hat{c}_{a,k,\sigma} \tag{5.5}$$

$$\hat{H}_{tunnel} = \sum_{a=L,R}\sum_{k,v,\sigma}\left(t_a\,\hat{c}_{a,k,\sigma}\hat{d}^\dagger_{v,\sigma} + h.c.\right) \tag{5.6}$$

$$\hat{H}_{bath} = \sum_{\mu}\hbar\omega_\mu\hat{b}^\dagger_\mu\hat{b}_\mu \tag{5.7}$$

$$\hat{H}_{cavity<->bath} = \hbar\sum_{\mu}\left(g_\mu\,\hat{b}_\mu + g^*_\mu\,\hat{b}^\dagger_\mu\right)\left(\hat{a}+\hat{a}^\dagger\right) \tag{5.8}$$

$$\hat{H}_{cavity<->transmon} = 2\,i\,\beta\,e\,V_0\,\left(\hat{q}^\dagger - \hat{q}\right)\left(\hat{a}^\dagger + \hat{a}\right) \tag{5.9}$$

$$\hat{H}_{cavity<->dot} = \hbar\,g_{dot}\,\hat{n}\,\left(\hat{a}+\hat{a}^\dagger\right) \tag{5.10}$$

with $\hbar\,\omega_t = \sqrt{8\,E_J\,E_C}$ and $\alpha = E_C$.

We consider the transmon as an anharmonic oscillator in the large E_J/E_C limit. We keep the most generic possible form for the dot Hamiltonian considering spin and valley of degree of freedom. The total number n of electrons in teh dot is defined as $\sum_{v,\sigma} d^\dagger_{v,\sigma}d_{v,\sigma}$. We do not consider the coupling of the photons to the contacts, which is dominated by gate coupling with most recent mQED designs. We use the following notations :

- the anharmonicity of the transmon is α, such that $\omega_{01} - \omega_{02}/2 = \alpha/2$
- the energy of the k^{th} level is :
  $E_k = \hbar\omega_k = cst + \hbar\,k\,(\omega_t - \frac{\alpha}{2}\,(k+1))$
- the transition frequency between the first two levels ω_{01} is given by :
  $\hbar\,\omega_{01} = \omega_t - \alpha(k+1)$.
- the coupling between the cavity and the first two levels is given by :
  $g_{tra} = g_{01} = \frac{e\,V_0}{\hbar}\,\beta\,\sqrt{\frac{\omega_t}{4\,\alpha}}$ and the coupling between levels k and k+1 is given by
  $g_{k->k+1} = \sqrt{k+1}\,g_{tra}$

In order to derive an effective Hamiltonian from which direct interactions with the cavity have been removed, we will use a Schrieffer-Wolff transformation (or adiabatic

elimination) as done in chapter 2 and project H in the subspace empty of photons. This seems reasonable at first as we consider an undriven cavity, but we should keep in mind that if the dot is close to the qubit frequency it will also be close to the cavity one and may emit photons in the cavity that could lead to small corrections. The detailed derivation of the effective Hamiltonian is presented in appendix B. The final result is:

$$\begin{aligned}\hat{H} = &\left(\epsilon - \frac{U}{2}\right)\hat{n} + \left(\frac{U}{2} - \hbar\frac{g_{dot}^2}{\omega_{cav}}\right)\hat{n}^2 \\ &+ \sum_j \hbar\left(\omega_j + g_{tra}^2 \frac{-j/2}{\Delta + \alpha\,(j-1)}\right)|j\rangle\langle j| \\ &+ \hbar\, g_{tra}\, g_{dot}\, n \sum_j \sqrt{j+1}\left(\frac{1}{\Delta + \alpha\, j} + \frac{1}{\omega_{cav}}\right)\hat{\tau}_{y,j}^1 \\ &+ \sum_{a=L,R}\sum_{k,\sigma} \xi_{k,\sigma}\hat{c}_{a,k,\sigma}^\dagger \hat{c}_{a,k,\sigma} + \sum_{a=L,R}\sum_{k,v,\sigma}\left(t_a\,\hat{c}_{a,k,\sigma}\hat{d}_{v,\sigma}^\dagger + h.c.\right) \\ &+ \sum_\mu \hbar\omega_\mu \hat{b}_\mu^\dagger \hat{b}_\mu + \sum_\mu g_\mu\,(\hat{b}_\mu + \hat{b}_\mu^\dagger)\left(\sum_j g_{tra}\,\frac{\sqrt{j+1}}{\Delta + \alpha\, j}\hat{\tau}_{y,j}^1\right)\end{aligned} \tag{5.11}$$

5.1.2 Dot induced static frequency shift:

The first impact of the dot, we can evaluate, is the shift induced on the transmon frequency per electron in the dot. When tuning the SD in the middle of Coulomb valley, we expect the number of electron on the dot to be completely frozen. In such a case we can consider n to be a constant, and the transmon to be in its ground state. The transmon part of the Hamiltonian can be reduced to :

$$\hat{H}_{tra} = \hbar\left(\omega_0 + \frac{g_{cav}^2}{\Delta}\right)|0\rangle\langle 0| + \hbar\left(\omega_1 + \frac{2\,g_{cav}^2}{\Delta + \alpha}\right)|1\rangle\langle 1| + i\,\hbar\frac{g_{tra}\,g_{dot}\,\hat{n}}{\Delta}\left(|1\rangle\langle 0| - |0\rangle\langle 1|\right) \tag{5.12}$$

$$= \hbar\frac{\tilde{\omega}_{01}}{2}\hat{\sigma}_z + \frac{g_{tra}\,g_{dot}\,n}{\Delta}\hat{\sigma}_y \tag{5.13}$$

$$= \hbar\,\frac{\tilde{\omega}_{01}}{2}\left(1 + \frac{4\,g_{transmon}^2\,g_{dot}^2}{\tilde{\omega_{01}}^2\,\Delta^2}\,\hat{n}^2\right)\tilde{\sigma}_z \tag{5.14}$$

For the reasonable values, $g_{dot} = 50MHz$, $g_{transmon} = 300MHz$, $\Delta = 1GHz$, $\omega_q = 6.5GHz$, we get a shift for a single excess electron :

$$\frac{2\, g_{transmon}^2\, g_{dot}^2}{\tilde{\omega}_{01}\, \Delta^2} \simeq 40kHz \tag{5.15}$$

For a good qubit we can hope to see it for n large enough directly in the spectroscopy. But we should also see it in the Ramsey fringes which should give a better resolution.

Such a measurement may seem quite trivial but may actually answer some quite deep questions about charge screening in quantum dot circuits. Indeed, we expect the deep electrons of the dot to be less sensitive to the electric field of the cavity than the ones occupying the last available orbitals. Hence the number n that enter the coupling to the cavity may be the number of electrons on this orbital. However this is far from obvious and if one could measure the shift per electron on a large number of consecutive Coulomb valleys, it may teach us more about how charge screening works in such structures.

5.1.3 Sequential tunneling approach:

In this section, we will use a rather naive approach. We will treat the tunneling to second order, like we did in chapter 2. This description is limited to the sequential tunneling regime $\Gamma \ll k_B\, T$ and as a consequence is rarely valid in practice. Furthermore to make the calculations lighter, we will approximate the transmon as a perfect two level system. Once again this is likely to give quantitatively incorrect results, but it is a good way to get some first intuitions.

We will only consider two different dot occupations (and write $\tilde{\epsilon_d}$ the energy of the occupied state), we however keep track of the total number of electron for the dot-qubit coupling term (n_0). By restraining the dot to only two possible occupations, we need to introduce a new d operator allowing to go from the occupied to the empty state. We could account for level degeneracy at a later stage by multiplying the electronic transitions rate by the degeneracy of the target level.

The Hamiltonian we consider is hence the following, in which we have kept only the leading order in the coupling and considered the re-normalized transmon frequency $\tilde{\omega}_q$

and dot energy $\tilde{\epsilon}_d$:

$$\hat{H} = \underbrace{\frac{\hbar\,\tilde{\omega}_q}{2}\,\hat{\tau}_z + \tilde{\epsilon_d}\,\hat{n} + \hbar\,\frac{g_t\,g_{dot}}{\Delta}\hat{\tau}_y\,(\hat{n}+n_0) + H_{bath} + H_{leads}}_{\text{free evolution}}$$
$$\underbrace{+\,H_{tunnel} + \frac{\hbar\,g_{transmon}}{\Delta}\sum_{\mu}\left(g_\mu\,b_\mu + g_\mu^*\,b_\mu^\dagger\right)\,\hat{\tau}_y}_{V} \tag{5.16}$$

We can derive a master equation for this system like we did in chapter 2 (both for the sequential tunneling regime and for the cavity photons). We assume as previously the bathes to be Markovian bathes and perfectly uncorrelated. As this derivation is very similar to the ones presented in chapter 2, it is not detailed here. The final result for the evolution of the density matrix of the system is:

$$\begin{aligned}\frac{d\rho}{dt} =& -\frac{i}{\hbar}\left[\frac{\hbar\,\tilde{\omega}_q}{2}\,\hat{\tau}_z + \tilde{\epsilon_d}\,\hat{n} + \hbar\,\frac{g_t\,g_{dot}}{\Delta}\hat{\tau}_y\,(\hat{n}+n_0), \rho\right] \\ &- \frac{g_t^2\,\kappa}{2\,\Delta^2}\,(\hat{\tau}_+\,\hat{\tau}_-\,\rho + \rho\,\hat{\tau}_+\,\hat{\tau}_- - 2\,\hat{\tau}_-\,\rho\,\hat{\tau}_+) \\ &+ \Gamma\,f(+\tilde{\epsilon}_d)\left(\hat{d}^\dagger\,\rho\,\hat{d} - \frac{1}{2}\hat{d}\,\hat{d}^\dagger\,\rho - \frac{1}{2}\rho\,\hat{d}\,\hat{d}^\dagger\right) + \Gamma\,f(-\tilde{\epsilon}_d)\left(\hat{d}\,\rho\,\hat{d}^\dagger - \frac{1}{2}\hat{d}^\dagger\,\hat{d}\,\rho - \frac{1}{2}\rho\,\hat{d}^\dagger\,\hat{d}\right)\end{aligned} \tag{5.17}$$

with as previously $\Gamma = \sum_{a\in\{S,D\}}\Gamma_a = \sum_{a\in\{S,D\}}\frac{2\,\pi\,\nu}{\hbar^2}|t_a|^2$, κ the cavity linewidth.

From this, we can derive the system of equations describing the system evolution. This system has analytic solutions, but those are impractical as the system does not have special symmetry. As there is no time dependence in the system we can solve the problem numerically by a simple matrix exponentiation.

In the next subsection, we will present numerical results on the impact of the coupling of the dot and the tunnel coupling to the leads on the relaxation of the transmon. We will work in the degenerate case at $\tilde{\epsilon}_d = 0$. All the results will be plotted as a function of 2Γ. The qubit and cavity parameters are set to :

$$\tilde{\omega}_q = 2\,\pi\,6.5\text{GHz} \qquad \kappa = 2\,\pi\,1\text{MHz}$$
$$g_t = 2\,\pi\,300\text{MHz} \qquad \Delta = 2\,\pi\,1\text{GHz}$$

5.1.3.1 Population evolution :

We study the evolution of the population in the exited qubit state. For each set of parameters we fit the evolution to an exponential decay and extract the relaxation time (T_1), the residual population at equilibrium, and the deviation from exponential behavior (measured as the χ^2 of the fit, i.e. the quadratic distance between the fitted data and the fit). Fig. 5.1 displays the results for T_1 and the residual population. The data for χ^2 are not displayed as it always smaller than 4.10^{-5}, which means that the decay is purely exponential.

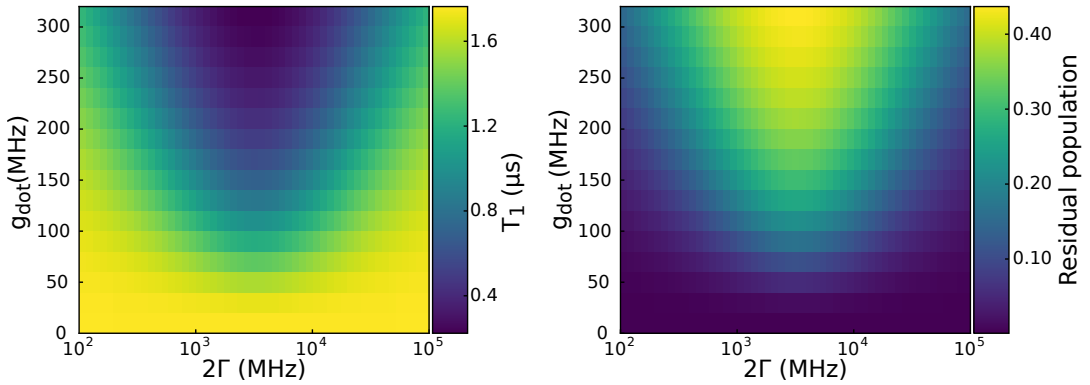

FIGURE 5.1: Transmon relaxation and equilibrium exited population:
The left plot displays the relaxation time of the transmon qubit as a function of the coupling of the dot to the cavity and the tunneling rates. The dot appears to have a measurable effect as soon as the coupling is larger than 50 MHz when $2\,\Gamma$ matches the transmon frequency. The right plot displays the population found in the exited state at the end of the decay. We can notice that, as the relaxation time gets shorter, it grows larger (up to 0.4). If such a large population can build up in the exited state, the other levels of the transmon are likely to start playing a role, which will motivate a more detailed treatment in the following section.
Note: The tunneling rate axis is logarithmic but the image is not distorted to reflect it. As a consequence, inside a decade, all samples have the same size which make their spacing incorrect.

In Fig.5.1, for accessible couplings and if the Gamma's are close enough to the qubit frequency, we observe a reduction of T_1 by a factor of 2 or more in some cases. In the same parameters area, we see a residual population. This residual population could be probed directly in the cavity transmission, as it should appear as a second transmission peak shifted by the dispersive shift. For the largest coupling, the residual population reaches 40%, which, if we take into account the large bandwidth nature of the dot, should actually populate higher levels of the transmon.

These first results appear encouraging, but they should be treated with caution. As the electronic temperature is around 2 GHz, most of them have actually been obtained outside the strict regime of validity of the sequential tunneling treatment ($\Gamma < k_B\,T$). This means that we have assumed that the electronic reservoirs are actually destroying electronic correlations much faster than they can and this can impact our results. Furthermore, as mentioned in section 5.1.3.1, higher levels of the transmon are likely to play a role and should be considered.

We will try to address both concerns in the next section in which we will treat the dot as a environment for the qubit. This will require some additional hypothesis on the interaction between those two systems but relax all constraints on the dot properties and in particular could allow us to treat the Kondo regime.

5.1.4 Single dot as an effective bath:

To overcome the validity issue of the sequential tunneling treatment used in the previous section, we will now ignore the details of the dot dynamics and treat the dot occupation as a random variable and use a master equation treatment to derive the qubit dynamics.

The detailed derivation of the master equation for the transmon is presented in appendix C. The final result is the following:

$$\begin{aligned}\frac{d}{dt}\tilde{\rho}(t) = &+\sum_j g_{tra}^2\,\frac{j+1}{(\Delta+\alpha\,j)^2}\kappa D(\tau_{-,j})\tilde{\rho}\\ &-\sum_j \tilde{g}_j^2\Bigg(i\,\frac{\bar{n}^2}{\omega_j}\left[\tilde{\tau}^1_{+,j}\tilde{\tau}^1_{-,l}-\tilde{\tau}^1_{-,j}\tilde{\tau}^1_{+,j},\tilde{\rho}\right]\\ &\qquad -S_{nn}(\omega_j)D(\hat{\tau}^1_{-,j})-S_{nn}(-\omega_j)D(\hat{\tau}^1_{+,j})\\ &\qquad +\frac{i}{2\,\pi}\Bigg(\mathcal{P}\left(\frac{1}{\eta\,\omega_j-\omega}\right)\int S_{nn}(\omega)d\omega\left[\hat{\tau}^1_{+,j}\hat{\tau}^1_{-,j},\rho\right]-\\ &\qquad\quad \mathcal{P}\left(\frac{1}{\eta\,\omega_j+\omega}\right)\int S_{nn}(\omega)d\omega\left[\hat{\tau}^1_{-,j}\hat{\tau}^1_{+,j},\rho\right]\Bigg)\end{aligned}$$

where $\tau_{+,j}=|j+1\rangle\langle j|$ and $\tau_{-,j}=|j\rangle\langle j+1|$. The dot contribution has been split between the contribution of the average value $\bar{n}$ and the contributions of the noise spectral density

$S_{nn}(\omega) = \int_{-\infty}^{\infty} dt e^{i\,\omega\,t} \langle (\hat{n}(t) - \bar{n})(\hat{n}(0) - \bar{n}) \rangle$. D is the super-operator associated with a collapse operator in the Linblad form $D(\hat{\tau})\,\rho = \hat{\tau}\tilde{\rho}\hat{\tau}^{\dagger} - \frac{1}{2}\left(\tilde{\rho}\hat{\tau}^{\dagger}\hat{\tau} + \hat{\tau}^{\dagger}\hat{\tau}\tilde{\rho}\right)$ and $\mathcal{P}\left(\frac{1}{\omega}\right)$ is the Cauchy principal value.

The expression we obtain is reminiscent of the one derived in [103] for the population evolution of a two-level system. The bath of the system induces transitions towards the excited states with a rate depending on the negative part of the spectral density, which corresponds to emission noise, while it absorbs energy at a rate given by the spectral density at positive frequency.

Furthermore, we see that in addition to the frequency re-normalization related to the static dot population, we have a second contribution coming from the spectral density. Using the fluctuation-dissipation theorem we can relate the spectral density to the imaginary part of the susceptibility as mentioned in chapter 2. In the high temperature regime, S_{nn} is simply proportional to $Im(\chi)$, which means, given the link between the real and imaginary part of χ stemming from the Kramers-Kronig relations[1], that the frequency re-normalization is linked to the real part of the susceptibility.

One key interest of this method is that it is not limited to the Coulomb blockade regime but can be applied to any regime in which we can compute the spectral density. It could for example be used in the Kondo regime in which the spectral density can be computed using re-normalization group techniques.

In chapter 2, we explicitly derived $S_{nn}(\omega)$ (cf equation (2.100)) in the case of the Coulomb blockade regime in the absence of interaction. We will now use this result to get the transmon evolution. As we are interested in finite temperature effects which will be responsible for populating the transmon states, we will adopt an all numerical scheme. First we will evaluate the spectral density at the transmon frequencies and compute the Cauchy principal values at the same frequency. Then, as we have once again a time-independent evolution, we will compute the evolution of the system through the exponentiation of the matrix of the linear set of equations.

In the following studies we will use the following set of parameters :

$$\omega_{01} = 2\,\pi\,6.5GHz \qquad \alpha = 2\,\pi\,300MHz \qquad g_{tra} = 2\,\pi\,300MHz$$
$$\omega_{cav} = 2\,\pi\,7500GHz \qquad g_{dot} = 2\,\pi\,150MHz \qquad k_B\,T = 2\,\pi\,2GHz(100mK)$$

[1] $Re(\chi)(\omega) = \frac{1}{\pi}\mathcal{P}\int_{-\infty}^{\infty} \frac{Im(\chi)(\omega')}{\omega' - \omega} d\omega'$ and $Im(\chi)(\omega) = \frac{1}{\pi}\mathcal{P}\int_{-\infty}^{\infty} \frac{Re(\chi)(\omega')}{\omega' - \omega} d\omega'$

Those parameters corresponds to reasonable values for the transmon and a rather good coupling of the dot to the cavity.

As previously, all the quantities discussed in the three following sections are extracted by fitting the simulation results to usual functions (exponential decay for the relaxation, decaying cosine for the ramsey fringes). In all cases the fit quality is excellent (as measured by χ^2) and will not be discussed in greater details.

5.1.4.1 Transmon levels:

One of the surprising prediction of the sequential model is the large residual population that the dot could create as shown by the predictions for T_1. If that prediction was to be trusted, we should expect to see multiple levels of the transmon populated. As a consequence, the first study we can conduct is the required number of transmon levels to consider to describe the system accurately. To do so we first compute the tunnel rate leading to the largest response at $\tilde{\omega}_{01}$ and then compute the transmon dynamics in a T_1 measurement experiment for different number of levels considered in the transmon.

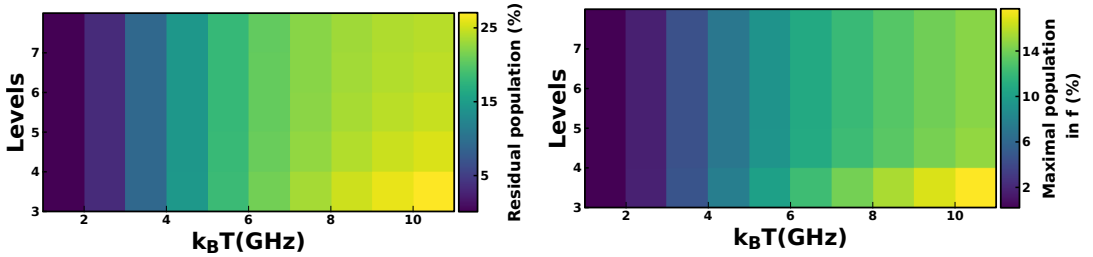

FIGURE 5.2: Transmon levels study:
When treating the transmon as an anharmonic oscillator we need to truncate the Hilbert space to get a finite dimension system to solve. In order to determine the proper truncation, we plot the residual population in the first exited state of the transmon (left) and the maximal population in the second exited state (right) during a T_1 measurement. The dot is tuned to have the maximal impact on the transmon. Both quantities are plotted as a function of the number of levels considered in the transmon and of the electronic temperature. For temperature smaller than 200 mK (4 GHz), the number of levels we consider does not appear to matter, as shown by the uniform result function of the number of levels.

In Fig. 5.2, we plot the residual population in the first exited state and the maximal population in the second one during a T_1 measurement as a function of the temperature and of the number of levels we consider in the transmon. Both quantities show that as long as the electronic temperature remains smaller than the transmon first transition

frequency, the higher levels of the transmon do not play a role in the dynamic. Based on those results we will consider only three levels in all the following as we will focus on $k_B T = 2$ GHz which is a reasonable value for our electronic temperature.

Looking back, this discrepancy between the two models is not as surprising as it may seem. The sequential tunneling approximation relies on the fact that the temperature of the fermionic baths is high enough to destroy all correlation between tunneling events. As a consequence the "noise temperature" will be impacted by this hypothesis and can be higher than the temperature set for the leads, which explain the high temperature experienced by the transmon when we use the sequential tunneling approximation outside of its range of validity.

5.1.4.2 Transmon relaxation:

In the sequential tunneling approximation, we have studied the transmon relaxation as a function of the tunneling rate and the coupling of the dot to the cavity. Here, we will focus on the tunneling rate and the dot level detuning. We will hence look at the transmon dynamics on the whole Coulomb peak and not only at the exact center of of it as before. We chose to proceed in this way because, outside of its strict regime of validity, the sequential tunneling underestimates the width of the Coulomb peak, while the current approach is correct, in the absence of interactions, for all tunnel rates. Fig. 5.3 displays the result obtained for $\Gamma \sim \omega_{01}$. The detuning is expressed in unit of Γ as the Coulomb peak width is related to Γ at large Gamma's.

The overall shape of the plot for the transmon lifetime and the population remaining in the excited state appears rather similar. In both cases, the impact of the dot is maximal for $\Gamma \simeq \tilde{\omega}_{01}$ and decreases away from $\tilde{\epsilon}_d = 0$. However in practice, the relaxation time is likely to prove a more reliable quantity as the residual population is always quite small (max $\sim 2.5\%$) and would be challenging to measure accurately. This residual population is much smaller than in the sequential tunneling approach which is more in phase with the electronic temperature (2 GHz) being small compared to the transmon frequency (6.5 GHz)

As we go to larger tunnel rate the impact of the dot decreases as illustrated in Fig. 5.4 in which the transmon relaxation time is plotted as a function of Γ at $\tilde{\epsilon}_d = 0$.

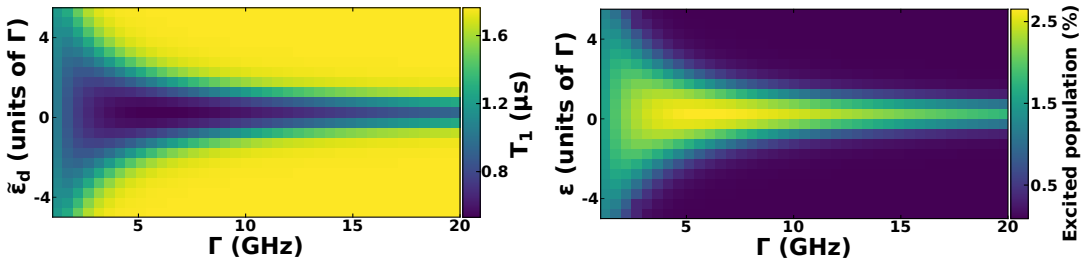

FIGURE 5.3: Transmon relaxation:
The left plot displays the relaxation time of the transmon qubit as a function of the detuning $\tilde{\epsilon}_d$ of the dot level with respect to the leads Fermi seas and the tunneling rate, the right plot the population in the first exited state at the end of the measure. The dot appears to have a stronger effect close to $\tilde{\epsilon}_d = 0$ and for $\Gamma \simeq \omega_{01}$. The residual population follows the same dependence as the relaxation time. In addition, it is much smaller than in the sequential tunneling approach which is more in phase with the electronic temperature (2 GHz) being small compared to the transmon frequency (6.5 GHz).

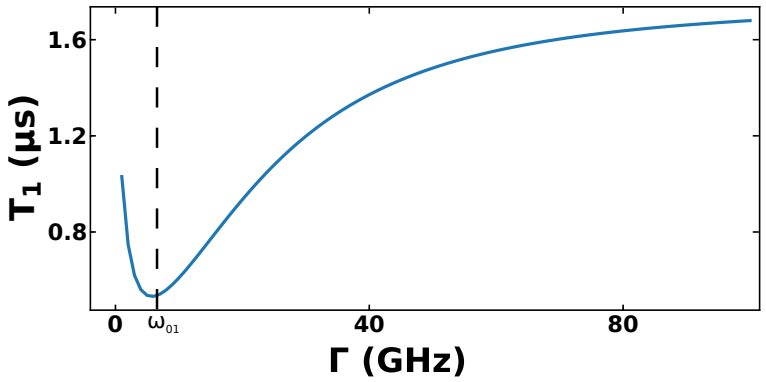

FIGURE 5.4: Transmon relaxation at $\tilde{\epsilon}_d = 0$:
Here we study the dependence of the relaxation time of the tunneling rate when the dot is at resonance ($\tilde{\epsilon}_d = 0$). Given the simulation parameters, the Purcell limited lifetime is 1.76 μs, which means that up to 50-60 GHz the lifetime is reduced by more than 100 ns. Such reduction of the lifetime should be detectable since we should be able to access the Purcell limit at large $\tilde{\epsilon}_d$.

This plot exhibits the strong impact of the dot around $\Gamma = \tilde{\omega}_{01}$ and allows us to estimate that for such parameters we could hope to study situations in which $\Gamma < 50$ GHz. This agrees with the sequential tunneling results as far as the relaxation time is concerned.

5.1.4.3 Kondo regime:

As mentioned earlier, one of the advantage of this approach is that it can also be used to treat other regime such as the Kondo regime. Through a collaboration with professor Mahn-Soo Choi, we compute the charge spectral density of a dot in the Kondo regime

at zero temperature, using numerical renormalization group techniques (NRG). Using those results, we deduced the transmon dynamics, for the same dot cavity coupling and transmon properties as before. Some preliminary results concerning the transmon lifetime are presented in Fig. 5.5.

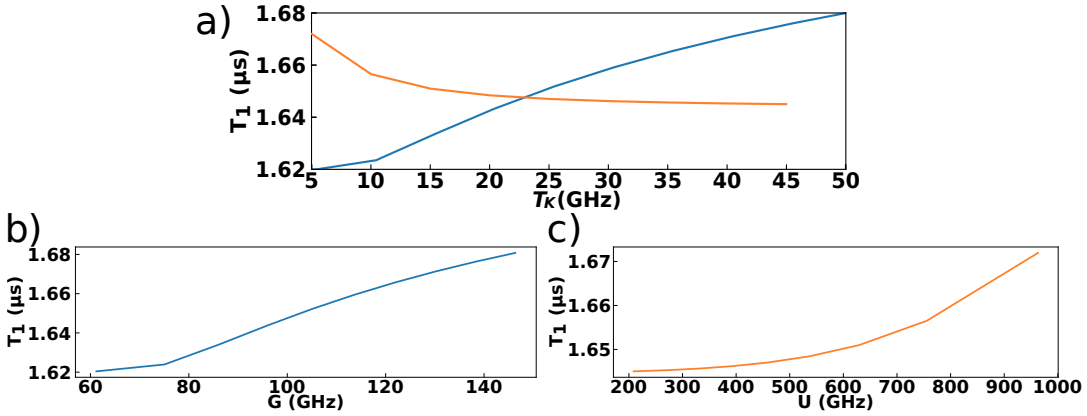

FIGURE 5.5: Lifetime in the presence of a Kondo dot:

a) Lifetime of the transmon as a function of the Kondo temperature. The blue curve corresponds to U = 500 GHz and a variable Γ , the orange one to a fixed Γ (100 GHz) and variable charging energy U.

b) Same plot than in figure a but in function of Γ

c) Same plot than in figure a but in function of U

The transmon parameters are the same as before which means that the expected lifetime is 1.76 μs. Hence the first interesting result is that we can expect to see a response from the system. This in itself is non-trivial since one expects the charge dynamics to be frozen in the Kondo regime , as discussed in 2.2.4 [23]. Furthermore, we studied two sets of parameters (fixing either U (blue curve) or Γ (orange curve)) which leads to the same Kondo temperature, and unexpectedly we find different responses for the same Kondo temperature. Usually in the Kondo problem the Kondo temperature is the only relevant energy scale, which it does not appear to be the case here. This is surprising and will investigated in more details, however one should note that for the parameters used we are not deep in the Kondo regime as we do not have $\Gamma \ll U$.

Those results should be considered with great care since the NRG results may not be quantitative at this early stage of the work. However they suggest that Kondo regime may be very interesting to probe using such techniques.

So far we have only looked at the most basic properties of this hybrid system. We focused on the equilibrium case which already proves to be rich and motivated our experimental work. Three interests have been identified so far:

- the possibility to calibrate in-situ the number of photon and hence determine the coupling between the cavity photons and the quantum dot circuit with accuracy.
- the study of the charge screening in quantum dot circuits through the shift of the transmon frequency.
- the possibility to perform relaxometry measurement to access the spectral density of the dot occupation at the transmon frequency. Such measurements could prove instrumental in the study of the charge dynamic of the Kondo cloud.

This project however still requires more work, in particular, in the case of the Kondo regime. The interplay with the cavity and possibilities to drive the dot out-of-equilibrium either through a bias voltage or through fast gating remain unexplored. Finally, one of the next step should be to reconsider the derivation of the effective Hamiltonian which leads to an instantaneous interaction while it is in practice a delayed one, as it would allow to study the impact of the dot on the transmon dephasing.

5.2 Sample fabrication and characterization:

At the beginning of this project, the sample fabrication appeared quite straightforward as we mastered the fabrication of each component separately and there was no obvious incompatibilities in the processes involved. However, it turned out to be more challenging than we expected as will be exposed in section 5.2.2. This explains why so far we have not performed any measurement on a sample with both a working transmon and a working SD. In the following sections, I will first briefly recall the design of the sample that was already partially discussed in chapter 3. Next, I will discuss the main issues we encountered in the fabrication of the sample. Finally I will present results obtained for a transmon embedded in a cavity with a SD that was not connected, and show that the parameter used in the previous section are at least for the transmon part within reach.

5.2.1 Sample design:

The design of this experiment sample has been the first one on which we used HFSS to guide our decisions. We tried to improve on several aspect over the previous ones:

- in the experiments presented in chapter 4, the cavity input and output ports were symmetric which means that we lost half of the signal. In further experiments, we made those ports asymmetric (output port more coupled) but it was the first time we could finely calibrate the asymmetry. We targeted a 1/10 ratio between κ_{in}/κ_{out}.
- in previous experiments, the external quality factor was much higher than the measured quality for a complete sample. This, in addition of lowering the output signal, means that our process increases the internal losses. To mitigate this, we reduced the external quality factor and changed the aspect ratio of the CPW as described in section 3.1.2.
- To get a coupling to the SD as large as possible, we chose to use the same scheme as the one used in chapter 4 with a top gate galvanically connected to the central conductor. To increase further the field we also prolonged the ground plane very close to the SD as discusses in section 3.1.4.
- finally we moved towards a straight cavity that allows us to add many bonds between the ground planes to efficiently suppress parasitic microwave modes (see discussion in section 3.1.5).

In the previous study we assumed that the only source of relaxation for the transmon was the emission of photons in the cavity. This is in principle not true. However as the dot influences the transmon through the cavity, we can expect a larger change if the cavity induced relaxation dominates the transmon relaxation. This is why we targeted values of the transmon coupling, detuning from the cavity and cavity linewidth such as to get a Purcell limited lifetime of few micro-seconds that we can hope to be dominated by photon emission.

5.2.2 Sample fabrication:

During the fabrication process we faced two main issues:

- a lack of reproducibility of the SD gate electrodes fabrication
- an apparent incompatibility in fabricating the transmon after the dot

The origin of the first issue, that was also observed on other samples in the group, remains mysterious as it manifested itself in what appear to be a random fashion.

At first we decided to fabricate the SD first and the transmon second for the following reasons:

- it avoided to expose the transmon to resist and high temperature which could degrade its properties
- it allowed to stamp in the same conditions as for other samples, which means we did not need to worry about MMA/MAA residue in the area of stamping
- it allowed to test the SD before completing the sample

Following what was done in other experiments in the group for normal contacts on CNTs, we made the contacts out of Pd at first. However it turned out that Pd does not stick enough on the substrate and that the lift-off of the transmon lithography pealed it off. Either completely, or very little but enough to prevent the contact with the CNT. Both cases are illustrated in Fig. 5.6.

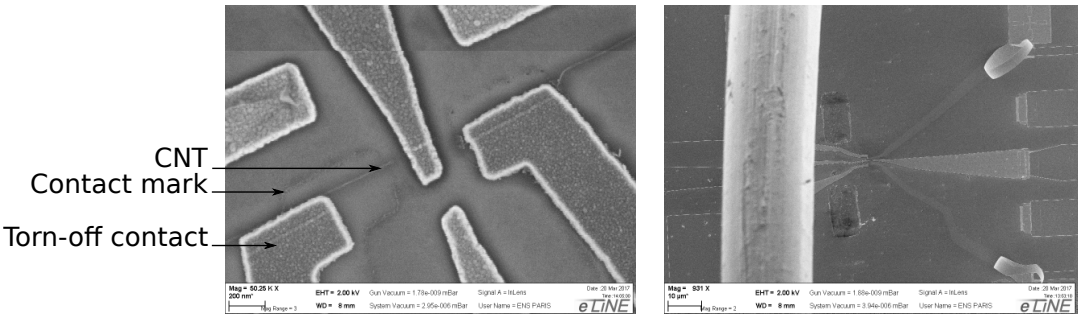

FIGURE 5.6: Contacts tearing off:
Electronic microscope image of the observed tearing off of the contact electrode after the transmon lithography. On the left image, the electrodes are still close to the sample, while on the right image they are completely torn off. In this second case the issue is also visible using an optical microscope.

Further attempt with Ti/Au based contacts did not produce any sample even if the reasons behind those failures have not been identified yet.

Given the recent progress made in the lab in the direction of ultra-clean nanotube fabrication 4.5.3, we may consider adapting such a scheme to this experiment.

5.2.3 Sample characterization:

The data presented in this section have all been obtained on a single sample in which the SD was not properly connected to its contacts. The characterization of the transmon demonstrates nonetheless that we can reach the targeted properties for the transmon. This sample did not reach the photon number resolved regime discussed in chapter 2, but one with only a transmon did and allowed to identify some defects in the filtering of our lines (as residual photons in the cavity).

5.2.3.1 Transmon characterization:

The first step in characterizing the transmon consists in performing its spectroscopy to extract its frequency and its anharmonicity. At low spectroscopic power, we expect a single line at the transmon first transition frequency. When we increase the power, additional lines can appear related to multi-photons processes. We are in particular interested in the two-photons transitions between the ground state of the transmon and the second excited level as it will allow us to extract the anharmonicity of the qubit since $\omega_{02} = \omega_{01} + \omega_{12} = 2\,\omega_{01} - \alpha$. Fig. 5.7 displays a typical spectroscopy of the transmon for different powers. Those data have been obtained using a continuous wave measurement scheme, which implies that the transmon line is broadened by the photons in the cavity. Once we have a rough estimate of its frequency, we can perform pulsed experiments, in which the cavity is empty of photons during the spectroscopic pulses, to narrow the linewidth and improve the accuracy of the transmon frequency determination.

From those data and additional ones taken with a pulsed excitation we can extract the transmon frequencies when it is dressed by the cavity:

$$\tilde{\omega}_{01} = \omega_{01} - \frac{g_{tra}^2/2}{\Delta} = 2\,\pi\,4.431 GHz \tag{5.18}$$

$$\tilde{\omega}_{02}/2 = \omega_{01} - \alpha/2 - \frac{g_{tra}^2/2}{\Delta + \alpha} = 2\,\pi\,4.22 GHz \tag{5.19}$$

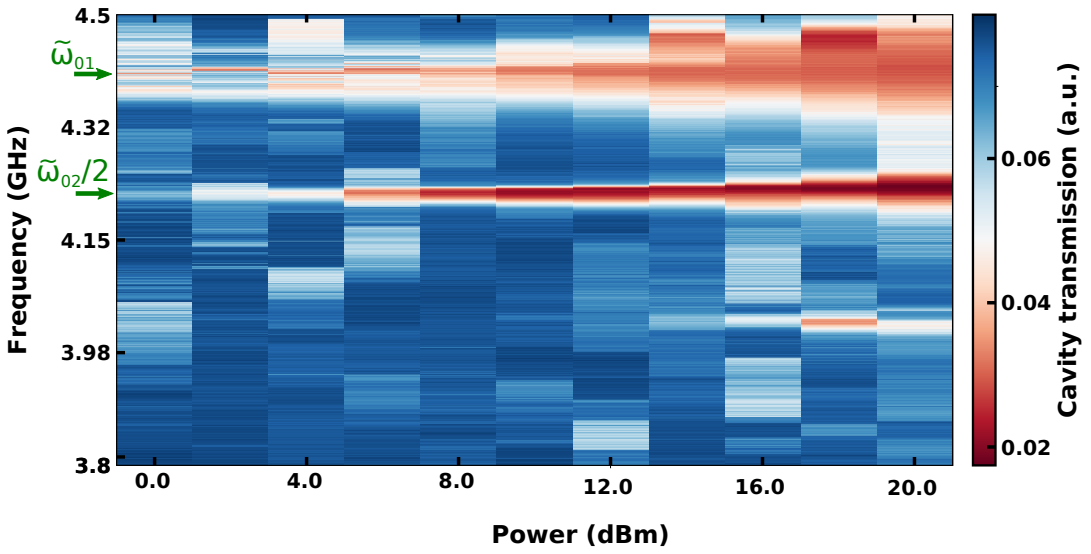

FIGURE 5.7: Transmon spectroscopy:
Two-tone spectroscopy of the transmon for varying power of the spectroscopic field. The cavity transmission decreases when the ground state of the transmon is depopulated. We can observe two main lines: the one at higher frequency corresponds to the transition between the ground and first exited state ($\tilde{\omega}_{01}$), the second one corresponds to the two-photons transition between the ground and second exited state. The third line may be related to higher order processes.

Once the frequency of the dressed transmon is known we can perform manipulations in a time-resolved manner. We start by performing a Rabi experiment as described in chapter 3. The main goal of this experiment is to calibrate the pulses used to transfer the population from the ground to the exited state (π pulse) and to put the transmon in a superposition of its ground and first exited state ($\pi/2$ pulse). Both those pulses are crucial in the following steps of the characterization. Fig. 5.8 displays the typical result of such a measurement.

As discussed in chapter 2, the cavity transmission can be related to the qubit population. A high transmission value means that the qubit is in its ground state while a low transmission means it is excited. The chevron patterns observed are characteristic of Rabi oscillations. When the drive is tuned to the qubit frequency, the qubit is driven on its x axis, while when it is off-resonant it is driven with respect to a tilted axis in the xz plane resulting in faster oscillation but of a lesser amplitude. The π pulse time can be identified at the time required to reach the first minimum.

The following steps of the characterization, detailed in appendix D, yield cavity and transmon characteristics that are not too different from the ones used in the theoretical

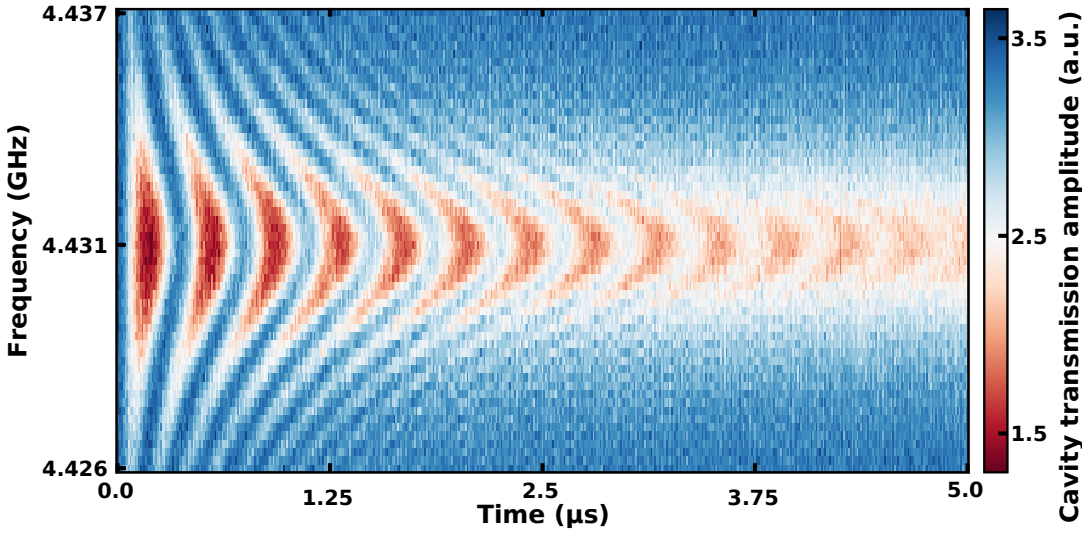

FIGURE 5.8: Transmon Rabi oscillation

study, save for its frequency:

$$\alpha = 2\,\pi\,420MHz \tag{5.20}$$

$$\omega_{01} = 2\,\pi\,4.47GHz \tag{5.21}$$

$$\Delta = 2\,\pi\,3.1GHz \tag{5.22}$$

$$g_{tra} = 2\,\pi\,230MHz \tag{5.23}$$

$$\kappa = 2\,\pi\,1.4MHz \tag{5.24}$$

$$T_1 \simeq 2.6\mu s \tag{5.25}$$

$$T_2^* \simeq 1\mu s \tag{5.26}$$

Because the qubit was far more detuned from the cavity than it should have been its lifetime is not limited by Purcell emission in the cavity. However, the measured lifetime is longer than the targeted value so this should not be an issue if we reach our target values.

It should be noted that the sample on which those data have been acquired is among the first one we made, and even though no full sample has been fabricated, we later tested another transmon whose parameters were much closer to the ones used in the simulation.

5.2.3.2 Dot circuit characterization:

A mentioned at the beginning of this subsection, the dot circuit was properly connected. Only one contact was connected. Its behavior is illustrated in Fig. 5.9.

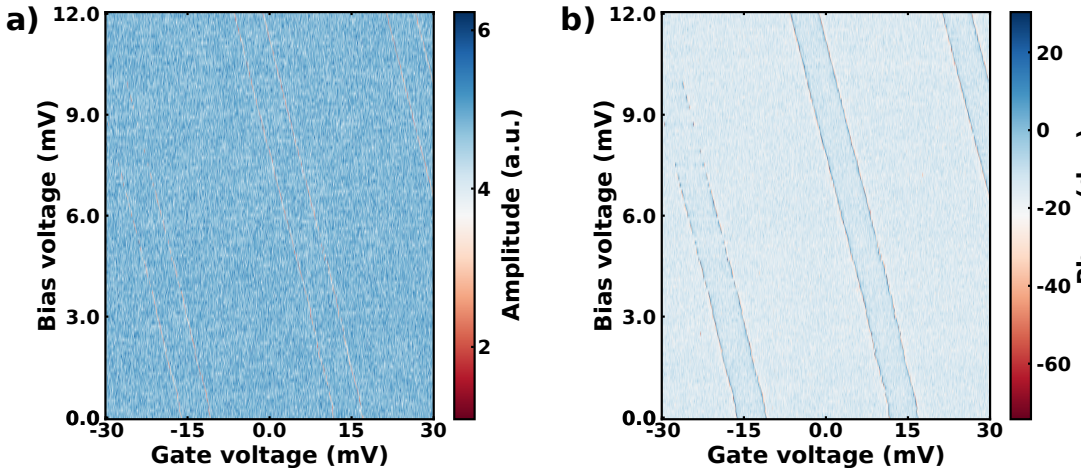

FIGURE 5.9: Dot characterization:
Transmission of the cavity (a amplitude, b phase) as a function of the gate voltage and bias voltage applied on the connected electrode. Because the contact is a contact, the slopes are reversed compared to what one would expect for the gate. The amplitude displays very thin pair of dips, while the phase displays sharp changes, matching the dips, and residual positive shift in between the dips.

Oddly enough, the system did not behave as a simple SD but more like a kind of double quantum dot in which the mutual charging energy would have been huge. We observe pairs of thin dips in the transmission, that can be associated with resonances, and matching patterns in phase, with a residual positive shift in between the dips. Knowing that a contact shift the chemical potential in the reverse direction compared to a gate, it looks like we are probing the area between the triple points of a double quantum dot, save that we never reached the triple points.

As in chapter 4, we observe large phase contrasts which points to an hybridization of the dot and the cavity. Studying the cavity transmission, as a function of the probing frequency and the dot gate voltage, does reveal a strong distortion of the cavity spectrum. However we do not reach the strong coupling regime.

This demonstrate that the dot was indeed coupled to the cavity. However in the area where it is the most strongly coupled, it also induces a strong dissipation which hinders the measurement. Because of this, we could not demonstrate any coupling between the

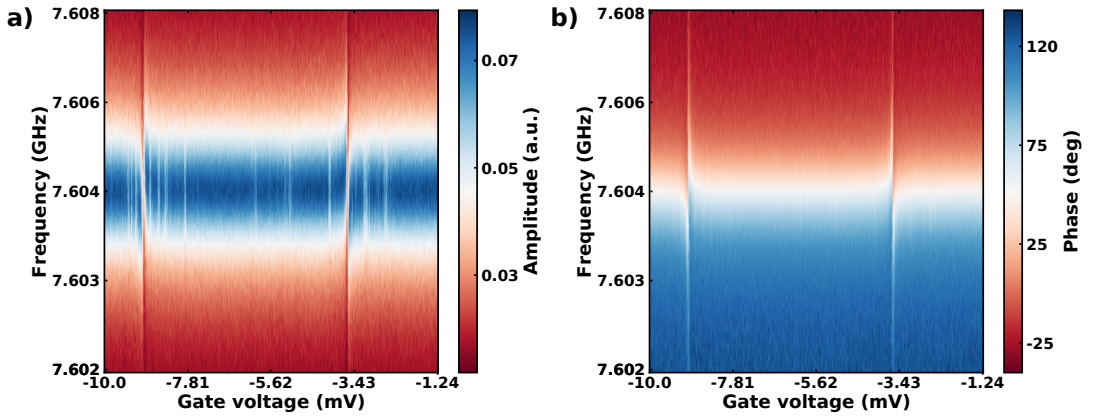

FIGURE 5.10: Dot-cavity characterization:
Transmission of the cavity (a phase, b amplitude) as a function of the gate voltage and cavity probe frequency. The cavity transmission appear strongly distorted in the vicinity of the resonance with the dot. In particular the phase allows to identify a few hundreds of kHz shift in the cavity frequency.

dot and the transmon. The reader should note however that the situation would be different for a single dot which would not induce such a large dissipation.

Chapter 6

Probing Majorana fermions using a cavity:

Majorana fermions, first proposed by Ettore Majorana in [130], are exotic spin-1/2 particles which are their own anti-particles. For a long time, neutrinos have been the only candidate particle. However, recently, Majorana fermions have been predicted to exist in condensed matter as excitations of some specific systems [131, 25, 26]. Because of their peculiar properties they have attracted a lot of attention. They have, for example been proposed as basic building blocks in fault tolerant quantum computation. A number of recent experiments [27, 28, 29, 30, 31, 32] claim to have observed Majorana fermions in semi-conducting nanowire systems. In those experiments, the main tool used to characterize the system is the measurement of the conductance from which the system density of state (DOS) can be deduced. However, those measurements cannot probe whether those excitations are indeed their own anti-particles. The development of new measurement schemes is hence essential. In this chapter, I will discuss a theoretical work whose goal is to explore the use of microwave cavities to study system expected to host Majorana fermions. After a general introduction, I will be following closely the presentation of [24]. My main contribution to this project has been to develop a numerical code which has been instrumental for this project.

6.1 Majorana fermions in condensed matter:

Majorana fermions, contrary to the other objects manipulated in this work, have not been presented in chapter 2. The following section will fill that gap and introduce their properties and why they are appealing in the context of quantum information. The state of the art experiment will also be discussed. They will provide an realistic ground to discuss the feasibility of the proposed experiments.

6.1.1 Majorana fermion properties:

In the context of condensed matter , Majorana fermions were first predicted to appear in a p-wave superconductor modeled as a Kitaev chain [131]. We will use it as a starting point to introduce Majorana fermions in condensed matter, before moving to more general cases better suited to illustrate the interest they raise in the context of quantum information processing [132].

6.1.1.1 The spin-less Kitaev chain:

In this model, one considers a 1D chain in the tight binding model with N sites and spin-less electrons. We will note μ the on site chemical potential and t the hoping between neighboring sites. In addition to the tunneling term, it also includes a superconducting pairing potential (Δ). The Hamiltonian reads:

$$H = -\mu \sum_j \hat{c}_j^\dagger \, \hat{c}_j + \sum_{j=1}^{N-1} \left(-t \left(\hat{c}_{j+1}^\dagger \, \hat{c}_j + \hat{c}_j^\dagger \, \hat{c}_{j+1} \right) - |\Delta| \left(\hat{c}_{j+1}^\dagger \, \hat{c}_j^\dagger + \hat{c}_j \, \hat{c}_{j+1} \right) \right) \tag{6.1}$$

To go further, we can then re-write this Hamiltonian in terms of Majorana operators $\hat{m}$ by remarking that we can decompose each fermionic operator in term of two Majorana operators (which are nothing else than the "real" and "imaginary" part of the fermionic operators) :

$$\hat{m}_{j,1} = \hat{c}_j + \hat{c}_j^\dagger \qquad \hat{m}j, 2 = -i \left(\hat{c}_j - \hat{c}_j^\dagger \right) \tag{6.2}$$

with the properties :

$$\hat{m}_{j,\alpha} = \hat{m}_{j,\alpha}^\dagger \qquad \{ \hat{m}_{i,\alpha}, \hat{m}_{j,\beta} \} = 2 \, i \, \delta_{ij} \delta_{\alpha\beta} \tag{6.3}$$

The fact that a Majorana fermion is its own anti-particle simply appears here in the self-adjoint character of the operators. In the absence of tunneling and of pairing, this rewriting is trivial. In the non-trivial case (here $\mu = 0$ and $t = |\Delta|$ for simplicity) the Hamiltonian takes a simple form in term of the Majorana operators:

$$\hat{H} = -i \, t \sum_{i=1}^{N-1} \hat{m}_{j,2} \, \hat{m}_{j+1,1} \tag{6.4}$$

In this Hamiltonian, two Majorana operators, one at each end of the wire, do not contribute to the system energy. Playing the inverse trick we can rewrite this Hamiltonian in terms of fermionic operators, but for fermions living between the chain sites. This construction, illustrated in Fig 6.1, does not touch the two edge Majorana operators, which can be though of as a very delocalized fermionic mode.

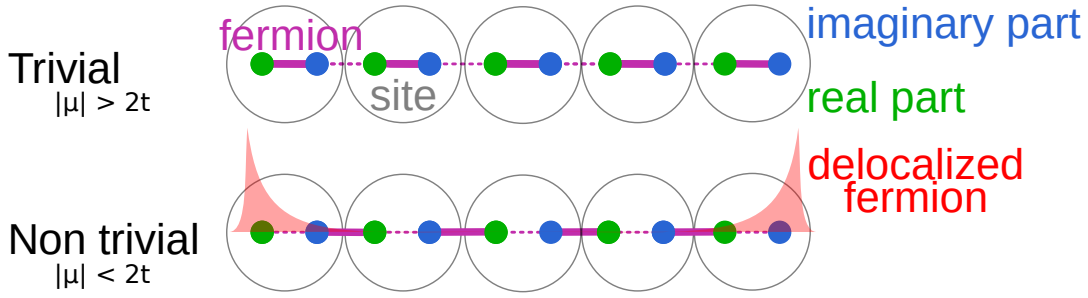

FIGURE 6.1: Kitaev chain in the trivial and non trivial phase: Each fermionic site is indicated by a grey circle. The two Majoranas stem from the partition (green/blue) between the real and imaginary parts of the electronic wavefunction. In the trivial phase (top), two Majoranas on each site are paired, whereas in the non-trivial phase (bottom), two Majoranas from neighboring sites are paired together. It leaves two unpaired Majorana at each extremity which forms a delocalized fermionic mode whose occupation does not cost any energy.

As a consequence, the system has a doubly degenerate ground-state corresponding to that delocalized fermionic mode being occupied or not. If the chain is connected to two electrodes, electrons can consequently be transmitted at zero bias, entering on one end and emerging directly on the other side. It is this signature that has been most widely used so far in experiments to detect the possible existence of a possible Majorana pairs, also referred to as a Majorana zero-mode because of this zero energy signature.

Furthermore, the Majorana fermionic mode is highly delocalized and does not couple to local perturbations of the Hamiltonian. One can then expect a long coherence time for the fermionic mode, because decoherence sources are, most of the time, local. Its robustness is also enhanced by the fact that in order to go from the trivial regime (or non-topological) to the non-trivial one (or topological) one must necessarily close the gap. These properties make Majorana fermions very promising for quantum information processing as they could be hardware efficient qubits.

Here, we have focused on the case $\mu = 0$ and $t = |\Delta|$, but the topological regime, corresponding to the existence of this delocalized fermionic mode, persists as long as $|\mu| < 2t$. The Majorana fermions appear in the middle of a gap whose value depends on μ, Δ and t. For $|\mu| = 2t$, the gap closes and reopens for $|\mu| > 2t$ but without Majorana fermions. Majorana fermions do not only appear at the edge of the chain but at any interface between a topological and a non-topological region. As a consequence, one can move a Majorana along the chain by tuning the chemical potential and even

consider merging two Majoranas together to extract information about the occupation of the corresponding fermionic mode.

One often refers to this occupation as the parity of the Majorana pair defined by $P_i \equiv 1 - 2c_i^\dagger c_i$, with c_i the fermionic operator built upon the two Majoranas. Considering several pairs of Majorana, one can show that two different parity operators P_i and P_j commute together and that the parity operators define a basis of Majorana pairs for the degenerate ground state of the system. As a Majorana is a superposition of an electron and a hole, the fusion of a pair of Majoranas gives either an electron or a hole, depending of the parity P_i of the pair, which can be detected.

In practice, the Majorana fermions have a finite spatial extension with an exponential decay, which, in this simple model, is governed by the superconducting gap $|\Delta|$. The ground state will be truly degenerate only if the two Majoranas are far enough and hence do not overlap. When bringing them closer together, they hybridize and the 0 or 1 fermionic occupancy is not degenerate anymore. These two states are split by an energy $2\,\epsilon$:

$$H_{merge} = i\,\epsilon \hat{m}_{i,1}\hat{m}_{i,2} = 2\,\epsilon\left(\hat{c}_i^\dagger \hat{c}_i - \frac{1}{2}\right) \tag{6.5}$$

This energy splitting will be central in the detection we will discuss in section 6.2.

So far, we know that quantum information can be encoded into the parity of a Majorana pair and that it should be protected as Majorana fermions are insensitive to local perturbations. This can be seen by computing the coupling between the two Majorana ($\psi_1(r)$ and $\psi_2(r)$) induced by a local potential $V(r)$: $\int \psi_1(r)V(r)\psi_2(r)$. Such a coupling vanishes for well separated Majorana fermions which do not have any wave-function overlap. Furthermore we have one mechanism to read out the parity. What we are missing is a way to manipulate the information and preferably in a way that is also free of errors. Such manipulations are possible, to an extent, and rely on another specific property of the Majorana fermions that will be the topic of the next section: their non-abelian statistics.

6.1.1.2 Generalization and non-Abelian statistics :

Another key-feature of Majorana fermions for quantum information processing, is their non-Abelian[1] statistics which allows to manipulate the quantum state using only geometric operations in the ground-state subspace. The advantage of such operations is that they do not suffer from the imperfections of usual manipulations.

Coming back to the pairing we chose, we can notice that it is rather unusual. We consider spin-less electrons which is equivalent to focusing on a single spin family. This means that the superconducting pairing couples electrons with the same spin contrary to s-wave superconductivity which couples electrons with opposite spins. This kind of pairing corresponds to p-wave superconductivity (the orbital part of the wave-function is anti-symmetric (p-type orbitals) rather than the spin part). One can show that Majorana fermions emerge not only at the edge of 1D p-wave superconductor like in the Kitaev chain, but also on defects, such as vortices in 2D p-wave superconductors. Because of their localized nature they are also referred to as Majorana Bound States (MBSs). Their non-Abelian statistics was first investigated theoretically in such 2D systems [133] as in 1D one cannot exchange two Majoranas without merging them.

For a set of N Majorana pairs, whose total parity is conserved, the ground state degeneracy is 2^{N-1}, depending on the parity of each pair. In such a state, one can perform two kinds of exchange (or braiding operations):

- exchange two Majoranas of the same pair. This will only produce a global phase factor, which is not so surprising as the other pairs do not care about the "order" of two Majoranas in a pair.
- exchange two Majoranas coming from two different pairs. Focusing on the two pairs concerned by the exchange, we can write the quantum state in term of the parity $|n_1 n_2\rangle$, $n_i = 0$ or 1. The braiding leads to transform $|00\rangle$ into $\frac{1}{\sqrt{2}}(|00\rangle + i\,|11\rangle)$, which does not change the total parity.

In the second case, the new state cannot be written as $e^{i\phi}\,|00\rangle$, and corresponds to a rotation on the Bloch sphere, $|00\rangle$ being the south pole and $|11\rangle$, the north pole. A direct

[1] A statistics is abelian when exchanging two identical particles yields only a phase factor for the many body states. For bosons the phase factor is $+1$ and fermions -1

consequence of this is that braiding operations between Majoranas of different pairs do not commute : the order of a braiding sequence matters. Importantly, in order to stay in the ground state manifold, the exchange should be adiabatic, i.e. slow compared to the time scale given by the energy gap that protects the manifold. Otherwise the system will be given enough energy to exit the ground state manifold. Using a network of 1D wires with T-junction allows to use similar schemes on 1D wires and not only in 2D.

The key advantage of such manipulations is that, as the result depends only on geometrical considerations, the speed of execution or the exact path do not matter, as long as it is slow enough to avoid exciting states above the topological gap. This should make, in principle, those operation much more robust to manipulation errors than time controlled manipulations.

So far the picture looks appealing, however, in truth, it is more complicated. First, for Majorana fermions, the protection by the gap is total only at zero temperature and not at finite temperature. Furthermore, braiding alone does not allow to prepare an arbitrary state and needs to be completed by more conventional manipulation techniques [132] which are not fault-tolerant. Nonetheless, MBSs may pave the way for more robust qubits and/or more complex quasi-particles offering topological protection for additonal operations [134, 135]

6.1.2 Experimental realizations:

As discussed in the previous section, Majorana fermions emerge at the interface of 1D p-wave superconductors or on defects in p-wave 2D superconductors. However, p-wave superconductivity is not a naturally occurring phenomenon and need to be engineered. In all the following we will focus on 1D systems.

6.1.2.1 Majorana fermions in 1D systems recipe:

In 2010, two proposals were made to induce a non trivial p-wave superconducting pairing in 1D quantum wire [25, 26]. Both relies on three main ingredients :

- a single conduction channel with spin-orbit coupling
- a magnetic field applied perpendicularly to the spin-orbit coupling axis

- an s-wave superconducting pairing induced by proximity effect.

The system Hamiltonian can then be written as:

$$H = \left(\frac{\hbar^2 k_x^2}{2m} - \mu - \alpha_{SO} k_x \, \sigma_y \right) \tau_z + E_z \, \sigma_z + \Delta \, \tau_x \tag{6.6}$$

Electrons move in the 1D channel along the x direction. The magnetic field induces a Zeeman splitting E_z in the z direction, perpendicularly to the axis of the spin orbit splitting, with a spin-orbit constant α_{SO}. Above $\sigma_{y,z}$ are the Pauli matrices for the spin, $\tau_{x,z}$ are those related to the Nambu (electron/hole) subspace and Δ pairs electrons and holes with opposite spin.

The resulting spectrum, and the impact of each term, is illustrated in Fig. 6.3:

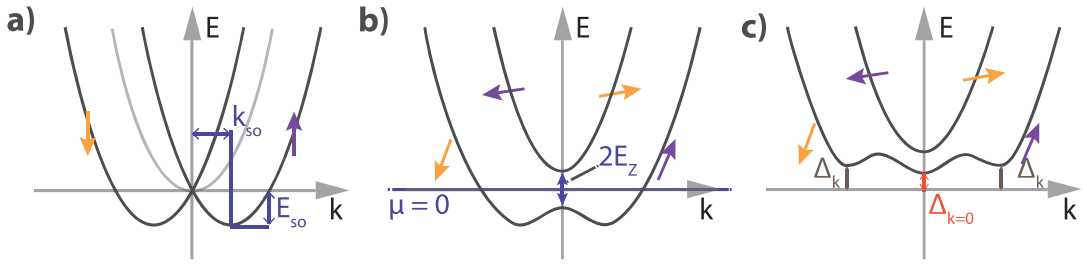

FIGURE 6.2: Spectrum of a 1D channel with a Rashba spin-orbit coupling, Zeeman splitting and s-wave superconductivity pairing/

a) In the absence of external magnetic field, the spin-orbit interaction shift the dispersion relation (grey parabola) by $\pm k_{SO}$ along the wire axis and by E_{SO} on the energy axis. The two parabolas correspond two orientations of the spin. The quantification axis is orthogonal to the wire axis.

b) A magnetic field applied along the axis of the wire competes with the quantification axis of the spin-orbit. At k=0, a pure Zeeman field opens, $\mu = 0$ is defined as the middle of this gap.

c) Adding the superconductivity while keeping the chemical potential fixed result in the opening of a gap at high momentum $k = 2k_{SO}$.

Figure adapted from [136]

To understand the interplay between the three ingredients lets consider their effect on the spectrum in an incremental fashion. As shown in Fig. 6.3, the spin-orbit coupling shifts by $k_{SO} = m\,\alpha_{SO}/\hbar^2$ (resp $-k_{SO}$) the parabola corresponding to spin $|+\rangle$ (resp $|-\rangle$) in the y direction. It also shifts the minimum of the parabolas by the spin-orbit energy $E_{SO} = m\,\alpha_{SO}^2/\left(2\hbar^2\right)$. When a Zeeman field is applied perpendicularly to the

spin-orbit coupling axis, it tilts the spin eigenvalues towards this second quantification axis and the mixing of the spin opens a gap at zero momentum. Inside the gap, there are two non-degenerate states with different spins. More precisely, the spin degree of freedom is locked to the momentum.

The superconductivity opens a gap at all momenta. It is the competition between this helical gap and the superconducting gap at zero momentum that leads to the formation of the MBSs. At zero magnetic field, there is no helical gap and the state is trivial (Fig. 6.3 a). However as the magnetic field increases, the helical gap increases too (Fig. 6.3 b) which can lead to a gap closing at $k = 0$ as illustrated in Fig. 6.3 c. The gap closing condition, separating the trivial and the non-trivial regimes, is given by:

$$E_z = \sqrt{\Delta^2 + \mu^2} \tag{6.7}$$

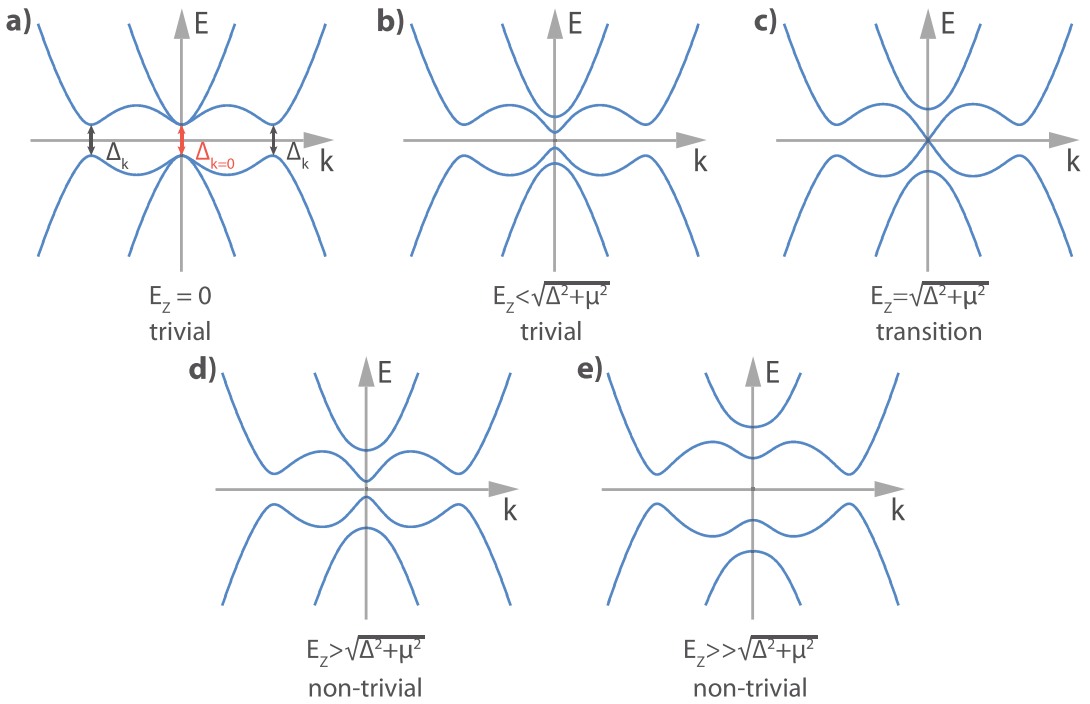

FIGURE 6.3: Kitaev spectrum under magnetic field:
Evolution of the spectrum when the magnetic field is increased (a to e), starting in the trivial phase, closing the gap and reopening the gap in the non-trivial phase. Contrary to Fig. 6.3 both the electron and hole branches are represented. Figure taken from[136].

If the Zeeman splitting is further increased, a gap reopens but with a different nature because the bands have been inverted (Fig. 6.3 d and e):

$$\Delta_{topological} = E_z - \sqrt{\Delta^2 + \mu^2} \tag{6.8}$$

When considering application for quantum computation, it is this gap that provides the protection of the states and limits the computational speed. It is also this gap that control the localization of the MBSs.

However, this is valid only if the gaps at high momenta remain open at all intermediate magnetic fields, which ensures that the bands become truly inverted. At zero magnetic field, the gap is equal to the induced superconducting gap. At finite Zeeman splitting, it is reduced by a factor depending on the ratio E_z/E_{SO}. If this ratio is small, the high momentum gap evolves as $\Delta_{k\neq 0} \sim \Delta\left(1 - \frac{1}{24}\frac{E_Z}{E_{SO}}\right)$ [136]. Therefore, even though the spin-orbit coupling does not enter in the condition for the opening of the topological gap, it is crucial that it is strong enough to preserve the gap at high momentum.

The change of nature of the gap cannot be deduced directly from the spectrum as it only shows the eigenvalues of the Hamiltonian and not the topology of the subspace defined by the eigenvectors.

MBSs appear when connecting a trivial and a non-trivial region. In such a case, the topological gap has to close to connect the inverted and non inverted bands which leaves a state at zero energy which is the Majorana fermion. Away from the interface between a topological and a non topological regions, the wave-function of the Majorana decays exponentially since the gaped phases act like insulators.

6.1.2.2 Samples and characterization :

In practice, the recipe presented in the previous section has been mostly applied to semiconducting nanowires with a strong-spin orbit coupling (InSb [27, 31], InAs [28]), proximized by a superconductor such as niobium titanium nitride [27] or aluminum [28, 31] and subject to an external magnetic field applied in the axis of the wire.

Such samples have then be characterized through tunnel spectroscopy by connecting them to normal contacts used as a tunnel probes. Conductance measurements carried out as a function of the magnetic field have revealed the appearance of a zero bias peak, as illustrated in Fig. 6.4, that is one signature of the MBSs .

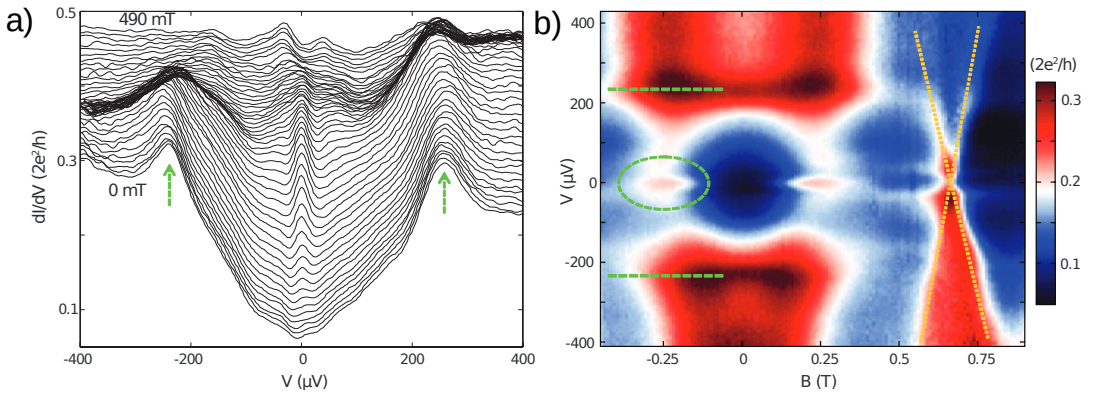

FIGURE 6.4: Zero bias peak signature of Majoranas fermions: Conductance maps as a function of the external magnetic field and the bias voltage. At finite field a conductance peak appear at zero-bias. Figure extracted from [27]

Yet, this transport signature is not fully specific only to Majorana fermions. We list below some alternative mechanisms that can lead to a similar signature and how they can be ruled out:

- The Kondo effect that we discussed in chapter 2 can compete with the superconductivity and lead to the appearance of a zero-bias conductance peak as the magnetic field weakens the superconductivity [137]. However, it should also disappear at higher field when the Zeeman energy becomes larger than the Kondo temperature, which can be directly related to the width of the peak.

- The superconductivity induced by proximity effect in the nanowire comes from Andreev reflections in which an electron is reflected as a hole as the interface with the superconductor. Multiple reflections can lead to the formation of doublet of bound states (ABSs) which in the absence of spin-orbit or Zeeman field are spin degenerate. When a magnetic field is applied, ABSs can split and cross on the zero-energy axis. If the superconducting gap is suppressed at the same time the ABSs cross, they stay close to zero bias, like Majoranas would [138].

- A zero-bias conductance peak could also appear because of a weak antilocalization effect induced by disorder in the nanowire [139].

The first experiments principally suffer from the fact that the gap induced by the superconducting proximity effect in the nanowire was soft (the subgap DOS was important).

This can be related to disorder at the interface between the nanowire and the superconductor. With the progress in sample fabrication, more detailed characterizations of the magnetic field dependence, and, even, the wire length dependence, as illustrated in Fig. 6.5, have been able to rule out a number of alternative explanations. However, such measurements do not probe the truly specific behavior of Majorana fermions such as their self-adjoint character, nor their non-Abelian statistics.

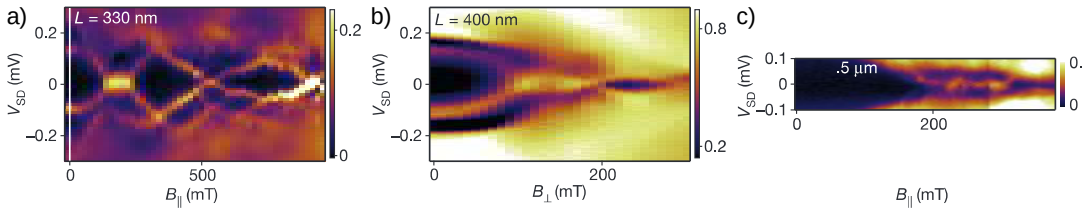

FIGURE 6.5: Majorana bound state oscillation in field:
Conductance maps as a function of the external magnetic field and the bias voltage, displaying oscillations of the supposed MBS, whose amplitude decreases when increasing the wire length. Figure extracted from[**albretch_exponential_2016**]

Protocols have been proposed to braid Majoranas fermions in such 1D wires. However they all require some kind of T-junction which are very challenging to fabricate and to tune in the proper regime. The goal of the study that will be presented in the next section will hence be to see if the use of the technique of cQED could provide some new detection scheme that would give a direct signature of the self-adjoint character of MBS with the current device geometry.

6.2 Direct cavity detection of Majorana pairs:

The self-adjoint character of MBSs, which draws so much interest, also makes them very difficult to detect. Photons trapped in a high-finesse cavity are a priori very appealing for probing these elusive excitations. The specific properties of the Majorana fermions however result in a quite peculiar form of the light-matter coupling that will be discussed.

6.2.1 Majorana fermions coupling to the light:

Light, contrarily to conductance measurements, preserves the occupation number encoded into a pair of MBSs, as it cannot create a fermion. Unfortunately, for the same

reason, a pair of MBSs cannot exchange energy with an electromagnetic field. As presented in the following, a pair of MBS hence has a 'longitudinal coupling' Hamiltonian to the electromagnetic field because of the particle/antiparticle duality of MBSs.

The general form for the coupling Hamiltonian of a MBS pair to photons is necessarily:

$$H_{coupling} = i\,\beta \hat{m}_1 \hat{m}_2 \left(\hat{a} + \hat{a}^\dagger\right) \tag{6.9}$$

since it is the only possible combination between the operator $\hat{m}_{1,2}^\dagger = \hat{m}_{1,2}$, as $\hat{m}_{1,2}^\dagger \hat{m}_{1,2} = 1/2$ [140]. As a consequence, the coupling Hamiltonian is then proportional to $i\,\hat{m}_1\hat{m}_2 = 2c^\dagger c - 1$, which commutes with the Hamiltonian 6.5 of the wire, so that there is no transverse coupling between the MBS and the cavity.

If we represent the two MBS on a Bloch sphere (the south and north pole being the parity), the coupling corresponds to a field in the z-direction, parallel to the quantification axis. If we consider a coupling of the field to the chemical potential of the wire, the electric field shakes the chemical potential of the wire but cannot induce any transitions inside the MBS pair.

In order to get a cavity signal, one must consider transitions outwards the Majorana doublet. One can consider different situations in which transitions towards other states could occur:

- in a situation involving not two but four Majorana fermions, the even parity subspace has two states $|00\rangle$ and $|11\rangle$, the odd parity subspace has two states $|01\rangle$ and $|10\rangle$, $|n_1 n_2\rangle$ being the number of electrons associated to the left, right MBS. The parity of the total number of fermions has to be conserved, due to the self-adjoint property of MFs. However inside each parity subspace, a transverse coupling can appear which produces a cavity signal [140].

- if the length of the nanowire is larger than the superconducting coherence length ξ (or in the presence of disorder [141]), trivial Andreev bound states can exist at higher energies. The coupling to microwave photons could induce transitions from the MBS to those states or to states above the superconducting gap. Close to the topological transition, transitions to the superconductor continuum of states are

resonant and induce a phase and amplitude shifts that decay exponentially away from the transition [142].

In this work we will focus on a different kind of transitions whose existence arises from the imperfections of realistic circuits such as the ones presented in section 6.1.2.2. First, such circuits must have a finite size to remain in the coherent regime. Therefore, MBSs can have a spatial overlap, which naturally generates ,for a pair of MBSs, an energy splitting $2\,\epsilon$ and a direct coupling β to the cavity electric field [140, 105]. The presence of zero-energy quasiparticles in superconducting or normal metal contacts, which is inherent to experimental setups demonstrated so far, switches on photoassisted tunnel processes between the reservoirs and the Majorana doublet. During these transitions, photons with frequency ε are exchanged between the cavity and the Majorana pair, with a rate set by β. However, transitions at frequency 2ε remain forbidden regardless of the circuit parameters. The purely longitudinal nature of β , thereby revealed, would represent a direct signature, in the simplest setup, of the self-adjoint character of MBSs.

The above result can be easily derived in an analytic fashion, at zero temperature and for a discrete set of levels, by considering the general Hamiltonian describing the wire and its coupling to the cavity:

$$\hat{H}_{tot} = \hat{H}_{wire} + \hbar\,\omega_0 \hat{a}^\dagger \hat{a} + \hat{H}_{coup}(\hat{a} + \hat{a}^\dagger) \tag{6.10}$$

with ω_0 the cavity frequency.

As both $\hat{H}_{wire}$ and $\hat{H}_{coup}$ are quadratic one can find a Bogoliubov transformation allowing to write :

$$\hat{H}_{wire} = \sum_a E_a \hat{\gamma}_a^\dagger \hat{\gamma}_a \tag{6.11}$$

$$\hat{H}_{coup} = \sum_{a,b} M_{a,b} \hat{\gamma}_a^\dagger \hat{\gamma}_b + N_{a,b} \hat{\gamma}_a^\dagger \hat{\gamma}_b^\dagger + N_{a,b}^\dagger \hat{\gamma}_b \hat{\gamma}_a \tag{6.12}$$

with $E_a > 0$ and γ_a Bogoliubov operators combining electron and hole excitations.

As discussed in the previous sections, the cavity response can be described in a semi-classical fashion in term of the system charge susceptibility. The susceptibility of the system is then given by:

$$\chi(t) = -i\,\theta(t)\langle[\hat{H}_{coup}(t), \hat{H}_{coup}(0)]\rangle \tag{6.13}$$

Because we work at zero temperature, the only contributions to the susceptibility are of the form $|N_{ab}|^2 e^{-i/\hbar(E_a+E_b)t}$ as all other terms involves terms containing $\gamma_a\,\gamma_b|0\rangle$, with $|0\rangle$ the fundamental state, which make them vanish. The susceptibility hence has the following form in the frequency domain :

$$\chi^* \simeq \sum_{a,b} \frac{|N_{ab}|^2}{2} \frac{1}{\omega_0 - E_a - E_b + i0^+} \tag{6.14}$$

Importantly, $N_{aa} = 0$ due to the Pauli exclusion principle. Hence, there is no transisition between conjugated electrons and holes. This result can be extended in an analytic way to a situation in which the level broadening is smaller than the interlevel spacing[2].

One should, however, note that this does not by itself forbid signatures at $\omega_0 = 2\,E_a$, as such signatures can come from degenerate states. This can for example happen with degenerate ABSs as observed in spin-degenerate atomic contacts [8, 143]. In the case of Majorana fermions, the degeneracy is lifted and the MBSs are formed from a non-degenerate Bogoliubov doublet $(\hat{\gamma}_1^\dagger, \hat{\gamma}_1)$. This means that we cannot have any cavity signal at $\omega_0 = 2\epsilon$ and this even in the case where the MBSs are coupled to the photonic field (ie $M_{11} \neq 0$).

One of the goal of the numerical studies will be to validate that those results hold true at finite temperature and in presence of a continuum of state providing dissipation.

6.2.2 Proximized nanowire model:

In order to properly describe the transitions between the MBS and the subgap states, our model must not only describe accurately the spectrum of the system but also the dissipation.

[2]The demonstration is presented in the supplemnetary Materials of [24]

We start from a tight binding model of a wire with spin-orbit coupling and subject to an external magnetic field:

$$\hat{H}_{wire} = \sum_n \hat{d}_n^\dagger \left(E_z\,\hat{\sigma}_z - \mu\right)\hat{d}_n - \left(\hat{d}_n^\dagger \left(t + \Lambda\,\hat{\sigma}_y\right)\hat{d}_{n+1} + h.c.\right) \tag{6.15}$$

with $\hat{d}_n^{dag} = \left\{\hat{d}_{n\uparrow}^{dag}, \hat{d}_{n\downarrow}^{dag}\right\}$ and $\hat{d}_{n\sigma}^{dag}$ the creation operator for an electron with spin σ in site $n \in [1, N_C]$ of the chain. We denote by E_z the Zeeman field on the sites, μ the sites chemical potential, which can be tuned with a gate voltage, t the hopping constant between the sites, and Λ the spin-orbit constant.

Many studies of MBS coupled to cavities have reduced the impact of the superconductor to an effective pairing effect described by the term in Δ of (6.6). However, this describes neither the induced level broadening in the nanowire nor the dissipation. Here we will treat the tunneling towards the superconducting contact explicitly. The Hamiltonian (6.15) is very similar to the ones already used to describe tunneling between a quantum dot and leads with the addition of the pairing term for the superconductor $\Delta \sum_k \left(c_{S,k,\uparrow}^\dagger c_{S,-k,\downarrow}^\dagger + h.c.\right)$ ($c_{S,k,\sigma}$ is the annihilation operator for electrons in the superconductor). To describe the superconductor density of states we will need, in addition to the superconductor gap Δ, a phenomenological parameter Γ_b describing the broadening of the BCS peaks and the sub-gap density of state. Both these imperfections of the superconductor can originate from the externally applied magnetic field and are relevant for all experiments carried out so far. The superconductor is supposed to be homogeneously connected to all sites and the tunneling is described by Γ_S. Furthermore, we will also consider that our wire is connected to two normal metal contacts, one at both ends. The tunneling between the wire and the contacts will be described by Γ_N. Finally, the coupling to the cavity is described as an overall modulation of the wire chemical potential, of amplitude g. The ensemble of the parameters is illustrated in Fig. 6.7.

Note that the superconducting lead, chemical potential should not be affected by the microwave field. This assumes that the sample has been designed in a careful way such that the contacts are properly grounded.

To treat on the same footing internal nanowire transitions and tunneling to the reservoirs, we use a Keldysh Green's function approach [22, 143, 144, 145, 146]. In the

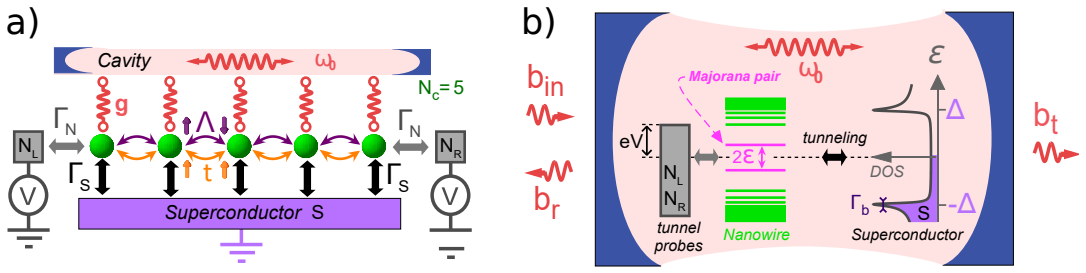

FIGURE 6.6: Wire model schematic:

a) Tight-binding model of our nanocircuit with $N_C = 5$ sites (green dots). The consecutive sites are coupled by a tunnel-hopping constant t and spin-orbit terms Λ. All sites are tunnel coupled to the superconductor S with a rate Γ_S. The extremal sites are tunnel coupled with a rate Γ_N to normal metal contacts $N_{L(R)}$ with a bias voltage V. All sites are coupled to the microwave cavity with a constant g.

b) Energetic scheme of the nanocircuit placed in the microwave cavity. The DOS in S depends on the superconducting gap Δ and the broadening parameter Γ_b. The cavity microwave transmission b_t/b_{in} or reflection b_r/b_{in} is measured, to probe the system charge susceptibility χ.

Figure extracted from[24]

following G will refer to the Green's functions including the effect of the cavity potential and $\mathcal{G}$ to the ones which do not include it.

For each site, the retarded Green's function $\mathcal{G}^r_{dd}$ is described by a 4×4 matrix whose structure in the Nambu(electron/hole)/spin subspace can be found in the supplementary material of [24]. We obtain:

$$\mathcal{G}^r_{dd}(\omega) = (\omega - H_{wire+leads}/\hbar - \Sigma^r_N - \Sigma^r_S)^{-1} \tag{6.16}$$

where Σ^r_N, and Σ^r_S corresponds to the self-energy describing the impact of the tunneling from the leads (see [24] for details).

The Green' function gives us a very direct access to the system DOS by summing on both spin species in the electron sector. In particular, the first site of the chain DOS reflects what would be seen in a conductance measurement[3]. We consider relatively short chains and choose our model parameters such that few subgap levels are visible in

[3]This formalism allows us to compute the conductance, but the computation is a bit more involved than the DOS. We did both, but we preferred to focus on the DOS as we get the same information from both.

the DOS, similar to what has been observed in recent experiments [31, 32]. We mainly focused on two sets of parameters whose DOSs are presented in Fig 6.7.

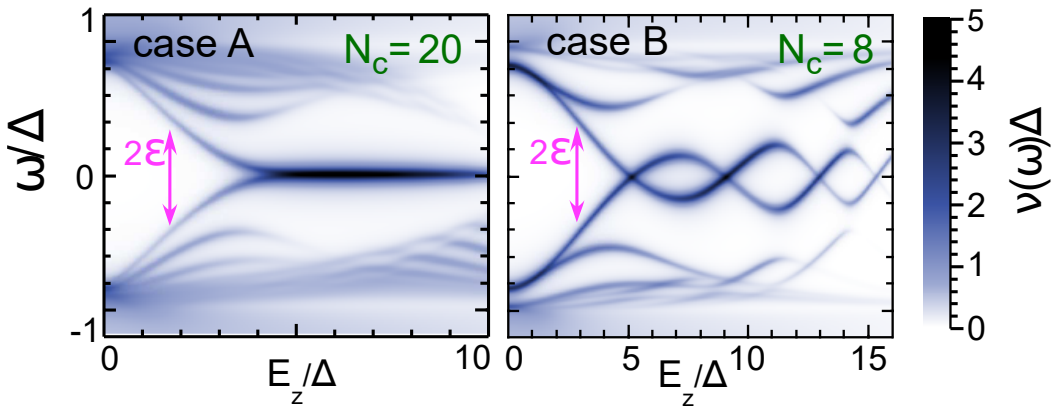

FIGURE 6.7: Short chains DOS:
Both plots present the DOS at one end of the nanowire as a function of ω and E_Z but for two different set of parameters.

a) case A: "long" wire with a negligible coupling to the normal contacts. Because the wire is long, the overlap between the MBSs is negligible and the peak in the DOS remains at zero energy.

b) case B: "short" wire with a coupling to the normal contacts similar to the coupling to the residual subgap DOS of the superconductor. Here the wire is short and the splitting in energy 2ϵ between the two MBSs oscillate with E_Z.

Figure extracted from[24]

The parameters used in each case are:

	N_C	t/Δ	Λ/Δ	Γ_b/Δ	Γ_N/Δ	μ/Δ
Case A	20	2.5	5	0.1	0.001	6
Case B	8	5	4	0.5	0.2	5.5

Furthermore we use $E_Z = \Delta$, $\Gamma_S = 5.5\Delta$ and $k_B T = 0.01\Delta$ in both cases.

The DOS at the ends of the wire reveals the occurrence of MBS above a certain critical field: in case A the MBSs go to zero energy and stay there while in the case B of the very short chain, one can observe an oscillation of the energy splitting of the Majorana doublet as a function of the magnetic field similar to what was observed in [31].

Like in previous chapters, we describe the response of the cavity in a semi-classical fashion in term of the system charge susceptibility. We start from the expression of the charge on site n Q_n. In our formalism, this quantity can be expressed as:

$$Q_n(t) = ie/2\, Tr\left(\hat{\tau}_n G^<(t,t)\right) - e \tag{6.17}$$

Above the lesser Green's function $G^<_{\hat{c}_{n,\sigma},\hat{c}^\dagger_{n,\sigma}}(t,t) = i\langle \hat{c}^\dagger_{n,\sigma}(t)\hat{c}_{n,\sigma}(t)\rangle$ gives the instantaneous occupation of site n and $\hat{\tau}_n$ the diagonal matrix which attributes a positive sign to electrons on site n and a negative sign to holes on site n and $e > 0$. The factor $1/2$ accounts for the fact that by summing on both the Nambu and the spin space we count twice each spin species.

The lesser Green's function can be expressed in terms of the retarded and advanced Green's function and the lesser self-energy using the Langreth theorem [147]:

$$G^<(t,t') = \int\int dt_1 dt_2 G^r(t,t1)\Sigma^<(t_1,t_2)G^a(t_2,t') \tag{6.18}$$

Next, we can expand the retarded and advanced (superscript a) Green's function to first order in the impact of the cavity potential: $\hat{E}_{ac}(t) = a\sum_n g_n\hat{\tau}_n e^{-i\,\omega_{RF}\,t}$, where g_n describes the strength of the photonic modulation on site n. This gives:

$$\begin{aligned} G^{r(a)}(t,t') &= \mathcal{G}^{r(a)}(t,t') \\ &+ \int dt_2 \mathcal{G}^{r(a)}(t,t_2)\hat{E}_{ac}(t_2)\mathcal{G}^{r(a)}(t_2,t') \end{aligned} \tag{6.19}$$

This allows to compute the impact of the field on Q, which we can identify to the susceptibility. The charge susceptibility of the system can then be expressed as [148] :

$$\chi^*(\omega_0) = -ig^2 \int \frac{d\omega}{4\pi} Tr\left(\mathcal{S}(\omega)\mathcal{G}^r(\omega)\Sigma^<(w)\mathcal{G}^a(\omega)\right) \tag{6.20}$$

with $\mathcal{S}(\omega) = \hat{\tau}\left(\mathcal{G}^r(\omega+\omega_0) + \mathcal{G}^a(\omega-\omega_0)\right)\hat{\tau}$. In the previous expression the retarded and advanced Green's function and the lesser self-energy $\Sigma^<(w)$ can all be computed from the wire and the leads Hamiltonian. The matrix τ describes the photon-particle coupling in the Nambu⊗spin space. We considered an homogeneous modulation of the chemical potential of the sites by the cavity electric field but we actually checked that

the results presented in the following remains similar for a coupling strength varying linearly along the wire.

In the following, we will mainly focus on the imaginary part of the charge susceptibility which should naturally reveal the effects of dissipative reservoir, but first we will quickly discuss the numerical methods used to perform those computations.

6.2.3 Numerical techniques:

The calculations necessary to access the system charge susceptibility are not overly complex however they can be time consuming. We need two main routines to perform those computations:

- a matrix inversion routine to compute the Green's functions
- an integration routine to compute the charge susceptibility

We suspected from the start that we would be able to focus on short chains, and hence a small number of sites, since the experimental data we used as reference displayed oscillation of the energy splitting between the MBSs. For matrices as small as the ones we have been considering (at most 80×80), we obtain the best performances using full matrices, even if one could think that given their low filling factor, sparse matrices could be more efficient. Furthermore, for the same size argument, there is not point in dedicating more than one core of the processor to the inversion operation. This means that we can very easily parallelize the computation of our maps, as each point can be computed independently.

Being very familiar with the Python language, it was my first choice as it would allow to quickly prototype the calculation. Python can leverage BLAS and LAPACK libraries for fast linear algebra computations (through Numpy) and optimized intergration algorithms through Scipy. However Python is not a "fast" language and the computation of the susceptibility was slow. Other languages, such as Julia, may have been viable options, but I chose to stick with Python and use the Numba library [149] to speed up the computation. Given a Python function, Numba performs a type analysis and, if it can infer all the types and that they can all be converted to a machine friendly representation, it compiles the function down to assembly using the LLVM compiler infrastructure

project. The resulting code can be as fast as hand-written C code in the best of cases. Having used it previously it to perform the simulation presented in chapter 4, I was aware of its capabilities and limitations.

The first limitation was actually that the matrices inversion routines, we needed, were not yet supported. Given the potential huge gain in using this library, I submitted a patch adding support for matrix inversion `https://github.com/numba/numba/pull/1651`. With that added capabilities, we first implemented the computation of the DOS and got very encouraging results: a map such as the ones presented in Fig 6.7 took less than a minute to compute on a simple laptop.

Next, to compute the susceptibility, we need to compute an integral. As we cannot infer the shape of the integrand, we needed to use an integrator with an adaptative step. The Scipy library provides such integrators by wrapping the quadpack FORTRAN library, which relies on Gauss-Kronrod quadrature formula. The first results we obtained, proved interesting but the computation was still too slow (to be carried out on a standard computer). The main bottleneck was the need for the integrator to call a Python-like function rather than a C-function. At the time, Numba did not provide the ability to make a Numba-function looks like a C-function (it does since version 0.26). The chosen solution was to re-write the integration routine using Numba itself. The implementation was tested to produce the same result as the original implementation and did improve the performances[4].

Using the above techniques, the figures presented in the following were obtained in some hours on a laptop. The code was then further optimized to take advantage of multiple cores and generalized to treat other problems such as the one of a semiconducting wire in an helicoïdal magnetic field.

6.2.4 Self-adjoint character signature:

From the simple argument given about the MBSs coupling to light given in section 6.2.1, we expect signatures of transitions occurring at ϵ and an absence of such signatures at 2ϵ. We will hence first look at the susceptibility as a function of the Zeeman energy and

[4] it was not checked since then whether the alternative solution available since Numba 0.26 was faster or not.

the cavity frequency. The results obtained for case A, in which ϵ tends towards 0 in the topological regime, are presented in Fig. 6.8.

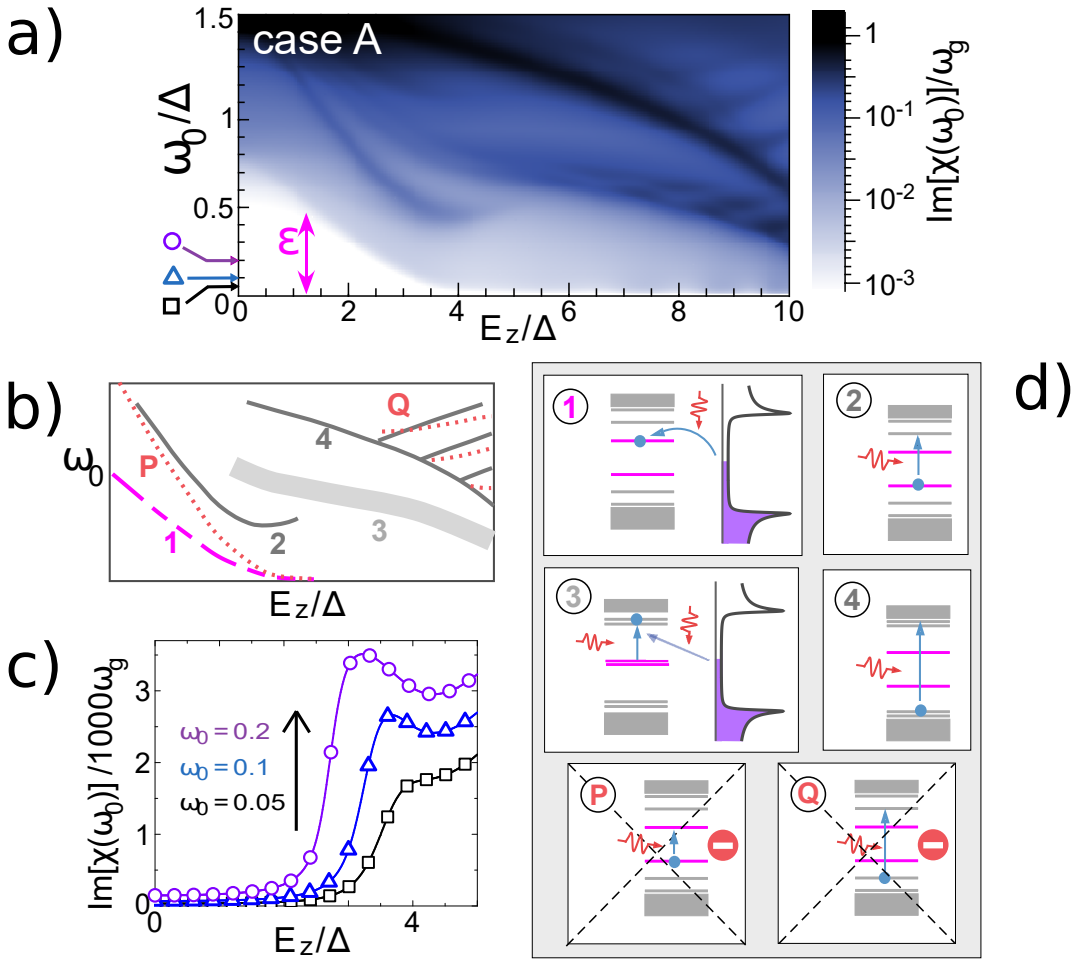

FIGURE 6.8: Case A: Im(χ) vs E_Z and ω_0:
Figure a presents the simulation results and display numerous features which are sketched in figure b. Figure c shows line cuts taken at three different energies of feature 1. The markers match the ones on the left of figure a). Finally figure d describes the nature of each feature sketched on figure b).

1 This feature corresponds to a transition between the subgap DOS of the superconductor and the MBS, it appears at $\omega_0 = \epsilon$

2 This feature corresponds to a transition between the lower MBS and the lower ABS.

3 This feature corresponds to a process involving transitions from both the MBS and the subgap DOS towards higher levels.

4 This feature correspond to transitions between the low energy ABS and the high energy ones.

P and Q These features, which are absent from the calculation, would correspond to transitions between the two MBSs or two non-degenerate ABSs.

Figures extracted from[24]

The susceptibility reveals a wealth of different features. These are sketched in Fig. 6.8b, while the process associated to each line is depicted in Fig. 6.8d.

The feature number one is a step in the susceptibility at $\omega = \epsilon$, which is the energy distance between one of the MBS and the Fermi level of the reservoirs. It is depicted in more details for constant ω in Fig. 6.8c. As in case A, the tunneling towards the normal reservoirs is negligible, we can attribute feature 1 to photo-assisted tunneling between the MBS and the residual subgap DOS of the superconductor. For a well grounded superconducting contact, such processes can only occur if the coupling of the MBS to the light is finite ($\beta \neq 0$). In Fig. 6.8b, the red dotted line marks the position of the $\omega = 2\epsilon$ condition which is not associated with any special feature in Fig. 6.8a. The simultaneous presence of a signal at ϵ and absence of it at 2ϵ occurs on a wide range of E_Z.

These features indicate that we are in presence of a non-degenerate electron-hole conjugated pair. Such a pair is the natural precursor of a Majorana pair. To confirm that it indeed becomes a Majorana pair, one can couple this measurement with a measurement of the DOS. Such a measurement, on top of providing an experimental determination of ϵ, can check that ϵ does vanish with increasing E_Z (or shows several zero-energy crossings), which would be a signature of the spatial isolation of the two MBS formed out of the nondegenerate electron-hole pair. By combining those measurements, one can conclude that the MBSs are self-adjoint.

The other features correspond to photo-assisted transitions towards other states close to the continuum and involve in the case of feature 3 also the subgap DOS of the superconductor. The exact nature of each transition has been deduced from a comparison with the system DOS and the dependence of transitions on the model parameters. Those transitions can be used to rule out other competing explanation. For example, feature 2 frequency-dependence on E_Z can be used to rule-out the case of an isolated zero-energy crossing of two ordinary ABSs caused by a trivial spin-degeneracy lifting. Indeed, in a such a case, its frequency will not depend on E_Z as the initial and final states have the same dispersion with respect to E_Z. This is in contrast to the Majorana case, where it strongly depends on E_Z due to the topological phase transition. Therefore, our setup is also able to rule out the case of a trivial superconducting wire with time-reversal symmetry-breaking impurities. The reader should keep in mind that this can already

be checked in the DOS, as the trivial case will only display a single crossing. However, our setup provides a second check.

We also carried out a similar study in case B as shown in Fig. 6.9. Feature 1 persists in this case as indicated by the pink circle. Furthermore other similar steps are observed on the edges of each conductance "bubble" as indicated by the yellow dots. Interestingly, those steps can have a much stronger contrast than the first one. Furthermore, the associated feature at 2ϵ always remains absent allowing to test the self-adjoint character of the MBSs on a large scale of E_Z.

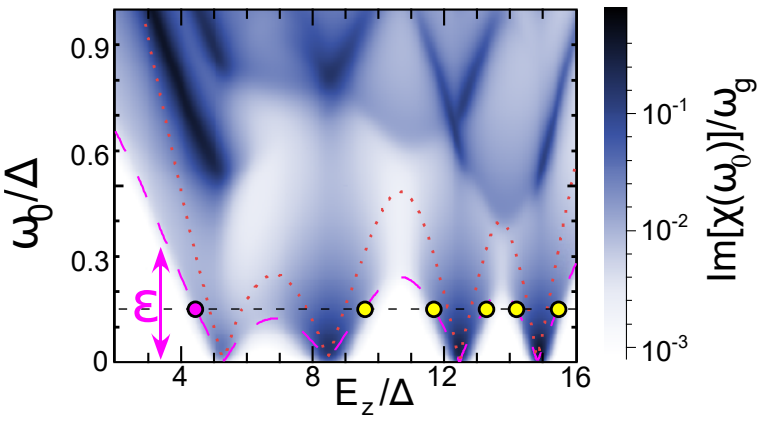

FIGURE 6.9: Case B: Im(χ) vs E_Z and ω_0:
The pink circle corresponds to feature 1 of Fig. 6.8, while the features with the yellow circles are specific to the short nanowire case, but are associated with the same kind of process.
Figure extracted from[24]

Importantly, feature 1 should be challenging to measure but accessible. For example, in case A, feature 1 has an amplitude of $3 \times 10^{-3} g^2/\Delta$ which corresponds to about 15 kHz for $\Delta = 180\mu$eV and a site-cavity coupling of $g = 2\mu\text{eV} \simeq 500$MHz. In case B, for the same parameters we have a contrast on the first step of $6.3 \times 10^{-2} g^2/\Delta$ which corresponds to 340 kHz. Both cases corresponds to situation in which the residual zero-energy DOS in the superconductor is small, about 5% (2.5%) of the maximal DOS, which is similar to the hard-gaps reported in [150]. The experimental challenge is then two fold:

- the cavity quality factor, which is degraded by the applied external field, needs to remain sufficiently large for the the cavity linewidth increase, induced by the wire, to be measurable.
- the coupling between the light and the nanowire needs to be large enough.

Recent developments in high-kinetic inductance resonator with a high-quality factor ($\sim 10^5$) under in plane magnetic fields of several T and large zero-point voltage fluctuations could allow to realize such an experiment with current state of the art experimental techniques [151].

6.2.4.1 Fixed frequency characterization:

So far, we have focused on signals depending on the probing tone energy and hence on the cavity frequency. While, it is experimentally possible to vary the frequency of a resonator [68, 152], it does add to the experiment complexity. It is hence relevant to adapt our predictions to the case of a fixed frequency cavity and use another control parameter to characterize the nano-circuit, such as the chemical potential which can be tuned using gate voltage. In Fig. 6.10, we show $Im(\chi)$ versus the Zeeman energy and the chemical potential for case B, probed at a frequency $\omega_0 = 0.15\Delta$ which corresponds to a frequency of 6.6 GHz for a gap of 180 μeV. Such a frequency was chosen, because it is compatible with present microwave techniques.

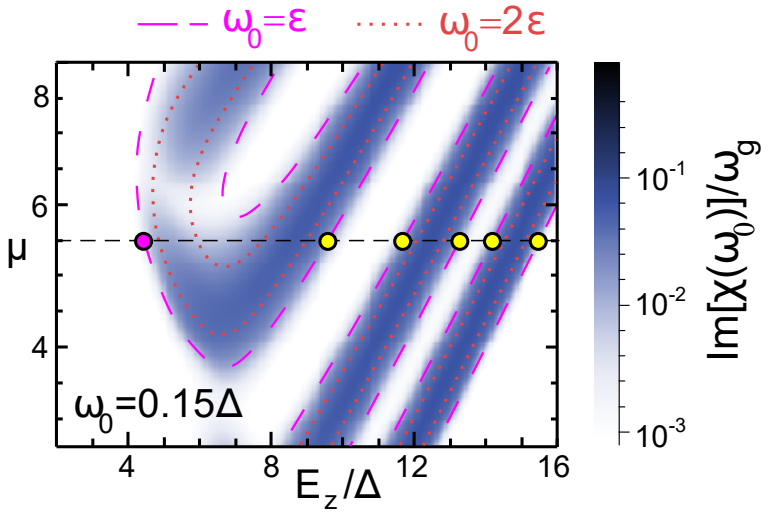

FIGURE 6.10: Case B: Im(χ) vs E_Z and μ:
The charge susceptibility signature display several stripes corresponding to the dispersion of ϵ with μ. Importantly, while the feature 1 at $\omega_0 = \epsilon$ remains clear, no feature at $\omega_0 = 2\,\epsilon$ appear and this no matter the parameters. The dots (pink and yellow) corresponds to the ones of Fig. 6.9
Figure extracted from[24]

In these conditions, $Im(\chi)$ display a series of stripes corresponding to photo-assisted tunneling which reveal the oscillation of ϵ as a function of E_Z and μ. The yellow and

pink points indicate the correspondence between Fig. 6.10 and Fig. 6.9. The stripes are absent for low values of E_Z, where the wire is in its trivial phase and no MBSs are present. Once again, no particular feature is associated with the condition $\omega_0 = 2\epsilon$ shown in red dotted lines in Fig. 6.9, whereas the condition $\omega_0 = \epsilon$ is well visible (as underlined by the pink dashed lines). Once again, it is important to stress that, in an experiment, the red and pink contours can be determined independently of any theory, by performing a conductance measurement to access the DOS of the system. As a conclusion, in the case where ω_0 cannot be varied, a $\mu - E_Z$ map, similar to the gate-field maps presented in chapter 4 for the spin-qubit, gives an efficient way to characterize the light-matter coupling in the circuit.

6.2.4.2 Voltage bias impact study:

In case B, the tunneling towards the superconducting contact and towards the normal leads are of the same order of magnitude which prevents us to discriminate between processes involving the superconductor and the ones involving the normal leads. To discriminate between those processes, we will in this last section study the impact of a bias voltage applied on both normal leads. We will see that it allows to discriminate these processes and to further check that the MBSs are well coupled to the cavity photons.

In Fig. 6.11, we plot the maps for $Im(\chi)$ as a function of E_Z and ω and as a function of E_Z and μ, for case B. We use a bias voltage of $V = 0.32\Delta$.

Fig 6.11a shows clear differences with the case $V = 0$ presented in 6.9. First, we can notice an additional step at lower frequency. This step, marked by a black circle, correspond to tunneling events between the MBSs and the normal reservoirs, which occur at $\omega = \epsilon - e\,V$. Meanwhile, the step, now associated only to the tunneling towards the superconductor, marked in pink, persists. The persistence of the pink circle ensures that the potential difference between the wire and the dot is indeed modulated and the MBSs coupled to light. The separation between the black and pink circle on the E_Z axis is λV with $\lambda \sim e/\Delta(\partial\epsilon/\partial E_Z)$. Furthermore, as soon as $V > \epsilon$ the upper MBS state becomes populated. This can result in two different processes:

- transitions between the upper MBS and upper Andreev bound states can contribute. Those can appear at very low frequency as indicated by the green circle.

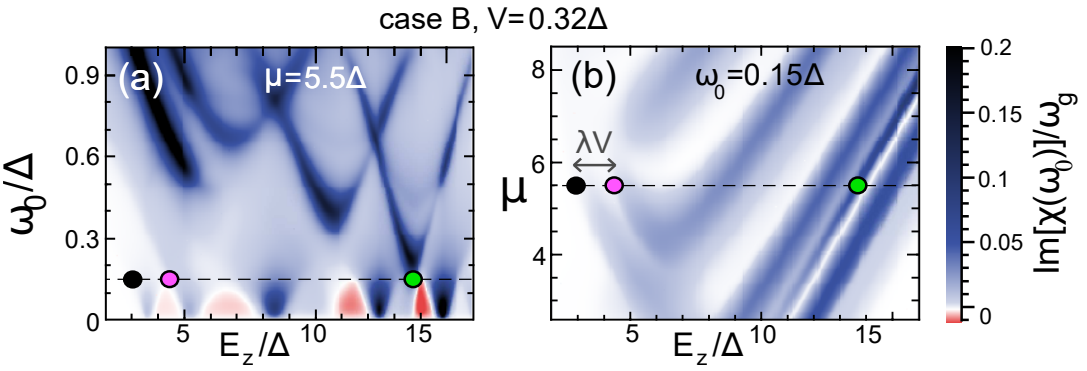

FIGURE 6.11: Case B: bias study:
The plotted maps are similar to the ones presented in Fig. 6.9 and 6.10 but in the presence of a bias voltage. Feature 1 appears doubled in this case, as marked by the black and pink dot, corresponding to the conditions $\omega = \epsilon$ and $\omega = \epsilon - eV$. The magnetic field distance between those point is related to the energy dispersion of the MBSs ($\lambda \sim e/\Delta(\partial\epsilon/\partial E_Z)$). Strikingly, two new features appear, related to the fact that the upper MBS can be populated. First, indicated by a green dot, low energy transition between the upper MBS and ABSs can appear, second a photon emission process, indicated by the positive values of $Im(\chi)$, and related to tunneling between the upper MBS and the normal contact can also appear.
Figure extracted from[24]

These transitions represent another signature of the photon-MBS coupling, although it is not the coupling constant $\beta = M11$ which is involved in this case but rather $N1\alpha$ with $\alpha \neq 1$ and $E\alpha > \varepsilon$.

- second, for $V > \epsilon + \omega_0$, inelastic tunneling between the normal contacts and the upper MBS leads to photon emission, characterized by $Im(\chi) > 0$.

In Fig 6.11b, in which we plot $Im(\chi)$ vs E_Z and μ, the splitting of the contributions of feature 1 is also visible. The transition between the upper MBS and upper Andreev states is also visible but the plot was obtained at too low bias for the photon emission to occur.

As a conclusion, we have shown that photo-induced tunneling processes could be used to demonstrate that a pair of MBSs is well composed of a non-degenerate pair of self-adjoint states. The direct microwave transitions inside the Majorana subspace are forbidden in a wide range of parameters, even in the case where the pair is directly coupled to cavity photons. Importantly, this protocol is independent from any theory if the conductance of the nanowire is measured simultaneously with the cavity response to determine the DOS of the device. Such crossed measurements are routinely achieved with mesoscopic QED devices.

Conclusion and perspectives

Summary and conclusion

In this thesis work, we have seen how the tools of cQED can be adapted to mesoscopic circuits to reach different goals.

Chapter 4 focused on using the particular resources of mesoscopic circuits such as the electronic spin and the possibility to tailor the spectrum of such systems using ferromagnetic contact metals. Using those resources, we demonstrated the first coherent interface between a single spin and microwave photons, reaching a cooperativity of about 2.

While this experiment provides new tools for quantum information processing, chapters 5 and 6 focused on how to use the tools of cQED for studying condensed matter problems. In chapter 5, we proposed a new hybrid system involving a single dot and a transmon both coupled to a microwave cavity and explored how this system could be used to study a single dot circuit, which can be a condensed matter model system. The experimental implementation encountered some difficulties, but those experiments will be carried forward in the lab after the end of this thesis. Chapter 6 proposed to adapt the use of a microwave cavity that already proved extremely useful in quantum dot circuits to the case of Majoranas devices based on semiconducting nanowires. In particular, we proposed a scheme relying on both standard transport measurements and microwave cavity measurements that could reveal the self-adjoint character of Majorana pairs.

Perspectives

Both experiments presented in this thesis work could benefit considerably from improvements in the quality of the sample and in the strength of the light matter coupling. As

discussed in chapter 4, one key improvement would be to work with ultra-clean carbon nanotubes. In devices incorporating such CNTs, one could control the confinement through electrostatic gates contrary to the situation encountered in the devices presented in this work where disorder plays a crucial role. Such a control could in particular allow to control the tunnel barrier between the CNT and the contacts, which would provide an electric control over the Zeeman field induced by the ferromagnetic contacts in the case of the spin qubit experiment and would allow to explore in a controlled manner the different regimes accessible to a single dot in the case of the hybrid dot transmon experiment.

In order to increase the light matter coupling, two directions should probably be explored:

- the geometry of the coupling electrodes can probably be optimized further allowing to increase the coupling.
- coplanar waveguide cavities could be replaced with high impedance resonators [58, 101].

The work presented in this thesis also opens some interesting theoretical perspectives. First, the current lack of understanding of the behavior of the spin-qubit presented in chapter 4 when a even number of electrons occupies the structure calls for more theoretical developments. Second, the properties of the system presented in chapter 5 has been only briefly studied and more work to treat the interaction between the transmon and the dot in a non-instantaneous fashion and to study the response of the transmon when the dot is driven out of equilibrium would be required.

Finally, recent developments in the lab may allow to fabricate CNT based Majorana devices.

Appendix A

Sample fabrication recipes:

This appendix presents the detailed recipes used for the fabrication of the samples. When pertinent the distinction between samples used in chapter 4 and chapter 5 is underlined. We aim at giving practical details for following PhD students and hence refer to specific equipment or recipes used in the ENS clean room. All metallic deposition are performed using the Plassys UHV of the laboratory.

A.1 Stamps:

The fabrication of the quartz stamp used to transfer the CNTs on the sample is quite independent from the main sample fabrication save for the last stages. It is usually more productive to carry out both processes simultaneously.

A.1.1 Quartz preparation:

Start by making a reversed F on the back side so that the side on which the pillars will be patterned can be identified by looking for a F.

A.1.1.1 Cleaning:

Clean the quartz substrate in the dedicated beakers, using the following procedure:

- 5 minutes acetone + ultrasonic waves

- 5 minutes acetone + ultrasonic waves
- 5 minutes IPA + ultrasonic waves

The maximum power can be used for the ultrasonic bath.

A.1.1.2 Resist coating:

Spin coat two layers of PMMA 550, using the 4000-4000-30 program of the spin coater (4000 turns/s^2, 4000 turns/s, 30s). Bake at 165deg C for 15 minutes (alternatively bake for 3 minutes at 185degC).

A.1.1.3 Aluminium deposition:

Deposit of 15 nm of aluminium (5 Å/s). The evaporation can be carried out as soon as the pressure is low enough, at this step there is no resist residue to eliminate (cf following sections)

A.1.2 e-Lithography:

A.1.2.1 SEM:

WARNING : When loading the samples, choose a single substrate orientation with respect to the F. This will make properly orienting the quartz for the stamping step easier.

SEM parameters :

- aperture : 10 μm
- acceleration voltage : 20 kV

Procedure (repeat for each substrate)

- Find bottom-left corner for origin correction, and first point of angle correction.
- Go to the middle of the bottom side and do the angle correction.

- Go to the middle of the chip, make contamination dots (zoom > 50k) to adjust the focus and align the writefield (100×100μm). Use the manual procedure with 5 μm marks and then 1 μm marks.
- FIRST CHIP ONLY: Measure the current.
- Create new position list, D& D the mask, in properties adjust position to 0.05, 0.05, adjust exposure parameters (dose 390 μC/cm^2×0.92, area 20 nm step) and compute dwell time.
- Perform the lithography (Scan position list)

A.1.2.2 Development:

- Remove Al layer in KOH solution (small beaker 2 to 3 pastilles): about 30 s, rinse in water and dry, check under the microscope whether or not all the Al was removed.
- Develop 1 min 50 s to 2 min in MIBK/IPA solution (1/3) and then rinse in IPA and dry. Check development under the microscope.

A.1.2.3 Nickel deposition:

Perform a 1 minute long oxygen etching in the RIE at low power (stripping program) as otherwise the nickel won't stick on the quartz.

Mount the sample on the evaporator sample holder and put the tungsten masks (previously cleaned in IPA + ultrasonic waves) under the binocular lens. One should be extremely careful when manipulating the sample as any scratch will impend the stamping will lead to the formation of spurious pillars.

Evaporate a layer of 2500 Å of Ni (5 Å/s).

Remove any spurious Ni deposit or dust under the binocular lens using a needle tip. DO NOT use ultrasonic wave at this step, as the Ni would be removed.

A.1.3 Ion etching:

NB : When starting this step it is interesting to also start preparing the catalyst deposition step A.1.4.1.

A.1.3.1 RIE:

Use the SiO_2 (160 W) program (requires O_2 and CHF_3), etching last 30 minutes. Quartz etching rate is 47.8 nm/min, Ni etching rate is 1.5 nm/min.

A.1.3.2 De-protection:

Remove the remaining Ni in an iron perchloride solution. This liquid has a dark brown color and is better rinsed in a succession of three bath of de-ionized water (2s, 20s, 1 minute) followed by one minute in water and ultrasonic wave, before being rinsed in IPA and dried.

Remove any spurious pillar using once again a needle tip, and remove dust in IPA. Quickly putting the sample in and out of the solution works best to remove large dust.

A.1.4 CNT growth:

A.1.4.1 Catalyst deposition:

- Put the catalyst solution in the ultrasonic waves bath for 1 hour.
- Let the catalyst solution sediment for 1 hour.
- (Need two people) Deposit two drops of the catalyst solution (from the surface) on the sample and dry immediately. (NB: can be done alone by having the tweezers holding the sample leaning on a beaker).

A.1.4.2 Growth:

- Check which panel is used and swap the hose if necessary (CNT).

- Load the samples into the quartz tube (last third).
- Switch on the computer (+ control_ four2 program), the oven, the flow meters power supply.
- Open the Ar, H_2, and CH_4 bottles and check the pressure.
- Purge all the lines at the same time for 3 minutes and check the flows (Ar: , H_2: , CH_4:).
- Start heating under Ar flow, and wait for the temperature to reach 900degC (about 20 minutes).
- Perform a 8 minutes H_2 flash.
- Do the growth under CH_4 and H_2 flows for 10 minutes.
- Start cooling down under Ar and H_2 flows. DON'T FORGET TO TURN THE HEATING OFF. (the CH_4 bottle can be closed)
- Under 350degC, stop the H_2 flow and open the oven. (the H_2 bottle can be closed)
- About room temperature, stop everything and get the samples.
- CHECK THAT ALL THE BOTTLES ARE CLOSED

After the growth the quartz cannot be cleaned anymore so the growth should be done just before the stamping if possible (the day before is fine).

A.2 Sample preparation:

A.2.1 Gold crosses:

The gold crosses patterned at this stage are used for all subsequent alignments.

A.2.1.1 Cleaning

- 5 min acetone + ultrasonic waves
- 5 min acetone + ultrasonic waves

- 5 min IPA + ultrasonic waves
- stripping O_2 in the RIE (program stripping) for 10 minute.
- PMMA coating (500 nm) using the 4000-4000-30 program.
- Baking at 165degC for 15 minutes

A.2.1.2 e-Lithography

NB: the resist must be scratched to allow the electron to flow, use the tip of metallic tweezers to scratch the resist.

SEM parameters :

- aperture : 10 μm
- acceleration voltage : 20 kV

Procedure (repeat for each substrate)

- find the bottom-left corner of the sample for origin correction, and first point of angle correction.
- go to the middle of the bottom side and do the angle correction.
- go to the middle of the chip, make contamination dots (zoom > 50k) to adjust the focus and align the write-field (100×100μm). Use the manual procedures with 5 μm marks and then 1 μm marks.
- save write-field parameters and colon parameters, switch to 120μm aperture.
- WITHOUT moving the stage, redo the focus on the spot and adjust the beam shift. Save the colon parameters.
- FIRST CHIP ONLY: Measure the current (DO NOT re-save the colon parameters).
- create new position list, D& D the 10μm parameters, the mask, the 120μm parameters, the mask.

- for the masks: in properties adjust position to 0.05, 0.05, adjust exposure parameters (dose 390 μC/cm^2×0.85, area 20 nm step) and compute the dwell time.
- scan position list

A.2.1.3 Gold deposition:

- Develop 1 min 50 s to 2 min in MIBK/IPA solution (1/3) and then rinse in IPA and dry. Check development under the microscope.
- Evaporate a thin layer of Ti (50Å) then the gold layer (450Å).
- Put the samples in an acetone bath warmed up at 50degC, after 20 minutes lift the majority of the gold using an eyedropper. Transfer the samples in a second acetone bath warm it and put it 1s in the ultrasonic wave bath. Finish lifting, rinse in IPA (30s) and dry. Check whether or not all the unwanted gold has been lifted, if no back to the beginning. Finally perform a 5 to 10 minute O_2 stripping (RIE).

A.2.2 Cavity fabrication:

A.2.2.1 Nobium deposition:

Because niobium has a high sublimation temperature, the evaporators cryo-panels needs to be filled with liquid nitrogen which takes about 20 minutes. Monitor the pressure of the nitrogen tank during the filling. Once the panels are cold, evaporate 100 to 150 nm of Nb at 10 Å/s.

A.2.2.2 Lithography:

Next, we define the niobium parts that need to be etched using either electronic or optical lithography. The electronic lithography is similar to the ones previously presented up to the following steps:

- we use a MMA-MAA/PMMA bilayer. First we heat the sample for 3 minutes at 185 degC and leave it to cool down for one minute before the first layer of resist,

which is baked for 3 minutes at 185 degC. We repeat the same steps (cooling, deposition, baking) for the second layer.

- after the angle correction, perform a third alignment step on the gold crosses previously lithographed in the middle of the ship.
- as all structures are large, only use the 120 μm aperture.
- to speed up the process we use 200×200 μm write fields. Given the size of those fields the alignment procedure must be carried out with great care.

After the lithography, develop the sample 45 seconds in a MIBK/IPA solution (1/3) and then rinse it in IPA.

The optical process was mostly abandoned during this work and won't be described in details here.

A.2.2.3 RIE:

Perform the etching of the exposed niobium in the RIE using the dedicated recipe (SF6 based). Monitor the progress of the etching using the reflectometry measurement. At first the etching clean the niobium surface and the reflectivity increases. At one point the reaction chamber appears misty and the reflectivity starts dropping. Depending on the substrate oxyde layer thickness, one can either observe a minimum of reflectivity or a abrupt change of slope in the drop, both of which mark the end of the niobium etching. Overetch for about 10s.

A.2.2.4 Cleaning:

Once the etching is completed, the sample need to be thoroughly cleaned to remove any resist residues that may decrease the quality factor of the cavity. This is done through several steps of cleaning in hot acetone (45 degC). Ultrasonic cleaning should be avoided save if the sample is placed in protective encasing in Teflon as otherwise shocks with the beaker may break the niobium film.

Finally the cleaning should be completed by 10 minutes of low power O_2 etching in the RIE (stripping program).

A.3 Stamping:

A.3.1 Mask preparation:

The stamping process is performed on the clean room MJB4 optical lithography machine. First the quartz substrate must be glued on a glass plate. As glass plates cannot be recycled, we use simple microscope slides.

- clean the microscope slide in IPA + ultrasonic bath for 1 minute and dry
- glue two bands of double sided tape side by side on the slide. One should be careful to minimize the number of bubbles trapped.
- glue the quartz on the tape. A light pressure on the quartz corner is sufficient to get it glued. One should be careful to put quartz far enough from one another to be able to stamp using a single quartz at a time.

A.3.2 Stamping:

To minimize the impact of spurious pillar or small angles between the sample chip and the quartz, we stamp in one area at a time.

- locate stamps on the quartz starting from the corner of the quartz chip.
- roughly align the pillars and the opening in the cavity ground plane.
- reduce the distance between the two chips by focusing alternatively on each one and adjust the alignment as necessary.
- when the pillars come into contact of the sample chip, one can observe interference patterns inside the pillars while pressing one onto the other (purple-blue oscillations). Keep increasing the pressure till the color disappear (one get a dark purple). At this point one can separate the two chips again or keep increasing the pressure. In the second case, if the pillars start breaking into pieces one must quickly separate the two chips to avoid depositing too much quartz pieces on the sample.

A.3.3 Localization:

The CNTs are localized using the SEM.

- set the acceleration voltage to 2kV
- do the usual alignment steps (origin and angle corrections, and three point alignment on the gold crosses at the center of the sample.
- adjust the focus and stigmation on one of the "large" gold cross nearby the stamping area. This step is crucial as poor settings will not allow to localize the CNTs. One should see the gold roughness at a magnification of 50 000.
- align the writefield onto the four small gold crosses around the stamping area (layer 63). In order to improve the precision one should perform "slow" scans (point average 10, line average 2).
- take one image of the full field to localize the big chunks of quartz and then take zoomed images (10×10 μm or 5×5 μm) that have no overlap.

A.4 Fine lithography:

A.4.1 Transmon lithography:

As mentioned in chapter 5, the transmon can be fabricated either before or after the quantum circuits, and so far we have not identified a preferable order for those two operations.

A.4.1.1 Resist coating:

The transmon lithography requires three layers of resist: two layers of MMA/MAA and one top layer of PMMA. The deposition is done as follows :

- heat up the sample for 3 minutes at 185 degC and let it cool down 1 minute
- spin-coat the first layer of resist (MMA/MAA) using the 4000/4000/30 recipe of the coating machine (see details in A.1.1.2)

- bake for 3 minutes at 185 degC and cool down 1 minute
- proceed as previously for the next two layers (MMA/MAA and PMMA)

A.4.1.2 Lithography:

As the transmon consist both in large pads forming the geometric capacitance and a small bridge for the JJ fabrication, we use 10μm and 120μm apertures and 20kV acceleration voltage. The procedure is similar to the ones previously described, once again the settings are done at 10 μm:

- perform the origin and angle correction and a three-point alignment on the central crosses.
- do a second three point alignment using the crosses around the transmon area.
- go to the top edge at the vertical of one of the cross around the transmon opening and do the focus on a resist crack. This focus is important for the next step and can be done at a magnification of 80000.
- go the left part of one of the crosses and make a contamination dots in the resist.
- use those dots to align the write-field (fields of 100×100μm
- switch to 120 μm aperture, correct for the beam shift and align the write-field
- measure both currents
- prepare the lithography using the following doses: 10 μm: 1.4×390μC/cm^2 120 μm: 0.85×390μC/cm^2

After the lithography the samples are developed for 17 seconds in a MIBK/IPA solution (1/3) and then rinsed in IPA.

A.4.1.3 Al deposition:

As the evaporator is not fitted with an Ar gun the samples needs to be left under vacuum in the evaporator for several hours (8-10 hours) before proceeding with the deposition. The deposition comports three steps:

- deposition of a first layer of aluminum (300 Å) at 0° (displayed -4°) and 10 Å/s
- oxidation for 5 minutes in the load-lock under a pressure of 5 mbar of pure O_2
- deposition of a second layer of aluminum (300 Å) at -40° (displayed 324°) and 10 Å/s

After the evaporation, the lift-off is performed in ho acetone and the sample subsequently rinsed in IPA.

A.4.2 Dot lithographies:

We usually perform two lithography steps on the CNTs to define the circuits: one for the gates and one for the contacts. They are quite similar, save when the contacts are made out PdNi.

A.4.2.1 Resist coating:

For gates and for contacts that are not made out of PdNi, spin coat a single layer of PMMA using the 4000/4000/30 recipe. For contacts made out of PdNi, we use a diluted PMMA solution leading after spin-coating (same recipe) to a layer of 330 nm.

A.4.2.2 Lithography:

After the localization step A.3.3, one can design the lithography masks (one per area) by loading the images in the SEM software (note that images should be re-centered around 0). The lithography procedure described below is done entirely at 10μm:

- perform the origin and angle correction and a three-point alignment on the central crosses.
- measure the current
- adjust the focus by doing a contamination dot in the vicinity of the dot area
- adjust the write-field by scanning the layer 63 of the mask corresponding to the area. Use the same procedure as in section A.3.3.

- do the lithography with a dose of $1.25 \times 390 \mu C/cm^2$
- repeat all steps save the first two on the other areas of the sample.

The sample are developed 2 minutes in a MIBK/IPA solution (1/3) and then rinsed in IPA.

A.4.2.3 Metal deposition:

In order to eliminate possible resist residues, the sample spend several hours (8-10 hours) in the evaporator prior to the metallic deposition.

Gates:

- 15 Å of Al (5Å/s), 10 minutes of oxidation under 1 mbar of O_2 (in the load-lock)
- **Repeat previous three times in total**
- 400 Å of Al (10Å/s) and 200 Å of Pd (3Å/s)

Normal contacts:

- 50 Å of Ti (3Å/s)
- 450 Å of Au (5Å/s)

Ferromagnetic contacts:

- 300 Å of PdNi (3Å/s)
- 50 Å of Pd (3Å/s)

Appendix B

Derivation of the effective Hamiltonian for the SD-transmon system:

This appendix is dedicated to the detailed derivation of the effective Hamiltonian used in chapter 5. We remind the reader that we start from the following Hamiltonian:

$$\begin{aligned}\hat{H} =&\hat{H}_{cavity} + \hat{H}_{transmon} + \hat{H}_{dot} + \hat{H}_{contacts} + \hat{H}_{tunnel} + \hat{H}_{bath} + \\ &\hat{H}_{cavity<->bath} + \hat{H}_{cavity<->transmon} + \hat{H}_{cavity<->dot}\end{aligned} \tag{B.1}$$

with :

$$\hat{H}_{cavity} = \hbar\,\omega_{cav}\hat{a}^\dagger\,\hat{a} \tag{B.2}$$

$$\hat{H}_{transmon} = \hbar\,\omega_t\,\hat{q}^\dagger\hat{q} - \hbar\,\frac{\alpha}{12}(\hat{q}^\dagger + \hat{q})^4 \tag{B.3}$$

$$\hat{H}_{dot} = \epsilon\,\hat{n} + \frac{U}{2}\,\hat{n}\,(\hat{n}-1) \tag{B.4}$$

$$\hat{H}_{contacts} = \sum_{a=L,R}\sum_{k,\sigma}\xi_{k,\sigma}\hat{c}^\dagger_{a,k,\sigma}\hat{c}_{a,k,\sigma} \tag{B.5}$$

$$\hat{H}_{tunnel} = \sum_{a=L,R}\sum_{k,v,\sigma}\left(t_a\,\hat{c}_{a,k,\sigma}\hat{d}^\dagger_{v,\sigma} + h.c.\right) \tag{B.6}$$

$$\hat{H}_{bath} = \sum_{\mu}\hbar\omega_\mu\hat{b}^\dagger_\mu\hat{b}_\mu \tag{B.7}$$

$$\hat{H}_{cavity<->bath} = \hbar\sum_{\mu}\left(g_\mu\,\hat{b}_\mu + g^*_\mu\,\hat{b}^\dagger_\mu\right)\left(\hat{a}+\hat{a}^\dagger\right) \tag{B.8}$$

$$\hat{H}_{cavity<->transmon} = 2\,i\,\beta\,e\,V_0\,\left(\hat{q}^\dagger - \hat{q}\right)\left(\hat{a}^\dagger + \hat{a}\right) \tag{B.9}$$

$$\hat{H}_{cavity<->dot} = \hbar\,g_{dot}\,\hat{n}\,\left(\hat{a}+\hat{a}^\dagger\right) \tag{B.10}$$

B.1 Closed system Hamiltonian :

In a first time, we only consider the closed system dot-cavity-transmon and forget about the bathes for the time being. We separate the Hamiltonian as follows :

$$H = \underbrace{H_{cavity} + H_{transmon} + H_{dot}}_{H_0} + \underbrace{H_{cavity<->transmon} + H_{cavity<->dot}}_{H_t} \tag{B.11}$$

The first step consists in deriving the S operator defining the transformation. We start from the following ansatz :

$$\begin{aligned}\hat{S} &= \sum_k \alpha_k\,\hat{a}\,|k\rangle\langle k+1| + \hat{a}^\dagger\,|k+1\rangle\langle k|) + \beta_k\,(\hat{a}^\dagger\,|k\rangle\langle k+1| + \hat{a}\,|k+1\rangle\langle k|) + i\,\gamma\,\hat{n}\,\left(\hat{a}-\hat{a}^\dagger\right)\\ &= \hat{S}_{tra} + \hat{S}_{dot}\end{aligned} \tag{B.12}$$

As we work in the large $\frac{E_J}{E_C}$, we have replaced q by $\sum_k \sqrt{k+1}|k\rangle\langle k+1|$ with $|k\rangle$ the eigenstates of the transmon. As a consequence the prefactor of the term in $(\hat{q}^\dagger - \hat{q})$

in H_t becomes g_{tra}. To eliminate the first order coupling between the cavity and the transmon, we then need :

$$\hat{S}_{tra} = \hat{q}_\alpha \, \hat{a}^\dagger + \hat{q}_\alpha^\dagger \, \hat{a} + \hat{q}_\beta \, \hat{a} + \hat{q}_\beta^\dagger \, \hat{a}^\dagger \tag{B.13}$$

with $\hat{q}_\alpha$ and $\hat{q}_\beta$ defined as follow:

$$\hat{q}_\alpha = \sum_k \frac{g_{tra}\sqrt{k+1}}{\omega_t - \alpha\,(k+1) - \omega_{cav}} \, |k\rangle\langle k+1| \tag{B.14}$$

$$\hat{q}_\beta = \sum_k \frac{g_{tra}\sqrt{k+1}}{\omega_t - \alpha\,(k+1) + \omega_{cav}} \, |k\rangle\langle k+1| \tag{B.15}$$

For the dot the computation gives:

$$\hat{S}_{dot} = i\,\frac{g_{dot}}{\omega_{cav}}\,\hat{n}\,\left(\hat{a} - \hat{a}^\dagger\right) \tag{B.16}$$

To get the effective Hamiltonian of the closed system, we then compute $i[S, H_t]$ and project on the vacuum of the cavity:

$$\begin{aligned}\hat{H}_{\text{eff closed}} = &\left(\epsilon - \frac{U}{2}\right)\hat{n} + \left(\frac{U}{2} - \hbar\frac{g_{dot}^2}{2\,\omega_{cav}}\right)\hat{n}^2 + \\ &+ \sum_k \hbar\left(\omega_k + \frac{g_{tra}^2}{2}\left(k\,\beta_k^- - (k+1)\,\beta_{k+1}^+\right)\right)|k\rangle\langle k| \\ &+ i\hbar\,\frac{g_{dot}\,g_{tra}}{2}\,\hat{n}\sum_k \sqrt{k+1}\left(-\frac{1}{\omega_{cav}} + \beta_{k+1}^- + \beta_{k+1}^+\right)\left(|k+1\rangle\langle k| - |k\rangle\langle k+1|\right)\end{aligned} \tag{B.17}$$

with:

$$\beta_k^\pm = \frac{1}{\omega_t - \alpha\,k \pm \omega_{cav}} \tag{B.18}$$

The Hamiltonian, we obtain, contains both renormalization of the dot and transmon energies by the cavity and a direct coupling term between the transmon and the cavity. We could simplify it further but first we will look at the re-normalization of the bathes.

B.1.0.1 Re-normalization of the baths:

We have two such terms to re-normalize :

$$\hat{H}_{tunnel} = \sum_{a=L,R} \sum_{k,v,\sigma} \left(t_a \, \hat{c}_{a,k,\sigma} \hat{d}^\dagger_{v,\sigma} + h.c. \right) \tag{B.19}$$

$$\hat{H}_{cavity<->bath} = \hbar \sum_{\mu} g_\mu (b_\mu + b^\dagger_\mu)(\hat{a} + \hat{a}^\dagger) \tag{B.20}$$

As $\hat{n} = \sum_{v,\sigma} \hat{n}_{v,\sigma}$, we have $[\hat{n}, \hat{d}_{v,\sigma}]_m = (-1)^m \hat{d}_{v,\sigma}$. Using the Baker-Campbell-Hausdorff formula, we can compute the re-normalized term :

$$\begin{aligned}
\hat{H}_{\text{tunnel eff}} = \hat{H}_{tunnel} &- \frac{g_{dot}}{\omega_{cav}} (\hat{a} - \hat{a}^\dagger) \sum_{a=L,R} \sum_{k,v,\sigma} \left(t_a \, \hat{c}_{a,k,\sigma} \hat{d}^\dagger_{v,\sigma} - t^*_a \, \hat{c}^\dagger_{a,k,\sigma} \hat{d}_{v,\sigma} \right) \\
&+ \frac{g^2_{dot}}{2\,\omega^2_{cav}} \left(\hat{a} - \hat{a}^\dagger \right)^2 \sum_{a=L,R} \sum_{k,v,\sigma} \left(t_a \, \hat{c}_{a,k,\sigma} \hat{d}^\dagger_{v,\sigma} + t^*_a \, \hat{c}^\dagger_{a,k,\sigma} \hat{d}_{v,\sigma} \right) \\
&+ i \, \frac{g_{tra} \, g_{dot}}{2\,\omega_{cav}} \sum_{a=L,R} \sum_{k,v,\sigma} \left(t_a \, \hat{c}_{a,k,\sigma} \hat{d}^\dagger_{v,\sigma} - t^*_a \, \hat{c}^\dagger_{a,k,\sigma} \hat{d}_{v,\sigma} \right) \\
&\sum_{l} \sqrt{l+1} \left(\beta^-_{l+1} + \beta^+_{l+1} \right) \left(|k+1\rangle\langle k| + |k\rangle\langle k+1| \right)
\end{aligned} \tag{B.21}$$

Here, we have not yet projected on the empty state of the cavity and we can see that we can have some photo-assisted tunneling processes that may be important to describe properly in the presence of a bias voltage. For the present treatment we will discard them.

For the cavity bath coupling, the re-normalization leads to:

$$\hat{H}_{\text{cavity<->bath-eff}} = \sum_{\mu} g_\mu \, (\hat{b}_\mu + \hat{b}^\dagger_\mu) \left(\sum_k i \, g_{tra} \, \sqrt{k+1} \left(\beta^-_{k+1} + \beta^+_{k+1} \right) \left(|k+1\rangle\langle k| - |k\rangle\langle k+1| \right) \right) \tag{B.22}$$

The computation of those two terms achieves the transformation and makes in particular appear the direct coupling of the transmon to the cavity bath. As in chapter 2, this will describe the relaxation of the qubit through the emission of photon in the cavity but here the results concern all the levels and not just the first exited one.

B.1.0.2 Approximations :

So far, we have used two approximations to simplify the calculations:

- the transmon approximation ($\frac{E_C}{E_J} << 1$) has been made to simplify the expression of the coupling
- the cavity has been assumed to remain in its ground state and we have already mentioned that this hypothesis may not always be verified.

We can go further by estimating some terms. We introduce $\Delta = \omega_{cav} - (\omega_t - \alpha)$, which is, up to the dispersive shift, the detuning between the cavity and the qubit.

Off resonant corrections:

In a number of the previous expressions appear the sum of β_k^- and β_k^+. Comparing the magnitude of the two terms it turns out that we can neglect terms in β_k^+.

$$\begin{aligned} \frac{\beta_k^+}{\beta_k^-} &= \frac{\omega_t - \alpha\, k - \omega_{cav}}{\omega_t - \alpha\, k + \omega_{cav}} \\ &\simeq \frac{\Delta}{\omega_{01} + \omega_{cav}} \end{aligned} \tag{B.23}$$

For reasonable values ($\Delta = 1.5\, GHz$, $\omega_{cav} = 7.5\, GHz$), this ratio is of the order of 0.1 which allows us to neglect β_k^+ terms in the following. It should be noted that as these terms are never isolated it will be easy to come back on that approximations if the need arises.

Tunneling re-normalization:

The leading order in the tunneling re-normalization is in $\frac{g_{dot}}{\omega_{cav}}$ which is, even in an

optimistic perspective, no larger than 5 per cent. As long as we work without any bias voltage we can hence neglect those corrections. The corrections resulting from the transmon state will be at least 5 times smaller (as we will work in the dispersive of the transmon) and hence can also be neglected. We will hence not consider any correction to the tunneling.

Simplified Hamiltonian:

The use of the previously discussed approximations allows to reduce the Hamiltonian of the system. We introduce the operators $\hat{\tau}^i_{x,j} = |j+i\rangle\langle j| + |j\rangle\langle j+i|$ and $\hat{\tau}^i_{y,j} = i\left(|j+i\rangle\langle j| + |j\rangle\langle j+i|\right)$:

$$\begin{aligned}\hat{H} = &\left(\epsilon - \frac{U}{2}\right)\hat{n} + \left(\frac{U}{2} - \hbar\frac{g_{dot}^2}{\omega_{cav}}\right)\hat{n}^2 \\ &+ \sum_j \hbar\left(\omega_j + g_{tra}^2\frac{-j/2}{\Delta+\alpha\,(j-1)}\right)|j\rangle\langle j| \\ &+ \hbar\, g_{tra}\, g_{dot}\, n\sum_j \sqrt{j+1}\left(\frac{1}{\Delta+\alpha\, j} + \frac{1}{\omega_{cav}}\right)\hat{\tau}^1_{y,j} \\ &+ \sum_{a=L,R}\sum_{k,\sigma}\xi_{k,\sigma}\hat{c}^\dagger_{a,k,\sigma}\hat{c}_{a,k,\sigma} + \sum_{a=L,R}\sum_{k,v,\sigma}\left(t_a\,\hat{c}_{a,k,\sigma}\hat{d}^\dagger_{v,\sigma} + h.c.\right) \\ &+ \sum_\mu \hbar\omega_\mu \hat{b}^\dagger_\mu\hat{b}_\mu + \sum_\mu g_\mu\left(\hat{b}_\mu + \hat{b}^\dagger_\mu\right)\left(\sum_j g_{tra}\,\frac{\sqrt{j+1}}{\Delta+\alpha\, j}\hat{\tau}^1_{y,j}\right)\end{aligned} \tag{B.24}$$

Appendix C

Master equation for the transmon subject to the dot noise:

This appendix is dedicated to the detailed derivation of the master equation for the transmon dynamics in which we treated the dot as a source of electrical noise. We start from the following Hamiltonian which describes the transmon as an anharmonic oscillator and does not detail the dynamic of the number of electron $\hat{n}$ in the dot:

$$\begin{aligned}\hat{H} = & \underbrace{\sum_j \hbar\,\tilde{\omega}_j |j\rangle\langle j| + \sum_\mu \hbar\omega_\mu \hat{b}_\mu^\dagger \hat{b}_\mu}_{\hat{H}_0} \\ & + \underbrace{\hbar\,\hat{n} \sum_j \tilde{g}_{td,j}\hat{\tau}_{y,j}}_{\hat{H}_{dt}} \\ & + \underbrace{\sum_\mu g_\mu\,(\hat{b}_\mu + \hat{b}_\mu^\dagger)\left(\sum_j g_{tra}\,\frac{\sqrt{j+1}}{\Delta+\alpha\,j}\hat{\tau}_{y,j}\right)}_{\hat{H}_{bath}}\end{aligned} \tag{C.1}$$

with $\tilde{\omega}_j = \omega_j + g_{tra}^2 \frac{-j/2}{\Delta+\alpha\,(j-1)}$, $\tilde{g}_{td,j} = g_t\,g_{dot}\,\sqrt{j+1}\left(\frac{1}{\Delta+\alpha\,j} + \frac{1}{\omega_{cav}}\right)$ and $\hat{\tau}_{y,j} = i(|j+1\rangle\langle j| - |j\rangle\langle j+1|$.

We will now derive the equation of evolution of the density matrix in the interaction picture the way we did in chapter 2. We start from:

$$i\hbar\frac{d\tilde{\rho}}{dt} = [\hat{H}_{dt} + \hat{H}_{bath}, \tilde{\rho}] \tag{C.2}$$

We then integrate formally the above equation and re-inject the result in it. Next we take the trace on the bathes, and use the decorrelation approximation to explicit the partial traces. As before we assume no correlations exist between the dot and the bath representing relaxation by emission in the cavity. The above leads to:

$$\begin{aligned}\frac{d}{dt}Tr(\tilde{\rho})(t) = &- i\,\bar{n}\Big[\sum_j \tilde{g}_{td,j}\hat{\tau}^1_{y,j}(t), Tr((\tilde{\rho})(0)\Big] \\ &- \int_0^t \sum_j \sum_l \tilde{g}_j\,\tilde{g}_j \Big(Tr\left(n(t)\,n(t-\tau)\,\tilde{\rho}\right)\left(\tilde{\tau}_{y,j}(t)\tilde{\tau}_{y,l}(t-\tau)\tilde{\rho} - \tilde{\tau}_{y,l}(t-\tau)\tilde{\rho}\tilde{\tau}_{y,j}(t)\right) \\ &\qquad + Tr\left(n(t-\tau)\,n(t)\,\tilde{\rho}\right)\left(\tilde{\rho}\tilde{\tau}_{y,l}(t-\tau)\tilde{\tau}_{y,j}(t) - \tilde{\tau}_{y,j}(t)\tilde{\rho}\tilde{\tau}_{y,l}(t-\tau)\right)\Big) \\ &- \frac{1}{\hbar^2}\int_0^\infty \Big[\hat{H}_{bath}(t), \Big[\hat{H}_{bath}(t-\tau), Tr(\tilde{\rho})(t-\tau)\Big]\Big] d\tau \end{aligned} \tag{C.3}$$

As before[1], we can replace $\tilde{\rho}(t-\tau)$ by $\rho(t)$, which we simply noted $\tilde{\rho}$ above. We recover the term related to the decay of the transmon as predicted by the Purcell effect and similar terms for the impact of the dots.

The decorrelation approximation to treat the Purcell bath is perfectly justified in the framework of the Caldeira-Legget model, as the bath is Markovian. In the case of the dot, it is worth examining in more details the validity of this assumption. As discussed in chapter 2, the decorrelation approximation consists in neglecting the correlations that can appear between the system and its "bath". Those correlations appear on a time scale set by $1/g_{td}$ here, and decay on a time scale given by the auto-correlation time of the bath:

- in the Coulomb blockade regime, we have shown in chapter 2 that $\langle\hat{n}(t)\hat{n}(t-\tau)\rangle$ decay on a time scale set by $1/\Gamma$.
- in the Kondo regime, all the physical properties are governed by the Kondo temperature T_K

[1] See chapter 2 for the full explanation

As a conclusion, the previous treatment will remain valid as long as:

- $g_{dt}/\Gamma \ll 1$ in the Coulomb regime. As we can expect g_{dt} to reach at most several hundreds of MHZ, this can possibly be false for very closed dots, but in these cases the previous sequential treatment should be valid.
- $\hbar\, g_{dt}/k_B\, T_K \ll 1$ in the Kondo regime, which should always be true as Kondo peaks with $T_K < 5GHz$ are rare.

To simplify the expression of the evolution of the density matrix, we will write explicitly $\hat{\tau}_{y,j}(t) = i\sum_{\eta=\pm1}\eta\hat{\tau}_{\eta,j}e^{i\,\eta\,\omega_j\,t}$ and split the $\hat{n}$ in its average value $\bar{n}$, which will still depends on the dot chemical potential, and quantum fluctuations and write $\hat{n} = \bar{n} + \delta\hat{n}$, with $\langle\delta\hat{n}\rangle = 0$. Furthermore, as the electronic correlation decays on short time scale, and because within the decoupling approximation it makes no sense to study the system evolution on time scales that are not much larger than the auto-correlation time of the bathes, we push all integrals involving them to infinity and neglect all terms which oscillate on short time scales compared to the qubit lifetime (RWA). This select $\eta' = -\eta$ and $j = l$. We then get:

$$\begin{aligned}\frac{d}{dt}\tilde{\rho}(t) = &+\sum_j g_{tra}^2\,\frac{j+1}{(\Delta+\alpha\,j)^2}\kappa\left(\hat{\tau}_{-,j}\tilde{\rho}(t)\hat{\tau}_{+,j} - \frac{1}{2}\left(\tilde{\rho}(t)\hat{\tau}_{+,j}\hat{\tau}_{-,j} + \hat{\tau}_{+,j}\hat{\tau}_{-,j}\tilde{\rho}(t)\right)\right)\\ &-\sum_j\sum_\eta \tilde{g}_{\mu,j}^2\Bigg(\int_0^t \bar{n}^2 e^{i\,\eta\,\omega_j\,\tau}\left[\tilde{\tau}_{\eta,j},\left[\tilde{\tau}_{-\eta,j},\tilde{\rho}\right]\right]\\ &\qquad+\int_0^\infty e^{i\,\eta\,\omega_j\,\tau}\langle\delta\hat{n}(t)\delta\hat{n}(t-\tau)\rangle\left(\hat{\tau}_{\eta,j}\hat{\tau}_{\eta',l}\tilde{\rho} - \hat{\tau}_{\eta',l}\tilde{\rho}\hat{\tau}_{\eta,j}\right)\\ &\qquad+\int_0^\infty e^{i\,\eta\,\omega_j\,\tau}\langle\delta\hat{n}(t-\tau)\delta\hat{n}(t)\rangle\left(\tilde{\rho}\hat{\tau}_{\eta',l}\hat{\tau}_{\eta,j} - \hat{\tau}_{\eta,j}\tilde{\rho}\hat{\tau}_{\eta',l}\right)\Bigg)\end{aligned} \tag{C.4}$$

In the following we will assume that the dot correlation functions are invariant under time translation which will allows us re-write the previous expression in term of $S_{nn}(\omega) = \int_{-\infty}^{\infty} dt e^{i\,\omega\,t}\langle\delta n(t)\delta n(0)\rangle$ (using $\langle\delta n(t)\delta n(0)\rangle = \int_{-\infty}^{\infty}\frac{d\omega}{2\,\pi}e^{-i\,\omega\,t}S(\omega)$). Computing the integrals and summing over η yields the following expression:

$$\begin{aligned}\frac{d}{dt}\tilde{\rho}(t) = &+ \sum_j g_{tra}^2 \frac{j+1}{(\Delta+\alpha\, j)^2}\kappa D(\tau_{-,j})\tilde{\rho} \\ &- \sum_j \tilde{g}_j^2 \Bigg(i\,\frac{\bar{n}^2}{\omega_j}\left[\tilde{\tau}^1_{+,j}\tilde{\tau}^1_{-,l} - \tilde{\tau}^1_{-,j}\tilde{\tau}^1_{+,j}, \tilde{\rho}\right] \\ &\qquad - S_{nn}(\omega_j) D(\hat{\tau}^1_{-,j}) - S_{nn}(-\omega_j) D(\hat{\tau}^1_{+,j}) \\ &\qquad + \frac{i}{2\,\pi}\left(\mathcal{P}\left(\frac{1}{\eta\,\omega_j - \omega}\right)\int S_{nn}(\omega) d\omega \left[\hat{\tau}^1_{+,j}\hat{\tau}^1_{-,j}, \rho\right] - \right. \\ &\qquad\qquad \left. \mathcal{P}\left(\frac{1}{\eta\,\omega_j + \omega}\right)\int S_{nn}(\omega) d\omega \left[\hat{\tau}^1_{-,j}\hat{\tau}^1_{+,j}, \rho\right]\right)\end{aligned}$$

where D is the super-operator associated with a collapse operator in the Linblad form $D(\hat{\tau})\,\rho = \hat{\tau}\tilde{\rho}\hat{\tau}^\dagger - \frac{1}{2}\left(\tilde{\rho}\hat{\tau}^\dagger\hat{\tau} + \hat{\tau}^\dagger\hat{\tau}\tilde{\rho}\right)$ and $\mathcal{P}\left(\frac{1}{\omega}\right)$ is the Cauchy principal value.

Appendix D

Characterization of the transmon:

This appendix details the characterization of the transmon beyond the spectroscopy and Rabi oscillations measurements presented in the main text.

In theory if we knew exactly the drive power on the transmon we could infer from the Rabi oscillations the coupling of the transmon to the electric field. However, we cannot determine this power with sufficient precision in practice to make such an estimate pertinent. In order to access the coupling, we will measure the dispersive shift χ induced by the transmon state on the cavity frequency. If we had not projected the Hamiltonian, we obtained in appendix B, on the empty state of the cavity we would have obtained a cavity term depending on the transmon state which reads:

$$H_{cav} = \hbar \left(\omega_{cav} + \sum_j g_{tra}^2 \frac{\Delta - \alpha}{(\Delta + \alpha\, j)\,(\Delta - \alpha + \alpha\, j)} |j\rangle\langle j| \right) a^\dagger a \tag{D.1}$$

This means that when measuring the cavity transmission spectrum we will get different central frequencies depending on the qubit state. Such a measurement will allow us to extract the coupling between the cavity and the transmon.

To perform this measurement, we first transfer the qubit in the exited state using a π pulse and measure the cavity transmission at a given frequency. We then repeat this experiment at different frequencies to obtain the cavity spectrum when the qubit is exited. We also perform a control experiment in which the qubit is not exited. The results of such a measurement are presented in Fig. D.1.

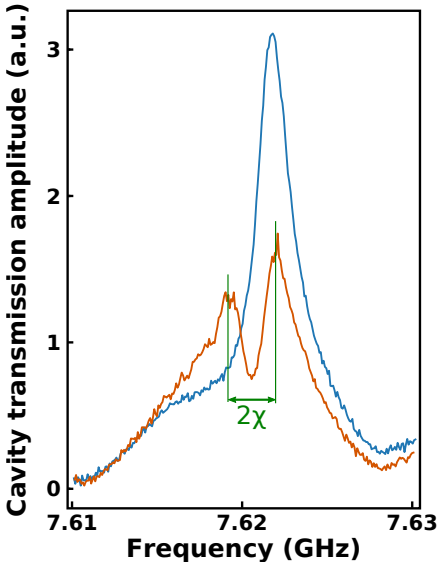

FIGURE D.1: Dispersive shift:
Measure of the frequency shift induced by the transmon state on the cavity. The orange curve corresponds to measurements in which a π is applied to the qubit before measuring the cavity transmission, for the blue one no pulse is applied. The two peaks observed for the orange curve corresponds to the two possible states of the transmon, since it relaxes during the measurement leading to a finite probability to find it in its ground state.

If the measurement was perfect, we would observe a single peak when the qubit has been driven to its exited state. However, because our pulses are not optimized and mostly because our read-out time is not short compared to the transmon lifetime, the ground state happens to also be populated which explains the presence of two peaks. From this measurement, we can extract the dressed cavity frequency (transmon in its ground state) $\tilde{\omega}_{cav}$ and the difference between the two cavity frequencies that we will note $2\,\chi$, whose expression can be computed from (D.1).

$$\tilde{\omega}_{cav} = \omega_{01} + \Delta + \frac{g_{tra}^2}{\Delta} = 2\,\pi\,7.625 GHz \tag{D.2}$$

$$2\,\chi = g_{tra}^2 \frac{1}{\Delta}\frac{2\,\alpha}{\Delta+\alpha} = 2\,\pi\,4 MHz \tag{D.3}$$

From the four quantity extracted so far we can deduce the model parameters:

$$\alpha = 2\,(\tilde{\omega}_{01} - \tilde{\omega}_{02}/2) + \chi \simeq 2\,\pi\,420MHz \tag{D.4}$$

$$\omega_{01} = \frac{1}{1 + \dfrac{3\,\chi}{2\,\alpha}} \left(\tilde{\omega}_{01} + \frac{\chi}{2} \left(1 + \frac{2\,\tilde{\omega}_{01} + \tilde{\omega_{cav}}}{\alpha} \right) \right) = 2\,\pi\,4.47GHz \tag{D.5}$$

$$\Delta = 2\,\tilde{\omega}_{01} + \tilde{\omega}_{c}av - 3\,\omega_{01} = 2\,\pi\,3.1GHz \tag{D.6}$$

$$g_{tra}^2 = \frac{\chi\,\Delta}{\alpha}\,(\Delta + \alpha) \rightarrow g_{tra} = 2\,\pi\,230MHz \tag{D.7}$$

Of course here, given the small value of χ and the low quality of the data used to measure it, those corrections are not relevant. However I give the full formulas for the benefit of the reader.

From the cavity transmission we can also extract the linewidth κ:

$$\kappa \simeq 2\,\pi\,1.4MHz \tag{D.8}$$

Those numbers are not too far from the one used in the previous simulations with the notable exception of the qubit bare frequency. It should be noted that the sample on which those data have been acquired is among the first one we made, and even though no full sample has been fabricated, we later tested another transmon whose parameters were much closer to the ones used in the simulation.

We also checked two other important quantities on this sample:

- the transmon relaxation time T_1
- the transmon decoherence time T_2^*

In our model, the lifetime of the transmon is only limited by the emission of photons in the cavity. As a consequence, our prediction will be accurate only if this process is the dominant decay process, as the dot influence the transmon decay through its ability to absorb photons. To measure the decay, we use the procedure described in chapter 3 which consists in applying a π pulse on the transmon and measure the population at a variable later time.

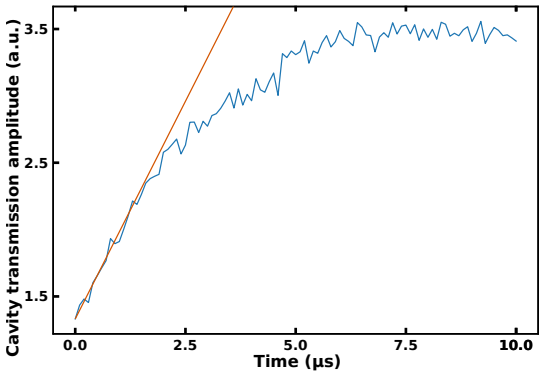

FIGURE D.2: Transmon relaxation time:
After preparing the trasmon in its exited state using a π pulse, we measure the cavity transmission which can be mapped to the transmon population. We observe the usual exponential decay (growth for the cavity transmission). The orange line is a guide to the eyes indicating the slope at the origin.

Fig. D.2 displays the result of such a measurement. We do observe the expected exponential decay of the exited state and we can extract $T_1 \simeq 2.6\mu s$. This time need to be compared to the Purcell decay rate given by $g_{tra}^2/\Delta^2\,\kappa$. From the previous characterization, the Purcell decay rate limits T_1 to $21\mu s$ which is much larger than the time we measure. However for the parameters we target, the Purcell limit is expected to be much shorter (1.76 μs) in which case it should be the dominant process.

Ramsey fringes measurements are a powerful tool to determine with precision the frequency of the qubit and detect the small shifts that can be induced by the dot occupation. Furthermore, the dephasing induced by the dot, that was not studied theoretically so far, may contain important information. For both reasons we are interested in having T_2^* as large as possible and ideally limited by T_1

We performed some Ramsey fringes measurements on this sample, whose typical result is illustrated in Fig. D.3. Even though the decoherence time was not as long as could be expected ($T_2^* \simeq 1\mu s$), the result is encouraging since, as previously mentioned, those results have been obtained on an early sample which had not yet been fully optimized.

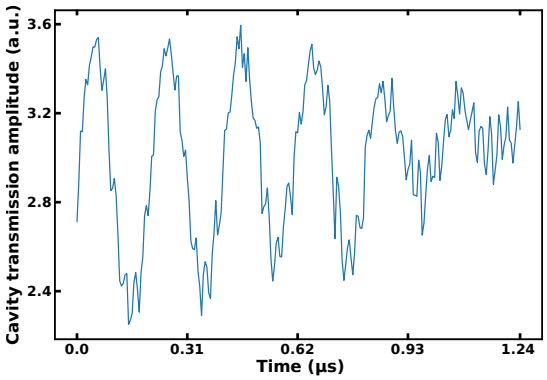

FIGURE D.3: Transmon Ramsey fringes:
Ramsey fringes obtained by using a drive tone detuned by 2 MHz from the transmon frequency.

Bibliography

1. M. Arndt *et al.*, *Nature* **401**, 680–682, ISSN: 0028-0836 (Oct. 14, 1999).
2. L. P. Kouwenhoven, D. G. Austing, S. Tarucha, *Reports on Progress in Physics* **64**, 701, ISSN: 0034-4885 (2001).
3. E. A. Laird *et al.*, *Reviews of Modern Physics* **87**, 703–764 (July 28, 2015).
4. D. Loss, D. P. DiVincenzo, *Physical Review A* **57**, 120–126 (Jan. 1, 1998).
5. L. M. K. Vandersypen *et al.*, *Nature* **414**, 883–887, ISSN: 0028-0836 (Dec. 20, 2001).
6. J. M. Raimond, M. Brune, S. Haroche, *Reviews of Modern Physics* **73**, 565–582 (Aug. 28, 2001).
7. A. Wallraff *et al.*, *Nature* **431**, 162–167, ISSN: 0028-0836 (Sept. 9, 2004).
8. C. Janvier *et al.*, *Science* **349**, 1199–1202, ISSN: 0036-8075, 1095-9203 (Sept. 11, 2015).
9. M. R. Delbecq *et al.*, *Physical Review Letters* **107**, 256804 (Dec. 16, 2011).
10. T. Frey *et al.*, *Physical Review Letters* **108**, 046807 (Jan. 25, 2012).
11. H. Toida, T. Nakajima, S. Komiyama, *Physical Review Letters* **110**, 066802 (Feb. 6, 2013).
12. A. Wallraff, A. Stockklauser, T. Ihn, J. R. Petta, A. Blais, *Physical Review Letters* **111**, 249701 (Dec. 12, 2013).
13. J. J. Viennot, M. R. Delbecq, M. C. Dartiailh, A. Cottet, T. Kontos, *Physical Review B* **89**, 165404 (Apr. 4, 2014).
14. J. Majer *et al.*, *Nature* **449**, 443–447, ISSN: 0028-0836 (Sept. 27, 2007).
15. M. A. Sillanpää, J. I. Park, R. W. Simmonds, *Nature* **449**, 438–442, ISSN: 0028-0836 (Sept. 27, 2007).

16. M. Veldhorst *et al.*, *Nature* **526**, 410–414, ISSN: 0028-0836 (Oct. 15, 2015).

17. J. R. Petta *et al.*, *Science* **309**, 2180–2184, ISSN: 0036-8075, 1095-9203 (Sept. 30, 2005).

18. L. Childress, A. S. Sørensen, M. D. Lukin, *Physical Review A* **69**, 042302 (Apr. 5, 2004).

19. Y.-Y. Liu *et al.*, *Science* **347**, 285–287, ISSN: 0036-8075, 1095-9203 (Jan. 16, 2015).

20. A. Cottet, T. Kontos, *Physical Review Letters* **105**, 160502 (Oct. 15, 2010).

21. J. J. Viennot, M. C. Dartiailh, A. Cottet, T. Kontos, *Science* **349**, 408–411, ISSN: 0036-8075, 1095-9203 (July 24, 2015).

22. L. E. Bruhat *et al.*, *Physical Review X* **6**, 021014, ISSN: 2160-3308 (May 2016).

23. M. M. Desjardins *et al.*, *Nature* **545**, 71–74, ISSN: 0028-0836 (May 4, 2017).

24. M. C. Dartiailh, T. Kontos, B. Douçot, A. Cottet, *Physical Review Letters* **118**, 126803 (Mar. 23, 2017).

25. Y. Oreg, G. Refael, F. von Oppen, *Physical Review Letters* **105**, 177002 (Oct. 20, 2010).

26. R. M. Lutchyn, J. D. Sau, S. Das Sarma, *Physical Review Letters* **105**, 077001 (Aug. 13, 2010).

27. V. Mourik *et al.*, *Science* **336**, 1003–1007, ISSN: 0036-8075, 1095-9203 (May 25, 2012).

28. A. Das *et al.*, *Nature Physics* **8**, 887–895, ISSN: 1745-2473 (Dec. 2012).

29. M. T. Deng *et al.*, *Nano Letters* **12**, 6414–6419, ISSN: 1530-6984 (Dec. 12, 2012).

30. H. O. H. Churchill *et al.*, *Physical Review B* **87**, 241401 (June 6, 2013).

31. S. M. Albrecht *et al.*, *Nature* **531**, 206–209, ISSN: 0028-0836 (Mar. 10, 2016).

32. H. Zhang *et al.*, *arXiv:1603.04069 [cond-mat]*, arXiv: 1603.04069, (2017; http://arxiv.org/abs/1603.04069) (Mar. 13, 2016).

33. C. Monroe, D. M. Meekhof, B. E. King, W. M. Itano, D. J. Wineland, *Physical Review Letters* **75**, 4714–4717 (Dec. 18, 1995).

34. Y. Kaluzny, P. Goy, M. Gross, J. M. Raimond, S. Haroche, *Physical Review Letters* **51**, 1175–1178 (Sept. 26, 1983).

35. D. Deutsch, R. Jozsa, *Proceedings of the Royal Society of London A: Mathematical, Physical and Engineering Sciences* **439**, 553–558, ISSN: 1364-5021, 1471-2946 (Dec. 8, 1992).

36. P. Shor, *SIAM Journal on Computing* **26**, 1484–1509, ISSN: 0097-5397 (Oct. 1, 1997).

37. M. Brune, S. Haroche, V. Lefevre, J. M. Raimond, N. Zagury, *Physical Review Letters* **65**, 976–979 (Aug. 20, 1990).

38. A. Lupaşcu *et al.*, *Nature Physics* **3**, 119–125, ISSN: 1745-2473 (Feb. 2007).

39. N. Ofek *et al.*, *Nature* **536**, 441–445, ISSN: 0028-0836 (Aug. 25, 2016).

40. A. A. Houck, J. Koch, M. H. Devoret, S. M. Girvin, R. J. Schoelkopf, *Quantum Information Processing* **8**, 105–115, ISSN: 1570-0755, 1573-1332 (June 1, 2009).

41. J. Koch *et al.*, *Physical Review A* **76**, 042319 (Oct. 12, 2007).

42. J. M. Gambetta *et al.*, *IEEE Transactions on Applied Superconductivity* **27**, 1–5, ISSN: 1051-8223 (Jan. 2017).

43. M. Stern *et al.*, *Physical Review Letters* **113**, 123601 (Sept. 19, 2014).

44. J. J. Pla *et al.*, *Nature* **489**, 541–545, ISSN: 0028-0836 (Sept. 27, 2012).

45. L. Childress *et al.*, *Science* **314**, 281–285, ISSN: 0036-8075, 1095-9203 (Oct. 13, 2006).

46. A. L. Falk *et al.*, *Nature Communications* **4**, 1819, ISSN: 2041-1723 (May 7, 2013).

47. E. A. Laird *et al.*, *Physical Review B* **82**, ISSN: 1098-0121, 1550-235X, DOI: 10.1103/PhysRevB.82.075403, arXiv: 1005.0273, (2017; http://arxiv.org/abs/1005.0273) (Aug. 4, 2010).

48. S. Foletti, H. Bluhm, D. Mahalu, V. Umansky, A. Yacoby, *Nature Physics* **5**, 903–908, ISSN: 1745-2473 (Dec. 2009).

49. X. Wu *et al.*, *Proceedings of the National Academy of Sciences* **111**, 11938–11942, ISSN: 0027-8424, 1091-6490 (Aug. 19, 2014).

50. S. Nadj-Perge, S. M. Frolov, E. P. A. M. Bakkers, L. P. Kouwenhoven, *Nature* **468**, 1084–1087, ISSN: 0028-0836, 1476-4687 (Dec. 23, 2010).

51. M. Pioro-Ladriere *et al.*, *Nature Physics* **4**, 776–779, ISSN: 1745-2473, 1745-2481 (Oct. 2008).

52. F. Martins *et al.*, *Physical Review Letters* **116**, 116801 (Mar. 16, 2016).

53. E. Kawakami *et al.*, *Nature Nanotechnology* **9**, 666–670, ISSN: 1748-3387 (Sept. 2014).

54. H. Bluhm *et al.*, *Nature Physics* **7**, 109–113, ISSN: 1745-2473 (Feb. 2011).

55. F. K. Malinowski *et al.*, *Nature Nanotechnology* **12**, 16–20, ISSN: 1748-3387 (Jan. 2017).

56. J. H. Prechtel *et al.*, *Nature Materials* **15**, 981–986, ISSN: 1476-1122 (Sept. 2016).

57. X. Mi, J. V. Cady, D. M. Zajac, P. W. Deelman, J. R. Petta, *Science* **355**, 156–158, ISSN: 0036-8075, 1095-9203 (Jan. 13, 2017).

58. A. Stockklauser *et al.*, *Physical Review X* **7**, 011030 (Mar. 9, 2017).

59. L. E. Bruhat *et al.*, *arXiv:1612.05214 [cond-mat]*, arXiv: 1612.05214, (2017; http://arxiv.org/abs/1612.05214) (Dec. 15, 2016).

60. P. Andrich *et al.*, *arXiv:1701.07401 [cond-mat, physics:quant-ph]*, arXiv: 1701.07401, (2017; http://arxiv.org/abs/1701.07401) (Jan. 25, 2017).

61. M. V. Gustafsson *et al.*, *Science* **346**, 207–211, ISSN: 0036-8075, 1095-9203 (Oct. 10, 2014).

62. M. R. Delbecq *et al.*, *Nature communications* **4**, 1400, ISSN: 2041-1723 (Jan. 2013).

63. J. P. Reithmaier *et al.*, *Nature* **432**, 197–200, ISSN: 0028-0836 (Nov. 11, 2004).

64. P. Michler *et al.*, *Science* **290**, 2282–2285, ISSN: 0036-8075, 1095-9203 (Dec. 22, 2000).

65. S. Strauf *et al.*, *Physical Review Letters* **96**, 127404 (Mar. 31, 2006).

66. D. I. Schuster *et al.*, *Nature* **445**, 515–518, ISSN: 0028-0836 (Feb. 1, 2007).

67. R. Deblock, Y. Noat, H. Bouchiat, B. Reulet, D. Mailly, *Physical Review Letters* **84**, 5379–5382 (June 5, 2000).

68. A. Palacios-Laloy *et al.*, *Journal of Low Temperature Physics* **151**, 1034–1042, ISSN: 0022-2291, 1573-7357 (May 1, 2008).

69. L. Quiroga, "Quenching across a quantum phase transition in radiation-semiconductor systems", ICPS conf., 2016.

70. R. J. Schoelkopf, A. A. Clerk, S. M. Girvin, K. W. Lehnert, M. H. Devoret, *arXiv:cond-mat/0210247*, arXiv: cond-mat/0210247, (2017; http://arxiv.org/abs/cond-mat/0210247) (Oct. 10, 2002).

71. A. Facon *et al.*, *Nature* **535**, 262–265, ISSN: 0028-0836 (July 14, 2016).

72. J.-M. Raymond, *private communication* (2017).

73. M. Pelliccione *et al.*, (http://arxiv.org/abs/1510.02780) (Oct. 2015).

74. M. Pelliccione, B. A. Myers, L. M. A. Pascal, A. Das, A. C. Bleszynski Jayich, *Physical Review Applied* **2**, 054014 (Nov. 25, 2014).

75. D. Schmid-Lorch *et al.*, *Nano Letters* **15**, 4942–4947, ISSN: 1530-6984, 1530-6992 (Aug. 12, 2015).

76. O. Donati, G. P. Missiroli, G. Pozzi, *American Journal of Physics* **41**, 639–644, ISSN: 0002-9505 (May 1, 1973).

77. L. Bruhat, PhD thesis, PSL Research University, Apr. 1, 2016, (2017; https://tel.archives-ouvertes.fr/tel-01430414/document).

78. P. W. Anderson, *Physical Review* **124**, 41–53 (Oct. 1, 1961).

79. K. Blum, *Density Matrix Theory and Applications* (Springer Science & Business Media, Oct. 31, 1996), 352 pp., ISBN: 978-0-306-45341-0.

80. W. J. De Haas, G. J. Van Den Berg, *Physica* **3**, 440–449, ISSN: 0031-8914 (June 1, 1936).

81. J. Kondo, *Progress of Theoretical Physics* **32**, 37–49, ISSN: 0033-068X (July 1, 1964).

82. S. Sasaki *et al.*, *Nature* **405**, 764–767, ISSN: 0028-0836 (June 15, 2000).

83. P. Jarillo-Herrero *et al.*, *Nature* **434**, 484–488, ISSN: 0028-0836 (Mar. 24, 2005).

84. J. R. Schrieffer, P. A. Wolff, *Physical Review* **149**, 491–492 (Sept. 16, 1966).

85. K. G. Wilson, *Reviews of Modern Physics* **47**, 773–840 (Oct. 1, 1975).

86. W. G. van der Wiel *et al.*, *Reviews of Modern Physics* **75**, 1–22 (Dec. 17, 2002).

87. G. Abulizi, A. Baumgartner, C. Schönenberger, *physica status solidi (b)* **253**, 2428–2432, ISSN: 03701972 (Dec. 2016).

88. L.-J. Wang *et al.*, *Applied Physics Letters* **99**, 112117, ISSN: 0003-6951, 1077-3118 (Sept. 12, 2011).

89. T. Hayashi, T. Fujisawa, H. D. Cheong, Y. H. Jeong, Y. Hirayama, *Physical Review Letters* **91**, 226804 (Nov. 26, 2003).

90. K. D. Petersson, J. R. Petta, H. Lu, A. C. Gossard, *Physical Review Letters* **105**, 246804 (Dec. 8, 2010).

91. G. Cao *et al.*, *Nature Communications* **4**, 1401, ISSN: 2041-1723 (Jan. 29, 2013).

92. Z. Shi *et al.*, *Physical Review B* **88**, 075416 (Aug. 13, 2013).

93. B. Yurke *et al.*, *Physical Review A* **39**, 2519–2533 (Mar. 1, 1989).

94. T. Yamamoto *et al.*, *Applied Physics Letters* **93**, 042510, ISSN: 0003-6951 (July 28, 2008).

95. N. Bergeal *et al.*, *Nature* **465**, 64–68, ISSN: 0028-0836 (May 6, 2010).

96. M. Tinkham, *Introduction to Superconductivity: Second Edition* (2017; http://store.doverpublications.com/0486435032.html).

97. V. Ambegaokar, A. Baratoff, *Physical Review Letters* **10**, 486–489 (June 1, 1963).

98. A. Cottet, PhD thesis, Université Pierre et Marie Curie - Paris VI, Sept. 30, 2002, (2017; https://tel.archives-ouvertes.fr/tel-00003511/document).

99. A. Blais, R.-S. Huang, A. Wallraff, S. M. Girvin, R. J. Schoelkopf, *Physical Review A* **69**, 062320 (June 29, 2004).

100. M. Göppl *et al.*, *Journal of Applied Physics* **104**, 113904, ISSN: 0021-8979 (Dec. 1, 2008).

101. A. Bienfait *et al.*, *Nature* **531**, 74–77, ISSN: 0028-0836 (Mar. 3, 2016).

102. A. O. Caldeira, A. J. Leggett, *Physical Review Letters* **46**, 211–214 (Jan. 26, 1981).

103. A. A. Clerk, M. H. Devoret, S. M. Girvin, F. Marquardt, R. J. Schoelkopf, *Reviews of Modern Physics* **82**, 1155–1208 (Apr. 15, 2010).

104. S. Fan, W. Suh, J. D. Joannopoulos, *JOSA A* **20**, 569–572, ISSN: 1520-8532 (Mar. 1, 2003).

105. A. Cottet, T. Kontos, B. Douçot, *Physical Review B* **91**, 205417 (May 13, 2015).

106. H. Grabert, M. Devoret, *Single Charge Tunneling - Coulomb Blockade Phenomena In | Hermann Grabert | Springer*, (2017; http://www.springer.com/gp/book/9781475721683).

107. Z. Leghtas *et al.*, *Physical Review A* **87**, 042315 (Apr. 15, 2013).

108. J. Gao *et al.*, *Applied Physics Letters* **92**, 152505, ISSN: 0003-6951 (Apr. 14, 2008).

109. A. J. Annunziata *et al.*, *Nanotechnology* **21**, 445202, ISSN: 0957-4484 (2010).

110. B. W. Maxfield, W. L. McLean, *Physical Review* **139**, A1515–A1522 (Aug. 30, 1965).

111. J. M. Chow, PhD thesis, 2010, (2017; http://adsabs.harvard.edu/abs/2010PhDT.....83C).

112. J. J. Viennot, J. Palomo, T. Kontos, *Applied Physics Letters* **104**, 113108, ISSN: 0003-6951 (Mar. 17, 2014).

113. Z. Jin *et al.*, *Nano letters* **7**, 2073–9, ISSN: 1530-6984 (July 2007).

114. J. Viennot, PhD thesis, Ecole Normale Supérieure de Paris - ENS Paris, June 6, 2014, (2017; https://tel.archives-ouvertes.fr/tel-01062841/document).

115. J. M. Binder *et al.*, *arXiv:1611.09146 [physics, physics:quant-ph]*, arXiv: 1611.09146, (2017; http://arxiv.org/abs/1611.09146) (Nov. 28, 2016).

116. S. Sahoo *et al.*, *Nature Physics* **1**, 99–102, ISSN: 1745-2473 (Nov. 2005).

117. C. Feuillet-Palma *et al.*, *Physical Review B* **81**, 115414 (Mar. 10, 2010).

118. J. R. Hauptmann, J. Paaske, P. E. Lindelof, *Nature Physics* **4**, 373–376, ISSN: 1745-2473 (May 2008).

119. A. Cottet, T. Kontos, W. Belzig, C. Schönenberger, C. Bruder, *Europhysics Letters* **74**, 320–326, ISSN: 0295-5075, 1286-4854 (Apr. 1, 2006).

120. X. Hu, Y.-x. Liu, F. Nori, *Physical Review B* **86**, 035314 (July 16, 2012).

121. J.-Y. Chauleau, *Physical Review B* **84**, DOI: 10.1103/PhysRevB.84.094416 (2011).

122. G. A. Steele, G. Gotz, L. P. Kouwenhoven, *Nature Nanotechnology* **4**, 363–367, ISSN: 1748-3387 (June 2009).

123. E. A. Laird, F. Pei, L. P. Kouwenhoven, *Nature Nanotechnology* **8**, 565–568, ISSN: 1748-3387 (Aug. 2013).

124. A. Cottet *et al.*, *Semiconductor Science and Technology* **21**, S78, ISSN: 0268-1242 (2006).

125. J. Waissman *et al.*, *Nature Nanotechnology* **8**, 569–574, ISSN: 1748-3387 (Aug. 2013).

126. B. Reulet, M. Ramin, H. Bouchiat, D. Mailly, *Physical Review Letters* **75**, 124–127 (July 3, 1995).

127. J. Basset, H. Bouchiat, R. Deblock, *Physical Review B* **85**, 085435 (Feb. 27, 2012).

128. R. Deblock, E. Onac, L. Gurevich, L. P. Kouwenhoven, *Science* **301**, 203–206, ISSN: 0036-8075, 1095-9203 (July 11, 2003).

129. J. Basset *et al.*, *Physical Review Letters* **108**, 046802 (Jan. 24, 2012).

130. E. Majorana, *Il Nuovo Cimento (1924-1942)* **14**, 171, ISSN: 1827-6121 (Apr. 1, 1937).

131. A. Y. Kitaev, *Physics-Uspekhi* **44**, 131, ISSN: 1063-7869 (2001).

132. C. Nayak, S. H. Simon, A. Stern, M. Freedman, S. Das Sarma, *Reviews of Modern Physics* **80**, 1083–1159 (Sept. 12, 2008).

133. D. A. Ivanov, *Physical Review Letters* **86**, 268–271 (Jan. 8, 2001).

134. J. Klinovaja, D. Loss, *Physical Review Letters* **112**, 246403 (June 18, 2014).

135. J. Alicea, A. Stern, *Physica Scripta* **2015**, 014006, ISSN: 1402-4896 (T164 2015).

136. K. Zuo, V. Mourik, (2017; https://repository.tudelft.nl/islandora/object/uuid%3A3fd0aed5-000c-4e50-a772-269436637fc4?collection=research) (2016).

137. E. J. H. Lee *et al.*, *Physical Review Letters* **109**, 186802 (Oct. 31, 2012).

138. D. Rainis, L. Trifunovic, J. Klinovaja, D. Loss, *Physical Review B* **87**, 024515 (Jan. 25, 2013).

139. D. I. Pikulin, J. P. Dahlhaus, M. Wimmer, H. Schomerus, C. W. J. Beenakker, *New Journal of Physics* **14**, 125011, ISSN: 1367-2630 (2012).

140. A. Cottet, T. Kontos, B. Douçot, *Physical Review B* **88**, 195415 (Nov. 13, 2013).

141. J. Liu, A. C. Potter, K. T. Law, P. A. Lee, *Physical Review Letters* **109**, 267002 (Dec. 28, 2012).

142. O. Dmytruk, M. Trif, P. Simon, *Physical Review B* **92**, 245432 (Dec. 21, 2015).

143. J. Sköldberg, T. Löfwander, V. S. Shumeiko, M. Fogelström, *Physical Review Letters* **101**, 087002 (Aug. 22, 2008).

144. M. Schiró, K. Le Hur, *Physical Review B* **89**, 195127 (May 21, 2014).

145. B. K. Agarwalla, M. Kulkarni, S. Mukamel, D. Segal, *Physical Review B* **94**, 035434 (July 21, 2016).

146. B. K. Agarwalla, M. Kulkarni, S. Mukamel, D. Segal, *Physical Review B* **94**, 121305 (Sept. 30, 2016).

147. A.-P. Jauho, N. S. Wingreen, Y. Meir, *Physical Review B* **50**, 5528–5544 (Aug. 15, 1994).

148. A. Cottet *et al.*, *arXiv:1709.00466 [cond-mat, physics:quant-ph]*, arXiv: 1709.00466, (2017; http://arxiv.org/abs/1709.00466) (Sept. 1, 2017).

149. S. K. Lam, A. Pitrou, S. Seibert, presented at the Proceedings of the Second Workshop on the LLVM Compiler Infrastructure in HPC, 7:1–7:6, ISBN: 978-1-4503-4005-2, DOI: 10.1145/2833157.2833162, (2017; http://doi.acm.org/10.1145/2833157.2833162).

150. W. Chang *et al.*, *Nature Nanotechnology* **10**, 232–236, ISSN: 1748-3387 (Mar. 2015).

151. N. Samkharadze *et al.*, *Physical Review Applied* **5**, 044004 (Apr. 7, 2016).

152. M. Sandberg *et al.*, *Applied Physics Letters* **92**, 203501, ISSN: 0003-6951 (May 19, 2008).

Résumé

Ce travail de thèse est centré autour de deux aspects des technologies quantiques: le calcul quantique et la mesure quantique. Il s'appuie sur la boîte à outils de la lumière micro-onde, développé en électrodynamique quantique, pour sonder des circuits mésoscopiques. Ces circuits, fabriqués ici à base de nanotubes de carbone, peuvent être conçus comme des bits quantiques ou comme des systèmes modèles de la matière condensée, et cette thèse explore les deux aspects. La réalisation d'une interface spin-photon cohérente illustre le premier. L'expérience repose sur l'utilisation de contacts ferro-magnétiques pour induire un couplage spin-orbit artificiel dans une double boîte quantique. Ce couplage hybride les degrés de liberté de charge et de spin de l'électron. En incluant ce circuit dans une cavité micro-onde, dont le champ électrique peut être couplé à la charge, nous réalisons une interface spin-photon. Un second project est centré sur l'utilisation de boites quantiques comme systèmes modèles pour l'étude de problèmes de matière condensée. Ce projet consiste à coupler, via une cavité micro-onde, un qubit supraconducteur, qui servira de sonde peu invasive, et une boîte quantique unique. Un tel circuit peut exhiber différents comportements dont l'effet Kondo, qui est un effet à N-corps. Dans ce travail, nous présentons à la fois une étude théorique, et des travaux expérimentaux. Finalement une proposition théorique pour détecter le caractère auto-adjoint des fermions de Majorana en utilisant une cavité micro-onde, est présenté.

Mots Clés

cQED, boîte quantique, spin, nanotube de carbone

Abstract

This thesis work is centered around two key aspects of quantum technologies: quantum information processing and quantum sensing. It builds up onto the microwave light toolbox, developed in circuit quantum electrodynamics, to investigate the properties of mesosocopic circuits. Those circuits, made out here of carbon nanotubes, can be designed to act as quantum bits of information or as condensed matter model system and this thesis explore both aspects. The realization of a coherent spin-photon interface illustrates the first one. The experiment relies on ferromagnetic contacts to engineer an artificial spin-orbit coupling in a double quantum dot. This coupling hybridizes the spin and the charge degree of freedom of the electron in this circuit. By embedding this circuit into a microwave cavity, whose electrical field can be coupled to the charge, we realize an artificial spin-photon interface. A second project, started during this thesis, focuses on using quantum dot circuits as model systems for studying condensed matter problems. This project consists in coupling, via a microwave cavity, a superconducting qubit, that will serve as a delicate probe, and single quantum dot circuit. Such a circuit can display several behaviors including the Kondo effect which is intrinsically a many-body effect. In this work, we present both a theoretical study of some possible outcomes of this experiment, and experimental developments. Finally, a theoretical proposition to detect the self-adjoint character of Majoration fermions using a microwave cavity, is presented.

Keywords

cQED, quantum dots, spin, carbon nanotube